

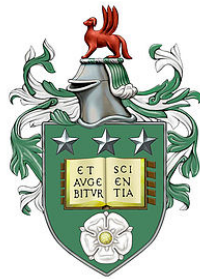
GRAVITY-DRIVEN THIN LIQUID FILMS: RIVULETS AND FLOW DYNAMICS

by

David Ronald James Slade

Submitted in accordance with the requirements for the degree of

Doctor of Philosophy



The University of Leeds
School of Mechanical Engineering

September 2013

The candidate confirms that the work submitted is his own, except where work which has formed part of jointly authored publications has been included. The contribution of the candidate and the other authors to this work has been explicitly indicated below. The candidate confirms that appropriate credit has been given within the thesis where reference has been made to the work of others.

ABSTRACT

The work presented in this thesis focuses on the classical problem of gravity-driven thin films flowing over rigid substrate. Two problems are considered, the formation of rivulets at the advancing front of a spreading liquid and the inner flow structures formed when a continuous fluid film flows over a substrate on whose surface topographical features are present. The governing equations for each problem are thus formulated in two distinct forms: one using the long-wave approximation theory and the other the full Navier-Stokes and continuity equations. Accordingly, two state-of-the-art computational methodologies are developed and utilised to extract tractable numerical solutions from the two equation sets.

The first problem of rivulet formation, explored using an error-controlled adaptive multigrid method to solve the lubrication equations, builds on the seminal work of Huppert (1982). By constructing a systematic and thorough data set for both fully and partially wetting liquids, a new expression for the wavelength of the rivulet pattern is obtained incorporating the wetting properties of the film. Long-time solutions uncover the transient dynamics that are associated with rivulet formation such as the merging of neighbouring fingers. The study is extended to consider film flow on the outer and inner surfaces of a cylinder; curvature effects becoming prevalent as the radius of the cylinder decreases. The cylinder's circumference counter-acts curvature effects in that at a critical value, the evolution of the contact line is restricted to a single rivulet. The impact of surface heterogeneities (topographic and chemical), as well as the presence of surface tension gradients, on rivulet evolution is also explored.

Distinctly different in focus, the induction of the transport of liquid from separated re-circulating regions in the valleys of substrate topography is investigated. Results from this preliminary work demonstrate how pulsed surface waves passing over the topography to break the symmetry and excite the separatrix, forming lobes which transport liquid across the boundary between the bulk and eddy flow. Using particle

tracking calculations to visualise this phenomena reveals the dependence of the transport enhancement on the size of the free-surface disturbance created.

PUBLICATIONS

1. D. Slade, S. Veremieiev, Y. C. Lee, and P. H. Gaskell. Gravity-driven thin film flow: The influence of topography and surface tension gradient on rivulet formation. *Chemical Engineering and Processing: Process Intensification*, 68(0):7–12, 2013.
2. D. Slade, S. Veremieiev, Y. C. Lee, and P. H. Gaskell. Gravity-driven thin film flow: The influence of topography and surface tension gradient on rivulet formation. *Proceedings of Seventh International Conference on Computational Fluid Dynamics (ICCFD7)*, 2012.
3. P. H. Gaskell, D. Slade, S. Veremieiev, and Y. C. Lee. Three-dimensional thin film flow problems solved accurately and efficiently: Rivulet formation, merger and evolution. *ECCOMAS 2012 - European Congress on Computational Methods in Applied Sciences and Engineering, e-Book Full Papers*, pages 1410–1420, 2012.

Work appearing in Chapter 4 published in "Rivulet evolution in gravity-driven thin-film flow", Proceedings of ICCFD7 (2012) - Slade, Veremieiev, Lee, Gaskell & "Three-dimensional thin film flow problems solved accurately and efficiently: rivulet formation, merger and evolution", ECCOMAS 2012, e-book full papers, pg 1410-1420 (2012) - Gaskell, Slade, Veremieiev, Lee All work completed by candidate - initial multigrid code provided by Lee, general supervision and corrections by Veremieiev and Gaskell

Work appearing in Chapter 5 published in "Gravity-driven thin film flow: the influence of topography and surface tension gradient on rivulet formation", Chemical Engineering and Processing: Process Intensification, Vol 68, pg 7-12 (2013) - Slade, Veremieiev, Lee, Gaskell All work conducted by candidate - guidance and supervision by other authors.

ACKNOWLEDGEMENTS

While the work contained within this thesis was primarily undertaken by myself, the realisation of the research would not have been achieved without the help of a number of key contributors. Firstly, I would like to express my utmost gratitude to my supervisors Prof. Philip H. Gaskell for giving me the opportunity to continue my academic journey, introducing me to the field of thin film flow and for demonstrating great patience while helping me progress and the guidance, advice and mathematical skills of Dr. Sergii Veremieiev which were invaluable in progressing the research. My thanks also extend to Dr. Yeaw Chu Lee for his support and guidance, particularly during my first year.

I'd also like to acknowledge the help of the technical and I.T. support team within the department and those who maintain and run the high performance computing cluster ARC1.

I'd like to acknowledge Dr. Hossein Ahmadian, Dr Richard Porter and the other academics and researchers involved for giving me the opportunity to undertake work in the University of Leeds-Procter & Gamble simulation centre during my last year.

The support and friendship from a number of people made my time in Leeds an incredibly fun one. My colleagues at the university; Rai, Falko, Yugal, Nick, Louise, Jen, Michael and the many others who made coming to work such an enjoyable experience. Of course a special mention of my roommates from the Magnet; Rick for housing me when I was homeless, Heskey for finding enthusiasm and debate in every subject and Graham for his entertaining wanton acts of destruction and mixed grills. Those outside university for providing me with a distraction when needed including Chris, Steve, Lianne, Lewis, Hunter, all the hockey boys and Susie for somehow coping with me.

Finally, my deepest gratitude to all my family for all their support and encouragement - my mum Anne, dad Mike, brother Peter and my niece Ava.

Contents

1	Introduction	1
1.1	Motivation	2
1.2	Stability of thin-films	4
1.2.1	Surface waves and topography	4
1.2.2	Rivulet phenomena	6
1.2.3	Effect of substrate heterogeneities on rivulets	11
1.3	Flow on heterogeneous surfaces	15
1.3.1	Flow over topography: Inner flow transport	17
1.4	Thesis outline	22
2	Mathematical formulation	25
2.1	Lubrication approximation - Rivulet formation	27
2.1.1	Governing equations	27
2.1.2	Contact line approach: disjoining pressure	32
2.1.3	Boundary conditions	39
2.1.4	Initial conditions	40
2.1.5	Topography definition	40
2.1.6	Linear stability analysis	41
2.2	Navier-Stokes equations - Inner flow structures	42
2.2.1	Non-dimensional governing equations	42
3	Method of solution	45
3.1	Numerical methods for investigating thin-film coating flows	46

3.1.1	Long-wave approximation	46
3.1.2	Three-dimensional solutions	47
3.1.3	Solving the Navier-Stokes equations	49
3.2	Lubrication equations	51
3.2.1	Spatial discretisation	51
3.2.2	Temporal discretisation	52
3.2.3	Adaptive multigrid strategy	54
3.3	Navier-Stokes equations	61
3.3.1	Discretisation	62
4	Long-time rivulet formation on planar substrates	71
4.1	Long-time rivulet formation - results	73
4.1.1	Fully wetting fluid	74
4.1.2	Partially wetting fluid	83
4.1.3	General expression for wavelength	91
4.1.4	Varying the inflow condition	94
4.2	Summary	97
5	Influence of surface tension gradient, substrate chemical heterogeneity and topographical features on rivulet formation	99
5.1	Constant surface tension gradient	100
5.1.1	Governing equations	100
5.1.2	Results	101
5.2	Chemical heterogeneity	110
5.2.1	Numerical results	111
5.3	Summary	121
6	Rivulet flow on the surface of a vertically aligned cylinder	123
6.1	Background	124
6.2	Governing equations of rivulet flow on a vertically aligned cylinder .	125
6.2.1	Cylindrical substrate LSA	127

6.3	Results : Three-dimensional numerical solutions	128
6.3.1	Fully wetting fluid	128
6.3.2	Partially wetting	138
6.3.3	Regime model for wavelength	147
6.3.4	Flow down the inner surface of a vertically aligned cylinder	148
6.4	Summary and Discussion	154
7	Preliminary investigations of material transport enhancement in film flows over wavy substrate	157
7.1	Turnstile lobes - transport enhancement	158
7.2	Flow visualisation	161
7.2.1	Streamlines	162
7.2.2	Eddy centre	162
7.2.3	Particle tracking	162
7.2.4	Stable and unstable manifolds	163
7.3	Results: material transport enhancement	163
7.3.1	Inner flow structures	164
7.3.2	Turnstile lobe transport: pulsed flow	169
7.3.3	Inertially induced eddy	182
7.4	Summary	183
8	Conclusion and Further Work	185
8.1	Conclusions of current study	186
8.2	Suggested future work	191
A	Long-wave approximation	194
A.1	Governing equations	195
B	Governing equations of rivulet formation on a vertically aligned cylinder	198
B.1	Long-wave approximation	199
B.2	Discretisation	204

B.2.1	Spatial discretisation	204
B.2.2	Temporal discretisation	205
C	Linear stability analysis	206
C.1	Planar, inclined substrate	207
C.1.1	Travelling wave solution	207
C.1.2	Perturbation Analysis and Eigenvalue Problem	208
C.2	Analysis of vertically aligned cylinder	209
C.2.1	Travelling wave solution	209
C.2.2	Perturbation Analysis	210
D	Adaptive multigrid performance	211
D.1	Efficiency of multigrid procedure	212
D.2	Jacobian calculation: Numerical vs Analytical	219
D.2.1	Numerical Jacobians	219
D.2.2	Analytical form of the Jacobian	219
D.2.3	Comparison of the two approaches	220
D.3	Relaxation schemes	222
D.3.1	Newtonian relaxation	222
D.3.2	Broyden's secant method	224
D.3.3	Conjugate gradient method	225
D.4	Comparison of iterative smoother efficiency	229
D.4.1	Two-dimensional problem	229
D.4.2	Three-dimensional flow	233
	Bibliography	236

List of Figures

1.1	Rivulet formation as demonstrated by Huppert (1982); finger shaped fluid channels growing from the advancing front of (e) silicone oil and (g) glycerin.	6
1.2	Examples of rivulets encountered when pouring sauce on a pudding or seen at the famous gun barrel opening sequence in a ‘Bond’ movie.	7
1.3	Sketch of the different forms of rivulets that emerge at the advancing front of a (a) fully wetting and (b) partially wetting fluid Silvi and Dussan (1985).	11
1.4	<i>Top:</i> Rivulet flow over randomly distributed heterogeneous patches from Zhao and Marshall (2006). The contact angle associated at each co-ordinate (x, y) using a random correlation function controlled by correlation length, l ; (a) $l = 6$, (b) $l = 13$ and (c) $l = 24$. Three time snapshots are shown - (i) $t = 12$, (ii) $t = 24$ and (iii) $t = 33$. Flow is from left to right and contours shown at $h = 0.2, 0.6, 1$ and 1.4 , grey shading is used when $h > 1.4$. <i>Bottom:</i> The network of patches created by the random function assigning the associated contact angle to the substrate; white areas are fully wetting, grey areas indicate where the contact angle is greater than 15° and in black shaded areas the contact angle is less than 9°	12

1.5	Example of a continuous thin film of water flowing over a peak and trench topography of non-dimensional height 0.25 from Gaskell, Jimack, Sellier, Thompson and Wilson (2004). Evident to see in the contour plots of free-surface height is the bow-wave shaped peak around the upstream topography boundary and the downstream surge not captured by two-dimensional simulations. The arrow on the plots indicates the direction of flow.	15
1.6	An example of eddy formation in flow under Stokes flow conditions in the topography of an undulating substrate, with amplitude of the wavy topography defined as $a = 2\pi/5$ and inclined at 45° to the horizontal, for increasing film thickness; (a) $h = 16\pi/25$, (b) $h = 18\pi/25$ and (c) $h = 24\pi/5$. The left hand side shows experimental observations of Wierschem and Aksel (2003) (with complex variable numerical solutions overlaid) and the right column showing corresponding finite element numerical results of Scholle <i>et al.</i> (2008).	18
1.7	Experimental images of mixing between two counter-rotating rollers via lobe formation, Wilson <i>et al.</i> (2006); the speed of one of the rollers is varied inducing a turnstile lobe mechanism of fluid transport creating the mixing pattern that can be observed.	21
2.1	Schematic of the side view of thin film flow down a flat plate (width, W_p , length, L_p) inclined at an angle α to the horizontal, featuring an advancing front before the onset of instability. The surface of the substrate is shown, for the sake of generality, to contain a rectangular topography (length L_t , width W_t and height/depth $S(X, Y)$). The film is fed by a constant inflow at the upstream boundary and H_0 denotes the asymptotic film thickness and — the contact line. . .	27
2.2	Schematic showing a liquid front spreading over a substrate displacing the vapour phase.	33

2.3	Schematic showing a spreading liquid with a contact angle of θ_c , displacing an area of Δa of the solid-vapour interface.	34
2.4	A diagram, from (Schwartz and Eley, 1998), of the contact line area; an integrated force balance is performed on the dotted area in the x direction to find the coefficient of the disjoining pressure term, B	36
2.5	Schematic of the side view of thin film flow down a plate (length, L_x) inclined at an angle α to the horizontal, featuring a wave-like trench of depth $\bar{A}(t)$ and wavelength $\bar{\lambda}_t$. The film is fed by a constant inflow at the upstream boundary and H_0 denotes the asymptotic film thickness.	43
3.1	Schematic diagram of the full multigrid algorithm incorporating one FAS W-cycle over four grid levels, \mathcal{G}_k with $k \in [0, 3]$. The solution on each grid \mathcal{G}_k , $k \in [1, 3]$, at the end of the FAS W-cycle on each level, k , is indicated by u_k ; the initial solution given by the coarse grid solution is u_0 . Full multigrid interpolation is indicated at the end of each FAS-cycle by Π_{k-1}^k . Restriction and interpolation is performed using inter-grid transfer operators R_k^{k-1} and I_{k-1}^k respectively, between grid levels \mathcal{G}_k and \mathcal{G}_{k-1}	59
3.2	Local barycentric coordinates for a triangular element in the domain Ω . \mathbf{u}/\mathbf{x} -nodes are denoted by both filled and unfilled circles, p -nodes by unfilled circles only.	63
3.3	An illustration of spines used to track the free-surface. Each base node \mathbf{x}_k^b and direction vector \mathbf{d}_k is associated with a spine k	66
4.1	Definitions of width, W_r , length, L and wavelength, λ of the rivulets.	73

4.2	free-surface colour maps of film thickness for the flow of ‘Fluid B’ down an inclined planar substrate at long times; cf the experiments of Johnson, see Figure 5.11 in (Johnson, 1997); (a) $\alpha = 13.9^\circ$, (b) $\alpha = 27.9^\circ$, (c) $\alpha = 60^\circ$ and (d) $\alpha = 90^\circ$. Lengths and heights are given in centimetres. The vertical axis is shifted to keep the advancing front central.	75
4.3	Colour maps of the evolution of the advancing front of ‘Fluid B’ on a substrate, with $\alpha = 90^\circ$, at four different increasing non-dimensional times showing the development and merging of rivulets - note that these snapshots are before the one shown in Figure 4.2(d). The ordinate in (b),(c) and (d) is shifted to keep the rivulets central to the plot.	77
4.4	(a) Contact line evolution for a thin film of fully wetting ‘Fluid B’ on a substrate inclined at 90° plotted with $\Omega = (0, 150) \times (0, 200)$. (b) is the capillary ridge height for $Y = 3.9\text{cm}$ and $Y = 10.7\text{cm}$ (indicated on (a) by dotted lines). At $y = 39$ no merging takes place so the height is relatively steady, however at $y = 105$ there is merging between two neighbouring rivulets; when they merge the capillary ridge height exhibits a sharp increase before settling to a height slightly higher than before the merger process.	78
4.5	(a) The final, long-time wavelength, λ_f , of the rivulet pattern at the advancing front for ‘Fluid B’. Comparison is between the experiments of (Johnson <i>et al.</i> , 1999) and the present work. For comparison purposes predictions via linear stability analysis (LSA), λ_f^{LSA} , are also provided. The grey shaded area indicates predicted linear stability. (b) The width of the rivulets, W_r , for long times of ‘Fluid B’ plotted against inclination angle, results are from numerical solutions and the experiments of Johnson <i>et al.</i> (1999).	80

4.6	LSA growth rates, ω , computed for the base states of the problem modelled for comparison to experiments by Johnson <i>et al.</i> (1999) for ‘Fluid B’ and for $\alpha = 13.9^\circ, 27.9^\circ, 60^\circ$ and $\alpha = 90^\circ$	82
4.7	Colour maps of the long-time evolution of the advancing front of ‘Fluid A’ on a substrate, with $\alpha = 36^\circ$, at three different times where the equilibrium contact angle, θ_c , is 0° on the left hand column, 20° in the centre column and 38° on the right. Note: the ordinate in the right column is shifted to keep the rivulets central to the plot.	86
4.8	Colour maps of the long-time evolution of the advancing front of ‘Fluid A’ on a substrate, with $\alpha = 60^\circ$, at $t = 30$, $t = 100$ and $t = 180$ where the equilibrium contact angle, θ_c , is 0° on the left hand column and 38° on the right.	87
4.9	Finger growth at the advancing front of ‘Fluid A’ flowing on an inclined plane with (a) different values of α with $\theta_c = 38^\circ$; (b) different values of θ_c (and S_{θ_c}) at $\alpha = 36^\circ$	88
4.10	(a) The long-time wavelength, λ_f of the rivulet pattern at the advancing front of ‘Fluid A’ for a range of inclination angles. Comparison is between the experiments of (Johnson <i>et al.</i> , 1999) and the present work when $\theta_c = 38^\circ$ and 0° . LSA prediction is shown for comparison purposes. (b) The width of the rivulets that emerge at the advancing front of ‘Fluid A’, when $\theta_c = 0^\circ$, $\theta_c = 15^\circ$ and $\theta_c = 38^\circ$, plotted against the inclination angle, α . Plotted for comparison are the experimental results of Johnson (1997).	89
4.11	LSA growth rates, ω , computed for a range of wavenumbers, k , generated from a linear stability analysis of ‘Fluid A’ on an inclined substrate with $\alpha = 60^\circ$. The analysis was performed for three different contact angles, $\theta_c = 0^\circ, 15^\circ$ and 38° . The associated base states are shown inset demonstrating the change in the capillary ridge height with θ_c	90

4.12	Relationships extracted from numerical data of current study, given by equation (4.2), shown for fully wetting fluid and when $\theta_c = 38^\circ$. The results of Johnson <i>et al.</i> (1999) are plotted for comparison; ‘Fluid A’ has a contact angle of 38° and ‘Fluid B’ is considered to be fully wetting. Also shown are the fits found by Huppert (1982) (interpreted by Troian <i>et al.</i> (1989)) and Johnson <i>et al.</i> (1999).	92
4.13	Results given by equation (4.2) for a range of spreading coefficient, S_{θ_c}	92
4.14	Free-surface colour map of ‘Fluid B’ flowing down a vertically inclined planar substrate with a temporally varying inlet given by equation (4.3) with amplitude fluctuation of $A_r = 0.5$, wavelength $3\lambda_f$ and frequency $f = 1/15$; also shown is the corresponding contour plot.	95
4.15	Free-surface colour maps of ‘Fluid B’ flowing down a planar substrate inclined at 27.9° with a temporally varying inlet controlled by parameters A_r (0.5 in all cases), wavelength $\beta\lambda_f$ and frequency f . (a) $\beta = 4, f = 1/60$; (b) $\beta = 6, f = 1/40$; (c) $\beta = 1, f = 1/60$; (d) no time dependence.	96
5.1	Color maps of free-surface profile for a water film spreading on a planar substrate inclined at 65° . The left profiles are for flow with no surface tension gradient, the middle column is flow when $\tilde{\tau} = -0.25$ and the right hand side is when $\tilde{\tau} = 0.25$. The top profiles are at $t = 100$ and the bottom profiles are at $t = 200$	103
5.2	Colour maps of the free-surface height, $h + s$, for gravity-driven flow over a planar substrate, $s_0 = 0$, and $\alpha = 65^\circ$: the rivulet pattern formed corresponds to $t = 50$ (top), $t = 100$ (middle) and $t = 150$ (bottom) when $\tilde{\tau} = -0.25$ (left), $\tilde{\tau} = 0.0$ (centre) and $\tilde{\tau} = 0.25$ (right), respectively. The streamwise direction of flow is from top to bottom in each sequence.	104

5.3	Colour maps of the free-surface, $h + s$, showing rivulet formation for flow over substrate containing different topographical heterogeneities, $ s_0 = 0.2$ and $\theta = 65^\circ$; top row $t = 100$, bottom row $t = 258$ (bottom). The substrate contains (from left to right) no topography; two square trench topographies; two peak topographies (dashed outline); and a square trench and a square peak topography. $\tilde{\tau} = -0.25$ in all cases. The streamwise direction of flow is from top to bottom in each sequence.	105
5.4	<i>Top:</i> Colour maps of free-surface film height for the case of a thin film climbing up a vertically inclined substrate due to Marangoni stress, $\tilde{\tau} = 1.6$ in this case. The direction gravity is acting is shown in (d) for clarity. <i>Bottom:</i> A typical evolution of a Marangoni driven advancing front from the experiments of Cazabat <i>et al.</i> (1990). . . .	107
5.5	The position of the tip of the longest rivulet formed at the advancing front of a $0.86\mu\text{m}$ thick film rising up a vertically aligned plate under the influence of a surface tension gradient of $\tilde{\tau}$. The dashed line indicates the corresponding trough position.	108
5.6	The low wettability patch pattern is shown in the top left figure. Free-surface contour maps showing the progression of the contact line of a thin film flowing down an inclined plane tilted at 30° onto a substrate with 5 equally spaced low wettability patches of equilibrium contact angle $\theta_c = 10.0$ and $S_{\theta_c} = 3.5$	111
5.7	Free-surface contour maps showing the progression of the contact line of thin film flowing down an inclined plane tilted at 30° onto a substrate with 5 equally spaced low wettability patches of equilibrium contact angle $\theta_c = 10.0$ and $S_{\theta_c} = 3.5$	112
5.8	Contact line plots of a thin water film flowing down an inclined plane tilted at 30° on a substrate containing areas of low wettability, indicated by grey patches, where $\theta_c = 10^\circ$ and $S_{\theta_c} = 3.5$	114

5.9	Three-dimensional free-surface plots to demonstrate the dramatic effect on rivulet formation of large areas of substrate heterogeneity. The fluid is a $100\mu\text{m}$ thick water film flowing down a substrate inclined at 65° with contact angle $\theta_c = 0^\circ$ on the majority of the substrate. The outline of the patches of low wettability are indicated with a white dashed line; on the patches $\theta_c = 10^\circ$	115
5.10	Rivulet formation and evolution for the flow of a thin film of ‘Fluid A’ on a vertically aligned substrate containing a variety of chemical heterogeneous patterned regions. The plots show the outline of the contact line as it progresses with time. Grey areas indicate areas where $\theta_c = 35^\circ$; the white areas denote fully wetting regions, $\theta_c = 0^\circ$.	117
5.11	Rivulet formation and evolution for the flow of a thin film of ‘Fluid A’ on a vertically aligned substrate containing a variety of chemical heterogeneous patterned regions. The plots show the outline of the contact line as it progresses with time. Grey areas indicate areas where $\theta_c = 35^\circ$; the white areas denote fully wetting regions, $\theta_c = 0^\circ$.	118
5.12	Contact line outline plots for a thin film of ‘Fluid A’ spreading on a substrate inclined at $\alpha = 36^\circ$ to the horizontal. (a) shows the development of the film on a fully wetting area before crossing onto an area of low wettability where the equilibrium contact angle is $\theta_c = 30^\circ$ (indicated by greyed areas); (b) shows the opposite arrangement.	118
6.1	Schematic view of thin film flow down a vertically inclined cylinder (circumference, C_R and length, L_R). The film is fed by a constant inflow at the upstream boundary and H_0 denotes the asymptotic film thickness. The radius to any arbitrary point in the Y direction is denoted by R . Note: the film thickness is exaggerated for clarity. .	125

6.2	Schematic view, three-dimensional (left) and cross-sectional (right), of thin film flow down a vertical cylinder (circumference, C_R and length, L_R). The film is fed by a constant inflow at the upstream boundary and H_0 denotes the asymptotic film thickness. Note: the film thickness height has been exaggerated for the sake of clarity.	126
6.3	Unfolded free-surface colour maps showing rivulet formation at the advancing front of a film of fully wetting silicone oil on the outside surface of a cylinder with radius 1.27cm.	129
6.4	Free-surface colour maps showing rivulet formation at the advancing front of a film of fully wetting silicone oil spreading down the outside surface of a cylinder of radius 1.27cm plotted on a three-dimensional representation of the cylinder.	130
6.5	Unfolded free-surface colour maps - a three-dimensional representation - for the flow of silicone oil down the surface of a cylinder with four different radii; (a) 3.5cm, (b) 1.27cm, (c) 0.635cm and (d) 0.159cm. C.f. Figure 6.4.	131
6.6	Free-surface colour maps of Figure 6.5 transferred onto the corresponding cylinder for visualisation purposes.	132
6.7	This figure shows dimensional rivulet length against scaled time for flow on three different cylinders with radii $R_0 = 3.5, 1.27,$ and 0.635 cm.	133
6.8	Wavelength of the rivulet pattern that emerges at the advancing front of a silicone oil film. Also plotted are the findings of Huppert (Huppert, 1982) and the current author for predicting the wavelength on a vertically inclined plane. Experimental data points for silicone oil of Smolka and SeGall (Smolka and SeGall, 2011) are also provided.	134
6.9	Results of linear stability analysis for flow of silicone oil coating a cylinder of radius 3.81cm performed for different values of precursor film thickness, h^*	134

6.10	Results of linear stability analysis for flow of silicone oil coating a cylinder of radius 3.81cm and 1.27cm, the values of ϵ/B_{OR} are indicated on the figure.	135
6.11	The average width of the rivulets for a range of ϵ_R/B_{OR} plotted with the experimental value of Smolka and SeGall (2011). Results here are for silicone oil (fully wetting) and glycerin (partially wetting, $S_{\theta_c} = 2.35$	135
6.12	Unfolded free-surface colour maps visualising the formation of rivulets at the contact line of a glycerin film flowing down the outer surface of a cylinder with radius 0.953cm plotted on a three-dimensional cylinder with $S_{\theta_c} = 2.35$ ($\theta_c = 40^\circ$).	139
6.13	Free-surface colour maps visualising the formation of rivulets at the contact line of a glycerin film flowing down the outer surface of a cylinder with radius 0.953cm plotted on a three-dimensional cylinder with $S_{\theta_c} = 2.35$ ($\theta_c = 40^\circ$). Plotted on the cylinder to visualise the reality of the flow.	140
6.14	Unfolded free-surface colour maps for the flow of glycerin down the surface of a cylinder with radius 0.953cm plotted on a three-dimensional cylinder. The flows are identical except for the contact angle. The range of spreading coefficient is $S_{\theta_c} =$ (a) 0.0, (b) 0.61 and (c) 2.35, corresponding to $\theta_c = 0^\circ, 20^\circ$ and 40°	141
6.15	Free-surface colour maps for the flow of glycerin down the surface of a cylinder with radius 0.953cm plotted on a three-dimensional cylinder. The flows are identical except for the contact angle. The range of spreading coefficient is $S_{\theta_c} =$ (a) 0.0, (b) 0.61 and (c) 2.35, corresponding to $\theta_c = 0^\circ, 20^\circ$ and 40° . Flows plotted on the cylinder.	142
6.16	Rivulet length against time for glycerin coating a cylinder of radius 0.953cm. Four different non-dimensional spreading coefficients are compared with one fully wetting and two partially wetting films - $S_{\theta_c} = 0.0, 0.61,$ and 2.35	143

6.17	Unfolded free-surface visualisations of glycerin coating a cylinder with varying radii but constant contact angle, 40° and $S_{\theta_c} = 2.35$. The four radii shown are (a) 0.4cm, (b) 0.7cm, (c) 2cm and (d) 2.5cm respectively.	144
6.18	Free-surface visualisations of glycerin coating a cylinder with varying radii but constant contact angle, 40° and $S_{\theta_c} = 2.35$. The four radii shown are (a) 0.4cm, (b) 0.7cm, (c) 2cm and (d) 2.5cm respectively.	145
6.19	Wavelength of the rivulet pattern that emerges at the advancing front of a glycerin film. Also plotted are the findings of Huppert (1982) and the current author for predicting the wavelength on a vertically inclined plane. Experimental data points for silicone oil of Smolka and SeGall (2011) are also provided.	146
6.20	Regime model plotted against numerical solutions for silicone oil (top) and glycerin (bottom). Experimental points are provided for reference, and critical values of ϵ_R/Bo_R are indicated by grey dashed lines. The regimes are indicated as ‘Planar’, ‘Cylinder’ and ‘Single’.	149
6.21	Illustration of the curvature of the inner and outer surfaces of the cylinder and how this affects the shape of the rivulet.	150
6.22	Free-surface visualisations of fully wetting silicone oil coating the inside surface of a cylinder of radius 0.635cm.	151
6.23	Unfolded free-surface visualisations of partially wetting glycerin ($S_{\theta_c} = 2.35$) coating the inside surface of a cylinder of radius 2.0cm.	152
6.24	Unfolded free-surface visualisations of fully wetting silicone oil coating the outside (left) and inside (right) surface of a cylinder of radius 1.27cm.	153
6.25	Unfolded free-surface visualisations of a partially wetting ($\theta_c = 40^\circ$, $S_{\theta_c} = 2.35$) glycerin film coating the outside (left) and inside (right) surface of a cylinder with radius 1.5cm.	153

7.1	Schematic diagram of the domain of interest, the wave topography is located nearer the upstream inlet boundary to allow the pulse to pass downstream to the outlet boundary condition. The domain is also subject to an inclination angle, α	159
7.2	(a) A schematic diagram of the unstable and stable invariant manifolds, $W_A^u(t)$ and $W_B^s(t)$, of the upstream and downstream hyperbolic separation points, A and B . The intersection of the manifolds, at points p, q , and r , create two lobes, L^{pq} and L^{qr} , that facilitate the transport of material across the boundary between overlying bulk flow and encapsulated eddy flow. (b) Steady-state schematic of the same flow showing the eddy region separated from the overlying bulk flow by the separatrix.	159
7.3	A sketch to demonstrate the turnstile lobe mechanism between time t_{n-1} and t_n	161
7.4	Streamlines of the unperturbed flow depicting the eddy in the topography of the substrate below the bulk flow.	166
7.5	Maximum free-surface disturbance above the centreline of the valley of the topography with increasing strength of the pulsed inlet via an increase in F_a	166
7.6	The time evolution of the film height above the centre-line of the topography and the change in associated eddy depth co-ordinate z_c	167
7.7	The maximum shift in the eddy centre in the x -direction during the pulsed flow.	168
7.8	The maximum and minimum eddy depth co-ordinate, D_e , as a pulse crosses above the topography for a range of F_a	168
7.9	Time evolution of particles entrapped within the eddy found in the valley of the substrate geometry, showcasing the enhancement of transport of material into the overlying flow. Here, the pulse strength is $F_a = 20$ and the inlet is pulsed at $t = 15$ and $t = 50$	171

7.10	Time evolution of particles as in Figure 7.9 but with a stronger pulse, $F_a = 40$	172
7.11	A snapshot from the experiments of Wierschem and Aksel (2004) showing the turnstile lobe mechanism for a film of liquid with $Re = 15$ flowing over a wavy topography. The candidate gratefully acknowledges the generosity of Andreas Wierschem and Markus Scholle in sharing the fascinating videos of their experimental work.	173
7.12	Long-time particle positions, $t = 145$, after experiencing two pulses of the same strength for a range of F_a ; (a) 5, (b) 10, (c) 15, (d) 20 and (e) 40.	174
7.13	Portions of the unstable and stable manifolds demonstrating the turnstile lobes that are formed by the pulsed inlet condition.	175
7.14	Percentage of particles remaining in the topography as time evolves for a range of strength of pulse (time of pulse indicated by dashed lines).	176
7.15	Percentage of particles remaining in the topography as time evolves when $F_a = 20$ for two pulses and five pulses (time of pulse indicated by dashed line).	176
7.16	<i>Top:</i> Number of particles removed via one pulse as the pulse strength increases. The two examples visualised show the particle tracers been transported in lobes for $F_a = 10$ and $F_a = 30$. <i>Bottom:</i> Estimated area of the outward moving turnstile lobe. Visualised are portions of the stable and unstable manifolds forming lobes for $F_a = 20$. The lobe area is shaded in green.	177
7.17	Particle tracking showing the stirring and transport enhancement created by pulsing the inlet condition multiple times.	179
7.18	Unstable and stable manifolds for multiply pulsed situation demonstrating the transport enhancement via turnstile lobe mechanism and the increased mixing.	180

7.19	<i>Left:</i> Streamlines of the steady flow of a film flowing over a wave topography with $Re = 10$, no eddy is present at $t = 10$. <i>Right:</i> Streamlines at $t = 16.3$ as the free-surface disturbance created by pulsing the inlet velocity with $F_a = 5$ reaches the topography - an inertially induced eddy is created.	180
7.20	The free-surface height above the topography and the eddy height, D_e . $D_e = 0$ indicates no eddy present.	180
7.21	The relative eddy motion of the two eddies present in topography with (left) $A_t = 0.7$ and (right) $A_t = 1$	181
7.22	Illustrative particle tracking showing the two areas of separated flow within a topography of amplitude, $A_t = 1$	182
7.23	<i>Left:</i> Streamlines of the steady flow of a film flowing over a wave topography with $Re = 30$, no eddy is present at $t = 10$. <i>Right:</i> Streamlines at $t = 16.3$ as the free-surface disturbance created by pulsing the inlet velocity with $F_a = 0.2$ reaches the topography - the eddy is suppressed.	183
D.1	The number of nodes on the specified finest level, K , is shown in (a) for three different variations of the multigrid method; strategies A,B and C. The corresponding CPU time for each K is then presented in (b). This is for the case of a thin film of ‘Fluid A’ on a substrate inclined at 60° where the coarsest grid is 257×65 nodes and the computational domain is $(0, 400) \times (0, 100)$	214
D.2	Plot to show how the number of nodes on the finest grid level, K , changes with the tolerance value for grid devolution, TOL_d	215

D.3	Graph showing the significant decrease in CPU time required when devolution is employed compared to when only mesh refinement is active in the multigrid algorithm. The solution is for identical initial conditions of a film of ‘Fluid A’, considered as fully wetting, flowing down a substrate inclined at 60° to the horizontal. The CPU time increases per iteration as the number of nodes increases due to the growth of rivulets at the advancing front area.	215
D.4	Left hand side figures show colour maps of the free-surface profiles of the advancing front of a water-glycerin film spreading on a substrate inclined at 60° at $t = 50, 100$ and 200 . The associated composite, finest multigrid levels are shown on the right hand side exhibiting grid refinement and coarse grid devolution.	217
D.5	The refined grid structure used in the multigrid solution of thin film flow for a fully wetting liquid spreading on an inclined substrate with $\alpha = 60^\circ$ when adaption strategies B), shown in (a), and C), shown in (b), (c) and (d), are utilised. The contact line is indicated in white and develops in (b), (c) and (d) which show subsequent times.	218
D.6	Free-surface profiles for continuous thin film flow over a trench topography; the left hand side is the profile found when using an analytical Jacobian, the right hand side the corresponding profile when a numerical approach is utilised. Flow direction is from top to bottom.	221
D.7	Colour maps of the percentage change of film height between the two solutions shown in Figure D.6 over the computational domain. .	222
D.8	Free-surface profiles for two-dimensional thin film flow over different spanwise topographies.	231
D.9	Free-surface profile of flow over three different trenches: Case 1,2 and 3, which are ordered from top to bottom.	234

List of Tables

4.1	Table of the fluid properties that are utilised here. The two fluids were used in experiments in Johnson <i>et al.</i> (1999).	72
5.1	Table of wavelength, λ , of the advancing front of a climbing film for a range of parameters obtained from numerical solutions and compared with the experimentally measured values in Cazabat <i>et al.</i> (1990), λ_{caz}	108
D.1	Time taken to complete a full numerical simulation involving 5002 time steps for two-dimensional thin film flow over various topographies.	230
D.2	Parameters of the numerical simulation of flow over topography. . .	231
D.3	Time taken to complete a full numerical simulation using a FMG and FAS method with time and mesh adaptivity for three-dimensional thin film flow over various topographies.	233

Chapter 1

Introduction

Contents

1.1	Motivation	2
1.2	Stability of thin-films	4
1.2.1	Surface waves and topography	4
1.2.2	Rivulet phenomena	6
1.2.3	Effect of substrate heterogeneities on rivulets	11
1.3	Flow on heterogeneous surfaces	15
1.3.1	Flow over topography: Inner flow transport	17
1.4	Thesis outline	22

1.1 Motivation

The deposition of thin liquid films is common place in many manufacturing processes and understanding the underlying physics that determine the quality of the final coating is vital in achieving even, defect-free surfaces. For example, the coating of devices such as television screens and microchips is required in a fast, continuous manner with a final uniform, defect-free surface being the goal. Such features are also encountered in medical and naturally-occurring phenomenon and thus the study of coatings encompasses a wide-range of applications and so garner much attention from the research community at large, a comprehensive summary of which can be found in the review paper by Craster and Matar (2009).

Much research has been undertaken and understanding achieved regarding thin film flows on flat, homogeneous substrates driven by gravity (Huppert, 1982), thermal/surface tension gradients (Cazabat *et al.*, 1990) or forces induced by spin-coating (Melo *et al.*, 1989). Flow on more complex, heterogeneous geometries containing topographical features or made up of different chemical compounds giving rise to a variation in wetting properties leads to considerable challenges both experimentally and computationally. To fully understand coatings in a manufacturing context, and the many others besides including those encountered in the field of microfluidics Lin (2011), it is necessary to address the role the wetting properties of the fluid, surface heterogeneities and topographies play in determining the final surface coverage. Uniform coverage determines the success and quality of a product, for instance when depositing an anti-reflective coating of a television screen a defect-free final surface is essential as is the case when creating electronic wafers (Schwartz *et al.*, 2004).

Engineering processes involving the manufacture of various devices where the coating flows of interest are a key component include a wide-range of industries. Examples of which include, the manufacture of micro-scale sensors (Menetrier-Deremble and Tabeling, 2006), heat exchanger devices (Focke and Knibbe, 1986), the pro-

duction of distillation trays (de Santos *et al.*, 1991; Stone *et al.*, 2004), flat-bed perfusion chambers (Horner *et al.*, 1998), the optimal design for aeroengine bearing chambers (Baxter *et al.*, 2010) and the de-icing of aircraft wings (Fitt and Pope, 2001). Designing efficient inkjet printers also requires the understanding of liquid motion, specifically droplet spreading, on substrates (Castrejon-Pita *et al.*, 2011; Xiao *et al.*, 2012). Coatings are also at the forefront of future technology that looks to address the increasing energy consumption in the modern world; for instance, the development of OLEDs (organic light-emitting diodes) that may be used in monitors and other electronic devices and which run with less energy needs than standard LEDs (Peters *et al.*, 2013), or the development of solar power cells, which require an in-depth knowledge of the complex coating process involved (Wengeler *et al.*, 2013).

Natural surfaces often have a much less uniform geometry containing random topographies which adds to the complex and fascinating dynamics that are induced. Medically, the understanding of how surfactants affect the spreading of a liquid film on the lungs is essential in treating respiratory distress syndrome (RDS) (Matar and Troian, 1999; Yong Liang *et al.*, 2002), also the coating of flexible tubes (Grotberg, 1994) and the motion of other linings. From an agricultural perspective maximal coverage of a leaf surface with pesticide solutions (Glass *et al.*, 2009) is vital in terms of pest control. Other examples include the lubricant film between the head and the cup of a hip replacement joint (Gao *et al.*, 2007; Meng *et al.*, 2011), the motion of a tear film on a contact lens (Nong and Anderson, 2010) and the formation of biofilms (Duddu *et al.*, 2009).

In the natural world major environmental events such as lava flow (Balmforth and Craster, 2000) and the movement of glaciers and ice sheets (Craster and Matar, 2009) can be thought of as thin film phenomenon.

The work in this thesis focuses on two diverse characteristics of thin-film coatings; the formation of fingers (rivulets) at the advancing front of a spreading film and the inner flow structure of a continuous liquid film flowing over topography. What

follows is a review of related work present in the literature, both theoretical and experimental. The stability of thin-films driven by gravity is considered in Section 1.2, including the theoretical and experimental observations of the rivulet phenomenon which forms a major part of this thesis. Flow on real surfaces is reviewed in Section 1.3 and the disturbance of flow over topography summarised in Section 1.3.1, focusing on how eddy structures found in the liquid are altered which can enhance inner flow transport. Lastly, an outline for the content of the thesis itself is given, Section 1.4.

Subsequently, Section 3.1 gives a summary of the common approaches adopted for the numerical investigation of thin-film flow both the long-wave approximation (Oron *et al.*, 1997) and the full Navier-Stokes and continuity equations.

1.2 Stability of thin-films

Stability considerations are important to understand the parameter space within which a stable flow can be established. The results of such analytical and numerical calculations, as well as corresponding experimental observations, can be used to guide the design of engineering processes or manufactured fluids such as pesticides.

1.2.1 Surface waves and topography

Early work on stability considered two-dimensional gravity driven flow on an inclined flat substrate establishing the existence of a critical Reynolds number, $Re_{crit} = \frac{5}{4} \cot \alpha$, where α is the angle of inclination, beyond which the flow is unstable to long waves, see Yih (1963); Chang (1994). These findings have been verified experimentally by Liu and Gollub (1993, 1994) and Alekseenko *et al.* (1994) who demonstrated the increasing amplitude of noise-driven surface waves with increasing inertia in a falling film.

The influence of inertia and topography has been investigated in a number of experimental studies; there is a strong-coupling between both inertia and topography in gravity-driven flow over a substrate having periodic spanwise topographic features, see Vlachogiannis and Bontozoglou (2002); Wierschem *et al.* (2005). Topography is found to have a stabilising effect on the flow if significantly steep; in the classical step-down topography problem, the capillary ridge generated by this feature is stable for a wide range of parameters due to surface tension and pressure gradients induced by the substrate geometry (Kalliadasis *et al.*, 2000; Kalliadasis and Homay, 2001; Davis and Troian, 2003). Trifonov (2007) showed, for corrugated geometry within a certain range of amplitude and wavelength, that infinitesimal disturbances decay - outside this range the flow is unstable.

Other effects that influence the stability of gravity-driven film flow include insoluble surfactant which has been shown to raise the critical Reynolds number, such that $Re_{crit} = \frac{5}{4} \cot \alpha + \frac{15Ma}{8Ca}$, Blyth and Pozrikidis (2004). Marangoni instability has been observed in thermocapillary driven flows, often manifesting itself as ruptures in the free-surface, as discussed by Davis (1987) and shown theoretically by Burelbach *et al.* (1988) and experimentally by Burelbach *et al.* (1990).

The recent work of D'Alessio *et al.* (2009, 2010); Ogden *et al.* (2011) have extended the knowledge of stability for film flow over undulating substrates. While stabilising the flow at moderate surface tension values, it was found that the bottom topography destabilises the flow at larger surface tension (D'Alessio *et al.*, 2009). When the substrate is heated the same observation is reported; however heating plays a destabilising role on both flat and undulating surfaces (D'Alessio *et al.*, 2010). If the substrate is porous then the interaction of heating and permeability effects destabilise the flow; both factors are also individually responsible for further destabilising the flow if they are increased in magnitude (Ogden *et al.*, 2011).

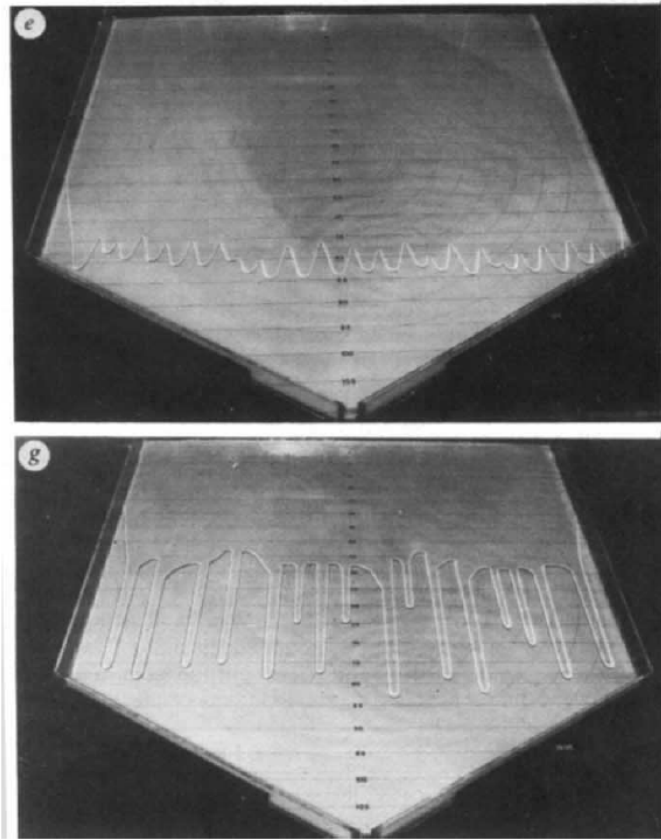


FIGURE 1.1: Rivulet formation as demonstrated by Huppert (1982); finger shaped fluid channels growing from the advancing front of (e) silicone oil and (g) glycerin.

1.2.2 Rivulet phenomena

While much of the literature on the stability of thin film flows is based around surface waves and inertia, there is another classical instability phenomenon which has garnered some attention within the research community, namely rivulet formation; these are finger-shaped structures that form at the advancing front of a spreading liquid film, as shown in the images of Figure 1.1. The instability can influence considerably the efficiency and final surface coverage. More commonly encountered everyday occurrences of rivulets include the pouring of sauce over a pudding or as seen in the opening credits of a ‘Bond’ film, as shown in Figure 1.2

The seminal work of Huppert (1982) first brought the instability that manifests itself as rivulets to a wider audience. He found that, after a short time period after release



FIGURE 1.2: Examples of rivulets encountered when pouring sauce on a pudding or seen at the famous gun barrel opening sequence in a 'Bond' movie.

of a fluid bulk, fingers grew at the subsequent advancing front from the volume of fluid spreading on an inclined perspex plate. The wavelength of the pattern was shown to scale linearly with the capillary length of the fluid (Troian *et al.*, 1989).

Following the interest sparked by the early work of Huppert, further experimental work was undertaken by Silvi and Dussan (1985); de Bruyn (1992); Jerrett and Bruyn (1992); Veretennikov *et al.* (1998); Johnson *et al.* (1999) to name a few. Silvi and Dussan (1985) followed Huppert's original work but by considering both partially and fully wetting fluids they observed very different pattern formation when the wetting properties of the fluids were contrasted. The work of de Bruyn (1992); Jerrett and Bruyn (1992) continued in the same vein, the fits for the data, of wavelength and width, were found to have different coefficients for fluids with different equilibrium contact angles. While such studies have revealed that the wettability of the coating liquid has a significant impact on the development of rivulets, a relationship has yet to be obtained that links the fully and partial wetting case in terms of wavelength, thus building on the work of Huppert (1982).

The usual approach adopted for experimental set ups used to explore rivulet formation is the release of a large volume of fluid initially confined behind a dam wall, with the liquid allowed to settle before releasing it; in contrast Johnson *et al.* (1999) used a continuous inflow approach and found, so long as a large enough volume of

fluid is deposited, the results were remarkably similar to the observations of others. The ability to model this experimental setup with relative ease makes the results generated in Johnson (1997) the ideal candidate data with which to compare theoretical predictions against.

Related theoretical work has mainly concentrated on the associated stability problem, the base state which exhibits a capillary ridge that forms at the advancing front (Troian *et al.*, 1989). This ridge is a direct indication of the instability; Troian *et al.* (1989) predicted the wavenumber of the manifesting instability, that is the fastest growing unstable wavenumber, correlated reasonably well with the findings of Huppert (1982). Bertozzi and Brenner (1997) considered the effect of inclination angle on the stability of the advancing front; as the inclination angle decreases the capillary ridge size also decreases until the flow becomes stable at low inclination angles. Other stability related work is contained in Schmuki and Laso (1990); Hocking (1990); Spaid and Homsy (1996, 1997); Ye and Chang (1999); Kalliadasis (2000); Davis and Troian (2003), and includes considerations of wetting and viscoelasticity. Hocking (1990) used linear and non-linear stability calculations to try and understand the delayed on-set of the instability that is seen in Huppert's experiments. Hocking (1990) also proposed that the mechanism of the instability may be the same as Rayleigh-Taylor instability, as motion is driven by gravity and influenced by surface tension, but modified by contact line and contact angle effects. Spaid and Homsy (1996) considered the linear stability of Newtonian and viscoelastic fluids at the contact line, finding that viscoelasticity stabilises the capillary ridge. The issue of contact line modelling was addressed by Davis and Troian (2003) who introduced a slip model to embody wetting effects; they found that as the slip length was decreased the magnitude of the instability increased. It should be pointed out at this stage that in theoretical studies, stability analysis and three-dimensional simulations, the contact line model employed (slip or precursor film) does not impact on the results so long as the precursor film height and slip length are of the same magnitude, see Spaid and Homsy (1996).

Theoretical studies involving the generation of two and three-dimensional numerical solutions have also been pursued alongside the above. Schwartz (1989) reported the first computational results in three-dimensions and found that fingering always occurs on a vertical plane, and that even at angles less than vertical the front profile develops sufficiently high curvature so that small disturbances evolve into rivulets. Subsequent three-dimensional investigations have been relatively sparse, with the exception of Moyle *et al.* (1999) and Eres *et al.* (2000) who began to consider the incorporation of wetting effects; rivulets developing at the front of a partially wetting fluid were seen to grow faster than for a fully wetting one. A large bulk of related literature is made up from the work of Kondic and Diez (Diez *et al.*, 2000; Diez and Kondic, 2001*b*, 2002; Kondic and Diez, 2001; Kondic, 2003; Kondic and Diez, 2004, 2005); their findings (Kondic and Diez, 2001) being in good agreement with the experimental work of Johnson *et al.* (1999). Their attention was directed in addition to the case of patterned surfaces and how these can influence the wavelength of the instability that emerges; this is discussed in more detail subsequently. Their main finding for planar substrates was that the length of the rivulets is limited at all inclination angles below the vertical, Kondic and Diez (2005).

While there has been much attention to rivulet formation on a flat inclined plane there is still much dispute over the wavelength that emerges naturally. While there is some consensus that the wavelength scales linearly with capillary length (Huppert, 1982; Troian *et al.*, 1989) other models have been devised which depend on different powers of the associated capillary number (Jerrett and Bruyn, 1992; Johnson *et al.*, 1999). There has also been very little attention paid to the impact of wetting dynamics at the advancing front and the influence this has on the wavelength, despite the observations of Silvi and Dussan (1985), see Section 1.3.

The rivulet instability occurs in a diverse range of situations other than the gravity-driven setting; the spin-coating of a drop of liquid, which is a process used within manufacturing, see for instance Melo *et al.* (1989); Fraysse and Homsy (1994); Wang and Choud (2001), also induces a rivulet type instability. Thermally-driven

films have also been shown to develop fingers (Cazabat *et al.*, 1990; Kataoka and Troian, 1997) and those containing surfactants (Matar and Troian, 1999; Warner *et al.*, 2004a,b; Edmonstone *et al.*, 2005; Craster and Matar, 2006; Edmonstone *et al.*, 2006; Mavromoustaki *et al.*, 2013a,b).

Also of significant interest is the growth of rivulets in scenarios that differ from that of an inclined flat substrate. The growth of rivulets on an inverted plane has been studied recently by Lin and Kondic (2010); Lin *et al.* (2012) who found that the instability is comprised of surface waves and contact line finger growth, both of which interact to form complex dynamics. Flow in other geometries is also of interest due to the diverse nature of surfaces used in manufacturing and found in nature. Takagi and Huppert (2010) consider flow on the outside of a sphere and a horizontally aligned cylinder. Flow on a horizontally aligned cylinder, both rotating and stationary, has received much consideration in the theoretical literature, see Duffy and Wilson (1999); Holland *et al.* (2001); Evans *et al.* (2004); Leslie *et al.* (2011), with attention given to the drop that forms at the bottom of the cylinder as well as the flow of a single rivulet flowing over the geometry.

Recently work has focused on film flow on the outside of a vertically-aligned cylinder. Smolka and SeGall (2011) considered the flow of two such fluids experimentally and found that the curvature of the cylinder impacted on the stability at small enough cylinder radius; the results obtained were shown to match well with theoretical findings. More recently Mayo *et al.* (2013) attempted to model the above flow using lubrication theory. Their three-dimensional numerical results matched well with experiments but found that curvature effects were minimal - the flow was stated to be analogous to the problem of film flow on an inverted plane (Lin and Kondic, 2010; Lin *et al.*, 2012). Work that considers the coating of geometries such as cylinders is pivotal in understanding how the curvature of a substrate influences the ability to coat it, this is particularly true in instances such as the coating of small bronchial tubes within mammalian lungs.

1.2.3 Effect of substrate heterogeneities on rivulets

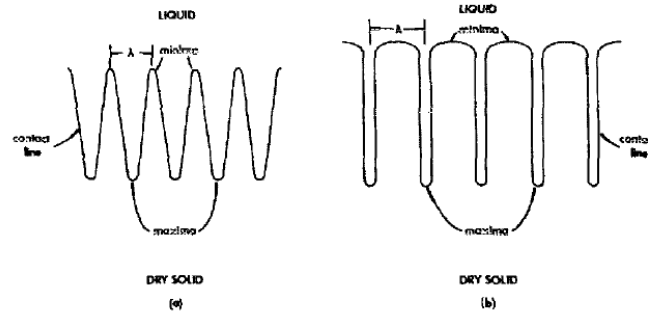


FIGURE 1.3: Sketch of the different forms of rivulets that emerge at the advancing front of a (a) fully wetting and (b) partially wetting fluid Silvi and Dussan (1985).

The wavelength of the rivulet pattern that forms at the advancing front of a spreading film can be altered by regular patterned trench stripes with equal spacing (Kondic and Diez, 2002); if the spacing is less than the natural wavelength of the instability then rivulets are forced to grow in close proximity to one another enforcing merging. If the spacing is greater than the natural wavelength then the rivulets form in regular spacing down the path of least resistance. For large spacing several rivulets form in each channel. Kondic and Diez (2004) further noted how small trench topographies could introduce a large enough disturbance to induce rivulet formation and that the spacing directly influenced the wavelength of the instability that emerged. Similar observations were made when considering chemical heterogeneity; experiments in Kondic and Diez (2004) (Figures 16,17 and 18 in their publication) were performed using PDMS (polydimethylsiloxane) to coat a glass surface; stripes of an oil-based paint were deposited on the substrate at controlled intervals. PDMS has a much higher contact angle with the paint (low wetting) so as the advancing front approaches the stripes the fluid travels down the non-painted areas, thus the spacing between the two directly impacts the wavelength of the rivulets.

The field of wetting and spreading, including hysteresis in droplet spreading, is a vastly researched area with still many opposing theories requiring validation. While neither the macro- or micro-scale science behind spreading is discussed in detail

here, the reader is directed to a recent thorough review by Bonn *et al.* (2009) and the references therein contained.

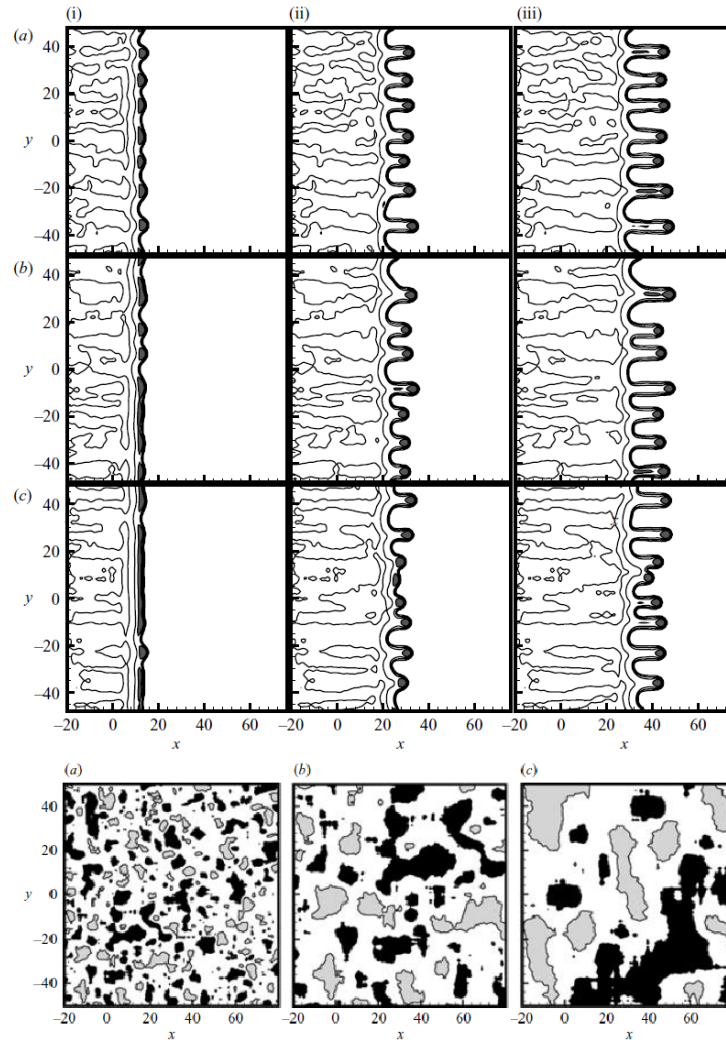


FIGURE 1.4: *Top:* Rivulet flow over randomly distributed heterogeneous patches from Zhao and Marshall (2006). The contact angle associated at each co-ordinate (x, y) using a random correlation function controlled by correlation length, l ; (a) $l = 6$, (b) $l = 13$ and (c) $l = 24$. Three time snapshots are shown - (i) $t = 12$, (ii) $t = 24$ and (iii) $t = 33$. Flow is from left to right and contours shown at $h = 0.2, 0.6, 1$ and 1.4 , grey shading is used when $h > 1.4$. *Bottom:* The network of patches created by the random function assigning the associated contact angle to the substrate; white areas are fully wetting, grey areas indicate where the contact angle is greater than 15° and in black shaded areas the contact angle is less than 9° .

Droplet spreading on a heterogeneous substrate was investigated by Schwartz and

Eley (1998); Schwartz (1998) employing a disjoining pressure model (Derjaguin *et al.*, 1987) to imitate the effect of hysteresis and assigning regular patchwork areas of high contact angle. They found that although the spreading rates/time scale of the simulations were out by a large factor, the numerical solutions obtained matched well with experiments for a droplet spreading over a low wetting Teflon cross and splitting into four micro-droplets. Further work including droplet spreading onto mound topographies with low wettability/high contact angle was carried out in Gaskell, Jimack, Sellier and Thompson (2004) employing a multi-grid method with error-controlled variable time-stepping to solve the lubrication equations. They found that the wettability of the liquid on the surface impacted the spreading dynamics and shape of the drop; for example, a drop on a highly wetting surface that spread towards a low wetting square mound would recede from the low wetting area and spread on the highly wettable surface creating a bow shaped interface at the corner of the low wetting region. In the reverse case, a low wetting substrate containing a highly wetting mound, the droplet would preferentially spread and climb onto the mound.

With respect to rivulets, surface patterning with chemical heterogeneities has garnered much less attention than other aspects of thin film flow. Silvi and Dussan (1985) observed that when silicone oil spread on a perspex surface the rivulets would take a much different form to those seen when glycerin, which has a much larger contact angle on perspex than silicone oil, was used to coat the substrate; see Figure 1.3 for a sketch of the saw-tooth pattern of a fully wetting fluid and long, thin fingers of a partially wetting fluid that were observed. The elongation of the rivulets was also observed to be much faster when glycerin was used, with the bulk staying almost stationary compared to the rivulets. Similarly, Jerrett and Bruyn (1992) considered three different liquids in their experiments; glycerin and two different types of mineral oil. The mineral oils had a static contact angle of 14° on the plexiglass substrate utilised, whereas glycerin had much higher contact angle of 60° . Their observations were similar to those of Silvi and Dussan (1985) in relation to the dif-

ferences in pattern and shape between the higher and lower wetting liquids. They also correlated the wavelength and found two different expressions for mineral oil and glycerin;

$$\lambda = \begin{cases} 14.1L_c \sin \alpha^{0.12} & \text{(glycerin)} \\ 19.2L_c \sin \alpha^{0.21} & \text{(mineral oil)}, \end{cases}$$

where α is the inclination angle and the capillary length $L_c = H_0/(3Ca)^{1/3}$, where H_0 is the asymptotic film thickness and Ca the capillary number. Clearly, the wavelength is smaller when the fluid is less wetting (glycerin) than another one (mineral oil); however, the expressions do not include the contact angle (which indicates wettability).

Numerical investigations have mostly ignored the effect of wetting properties on the wavelength in the context of rivulet formation. Of those that attempt to assess their impact, Eres *et al.* (2000) found, for single rivulets, that an increase in contact angle made a rivulet longer and thinner. Marshall and Wang (2005) and Zhao and Marshall (2006) uncovered the subtle influence that both periodically and randomly distributed heterogeneous regions can have over the rivulet instability - see Figure 1.4 for an example of flow over randomly distributed patches of varying wettability - finding that when the regions were small (a small correlation length l , see Figure 1.4) the wavelength that emerged was similar to that calculated from linear stability theory. However, when the regions were large the wavelength varied significantly around the predicted value. Kondic and Diez (2004) showed experimentally that rivulets of PDMS form within the spacings between regularly arranged low wetting patches (created with an oil-based paint), as discussed previously. A similar observation to this was noted for a climbing film, a phenomena seen when a temperature gradient is applied to a vertically aligned substrate in such a manner that the Marangoni forces, induced by the surface tension gradient associated with the temperature profile, are large enough to overcome gravity (Cazabat *et al.*, 1990; Kataoka and Troian, 1997, 1999). An example of this is explored in Kataoka and Troian (1999) using chemically striped silicone wafers. A flow of PDMS, driven

by Marangoni forces, develops rivulets at the advancing front climbing the substrate. The rivulet pattern was seen to develop a wavelength that correlated with the spacing of the chemical heterogeneity, much like in the gravity-driven case.

1.3 Flow on heterogeneous surfaces

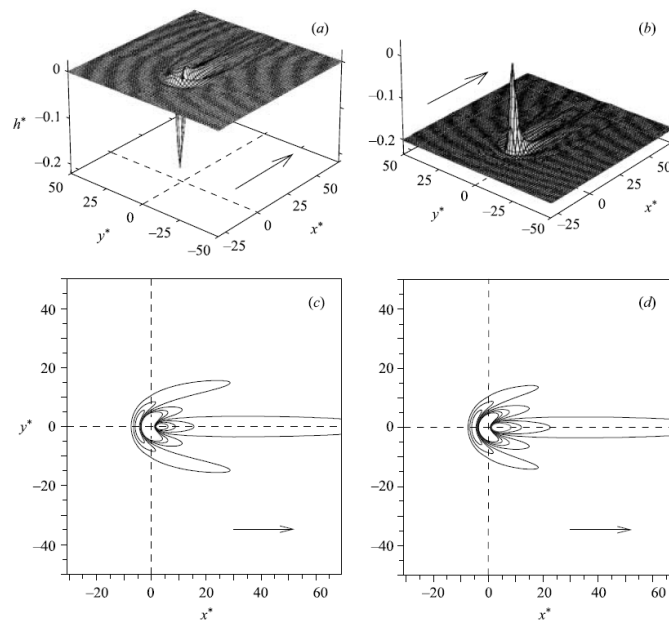


FIGURE 1.5: Example of a continuous thin film of water flowing over a peak and trench topography of non-dimensional height 0.25 from Gaskell, Jimack, Sellier, Thompson and Wilson (2004). Evident to see in the contour plots of free-surface height is the bow-wave shaped peak around the upstream topography boundary and the downstream surge not captured by two-dimensional simulations. The arrow on the plots indicates the direction of flow.

Real surfaces encountered in the diverse applications discussed above often contain a variety of randomly distributed heterogeneities; these often are made up of topographic features and areas of varying wettability due to the chemical make up of the surface to be coated.

Free-surface flows of continuous films over topographical features reflect substrates more often encountered within industry or in nature. The long-wave approxima-

tion (see Section 3.1) has been utilised to generate equations that have been used to investigate the free-surface deformation created by step-up, step-down, trench and mound topographies; Stillwagon *et al.* (1987); Stillwagon and Larson (1988, 1990) were the first to consider such an approach and found remarkable agreement with features observed in practice. Gaskell, Jimack, Sellier, Thompson and Wilson (2004) compared results with the experiments of Decré and Baret (2003) and found very good agreement; they were the first to attempt and successfully obtain such solutions. A bow-wave upstream of the trench and a downstream surge are found to exist both computationally and experimentally. The computations enabled the loci of the capillary ridges forming the bow-wave to be determined and showed just how well lubrication theory is suited for modelling such flows. An example of such numerical solutions is given in Figure 1.5 for flow over a trench and a mound.

Subsequent, complementary investigations have considered evaporating flow over trenches (Gaskell *et al.*, 2006); the results allowing the identification of three regimes of free-surface development (thinning, thickening and a combination of both), the onset of each regime depending on solvent concentration, the evaporation rate and the sensitivity of the viscosity to the solvent concentration. Film flow around occlusions (Lee *et al.*, 2007; Baxter *et al.*, 2009) within a lubrication context has also been explored identifying the free-surface height around obstacles when a constant contact angle with the occlusion is specified.

Rarely will a substrate contain just one topographical feature and it has been observed that multiple and/or complex patterned topographies induce more wide spread free-surface deformation (Lee *et al.*, 2008; Gaskell *et al.*, 2010) as do multiple protruding obstacles (Baxter *et al.*, 2010); if the topographies are close together then the free-surface distortion induced by each feature may interact creating a larger deformation.

One of the drawbacks in the use of lubrication theory to model the above flows is the removal of inertial effects from the equation set as the Reynolds number is assumed negligible, understanding the impact of inertia is important for making

global conclusions about film flow. To this end, Veremieiev *et al.* (2010) extended the previously mentioned work of lubrication theory to include inertial effects by using a depth-averaged form (DAF) of the equations; within this derivation, the velocity profile of the film is assumed to be parabolic across the depth. The DAF approximation is equivalent to the integral-boundary-layer (IBL) approximation, see for example Shkadov (1967). When inertia is increased the bow-wave around the upstream of a trench topography gradually rises and becomes wider, while the extent of the downstream surge is reduced. Furthermore, Veremieiev *et al.* (2012) included the effects of an electric field within the DAF formulation finding the electric field to dominate inertial effects, suppressing inertially-induced disturbances. Introducing an electric field initially enhances the size of the free-surface disturbance but as the strength is increased the electric field can be used to suppress the bow-wave disturbance. The downstream surge can also be reduced as the pressure in the trench is increased thus restricting the flow of liquid into the topography as the film flows over it.

1.3.1 Flow over topography: Inner flow transport

While being computationally advantageous, solution of equation sets based on the long-wave approximations are limited to exploring free-surface features only, they reveal nothing about the internal flow structures within the film.

Continuous film flow over step-up and step-down topographies have become classical problems where the associated inner flow structure induced is other than purely unidirectional. Eddies are observed to exist, an example of which is shown in Figure 1.6; here, flow structures formed under Stokes flow conditions can be seen from experiments and complementary numerical solutions for increasing film thickness on an undulating plane inclined at 45° - as the film thickness increases the emergence of an eddy can be observed, a further increase induces an increase in magnitude of the size of the separated flow region. The potential existence of eddies is important

as flow separation, between the bulk flow coating the surface and eddies trapped within a topographical feature, can strongly influence the flow and thus the associated rates of chemical reactions, heat (Scholle, Haas, Aksel, Thompson, Hewson and Gaskell, 2009) and mass transfer (Wierschem and Aksel, 2004).

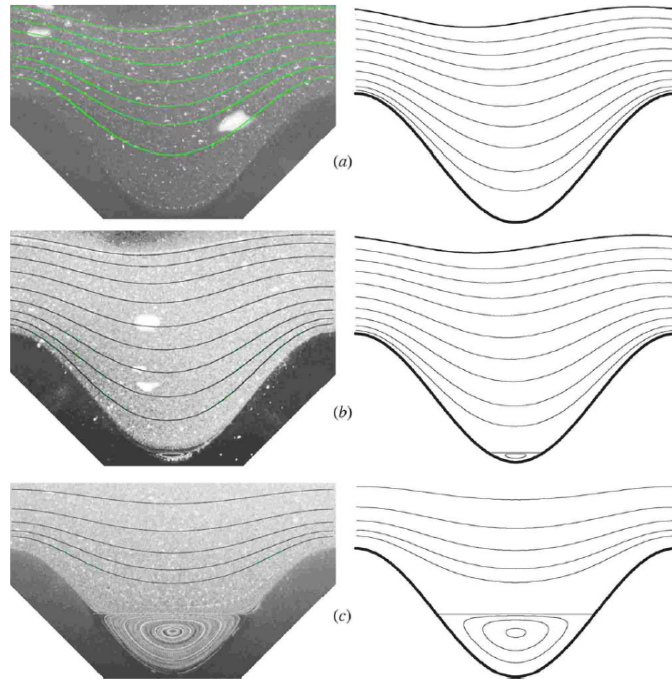


FIGURE 1.6: An example of eddy formation in flow under Stokes flow conditions in the topography of an undulating substrate, with amplitude of the wavy topography defined as $a = 2\pi/5$ and inclined at 45° to the horizontal, for increasing film thickness; (a) $h = 16\pi/25$, (b) $h = 18\pi/25$ and (c) $h = 24\pi/5$. The left hand side shows experimental observations of Wierschem and Aksel (2003) (with complex variable numerical solutions overlaid) and the right column showing corresponding finite element numerical results of Scholle *et al.* (2008).

Flow separation is found for a variety of substrate undulations, depending on the level of inertia and topography shape and steepness. Taneda (1979) visualised the flow of silicone oil over square and triangular shaped topographies demonstrating the effect the topographies had on the formation of eddies including separation of eddies with increasing trench topography length; such results have been observed in full three-dimensional computations see, for example, Veremieiev (2011). Zhao and Cerro (1992) found eddies to exist even under laminar flow conditions for a

large range of film thickness; Wierschem *et al.* (2003) found that the generation of eddies at very low Reynolds numbers depended on surface tension, film thickness and substrate waviness. Wierschem and Aksel (2004) observed eddies created at low Reynolds numbers were then modified by increasing inertia, and similar observations have been reported in Scholle *et al.* (2004, 2006).

The subtle interplay between geometric and inertial effects on the formation of local flow structures in the corrugations of a wavy substrate was revealed by Scholle *et al.* (2008). The effects can be measured by considering local (based on topography length scale) and global Reynolds numbers; two types of eddies were observed, those induced kinematically and those induced by inertia. The manipulation of eddies has also been investigated for shear-driven flow over a corrugated substrate (Scholle, Haas, Aksel, Wilson, Thompson and Gaskell, 2009); it was found that, as well as geometric and inertial effects seen in free-surface flow, the mean plate separation (the average distance between the top moving plate and bottom corrugated plate) also influences the associated flow structures. Should no eddies be present in the flow at a certain mean separation, by decreasing the mean separation an eddy could be induced - this is the opposite to free-surface flow where increasing the Nusselt film thickness would induce an eddy where previously there was none (Scholle *et al.*, 2008).

Waves are generated on the surface of a film coating an undulating substrate when inertia becomes an important factor due to instability. Wierschem and Aksel (2003) found that the critical Reynolds number for the instability was higher than on a flat inclined plate. The generation of surface waves and the resonance phenomena, the amplification of the free-surface and film thickness amplitude, seen in the case of flow over topography, has been investigated extensively; see for example Bontozoglou and Papapolymerou (1997), Malamataris and Bontozoglou (1999), Bontozoglou (2000), Vlachogiannis and Bontozoglou (2002) and Heining *et al.* (2009). Linear resonance is investigated within the context of corrugations whose depth is much smaller than its wavelength and the film thickness Wierschem *et al.* (2008)

whereas non-linear resonance effects are influential when this assumption no longer holds (Heining *et al.*, 2009). As inertia is increased the free-surface of the flow is further disturbed, the magnitude of the disturbances have been found to depend on the depth of the valleys comprising the substrate (Argyriadi *et al.*, 2006). Wierschem and Aksel (2004) found that material transport between eddies was induced by disturbances to the free-surface resulting in the formation of surface waves; they observed the motion of the separatrix created by the local changes in film thickness induced a lobe mechanism of material transfer between the re-circulating flow and the bulk flow above.

Mass transfer and mixing is an important aspect within fluid flows in general in an engineering context. The enhancement or suppression of transport rates from re-circulation zones is important in the cleansing of rough surfaces (Tighe and Middleman, 1985), the mechanisms involved in pitting corrosion (Frankel, 1998) and transport to cells in perfusion bioreactors (Horner *et al.*, 1998). Investigations into mixing and transport enhancement in open cavities are limited; Jana and Ottino (1992) briefly looked at how oscillating the motion of an impinging jet above a cavity can induce removal of material, Howes and Shardlow (1997) pulsed the inlet flow to clean out a number of cavities in a channel. By placing obstacles upstream of an open cavity, oscillations can be induced in the flow to enhance transport (Garrison and Rogers, 1994). Horner *et al.* (2002) considered oscillating the shape and speed of a moving wall, driving flow past an open square cavity to increase the rate of fluid transport between the bulk and the cavity flow; the authors noted that changing the frequency and amplitude of the forcing induced a turnstile lobe mechanism of transport. The dependence of the increased flux of fluid transport reaches a maximum at a critical value of the frequency of the forcing, after which the flux decreases. In the case where the amplitude of the wall forcing is increased there is no limiting criteria, the flux is always increased.

The turnstile lobe mechanism is the same phenomenon as observed in free-surface flow over an undulating substrate (Wierschem and Aksel, 2004). Transport in the

bulk flow over a wavy substrate can be enhanced by optimising the film thickness for an increase in mean transport velocity, Scholle *et al.* (2006); for small to moderate waviness they found a reduction in the mean transport velocity, when the onset of eddies is observed the reduction in material transport is partially compensated for by these inner flow structures which act like a fluid roller bearing promoting material transport. Heining *et al.* (2012) investigated film flow over undulating surfaces that were both partially- and fully-submerged focusing on how laminar mixing is affected by the topography.

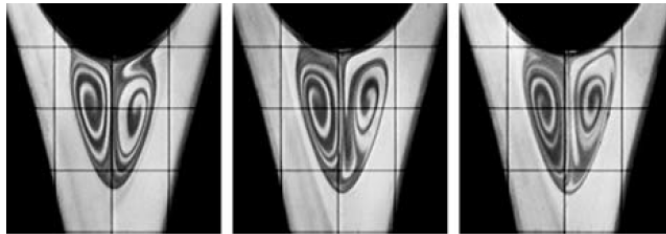


FIGURE 1.7: Experimental images of mixing between two counter-rotating rollers via lobe formation, Wilson *et al.* (2006); the speed of one of the rollers is varied inducing a turnstile lobe mechanism of fluid transport creating the mixing pattern that can be observed.

Mixing and transport enhancement is important in many different thin film based applications, for instance in roll coating. Stirring and transport enhancement of fluid entrapped in the nip between two counter-rotating rollers was shown to increase when increasing the speed ratio of the two rollers by Wilson *et al.* (2006), one rotating at fixed speed, the other varying. As above, they noted that transport and mixing were described by a turnstile lobe mechanism induced by the tangling of the invariant stable and unstable manifolds associated with the separation boundary, see Figure 1.7. A complication with this method of transport enhancement was the disturbance induced at the free-surface - the percentage change in film thickness at the free-surface was found to be approximately a quarter of the percentage change of roll speed although this could be counter-acted by modulating the speed of both rollers.

1.4 Thesis outline

Due to the formidable challenges faced when investigating the problems of interest contained in this thesis experimentally, as well as the fact that closed analytical solutions remain elusive, use is made of mathematical models and efficient numerical solutions of the same to explore the associated flow - the free-surface disturbance generated, rivulet formation and internal flow structures. The solutions reveal the behaviour of liquid flow in a variety of scenarios focusing on a number of aspects.

The work focuses on a number of areas associated with coating flows:

1. The use of an efficient, accurate and adaptive multigrid method to solve the governing equations of thin-film flow derived via a long wave approximation for a variety of flow problems.
2. An in-depth investigation of rivulet formation on an inclined plane for both fully and partially wetting fluids utilising this multigrid methodology.
3. Exploring the effect on rivulet formation of substrate heterogeneities including trench and mound topographies and patches of varying wettability; also considered is the inclusion of a surface tension gradient (induced by, for instance, a temperature profile) that is used to drive the climbing of thin films.
4. An in-depth investigation of rivulet formation on the inner and outer surfaces of a vertically aligned cylinder, with direct comparison drawn to the planar case to reveal the effects of curvature and with recently reported experiments.
5. An explanation of the inner-flow dynamics induced by free-surface excitation creating transport across the separatrix associated with eddies contained within surface topography via a turnstile lobe mechanism.

The thesis proceeds as follows:

Chapter 2 introduces a rigorous mathematical formulation of the long-wave approximation which is utilised to investigate rivulet formation on both inclined planes and vertically-aligned cylinders. A disjoining pressure model is introduced, outlining its underlying and formulation. Also shown is the non-dimensional form of the Navier-Stokes and continuity equations. The numerical methods used to solve discrete analogues of both sets of equations are introduced in Chapter 3. The multigrid algorithm embodies local mesh refinement and truncation error controlled variable time stepping. An additional feature enhancing the method, called grid devolution, is developed to further improve the efficiency of the solution procedure. A demonstration of the multigrid efficiency is showcased in Appendix D for the interested reader, revealing the exceptional speed of the solver when compared to previous algorithms. The finite element method used to solve the Navier-Stokes and continuity equations is described and the discretisation methodology explained, including the parametrisation of the free-surface by the method of spines.

Following this, an in-depth investigation of the classical problem of a spreading film on an inclined substrate is considered in Chapter 4. The formation of rivulets is investigated and the effect of wetting properties quantified and compared with the findings of the experiments of Johnson *et al.* (1999). A new relationship describing the global characteristics of the rivulet pattern that links together the case of a fully wetting fluid with a partially wetting one via a partial wetting parameter is formulated. The concept of flow on real surfaces is considered in Chapter 5 by exploring film flow on substrates containing heterogeneities, topographical and chemical, revealing in some cases asymmetry effects that can be imposed on the evolution of rivulets. Additional physical effects are incorporated into the problem formulation by considering the effect of surface tension gradients on the spreading and climbing of a film.

The effect on rivulet formation from the curvature of a cylinder is quantified in Chapter 6. The equations are formulated via a different long-wave approximation to that used in lubrication theory but solved using the same multigrid algorithm.

Flow on the inside and outside surfaces of the cylinder is considered, as well as the effect of wetting properties. A regime model, based upon a sequence of numerical solutions, is provided; the model term for wavelength links the planar case to the cylindrical scenario demonstrating that curvature does indeed affect rivulet formation.

Finally, the transport of re-circulating material from eddy structures, formed within the valleys of a topography in the substrate, to the bulk flow is considered in Chapter 7. Numerical solutions are sought and reveal how a turnstile lobe mechanism can be induced by perturbing the free-surface which creates a symmetry-breaking effect which enhances transport across the separatrix boundary. Snapshots of the dynamic simulations and the use of an inert-particle tracking scheme illustrate the phenomenon, mimicking the dynamics observed in experiments. The concept is explored revealing the influence of geometry and inertia on the ability to induce the lobe mechanism.

The content of the thesis is summarised in Chapter 8 and conclusions drawn from the results discussed. Recommendations for future work are provided.

Chapter 2

Mathematical formulation

Contents

2.1	Lubrication approximation - Rivulet formation	27
2.1.1	Governing equations	27
2.1.2	Contact line approach: disjoining pressure	32
2.1.2.1	Contact line forces - Young's equation	33
2.1.2.2	Disjoining pressure	35
2.1.2.3	Precursor film	38
2.1.3	Boundary conditions	39
2.1.4	Initial conditions	40
2.1.5	Topography definition	40
2.1.6	Linear stability analysis	41
2.1.6.1	Inclined planar substrate	41
2.2	Navier-Stokes equations - Inner flow structures	42
2.2.1	Non-dimensional governing equations	42

The research contained in this thesis considers two distinct features of gravity-driven thin film flow. The first concerns rivulet formation at the unstable advancing front of a thin film; the second, the inner flow structures formed when a continuous film flows over a substrate containing topographical features, the focus being the fate of material trapped within eddies. Accordingly, two different approaches are employed to generate the numerical solutions required to solve these two related but different flow problems.

The governing equations for the first class of problems considered arise from using the long wave approximation (Oron *et al.*, 1997) to generate what is commonly referred to as the lubrication approximation to the Navier-Stokes and continuity equations. Written and solved in finite-difference form, this equation set is well suited to the numerical investigation of three-dimensional free-surface disturbances due to its computational efficiency in generating solutions, compared to the computationally exhaustive process of solving the full Navier-Stokes equations. This efficiency is particularly pertinent when investigating a transient process such as rivulet growth, which requires long-time solutions to be obtained over large domains (Gaskell, Jimack, Sellier, Thompson and Wilson, 2004; Gaskell *et al.*, 2010) to fully reveal the flow characteristics of interest. Furthermore, wetting properties can be readily introduced into the formulation using a disjoining pressure term, adding depth to the possible scope of investigations and conclusions.

The second problem considered, which includes exploring the internal flow structure within the fluid film also, utilises the full Navier-Stokes and continuity equations which are solved using an appropriate finite element formulation.

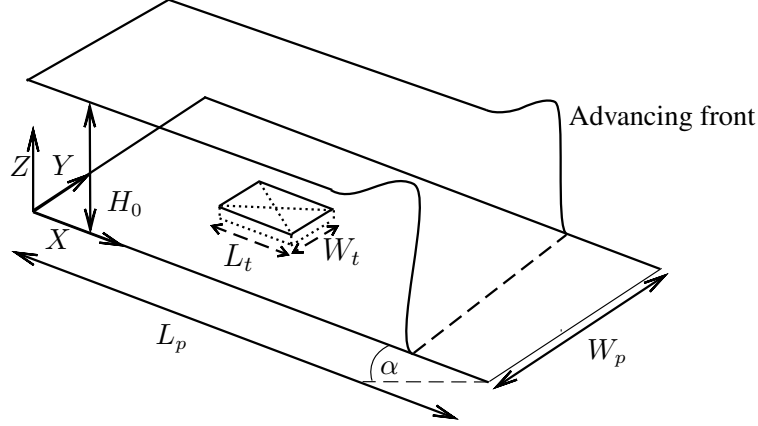


FIGURE 2.1: Schematic of the side view of thin film flow down a flat plate (width, W_p , length, L_p) inclined at an angle α to the horizontal, featuring an advancing front before the onset of instability. The surface of the substrate is shown, for the sake of generality, to contain a rectangular topography (length L_t , width W_t and height/depth $S(X, Y)$). The film is fed by a constant inflow at the upstream boundary and H_0 denotes the asymptotic film thickness and — the contact line.

2.1 Lubrication approximation - Rivulet formation

2.1.1 Governing equations

The first problem of interest takes the form of a constantly fed thin liquid layer, with flux Q_0 at the inlet, of asymptotic thickness H_0 flowing down a rigid planar substrate (length L_p , width W_p) inclined at an angle α to the horizontal; as illustrated schematically in Figure 2.1. The free-surface position at time T is denoted by $F(X, Y, T)$; as such the film thickness is given by $H(X, Y, T) = F(X, Y, T) - S(X, Y)$. The fluid involved is assumed incompressible with constant density, ρ , dynamic viscosity, μ , and surface tension, σ , such that the governing Navier-Stokes and continuity equations for the system, can be written as:

$$\rho \left(\frac{\partial \mathbf{U}}{\partial T} + \mathbf{U} \cdot \nabla \mathbf{U} \right) = -\nabla P + \nabla \cdot \underline{\underline{\mathbf{T}}} + \rho \mathbf{G} \quad (2.1)$$

$$\nabla \cdot \mathbf{U} = 0 \quad (2.2)$$

where $\mathbf{U} = (U, V, W)$ is the fluid velocity, P the pressure, $\underline{\mathbf{T}} = \mu (\nabla \mathbf{U} + (\nabla \mathbf{U})^T)$ is the viscous stress tensor and $\mathbf{G} = (g \sin \alpha, 0, -g \cos \alpha)$ the gravity vector. In Cartesian co-ordinates with a general point in the plane denoted by (X, Y, Z) .

The Navier-Stokes equations are supplemented by an appropriate no-slip condition at the substrate surface $Z = S(X, Y)$, namely:

$$U(X, Y, 0) = V(X, Y, 0) = W(X, Y, 0) = 0. \quad (2.3)$$

The kinematic and stress balance conditions (expanded into tangential and normal components) at the free-surface, $Z = F(X, Y, T) = H(X, Y, T) + S(X, Y)$, are given (Sellier, 2003) by:

$$\frac{\partial F}{\partial T} + U \frac{\partial F}{\partial X} + V \frac{\partial F}{\partial Y} = W, \quad (2.4)$$

$$\mathbf{t} \cdot (-P\mathbf{I} + \underline{\mathbf{T}}) \cdot \mathbf{n} = 0, \quad (2.5)$$

$$\mathbf{n} \cdot (-P\mathbf{I} + \underline{\mathbf{T}}) \cdot \mathbf{n} = \sigma \kappa + \Pi(H), \quad (2.6)$$

where $\Pi(H)$ is the disjoining pressure generated by intermolecular forces at the contact line, the form and significance of which is discussed further in Section 2.1.2, and \mathbf{I} is the identity matrix. The pressure variable P has been shifted with respect to the atmospheric pressure, $P \rightarrow P + P_A$, to denote a reference pressure which is utilised from here on in. The unit normal to the surface denoted by \mathbf{n} is defined as:

$$\mathbf{n} = \frac{(-F_X, -F_Y, 1)}{(F_X^2 + F_Y^2 + 1)^{\frac{1}{2}}}, \quad (2.7)$$

where F_X, F_Y denote the partial derivative of F with respect to X and Y , this

notation is adopted for clarity and the curvature of the surface, κ , is given by:

$$\kappa = -\nabla \cdot \mathbf{n}. \quad (2.8)$$

The tangent vector, denoted by \mathbf{t} , in the X -direction is:

$$\mathbf{t}_X = \frac{(1, 0, F_X)}{(1 + F_X^2)^{\frac{1}{2}}}, \quad (2.9)$$

and in the Y -direction is obtained from:

$$\mathbf{t}_Y = \frac{(0, 1, F_Y)}{(1 + F_Y^2)^{\frac{1}{2}}}. \quad (2.10)$$

The governing system of equations (2.1)-(2.6) is complete and fully describe the dynamics of free-surface thin film flow.

In the case of the problem of rivulet formation, there is a large difference between the fully developed asymptotic film thickness and the characteristic length L_0 in the direction of flow. This can be exploited to reduce equations (2.1) and (2.2) to a dimensionless and more computationally tractable form by invoking the long-wave approximation (Oron *et al.*, 1997) for the case $H_0/L_0 = \epsilon \ll 1$, where $L_0 = H_0/(6Ca)^{1/3}$ is the associated capillary length (Decré and Baret, 2003) and $H_0 = (3\mu Q_0/\rho g \sin \alpha)^{\frac{1}{3}}$ the fully developed film thickness. Ca denotes the capillary number, measuring the ratio of viscous to surface tension forces, given by $\mu U_0/\sigma \sim O(\epsilon^3) \ll 1$, where $U_0 = 3Q_0/2H_0$ is the surface velocity of the fully developed film.

Scaling dimensional variables in equation (2.1) by appropriate characteristic lengths,

heights and velocities via:

$$\begin{aligned} (x, y, l_p, w_p, l_t, w_t) &= \frac{(X, Y, L_p, W_p, L_t, W_t)}{L_0}, & (z, h^*) &= \frac{(Z, H^*)}{H_0}, & t &= \frac{T}{T_0}, \\ (h, s)(x, y, t) &= \frac{(H, S)(X, Y, T)}{H_0}, & p(x, y, z, t) &= \frac{2P(X, Y, Z, T)}{\rho g L_0 \sin \alpha}, \\ (u, v, w) &= \left(\frac{U}{U_0}, \frac{V}{U_0}, \frac{W}{\epsilon U_0} \right), & T_0 &= \frac{L_0}{U_0}; \end{aligned}$$

leads to the following non-dimensional form of the Navier-Stokes equation:

$$\epsilon Re \left(\frac{\partial u}{\partial t} + u \frac{\partial u}{\partial x} + v \frac{\partial u}{\partial y} + w \frac{\partial u}{\partial z} \right) = -\frac{\partial p}{\partial x} + \epsilon^2 \left(\frac{\partial^2 u}{\partial x^2} + \frac{\partial^2 u}{\partial y^2} \right) + \frac{\partial^2 u}{\partial z^2} + 2, \quad (2.11)$$

$$\epsilon Re \left(\frac{\partial v}{\partial t} + u \frac{\partial v}{\partial x} + v \frac{\partial v}{\partial y} + w \frac{\partial v}{\partial z} \right) = -\frac{\partial p}{\partial x} + \epsilon^2 \left(\frac{\partial^2 v}{\partial x^2} + \frac{\partial^2 v}{\partial y^2} \right) + \frac{\partial^2 v}{\partial z^2}, \quad (2.12)$$

$$\epsilon^3 Re \left(\frac{\partial w}{\partial t} + u \frac{\partial w}{\partial x} + v \frac{\partial w}{\partial y} + w \frac{\partial w}{\partial z} \right) = \quad (2.13)$$

$$-\frac{\partial p}{\partial z} + \epsilon^4 \left(\frac{\partial^2 w}{\partial x^2} + \frac{\partial^2 w}{\partial y^2} \right) + \epsilon^2 \frac{\partial^2 w}{\partial z^2} - 2\epsilon \cot \alpha. \quad (2.14)$$

Assuming the Reynolds number, $Re = \rho U_0 H_0 / \mu$, is small and of order ϵ and retaining leading order terms up to $O(\epsilon^2, \epsilon Re)$ only, together with introducing the continuity equation from (2.2), the above equation set can be reduced further to give:

$$\frac{\partial^2 u}{\partial z^2} = \frac{\partial p}{\partial x} - 2, \quad (2.15)$$

$$\frac{\partial^2 v}{\partial z^2} = \frac{\partial p}{\partial y}, \quad (2.16)$$

$$\frac{\partial p}{\partial z} = -2\epsilon \cot \alpha, \quad (2.17)$$

$$\frac{\partial u}{\partial x} + \frac{\partial v}{\partial y} + \frac{\partial w}{\partial z} = 0. \quad (2.18)$$

If the non-dimensional variables are substituted into the conditions of no-slip, kine-

matic balance at the free-surface (2.4), tangential stress (2.5) and normal stress (2.6), then the lubrication boundary conditions, retaining leading order terms up to $O(\epsilon^2)$, become:

$$\overline{u} = \overline{v} = \overline{w} = 0 \quad \text{at } z = s(x, y), \quad (2.19)$$

$$\frac{\partial f}{\partial t} + u \frac{\partial f}{\partial x} + v \frac{\partial f}{\partial y} = w \quad \text{at } z = f(x, y, t), \quad (2.20)$$

$$\frac{\partial u}{\partial z} = \frac{\partial v}{\partial z} = 0 \quad \text{at } z = f(x, y, t), \quad (2.21)$$

$$p = -\frac{\epsilon^3}{Ca} \nabla^2 h - \Pi(h) \quad \text{at } z = f(x, y, t). \quad (2.22)$$

By integrating equations (2.15) and (2.16) twice with respect to z over the film thickness (i.e $s \leq z \leq f$, where $f = h - s$), applying the above boundary conditions followed by combining the terms for u and v with the dimensionless version of equation (2.4) and Leibniz's integral rule (Woods, 1926), leads to the following time-dependent governing equation for film thickness h ;

$$\frac{\partial h}{\partial t} = \frac{\partial}{\partial x} \left[\frac{h^3}{3} \left(\frac{\partial p}{\partial x} - 2 \right) \right] + \frac{\partial}{\partial y} \left[\frac{h^3}{3} \left(\frac{\partial p}{\partial y} \right) \right]. \quad (2.23)$$

Integrating equation (2.17) once with respect to z and applying equation (2.22) at the free-surface leads to the following expression for the non-dimensional pressure, p :

$$p = -\frac{\epsilon^3}{Ca} \nabla^2 (h + s) + 2\epsilon (h + s - z) \cot \alpha - \Pi(h). \quad (2.24)$$

Equations (2.23) and (2.24) describe the evolution of thin film flow on an inclined substrate; these equations based on a lubrication approach to the problem are analogous to a first order accurate long-wave approximation, see Appendix A, under the assumption that $Re = O(\epsilon)$ (Stillwagon and Larson, 1988). Most often in the literature these equations are combined to create a fourth-order equation in h , see

for example Kondic and Diez (2001) and Bertozzi and Brenner (1997). However, it has been shown that the above coupled form is most suitable for use with multigrid algorithms (Cowling *et al.*, 2011) and is thus the approach adopted in this thesis.

2.1.2 Contact line approach: disjoining pressure

A singularity exists at a three-phase contact line when a no-slip boundary condition is prescribed there; liquid displaces air as the film advances along the substrate, leading to a multi-valued velocity field at the contact line (Bertozzi *et al.*, 1998). The two most commonly used methods for relieving this singularity involve either specifying a disjoining pressure term in the pressure equation, (Schwartz and Eley, 1998), by introducing a thin precursor film ahead of the advancing front (Diez and Kondic, 2002) or specifying a slip condition at the substrate (Davis and Troian, 2003).

While there is evidence to suggest, for fully wetting fluids, that the two lead to comparable results when the precursor film thickness and slip-length have a similar value, (Spaid and Homsy, 1996), adopting the former approach is preferable in that it is more efficient from a computational perspective (Diez *et al.*, 2001). The solutions generated are independent of the choice of precursor film thickness provided it is sufficiently small (Diez and Kondic, 2001a) and the associated computational mesh of the same order so as to ensure adequate resolution of the contact line region (Diez *et al.*, 2001). Precursor films have been observed experimentally and measured at the advancing foot of a droplet and thus give some physical reality to the model (Popescu *et al.*, 2012). The related rivulet experiments of Johnson (1997) employed a pre-wetted substrate, the data from which are used for direct comparison purposes in Chapter 4. For all these reasons the disjoining pressure/precursor film approach was adopted in the work presented in Chapter 4, the formulation of which is reported more thoroughly below.

2.1.2.1 Contact line forces - Young's equation

As a liquid spreads over a substrate it displaces air from the surface. As this happens there is a shift in the surface free energy of the system; if the area of the interface increases, the surface free energy also increases, Rosen (2004), and vice versa when the area decreases. If a liquid spreads from A to B on a substrate, see Figure 2.2, then the decrease in surface free energy due to the decrease in the vapour-solid interface area is given by $a \times \gamma_{SV}$, where a is the area from A to B. The free energy increases for the liquid-vapour and liquid-solid interfaces in a similar manner. This gives the increase in surface free energy per unit area (force per unit length) as $S' = \gamma_{SV} - (\gamma_{SL} + \gamma_{LV})$. This quantity is a measure of the driving force behind the spreading of a liquid on a solid substrate and is called the spreading coefficient, S' (de Gennes, 1985).

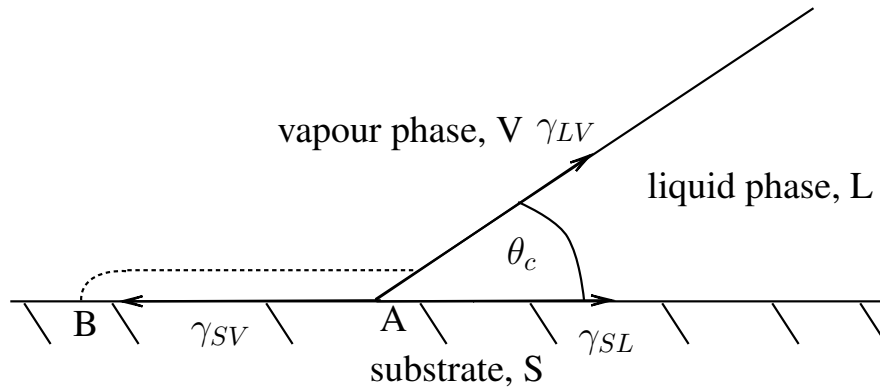


FIGURE 2.2: Schematic showing a liquid front spreading over a substrate displacing the vapour phase.

If the liquid makes a contact angle, θ_c , with the substrate, see Figure 2.3, and is considered to spread a small distance only, while maintaining the contact angle as θ_c , so as to cause an increase, Δa , in the area of the liquid-solid interface (the solid-vapour interface decreases by the same amount), the change in area of the liquid-vapour interface is then given by $\Delta a \cos \theta_c$. Therefore, the increase in surface free energy is:

$$\Delta E = -\gamma_{SV}\Delta a + \gamma_{SL}\Delta a + \gamma_{LV}\Delta a \cos \theta_c, \quad (2.25)$$

i.e.

$$\frac{\Delta E}{\Delta a} = -\gamma_{SV} + \gamma_{SL} + \gamma_{LV} \cos \theta_c. \quad (2.26)$$

Noting that as $\Delta a \rightarrow 0$ so does ΔE , equation (2.26) leads (de Gennes, 1985) to:

$$\gamma_{LV} \cos \theta_c = \gamma_{SV} - \gamma_{SL}, \quad (2.27)$$

which is the well known Young's equation, found by considering a droplet in equilibrium on a solid substrate (Butt *et al.*, 2013).

Note that γ_{LV} is equivalent to the surface tension of the liquid, σ , as it represents the interfacial free energy density.

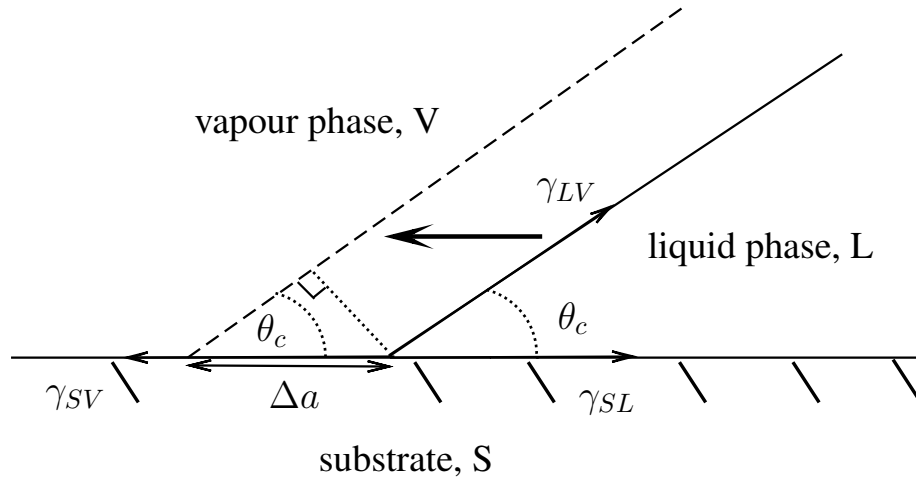


FIGURE 2.3: Schematic showing a spreading liquid with a contact angle of θ_c , displacing an area of Δa of the solid-vapour interface.

Substituting Young's equation, equation (2.27), into the equation for the spreading coefficient, $S' = \gamma_{SV} - (\gamma_{SL} + \gamma_{LV})$, one obtains a term for the spreading coefficient for a fluid with equilibrium contact angle, θ_c , namely:

$$S'_{\theta_c} = \gamma_{LV} (\cos \theta_c - 1), \quad (2.28)$$

which is a measure of the driving force of spreading at the contact line.

In the next section, by considering the forces imparted on the contact line are via

gradients of disjoining pressure, caused by molecular, electrostatic and structural forces, a model can be developed which recovers the physics discussed above.

2.1.2.2 Disjoining pressure

The basis for all subsequent work on disjoining pressure at the contact line of thin films and colloids was forged by Frumkin and Derjaguin (Frumkin, 1938; Derjaguin, 1940). They showed that the disjoining pressure, denoted by Π , can be divided split into contributions from molecular, electrostatic and structural forces acting on the fluid at the contact line. Derjaguin (1955) was the first to suggest the motion of the contact line was caused by gradients of the disjoining pressure. An important equation from the theory of Frumkin and Derjaguin is the one for finding the equilibrium contact angle (Churaev and Derjaguin, 1985) via:

$$\cos \theta_c = 1 - \frac{1}{\sigma} \int_{H_{min}}^{\infty} \Pi(H) dH, \quad (2.29)$$

which is now often referred to as the augmented Young-Laplace equation (Teletzke *et al.*, 1987), representing the balance of capillary, hydrostatic and disjoining pressures.

The form which the disjoining pressure term takes was also considered in the work of Derjaguin *et al.* (1987) and may be written in general form (Churaev and Sobolev, 1995) as:

$$\Pi = \frac{A_1}{H^3} - \frac{A_2}{H^2} + A_3 \exp\left(\frac{-H}{\lambda}\right), \quad (2.30)$$

where the first two terms are the molecular attraction forces and electrostatic repulsion forces; the third term embodies the structural forces. The coefficients A_i are non-arbitrary constants relating to the forces concerned and λ is the decay length of the structural forces.

Neglecting polar structural forces (Mitlin, 1995), which are considered short range

and exponentially decaying (Jameel and Sharma, 1994), the form of the disjoining pressure incorporating liquid-solid attraction and liquid-solid repulsion can be written (Mitlin and Petviashvili, 1994) as:

$$\Pi = \frac{B}{H_{min}^n} \left[\left(\frac{H_{min}}{H} \right)^n - \left(\frac{H_{min}}{H} \right)^m \right], \quad (2.31)$$

if a precursor film is incorporated H_{min} which naturally becomes the precursor layer thickness H^* [in the work of Derjaguin and others, H_{min} is the thickness of the film when $\Pi = 0$]. The coefficients (n, m) from the theory of Derjaguin, who found terms describing the molecular and electrostatic forces which were also considered by Teletzke *et al.* (1987), would be given as $(3, 2)$ as used in (Churaev and Derjaguin, 1985; Churaev and Sobolev, 1995; Schwartz and Eley, 1998); alternatively, the pair $(9, 3)$ comes from the integration of the Lennard-Jones 6-12 potential describing molecular forces between the bulk and precursor layer, as used in (Mitlin and Petviashvili, 1994).

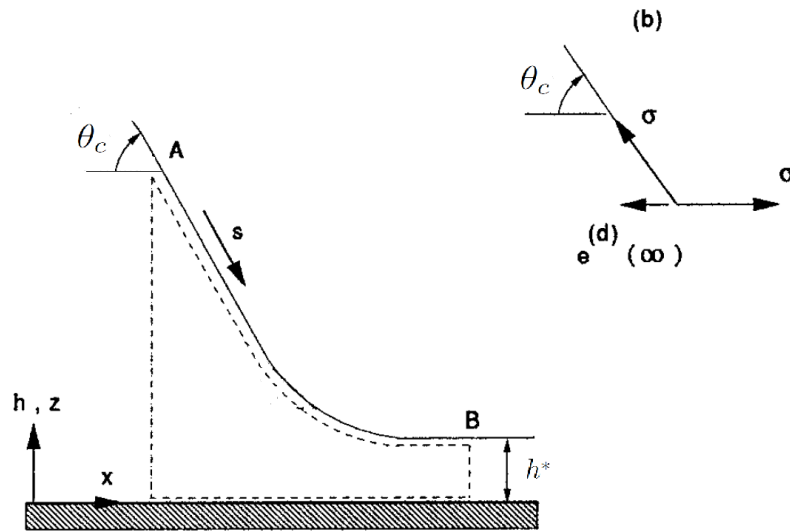


FIGURE 2.4: A diagram, from (Schwartz and Eley, 1998), of the contact line area; an integrated force balance is performed on the dotted area in the x direction to find the coefficient of the disjoining pressure term, B .

The coefficient B can be found by considering an integrated force balance in the x -direction at the contact line area, see Figure 2.4, and defining the local energy per unit area (or local disjoining energy density) (Derjaguin, 1940; Schwartz and Eley, 1998) as:

$$e_d(H) = - \int_{H^*}^H \Pi(H') dH'. \quad (2.32)$$

By assuming that H at A in Figure 2.4 is essentially ∞ relative to H^* then $\Pi = 0$ there; also note that the inclination at A is constant so the total pressure equates to zero. A similar argument applies at point B. The force balance equation then reads (Schwartz and Eley, 1998):

$$\int_{H^*}^{\infty} P(H) dH = \sigma \int_{H^*}^{\infty} \frac{d\theta}{ds} dH - \int_{H^*}^{\infty} \Pi(H) dH = 0, \quad (2.33)$$

with s the arc length on the free-surface giving $dH/ds = -\sin \theta$, allowing the integral $\sigma \int_{H^*}^{\infty} \frac{d\theta}{ds} dH$ to be written as $\sigma \cos \theta|_0^{\theta_c}$. Hence from equations (2.29), (2.32) and (2.33) it follows that:

$$\sigma \cos \theta_c = \sigma - e_d(\infty), \quad (2.34)$$

which is the disjoining pressure model equivalent of Young's equation, also called the augmented Young-Laplace equation as given by the Frumkin-Derjaguin theory (Churaev and Derjaguin, 1985). Rewriting Young's equation, equation (2.27), as $\gamma_{SL} + \sigma \cos \theta_c = \gamma_{SV}$, where γ_{SL} , σ and γ_{SV} are the interfacial energies at the solid-liquid, liquid-vapour (surface tension) and solid-vapour interfaces, respectively, when combined with equation (2.34) gives:

$$-e_d(\infty) = S'_{\theta_c} = \gamma_{SL} - \sigma - \gamma_{SV} = \sigma (\cos \theta_c - 1), \quad (2.35)$$

showing that $e_d(\infty)$ is analogous to the spreading coefficient, S'_{θ_c} .

By combining the definition of $e_d(H)$, equation (2.32), and the augmented Young's

equation, equation (2.34), it can be shown that:

$$\begin{aligned} e_d(\infty) &= \sigma (1 - \cos \theta_c) \\ &= \frac{B}{H^{*n-1}} \frac{n-m}{(m-1)(n-1)} \left[1 - \frac{n-1}{n-m} \left(\frac{H^*}{H} \right)^{m-1} + \frac{m-1}{n-m} \left(\frac{H^*}{H} \right)^{n-1} \right] \end{aligned} \quad (2.36)$$

and as $h = \infty$,

$$B = \frac{H^{*n-1} (n-1) (m-1) \sigma (1 - \cos \theta_c)}{(n-m)}, \quad (2.37)$$

$$\Pi(H) = \frac{(n-1) (m-1) \sigma (1 - \cos \theta_c)}{(n-m) H^*} \left[\left(\frac{H^*}{H} \right)^n - \left(\frac{H^*}{H} \right)^m \right]. \quad (2.38)$$

If the scalings adopted in deriving the governing equations of a thin film are implemented into the derivation of B then Π becomes:

$$\frac{S_{\theta_c} (n-1) (m-1)}{(n-m) h^*} \left[\left(\frac{h^*}{h} \right)^n - \left(\frac{h^*}{h} \right)^m \right]. \quad (2.39)$$

and

$$S_{\theta_c} = 6 (6Ca)^{-2/3} (1 - \cos \theta_c), \quad (2.40)$$

where the non-dimensional precursor film thickness $h^* = H^*/H_0$. and S_{θ_c} is termed here the non-dimensional spreading coefficient. This form of the disjoining pressure is the one adopted in equation (2.24) and utilised to investigate the role of wetting properties in rivulet formation. It is of note that if the fluid fully wets the substrate, i.e. $\theta_c = 0^\circ$, then the disjoining pressure term becomes zero.

2.1.2.3 Precursor film

The thickness of the precursor film H^* is a determining factor in the evolution of the contact line. The instability at the advancing front is damped by a thick precursor

film (Bertozi and Brenner, 1997) and can even be completely suppressed. The spreading rate of the film is also dependent on the choice of H^* (Schwartz and Eley, 1998). A realistic range for precursor film thickness is thought to lie in the region 1 – 100nm (Schwartz and Eley, 1998). The computational mesh size must then be specified to have a similar order of magnitude to the non-dimensional precursor film thickness h^* ; which is prohibitively expensive from a computational standpoint.

Kondic and Diez (2001) found that for values of $h^* < 0.02$ the global features of the flow remained unchanged. As the spreading rate itself is of little interest in the current work a slightly thicker than physically real precursor film with a value somewhere in this region may be employed while being confident the reported results are equivalent to those obtained with a smaller h^* . Throughout the thesis a value of $h^* = 0.01$ is used.

2.1.3 Boundary conditions

Numerical solutions to equations (2.23) and (2.24) are sought on a rectangular domain defined by $(x, y) \in \Omega = (0, l_p) \times (0, w_p)$. To close the problem suitable boundary conditions are required at the edges of the solution domain. At the upstream a constant flux condition is applied via a constant film thickness condition, $h(0, y) = 1$, at the downstream the film thickness is assumed to be that of the precursor film thickness, $h(l_p, y) = h^*$. On all boundaries zero flux (Neumann) conditions for both h and p are calculated via:

$$\left. \frac{\partial h}{\partial x} \right|_{x=0} = \left. \frac{\partial p}{\partial x} \right|_{x=0} = \left. \frac{\partial h}{\partial x} \right|_{x=l_p} = \left. \frac{\partial p}{\partial x} \right|_{x=l_p} = 0, \quad (2.41)$$

$$\left. \frac{\partial p}{\partial y} \right|_{y=0} = \left. \frac{\partial h}{\partial y} \right|_{y=0} = \left. \frac{\partial p}{\partial y} \right|_{y=w_p} = \left. \frac{\partial h}{\partial y} \right|_{y=w_p} = 0. \quad (2.42)$$

2.1.4 Initial conditions

At time $t = 0$, the film is designated to be a flat profile with a near square front given by:

$$h(x, y, 0) + s(x, y) = 0.5 \left\{ 1 + h^* - (1 - h^*) \tanh \left[\frac{(x - x_f(y))}{\delta} \right] \right\}, \quad (2.43)$$

where δ defines the steepness at the front. The contact line is perturbed, see Kondic and Diez (2001), in the spanwise direction with a superposition of N modes characterised by wavelengths $\lambda_{0,j} = 2w_p / j$ for $j = 1, \dots, N$ and random length $l_j \in [-0.2, 0.2]$ so that the position of the front at a given y location is:

$$x_f(y) = x_u - \sum_{j=1}^N l_j \cos \left(\frac{2\pi y}{\lambda_{0,j}} \right), \quad (2.44)$$

where x_f and x_u are the positions of the perturbed front and the unperturbed front slopes, respectively. When obtaining all the results discussed in subsequent chapters the initial film profile was taken to be the same, with $\delta = 0.01$ and $x_u = 30$, and guaranteed to be independent of the starting condition by taking N to be sufficiently large; accordingly the value $N = 50$ was used.

2.1.5 Topography definition

Although the model allows for the incorporation of complex topographies (Lee *et al.*, 2008), in the current work only the effect of simple rectangular peak and trench features on rivulet formation is considered. It is impossible to consider trenches/peaks with completely sharp edges as the height/depth of the substrate appears in the equations of interest as a function of x and y . Thus arctangents are used to create the required shape (Kalliadasis *et al.*, 2000; Bielarz and Kalliadasis, 2003; Gaskell, Jimack, Sellier, Thompson and Wilson, 2004; Lee *et al.*, 2007).

Accordingly, topography, $s(x, y)$, with height (depth) $s_0 = S_0/H_0 > 0$ ($s_0 < 0$),

length $l_t = L_t/L_0$ and width $w_t = W_t/L_0$, is defined via:

$$s(x, y) = \frac{s_0}{b_0} \left[\tan^{-1} \left(\frac{x - x_t - \frac{l_t}{2}}{\gamma l_t} \right) + \tan^{-1} \left(\frac{x_t - x - \frac{l_t}{2}}{\gamma l_t} \right) \right] \times \left[\tan^{-1} \left(\frac{y - y_t - \frac{w_t}{2}}{\gamma w_t} \right) + \tan^{-1} \left(\frac{y_t - y - \frac{w_t}{2}}{\gamma w_t} \right) \right], \quad (2.45)$$

with the centre of the topography at co-ordinates (x_t, y_t) . The steepness of the topography is controlled by γ and:

$$b_0 = 4 \left[\tan^{-1} \left(\frac{1}{2\gamma} \right) \right]^2. \quad (2.46)$$

2.1.6 Linear stability analysis

There has been considerable of attention directed at rivulet flow from a linear stability analysis perspective, see for example Troian *et al.* (1989), Spaid and Homsy (1996), Davis and Troian (2003); however, far less attention has been paid to three-dimensional transient simulations. Results of linear stability analysis are computed within this thesis for comparison with the latter and with corresponding experimental results.

2.1.6.1 Inclined planar substrate

A full derivation of the linear stability equations for film flow down an inclined planar substrate can be found in Appendix C. The usual approach, considering spanwise perturbations of the base state travelling wave solution of the governing equations, is adopted.

In brief, consider a base state solution of the equation set, equations (2.23) and (2.24), in an inertial frame of reference, $h(x, y, t) = h_0(\xi) + \varsigma h_1(\xi, y, t)$, where $\xi = x - U_w t$, with $U_w = 2(1 - h^{*3})/(1 - h^*)$ the velocity of the travelling wave solution; h_0 is the base state and h_1 the perturbation. Substituting the perturbed so-

lution into equations (2.23) and (2.24), keeping terms of $O(\varsigma)$ only and applying an appropriate Fourier transform (see Appendix C), results in a fourth order equation for the perturbation h_1 ;

$$\begin{aligned} \frac{\partial h_1(\xi, k, t)}{\partial t} = & \left(h_0^2 h_1 p_{0\xi} + \frac{h_0^3}{3} p_{1\xi} \right)_\xi - (2h_0^2 h_1)_\xi + U_w h_{1\xi} - \frac{k^2 h_0^3}{3} p_1 \\ & + \frac{k^2 \epsilon^3}{Ca} \left[\left(\frac{h_0^3}{3} h_{1\xi} \right)_\xi - \frac{k^2 h_0^3}{3} h_1 \right], \end{aligned} \quad (2.47)$$

where k is the wavenumber of the spanwise perturbation, p_0 is given by equation (2.24) and p_1 the perturbation of the same.

The exponential dependence on t of h_1 gives an eigenvalue problem written as:

$$\omega(k)\phi = \mathbf{A}(\xi, k)\phi, \quad (2.48)$$

where \mathbf{A} is the matrix operator of equation (2.47). The growth rates of the perturbation are denoted by ω ; positive values imply instability of the perturbation with wavenumber k .

The growth rates $\omega(k)$ are found by solving the eigenvalue problem (2.48), in the present work via Matlab using the *eig* function to obtain the associated eigenfunctions and eigenvalues. The most positive real part of the eigenvalues is the required growth rate for a particular k .

2.2 Navier-Stokes equations - Inner flow structures

2.2.1 Non-dimensional governing equations

The second problem of interest in this thesis, shown schematically in Figure 2.5 and considered in the (X, Z) plane, is comprised of a fully developed film of thickness H_0 , fed by a constant inflow, that is flowing over a substrate inclined at an angle α

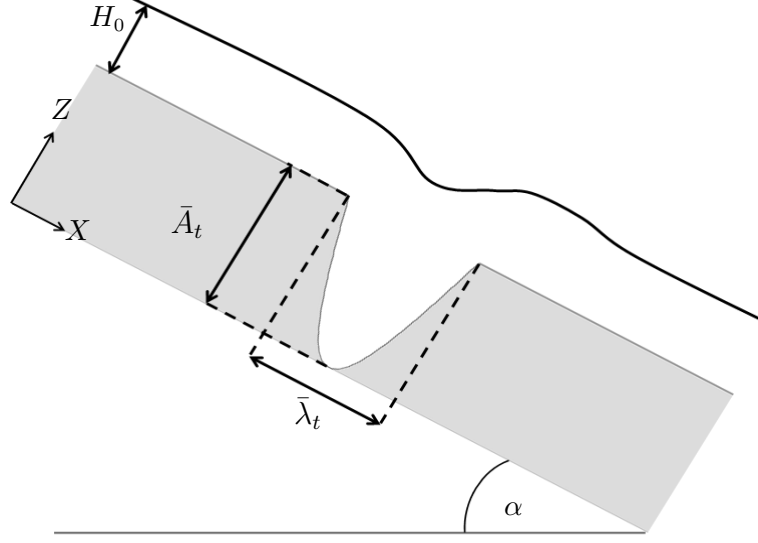


FIGURE 2.5: Schematic of the side view of thin film flow down a plate (length, L_x) inclined at an angle α to the horizontal, featuring a wave-like trench of depth \bar{A}_t and wavelength $\bar{\lambda}_t$. The film is fed by a constant inflow at the upstream boundary and H_0 denotes the asymptotic film thickness.

to the horizontal and containing a wave-like trench topography of height $S(X)$ and wavelength $\bar{\lambda}_t$. The film flows with velocity $\mathbf{U} = (U, W)$ and the fluid pressure is denoted by P .

The equations used to describe the flow in two-dimensions (variables in the Y plane become zero) are the full Navier-Stokes and continuity equations, given by equations (2.1) and (2.2). These equations are supplemented by the boundary conditions defined via equations (2.3)-(2.6) and the specification of inflow and outflow conditions in the form of fully developed inflow/outflow via a parabolic velocity field there, namely:

$$H|_{X=0} = H_0, U|_{X=0, L_p} = U_0 \frac{Z}{H_0} \left(2 - \frac{Z}{H_0} \right), W|_{X=0, L_p} = 0. \quad (2.49)$$

Non-dimensional forms of the governing equations are derived in a similar manner to the lubrication equations, here the assumption that $\epsilon = H_0/L_0 \ll 1$ is relaxed. The variables are scaled in the same manner except lengths which are now scaled by H_0 rather than L_0 .

Substitution of the non-dimensional variables into equations (2.1) and (2.2), as well as boundary conditions (2.3)-(2.6) & (2.49), leads to the following full, well-posed, non-dimensional Navier-Stokes and continuity equations, plus boundary conditions:

$$Re \left(\frac{\partial \mathbf{u}}{\partial t} + \mathbf{u} \cdot \nabla \mathbf{u} \right) = -\nabla p + \nabla \cdot \underline{\underline{\tau}} + St \mathbf{g}, \quad (2.50)$$

$$\nabla \cdot \mathbf{u} = 0, \quad (2.51)$$

$$\mathbf{u}|_{z=s} = 0, \quad (2.52)$$

$$h|_{x=0} = 1, u|_{x=0,l_p} = z(2-z), w|_{x=0,l_p} = 0, \quad (2.53)$$

$$\frac{\partial f}{\partial t} + u|_{z=f} \frac{\partial f}{\partial x} = w|_{z=f}, \quad (2.54)$$

$$\mathbf{n} \cdot (-p\mathbf{I} + \underline{\underline{\tau}})|_{z=f} \cdot \mathbf{n} = \frac{\kappa}{Ca}. \quad (2.55)$$

Noting that there is no disjoining pressure in this case, as there is no contact line singularity to deal with or contact angle to introduce, and that $\underline{\underline{\tau}}$ is the non-dimensional form of the viscous stress tensor. The non-dimensional fluid velocity is denoted by $\mathbf{u} = (u, w)$ and gravity component $\mathbf{g} = \mathbf{G}/g$. Any point in the non-dimensional coordinate system is expressed by $\mathbf{x} = (x, z)$. The Reynolds number $Re = \rho U_0 H_0 / \mu$ is a measure of the relative importance of inertial and viscous forces and the Stokes number, defined as $St = 2/\sin \alpha$, represents the ratio of gravitational to viscous forces.

The substrate height, $s(x)$, for a wave-like trench is created via a sin function of the form:

$$s(x) = \begin{cases} -A_t \sin \left[\pi \left(\frac{x-x_t + \frac{\lambda}{2}}{\lambda} \right) \right] & \text{if } |x - x_t| < \frac{\lambda}{2} \\ s(x) = 0 & \text{otherwise,} \end{cases}$$

with amplitude, $A_t = \bar{A}_t/H_0$, and wavelength, $\lambda_t = \bar{\lambda}_t/H_0$.

The initial profile is taken as a fully developed film with with flat free-surface (non-dimensional height 1) and parabolic inlet velocity profile - see equation (2.53).

Chapter 3

Method of solution

Contents

3.1	Numerical methods for investigating thin-film coating flows .	46
3.1.1	Long-wave approximation	46
3.1.2	Three-dimensional solutions	47
3.1.3	Solving the Navier-Stokes equations	49
3.2	Lubrication equations	51
3.2.1	Spatial discretisation	51
3.2.2	Temporal discretisation	52
3.2.2.1	Variable time-stepping	53
3.2.3	Adaptive multigrid strategy	54
3.2.3.1	Full approximation storage algorithm	54
3.2.3.2	Full Multigrid method	58
3.2.3.3	Local mesh refinement	58
3.2.3.4	Grid devolution	59
3.3	Navier-Stokes equations	61
3.3.1	Discretisation	62
3.3.1.1	Basis functions and interpolation	62
3.3.1.2	Free-surface spine method	66
3.3.1.3	Calculation of integrals	67
3.3.1.4	Solution strategy	69

In order to generate meaningful numerical results and useful numerical data, the governing equations of thin film flow were discretised and solved in a highly accurate, yet efficient, manner. This was achieved in two very different ways: the first, for the lubrication equations, involves defining a robust, adaptive multigrid algorithm to solve discrete finite difference analogues of equations (2.23) and (2.24); the second, for the accompanying internal flow of continuous films, is based on a Bubnov-Galerkin finite-element formulation of the Navier-Stokes and continuity equations, solved via a multifrontal solver (Veremieiev, 2011). Below, an overview of numerical techniques used is provided.

3.1 Numerical methods for investigating thin-film coating flows

The problematic task of investigating thin-film flows experimentally is, by the nature of the topic, the micro-scale of the characteristics of interest and the difficulty in controlling the influencing physical parameters. This has brought numerical investigations to the forefront of the research topic and with it the development of accurate and efficient numerical methods of solution has become pivotal to producing in-depth three-dimensional solutions.

3.1.1 Long-wave approximation

Rather than solving thin film flows numerically from the stand point of the Navier-Stokes and continuity equations, the task can be made much simpler and computationally tractable by utilising a long-wave approximation (Oron *et al.*, 1997). Such an approach is well suited to flows in which the disparity between the asymptotic fully-developed film thickness and the characteristic in-plane length scale is large, see for example Gaskell, Jimack, Sellier, Thompson and Wilson (2004). Ex-

panding the velocity and pressure in terms of the long-wave parameter within the Navier-Stokes and continuity equations, then retaining leading order terms reduces the governing equations to a fourth order, highly non-linear coupled equation set or alternatively, as shown in Chapter 2, a coupled equation set for the film height and pressure. Obtaining numerical solutions to the lubrication equations, although still forming a considerable challenge, requires substantially less and thus much more reasonable computational resources.

3.1.2 Three-dimensional solutions

The long-wave approach has been adopted in numerous investigations and for many different problems including continuous flow over topography (Stillwagon and Larson, 1990; Kalliadasis and Homsy, 2001; Gaskell, Jimack, Sellier, Thompson and Wilson, 2004), flow on flexible substrates (Lee *et al.*, 2009a) and past occlusions (Lee *et al.*, 2008), rivulet flow driven by gravity (Kondic and Diez, 2001) and thermal gradients (Kataoka and Troian, 1997). The stability of gravity-driven flow of a single rivulet has been investigated also by the lubrication approach, see for instance (Wilson and Duffy, 1998; Wilson *et al.*, 2002; Wilson and Duffy, 2005).

While computing two-dimensional solutions is relatively straightforward and reveals characteristics of the free-surface disturbance experienced by the film (Gaskell, Jimack, Sellier, Thompson and Wilson, 2004), only three-dimensional results give a complete picture of the free-surface dynamics. For instance when considering a continuous film flowing over a trench topography, see for example Decré and Baret (2003), Lee *et al.* (2007), in two-dimensions a capillary ridge forms at the upstream side of the trench. Corresponding three-dimensional solutions reveal much more detail: a downstream surge is also found to be present and the capillary ridge actually forms a bow-wave around the front of the trench Gaskell, Jimack, Sellier, Thompson and Wilson (2004), see Figure 1.5 of Chapter 1.

While generating steady-state solutions may be suitable for continuous flow, further

computational time is required for calculating transient processes such as a spreading film. A further complication comes when attempting to find solutions in the vicinity of a three-phase contact line; a well-known singularity is associated with the advancing front when a no-slip boundary condition is applied. As described in full in Section 2.1.2 of Chapter 2, a method of relieving this complexity is to assign a thin precursor film ahead of the spreading film; to fully resolve this area a mesh size of a similar order to that of the precursor film must be defined (Bertozzi *et al.*, 1998). This requirement is emphasised further still if a disjoining pressure model is utilised, in conjunction with the precursor film model, due to the large gradients in pressure in the region of the attendant contact line (Schwartz and Eley, 1998).

The formidable numerical challenge posed thus requires the development of state-of-the-art numerical methods for the efficient solution of the governing equations. The ever increasing ability and power of computers available to researchers allows for the extraction of grid independent results; Schwartz (1989) employed approximately 10,000 nodes in typical computations of rivulet formation, whereas most computations described in the recent literature use much finer and larger grid systems containing up to $O(10^6)$ nodes, see for example Gaskell, Jimack, Sellier and Thompson (2004); Gaskell *et al.* (2008); Mayo *et al.* (2013). Solving the discretised analogues of the governing equations on a scale such as this can become more manageable if devolved onto multiple processors, see for instance (Lee *et al.*, 2009a) where a multigrid framework is utilised to explore film flow on substrates containing densely distributed and complex topographies. An alternate approach to utilising parallel computing is to use an efficient solution procedure and implement various forms of error-controlled mesh and time adaptivity.

The most popular approach is to solve the governing fourth order partial differential lubrication equation - formed by combining equations (2.23) and (2.24) in Chapter 2 - using a semi-implicit time-splitting method (Cowling *et al.*, 2011) in conjunction with an alternating-direction implicit (ADI) scheme (Weidner *et al.*, 1997; Schwartz and Eley, 1998). This method exploits the stability of implicit schemes

and combines it with the CPU efficiency of explicit ones. While successful in its objective, in terms of efficiency multigrid methods are much better, in theory, to solve such problems having N unknowns in, at most, $O(N)$ operations (Wesseling, 1992; Trottenberg *et al.*, 2001) thus showcasing the method as a far more attractive alternative.

In practice multigrid methods have been applied to thin film problems in a variety of scenarios. A method which also incorporated an automatic, error-controlled variable time-stepping algorithm was used to consider droplet spreading on heterogeneous substrates (Gaskell, Jimack, Sellier and Thompson, 2004) demonstrating not only the accuracy of the method but also the vast savings in CPU time achieved by employing such a solver. Further efficiency can be incorporated via local mesh refinement, especially appropriate when there are large areas where the solution is known or demonstrates small gradients in the film thickness, which offers the opportunity to enhance further the computations - see Lee *et al.* (2007) for details. This method has also been used to investigate flow over complex topography and occlusions (Sellier and Panda, 2009), the effect of flexible membrane (Lee *et al.*, 2009b) and to consider an evaporating thin film on a substrate containing trench topographies (Gaskell *et al.*, 2006). Recently, the framework has been adopted to solve inertial thin-film flow Veremieiev *et al.* (2010) via a depth-averaged form of long-wave equations with and without the effect of an electric field on the flow dynamics (Veremieiev *et al.*, 2012).

3.1.3 Solving the Navier-Stokes equations

Solving the full governing equations of thin-film flow, the Navier-Stokes and continuity equations, alleviates the restrictions imposed by long-wave theory; namely, those related to film thickness, in-plane length scale and Capillary number. While it may be prohibitively expensive to solve such problems in three-dimensions (and even in two-dimensions) it is the most accurate way of investigating both the in-

ner flow structure and free-surface disturbance present in situations other than for Stokes flow - in which case a boundary element approach can prove more suitable to adopt, see for example (Pozrikidis and Thoroddsen, 1991; Blyth and Pozrikidis, 2006; Baxter *et al.*, 2009, 2010).

Analytical solutions of the Stokes and Navier-Stokes equations for flow over a wavy wall can be constructed via a perturbation analysis based on assumptions such as disparity between film thickness, substrate wavelength and amplitude (Wierschem *et al.*, 2002). This technique has been used effectively for two-dimensional flow over a wavy substrate (Wang, 1981; Wierschem *et al.*, 2002) and three-dimensional flow (Wang, 2005; Luo and Pozrikidis, 2007; Heining and Aksel, 2009). This calculation method does not, however, have the ability to predict, for example, the presence of eddies in the valleys of an undulating substrate. To overcome this limitation, a semi-analytical approach can be employed where complex function theory reduces the two-dimensional Stokes equations to a system of ordinary differential and integral equations, solved employing Fourier analysis and an iterative algorithm (Scholle *et al.*, 2004, 2006; Scholle and Aksel, 2007). This method has been shown to give good agreement to experimental observations. To investigate the inertial influence on the inner flow the full Navier-Stokes equations must be considered as in Scholle *et al.* (2008); a volume-of-fluid (VOF) method was used by Heining *et al.* (2012) to solve full equations to investigate flow over undulating substrates and the associated laminar mixing in the flow.

Parallel computing is necessary, even in two-dimensions, to achieve the required resolution to capture the re-circulating flow structures, eddies, that form in a reasonable time for transient flow situations. A multi-frontal solver has been shown to be a suitable means of achieving this as efficiently as possible (Veremieiev, 2011). Transient solutions to the Navier-Stokes equations can be solved using a finite element discretisation to understand how applying perturbations to a system alters the flow (Wilson *et al.*, 2006). When a free-surface is present a further unknown is added to the system; by making the node co-ordinates of the mesh one of the

unknowns it is possible to find the free-surface boundary using a method of spines (Kistler and Schweizer, 1997). A combination of all these techniques gives an efficient algorithm for producing revealing transient data of the inner flow.

3.2 Lubrication equations

The discrete form of the governing lubrication equations is provided below for the case of film flow down a planar substrate; the equations particular to the case of film flow down a vertically aligned cylinder, investigated in Chapter 6, can be found in Appendix B.

3.2.1 Spatial discretisation

Equations (2.23) and (2.24) are solved on a rectangular domain $\Omega = (0, l_p) \times (0, w_p)$ subject to the boundary conditions given in Section 2.1.3, meshed using a regular grid of nodes with increments of Δx and Δy in the x and y directions, respectively [for simplicity only square meshes are considered with $\Delta = \Delta x = \Delta y$]. Values of h and p are assigned to each node (i, j) in the domain, Ω . Spatial derivatives are approximated via the standard second-order accurate, central differencing scheme as in Lee *et al.* (2007), which leads to the following discrete forms of equations (2.23) and (2.24):

$$\begin{aligned} \frac{\partial h_{i,j}}{\partial t} = \frac{1}{\Delta^2} & \left[\frac{h^3}{3} \Big|_{i+\frac{1}{2},j} (p_{i+1,j} - p_{i,j}) - \frac{h^3}{3} \Big|_{i-\frac{1}{2},j} (p_{i,j} - p_{i-1,j}) \right. \\ & \left. + \frac{h^3}{3} \Big|_{i,j+\frac{1}{2}} (p_{i,j+1} - p_{i,j}) - \frac{h^3}{3} \Big|_{i,j-\frac{1}{2}} (p_{i,j} - p_{i,j-1}) \right] - \frac{2}{\Delta} \left(\frac{h^3}{3} \Big|_{i+\frac{1}{2},j} - \frac{h^3}{3} \Big|_{i-\frac{1}{2},j} \right), \end{aligned} \quad (3.1)$$

$$p_{i,j} + \frac{\epsilon^3}{Ca\Delta^2} [(h+s)_{i+1,j} + (h+s)_{i-1,j} + (h+s)_{i,j+1} + (h+s)_{i,j-1} - 4(h+s)_{i,j}] - 2\epsilon(h+s)_{i,j} \cot \alpha + \Pi(h_{i,j}) = 0. \quad (3.2)$$

The terms $\frac{h^3}{3}|_{i\pm\frac{1}{2},j}$, $\frac{h^3}{3}|_{i,j\pm\frac{1}{2}}$, known as prefactors, are obtained using linear interpolation between neighbouring grid points and are given, for example, by:

$$\frac{h^3}{3}|_{i+\frac{1}{2},j} = \frac{1}{2} \left(\frac{1}{3}h_{i+1,j}^3 + \frac{1}{3}h_{i,j}^3 \right),$$

and similarly for the other prefactors (Kondic and Diez, 2001).

Neumann (no flux) boundary conditions are implemented by introducing ghost nodes at the edge of the computational domain; values defined by Dirichlet boundary conditions can be assigned exactly at the appropriate boundary nodes.

3.2.2 Temporal discretisation

Here, $F_{i,j}^h(h^n, p^n)$, $F_{i,j}^p(h^{n+1})$ are used to represent the spatial discretisation, defined in equations (3.1) and (3.2), of the associated h and p equation at the n -th time step, where $t = t^n$, at node (i, j) . To advance the solution in time an implicit, unconditionally stable Crank-Nicolson scheme (Gaskell, Jimack, Sellier and Thompson, 2004) is employed:

$$h_{i,j}^{n+1} - \frac{\Delta t^{n+1}}{2} F_{i,j}^h(h^{n+1}, p^{n+1}) = h_{i,j}^n + \frac{\Delta t^{n+1}}{2} F_{i,j}^h(h^n, p^n), \quad (3.3)$$

$$p_{i,j}^{n+1} + F_{i,j}^p(h^{n+1}). \quad (3.4)$$

For simplicity, the fully discretised forms of equations (2.23) and (2.24) can be written in terms of non-linear operators:

$$\mathcal{N}^h(\underline{h}^{n+1}, \underline{p}^{n+1}) = \underline{f}^h(\underline{h}^n, \underline{p}^n), \quad (3.5)$$

$$\mathcal{N}^p(\underline{h}^{n+1}, \underline{p}^{n+1}) = 0, \quad (3.6)$$

where $\mathcal{N}^h, \mathcal{N}^p$ represent the non-linear operator of the left hand side of equations (3.3) and (3.4), and \underline{f}^h the right hand side of equation (3.3). Thus, writing the solution at time n as $\mathbf{u}^n = (h^n, p^n)^T$, the full system of discrete equations (3.3) and (3.4) may be written in the form:

$$\mathbf{N}\mathbf{u}^{n+1} = \mathbf{f}(\mathbf{u}^n). \quad (3.7)$$

3.2.2.1 Variable time-stepping

To obtain an optimal time step, and so increase the efficiency of the method, automatic-error-controlled variable time-stepping is incorporated via an analysis of an estimate of the local truncation error (LTE). This is achieved by comparing predicted and previous solutions with the current solution (Gaskell, Jimack, Sellier and Thompson, 2004); predicted values for h and p are obtained via explicit, second-order in time discretisation of the governing equations:

$$h_{pred}|_{i,j}^{n+1} = \gamma_t^2 h_{i,j}^{n-1} + (1 - \gamma_t^2) h_{i,j}^n - \Delta t^{n+1} (1 + \gamma_t) F_{i,j}^h(h^n, p^n), \quad (3.8)$$

$$p_{pred}|_{i,j}^{n+1} + F_{i,j}^p(h_{pred}^{n+1}) = 0, \quad (3.9)$$

where $\gamma_t = \Delta t^{n+1}/\Delta t^n$, with $\Delta t^n = t^n - t^{n-1}$.

The LTE for h_{pred} can be defined via a Taylor series expansion of equation (3.8), given by:

$$(\text{LTE})_{pred}|_{i,j} = \frac{\Delta t^{n+1} \Delta t^n (1 + \gamma)}{6} \frac{\partial^3 h_{i,j}}{\partial t^3} \Big|_{t=t_p}, \quad (3.10)$$

for $t_p \in (t_n, t_{n+1})$. Similarly, a Taylor expansion of equation (3.3) leads to a term for the LTE for h at the solution stage, namely:

$$(\text{LTE})_{sol}|_{i,j} = -\frac{(\Delta t^{n+1})^3}{12} \frac{\partial^3 h_{i,j}}{\partial t^3} \Big|_{t=t_s}, \quad (3.11)$$

for $t_s \in (t_n, t_{n+1})$.

Under the assumption that the third order derivative of h varies by a small amount only over a time step, allows an estimate for the local truncation error to be calculated via:

$$(\text{LTE})_{i,j} = \frac{-1}{1 + 2 \left(\frac{1+\gamma}{\gamma} \right)} (h_{i,j}^{n+1} - h_{pred\ i,j}^{n+1}). \quad (3.12)$$

This in turn can be used to estimate the overall truncation error by finding the Euclidean norm, $\|\text{LTE}\|$, Dormand (1996), which can then be used to define the next time step, Δt^{n+1} , as:

$$\Delta t^{n+1} = 0.9 \Delta t^n \left(\frac{\text{TOL}}{\|\text{LTE}\|} \right)^{\frac{1}{3}}, \quad (3.13)$$

if $\|\text{LTE}\| \leq \text{TOL}$, where TOL is a user prescribed tolerance. However, if $\|\text{LTE}\| > \text{TOL}$ then the previous time step is restarted with half the current time step.

3.2.3 Adaptive multigrid strategy

3.2.3.1 Full approximation storage algorithm

The system of equations (3.7) is solved via a multigrid solution strategy exploiting the method's ability to solve a problem having N unknowns in $O(N)$ operations (Lee *et al.*, 2007). Problems can be solved even more efficiently by employing in addition error-controlled automatic mesh refinement/de-refinement strategies. Such a procedure has been utilised and applied successfully to solve the lubrication equations to explore thin film flow over topography and droplet spreading, see for example Gaskell, Jimack, Sellier, Thompson and Wilson (2004), Gaskell, Jimack, Sellier and Thompson (2004), Gaskell *et al.* (2006), Lee *et al.* (2007).

The approach of multigridging, the detailed theory of which can be found in a number of books - see for example Brandt and Livne (1984), Wesseling (1992), Trottenberg *et al.* (2001) - is to use a simple but efficient iterative technique as a smoother to reduce high frequency (local) errors on a particular computational

grid that spans the solution domain, while using a hierarchy of successively finer grids \mathcal{G}_k , $k \in [0, 1, 2, \dots, K]$, to smooth low frequency (global) errors. Here, \mathcal{G}_K represents the finest grid level and \mathcal{G}_0 the coarsest.

\mathcal{G}_0 contains $n_0 = A_x + 1$ nodes in the x -direction and $m_0 = A_y + 1$ in the y -direction, where A_x and A_y are integers greater or equal to 1. These values are used to define the resolution of the finer grids; for any grid \mathcal{G}_k , $n_k = A_x 2^k + 1$ and $m_k = A_y 2^k + 1$, which gives a grid resolution (spacing) of $\Delta x = l_p / n_k$ and $\Delta y = w_p / m_k$.

Writing the system of equations to be solved, equation (3.7), incorporating the multigrid notation, on a computational grid \mathcal{G}_k the equations to be solved are:

$$\mathbf{N}\mathbf{u}_k^{n+1} = \mathbf{f}_k(\mathbf{u}_k^n). \quad (3.14)$$

Taking the current multigrid iteration as m with $m = 0$ at the start of each multigrid cycle, consider for the sake of clarity a two grid set up, \mathcal{G}_0 and \mathcal{G}_1 ; for an initial fine grid approximation on \mathcal{G}_1 of $\mathbf{u}_1^m = \left(\underline{h}_1^m, \underline{p}_1^m \right)^T$ a set number, ν_{pre} , of pre-relaxation sweeps is performed on \mathcal{G}_1 to give relaxed fine grid values $\tilde{\mathbf{u}}_1^m$. A restriction inter-grid transfer operator, R_k^{k-1} , is used to transfer $\tilde{\mathbf{u}}_1^m$ to \mathcal{G}_0 and the coarse grid solver employed to give a coarse grid solution \mathbf{w}_0^m . From this correction terms are calculated via $\mathbf{v}_0^m = \mathbf{w}_0^m - \tilde{\mathbf{u}}_0^m$, which are then interpolated onto the finer grid via another interpolation operator I_{k-1}^k and used to update $\tilde{\mathbf{u}}_1^m$ to $\mathbf{u}_1 = \tilde{\mathbf{u}}_1^m + \mathbf{v}_1^m$. Finally ν_{post} relaxation sweeps are applied to the updated solution on the fine grid to give a new, updated solution \mathbf{u}_1^{m+1} .

The number of so-called FAS (Full Approximation Storage, see below) iterations at each level is specified by κ and this determines what type of cycle is employed, so if $\kappa = 1$ then the process is completed using V-cycles, if $\kappa = 2$ then W-cycles are employed, see Figure 3.1, and so on. The maximum and minimum number of iterations, i.e. the number of FAS-cycles, on the current grid level are defined; should the residual error reduce to a suitable level before the maximum number of iterations are performed then the multigrid iterations on the current grid level are

terminated and the next level of the so-called FMG (Full Multigrid, see Section 3.2.3.2) iteration is performed.

The FAS multigrid algorithm is described below in the same pseudo-code formalism as seen in Trottenberg *et al.* (2001) and Lee *et al.* (2007):

$$\mathbf{u}_k^{m+1} = \text{MGFASCYC}(k, \mathbf{u}_k^m, \mathbf{f}_k, \nu_1, \nu_2, \kappa)$$

Pre-relaxation sweeps

- Perform ν_{pre} relaxation sweeps $\tilde{\mathbf{u}}_k^m = \text{RELAX}(\mathbf{u}_k^m, \mathbf{f}_k)$

Coarse grid correction

- Compute residual on \mathcal{G}_k

$$\mathbf{d}_k^m = \mathbf{f}_k - \mathbf{N}_k \tilde{\mathbf{u}}_k^m$$
- Restrict residual and fine grid solution on to the next coarsest grid \mathcal{G}_{k-1}

$$\mathbf{d}_{k-1}^m = R_k^{k-1} \mathbf{d}_k^m, \tilde{\mathbf{u}}_{k-1}^m = R_k^{k-1} \tilde{\mathbf{u}}_k^m$$
- Compute the right hand side of equation (3.14), \mathbf{f}_{k-1}

$$\mathbf{f}_{k-1} = \mathbf{d}_{k-1}^m + \mathbf{N}_{k-1} \tilde{\mathbf{u}}_{k-1}^m$$
- If $k = 1$ and thus \mathcal{G}_{k-1} is the coarsest grid then solve for coarse grid solution
$$\mathbf{w}_{k-1}^m$$

$$\mathbf{N}_{k-1} \mathbf{w}_{k-1}^m = \mathbf{f}_{k-1}$$
- If $k > 1$ then perform κ iterations of the multigrid cycle
$$\mathbf{w}_{k-1}^m = \text{MGFASCYC}(k-1, \tilde{\mathbf{u}}_{k-1}^m, \mathbf{f}_{k-1}, \nu_1, \nu_2, \kappa)$$
- Compute corrections, \mathbf{v}_{k-1}^m on \mathcal{G}_{k-1}

$$\mathbf{v}_{k-1}^m = \mathbf{w}_{k-1}^m - \tilde{\mathbf{u}}_{k-1}^m$$
- Interpolate corrections on to \mathcal{G}_k

$$\mathbf{v}_k^m = I_{k-1}^k \mathbf{v}_{k-1}^m$$

- Update solution on fine grid \mathcal{G}_k via

$$\mathbf{u}_k^m = \tilde{\mathbf{u}}_k^m + \mathbf{v}_k^m$$

Post-relaxation sweeps

- Perform ν_{post} relaxation sweeps to complete cycle

$$\mathbf{u}_k^{m+1} = \text{RELAX}(\mathbf{u}_k^m, \mathbf{f}_k)$$

The full realisation of the benefits of using a multigrid strategy can only be achieved if a suitable post and pre-relaxation iterative smoother is utilised that is stable, accurate and efficient. To this end a red-black Gauss-Seidel Newton relaxation scheme is employed. Other node by node smoothing schemes have been tested extensively and were found wanting in comparison to the speed of the Newton solver, see Appendix D.3.

Another detail concerning obtaining numerical solutions via Newtonian smoothers is the calculation of the associated Jacobian of the governing equation set, see Appendix D.3 and Gaskell *et al.* (2010). For ease of use and flexibility of the method, a numerical Jacobian can be calculated by considering a small change in the current solution and calculating the gradient induced by this small perturbation, i.e.

$$\mathbf{J} = \frac{\mathbf{N}(\mathbf{u}_k^{n+1} + \varsigma) - \mathbf{N}\mathbf{u}_k^{n+1}}{\varsigma}. \quad (3.15)$$

An alternative but less general approach is to calculate the Jacobian analytically - from a computational perspective this would require the Jacobian to be reformulated and hard-coded when solving different forms of the governing equations, for example including surface tension gradient effects, solving the flow on a cylinder, or incorporating additional physics.

The two methods - analytical and numerical - were compared for computational efficiency with the difference between the two shown to be minimal, see Appendix D. As such the numerical Jacobian was employed in carrying out the work reported in this thesis.

3.2.3.2 Full Multigrid method

A full multigrid (FMG) approach is used to avoid possible divergence due to a poor initial solution. The basis of the method is to use smoothed solutions from coarser grids to generate an appropriate initial estimate of the solution on the finer grids. A interpolation operator Π_{k-1}^k is used to transfer information from \mathcal{G}_{k-1} to \mathcal{G}_k , the order of Π_{k-1}^k may or may not be equal to the order of the interpolation operator used within the FAS algorithm (Lee *et al.*, 2007). Combined with the previously described FAS multigrid algorithm, see Figure 3.1 for a schematic diagram, the procedure is as follows:

For grid levels $k = 0, 1, \dots, K$

- If $k = 0$, solve $\mathbf{N}_0 \mathbf{u}_0^{m+1} = \mathbf{f}_0$ to obtain initial guess \mathbf{u}_0^m
- If $k > 0$ then interpolate onto fine grid, thus

$$\mathbf{u}_k^m = \Pi_{k-1}^k \mathbf{u}_{k-1}^m$$

$$\mathbf{u}_k^{m+1} = \text{MGFASCYC}(k, \mathbf{u}_k^m, \mathbf{f}_k, \nu_{\text{pre}}, \nu_{\text{post}}, \kappa)$$

3.2.3.3 Local mesh refinement

Automatic mesh adaptation is implemented via a local truncation error analysis that measures the value, τ_k^{k-1} , for each grid level via:

$$\tau_k^{k-1} = \mathbf{N}_k \mathbf{R}_k^{k-1} \tilde{\mathbf{u}}_k - R_k^{k-1} (\mathbf{N}_k \tilde{\mathbf{u}}_k), \quad (3.16)$$

as in Lee *et al.* (2007). For all grids $k = R+1, \dots, K$, giving the number of adaptive multigrid levels as $K - R$, local refinement takes place wherever $\tau_k^{k-1} \geq v$, where v is a user defined tolerance. This means that the grids are refined only in the areas of highest error in the next grid level's solution; accordingly, unnecessary refinement is avoided creating improved efficiency at each time step. For full details see Lee *et al.* (2007).

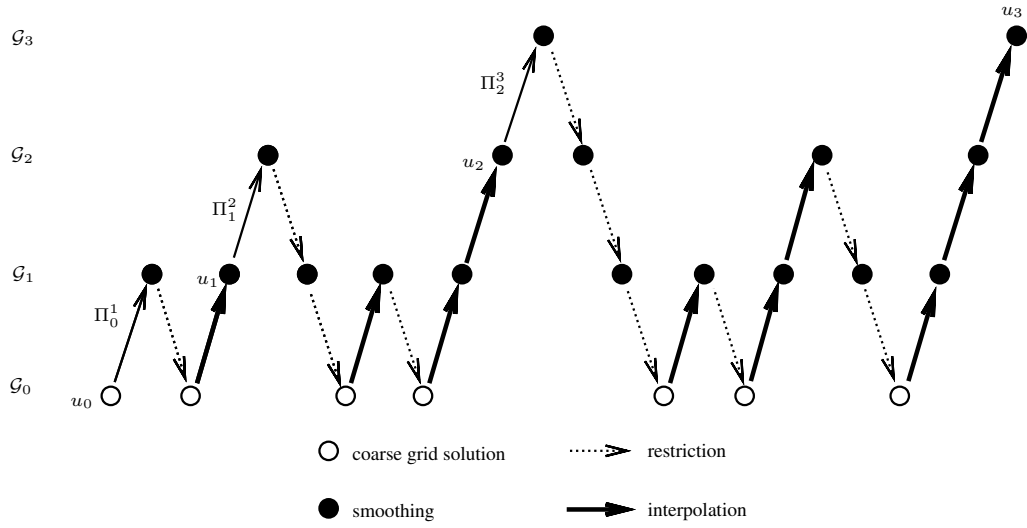


FIGURE 3.1: Schematic diagram of the full multigrid algorithm incorporating one FAS W-cycle over four grid levels, \mathcal{G}_k with $k \in [0, 3]$. The solution on each grid \mathcal{G}_k , $k \in [1, 3]$, at the end of the FAS W-cycle on each level, k , is indicated by u_k ; the initial solution given by the coarse grid solution is u_0 . Full multigrid interpolation is indicated at the end of each FAS-cycle by Π_{k-1}^k . Restriction and interpolation is performed using inter-grid transfer operators R_k^{k-1} and I_{k-1}^k respectively, between grid levels \mathcal{G}_k and \mathcal{G}_{k-1} .

3.2.3.4 Grid devolution

The methodology described above has been developed specifically to fully maximise efficiency when considering the flow of continuous films over complex topography; however, the long-time growth of rivulets over a large computational domain leads to the possibility of introducing further time saving measures while retaining the accuracy of the multigrid process. Li *et al.* (2011) used a multigrid method with no adaptivity to consider thermally driven rivulet growth; they designed an automatic domain shifting algorithm so that long-time evolutions could be considered. This methodology essentially redefines the computational domain as the front approaches the end of the current domain and disregards the free-surface data in the vicinity of the upstream boundary. Its disadvantages are that it makes the implementation of grid adaptivity increasingly complex and difficult to manage and there must be extra care taken over when to ‘shift’ the current domain so the false boundary conditions do not pollute the final solution.

Alternatively, Gomba (2012) has suggested formulating the lubrication equations, but in two dimensions only, in a moving frame of reference so as to minimise the size of the computational domain required to compute solutions; for the problems considered the saving in computational time over that spent with a non-adaptive grid was shown to be vast. However, this method can prove to be problematic as the time-step variable must be kept small enough to adequately estimate the changing velocity of the moving frame to minimise the ‘slip’ of the advancing front. Additionally, for the rivulet problem of interest here, individual rivulets extend in length from a starting value of zero to as much as $100L_0$ or greater (depending on simulation time and fluid properties the final length of the rivulets varies greatly). So, even with the adoption of a moving frame of reference, the size of the computational domain must still be large enough to contain the long-time evolution length of the associated rivulets. A dynamically changing computational domain is the obvious answer, especially given the size of the solution domain typical in rivulet flows; this idea is developed below.

A method of devolving the solution grid in regions where the film profile exhibits no change is implemented; it is well suited to rivulet formation on a large substrate as the area of interest is confined to the contact line region, away from which the film is either fully developed upstream, i.e $h = 1$, or, downstream ahead of the advancing front, is equal to the precursor film thickness, h^* . This implies that a suitable criteria for grid devolution can be based on the gradient of the solution at the starting grid level for devolution, $k = D$.

Accordingly, for each node in the computational domain the norm of the gradient of the solution is calculated on the grid level D at time iteration n to determine whether the node is to be removed by the devolution routine:

$$Grad = |\nabla h_D^n| + |\nabla p_D^n| < TOL_d. \quad (3.17)$$

$Grad$, the absolute sum of the gradient, will be largest in areas where the gradient of

h and/or p is large; therefore if for any node in the solution domain $Grad < TOL_d$, where TOL_d is a user defined tolerance, that node is marked for devolution. At the beginning of each time iteration $Grad$ is calculated at each node on D and if $Grad$ is within the specified tolerance then the node is removed from subsequent calculations in the cycle. This process essentially re-defines the computational domain to a much smaller, appropriate size while not affecting the final solution. The criteria for devolution is determined on grid level D and corresponding nodes are also removed from subsequent calculations on levels $k < D$.

For a comparison of the relative efficiency of the three variants of the multigrid method described here - non-adaptive, local mesh refinement only and local mesh refinement in conjunction with grid devolution - see Section D.1 in Appendix D.

3.3 Navier-Stokes equations

The two-dimensional, time-dependent Navier-Stokes equations and associated boundary conditions, (2.50)-(2.55), are solved using a finite element formulation; the equations are written:

$$Re \left(\frac{\partial \mathbf{u}}{\partial t} + \mathbf{u} \cdot \nabla \mathbf{u} \right) = -\nabla p + \nabla \cdot \underline{\underline{\tau}} + St\mathbf{g}, \quad (3.18)$$

$$\nabla \cdot \mathbf{u} = 0, \quad (3.19)$$

$$\mathbf{u}|_{z=s} = 0, \quad (3.20)$$

$$h|_{x=0} = 1, u|_{x=0,l_p} = z(2-z), w|_{x=0,l_p} = 0, \quad (3.21)$$

$$\frac{\partial f}{\partial t} + u \frac{\partial f}{\partial x} = w, \quad (3.22)$$

$$\mathbf{n} \cdot (-p\mathbf{I} + \underline{\underline{\tau}})|_{z=f} \cdot \mathbf{n} = \frac{\kappa}{Ca}. \quad (3.23)$$

Although well-known, the Navier-Stokes equations require substantial computational resources to be solved even in two dimensions, further complexity arises due to the presence of a transient free-surface, the position of which must be obtained

as part of the solution. Here, a generalisation of the spinal method, introduced in Kistler and Schweizer (1997), and the Arbitrary Lagrangian Eulerian (ALE) formulations of Cairncross *et al.* (2000) is employed. In brief, the grid adapts depending on the free-surface shape, like a Lagrangian method, and remains fixed where necessary, as per a Eulerian formulation; thus the grid co-ordinates are treated as unknowns and must be solved for. A truncated formulation of the discretisation is provided in the next section and a brief explanation of how the domain integrals are calculated is given; the reader can find the remaining details if required in Veremieiev (2011).

3.3.1 Discretisation

3.3.1.1 Basis functions and interpolation

Within the finite element method, the unknown velocity, pressure and coordinate fields are written in terms of basis functions (also known as trial, interpolation or shape functions - the reason for naming them basis functions becomes apparent later in the text):

$$\mathbf{u} = \sum_{i=1}^{n^i} \mathbf{u}_i \phi_i, \quad p = \sum_{j=1}^{n^j} p_j \psi_j, \quad \mathbf{x} = \sum_{i=1}^{n^i} \mathbf{x}_i \phi_i, \quad (3.24)$$

where $\mathbf{u}_i = (u_i, w_i)$, p_j and $\mathbf{x}_i = (x_i, z_i)$ are the unknown nodal values of velocity, pressure and coordinates, respectively. The total number of domain \mathbf{u}/\mathbf{x} -nodes is denoted by n^i and the total number of p -nodes is n^j with $i \in [1, n_e^i]$, $j \in [1, n_e^j]$. The basis functions for velocity and coordinates are represented by ϕ_i and for pressure by ψ_j .

A Bubnov-Galerkin weighted residual formulation that assumes values of the test functions are the same as the basis functions is employed for the discretisation of equations (3.18), (3.19) and (3.22). A mixed-formulation approach is adopted with

the number of u/x -nodes per element denoted by n_e^i and, similarly, the number of p -nodes is n_e^j . Such a formulation is applied in Chung (2002) and, as seen in the same, to calculate the local integrals for the triangular elements it is appropriate to introduce local barycentric coordinates L_β for $\beta \in [1, n_e^j]$. The value of L_β ranges between zero, along the edges, and 1 at the vertices of the element; the value vary linearly between vertices within the element, see Figure 3.2.

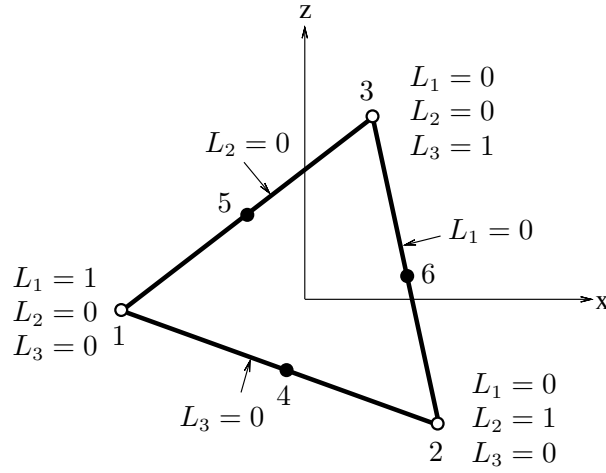


FIGURE 3.2: Local barycentric coordinates for a triangular element in the domain Ω . u/x -nodes are denoted by both filled and unfilled circles, p -nodes by unfilled circles only.

The basis functions, ϕ_i and ψ_j , are then written in terms of local coordinates as:

$$\phi_i = \begin{cases} L_i (2L_i - 1), & i \in [1, n_e^j], \\ 4L_{i_1} L_{i_2}, & i \in (n_e^j, n_e^i), \end{cases} \quad \psi_j = L_j, j \in [1, n_e^j], \quad (3.25)$$

where i_1 and i_2 are defined as:

$$i_1(i) = \text{trunc} \left[\frac{3 + \sqrt{8(i - n_e^j) - 7}}{2} \right], \quad i_2(i) = i - n_e^j - \frac{(i_1 - 1)(i_1 - 2)}{2}, \quad (3.26)$$

where $\text{trunc}(x)$ truncates x from a real number to an integer. A final condition of

the local coordinate system is that the sum of L_β is equal to 1, i.e. :

$$\sum_{j=1}^{n_e^j} L_j = 1. \quad (3.27)$$

Accordingly, the interpolation of velocity and coordinates within the triangular element is quadratic and linear for pressure, also known as a ‘mixed interpolation formulation, see Hood and Taylor (1974). This means that the number of nodes for \mathbf{u} and p are different; the interpolation for coordinates may be of the same order as the velocities (Christodoulou *et al.*, 1997) thus giving second-order accurate free-surface coordinates for a similar computational cost. Triangular V6/P3/X6 elements are therefore employed, meaning elements with 6 \mathbf{u}/x -nodes and 3 p -nodes, for the two-dimensional problem at hand.

The momentum equation, (3.18), is discretised by multiplying it with appropriate weighting functions, integrating over the computational domain, Ω , then converting it into divergence form by applying equation (3.19) and the divergence theorem, giving:

$$\begin{aligned} \mathcal{N}_i^{mom} &= \int_{\Omega} [Re(\dot{\mathbf{u}} + (\mathbf{u} - \dot{\mathbf{x}}) \cdot \nabla \mathbf{u}) + \nabla p - \nabla \cdot \underline{\underline{\tau}} - St\mathbf{g}] \phi_i d\Omega \\ &= \int_{\Omega} \{ Re\dot{\mathbf{u}} + \nabla [Re((\mathbf{u} - \dot{\mathbf{x}}) \otimes \mathbf{u}) + p\mathbf{I} - \underline{\underline{\tau}}] - St\mathbf{g} \} \phi_i d\Omega = \mathbf{0}, \end{aligned} \quad (3.28)$$

where \otimes denotes the dyadic product of two vectors, $\dot{\mathbf{u}}$ is the time derivative of \mathbf{u} and the mesh velocity is denoted by $\dot{\mathbf{x}}$. Note that due to the movement of the computational grid in response to the free-surface deformation, the material derivative in the momentum equation must be modified (Jimack and Wathen, 1991). Time derivatives were discretised using a backward Euler scheme, following the work of Wilson *et al.* (2006), via:

$$\dot{\mathbf{u}} = \frac{\mathbf{u}^{n+1} - \mathbf{u}^n}{\Delta t}, \quad (3.29)$$

where \mathbf{u}^n is the velocity calculated at time-step n . The time step, Δt , must be

kept sufficiently small to capture the temporal gradients in the flow that exist, as in Wilson *et al.* (2006). This scheme was found to be sufficient in describing the temporal flow dynamics accurately.

Equation (3.28) can be split into two integrals:

$$\mathcal{N}_i^{mom} = \mathcal{N}_i^{mom,d} + \Delta_{i,k} \mathcal{N}_k^{mom,fs}; \quad (3.30)$$

where $\Delta_{i,k}$ is only non-zero if global \mathbf{u}/\mathbf{x} -node i corresponds to free-surface \mathbf{u}/\mathbf{x} -node k , $k \in [1, n_e^k]$. $\mathcal{N}_i^{mom,d}$ the integral over the interior of the domain Ω is calculated via:

$$\mathcal{N}_i^{mom,d} = \int_{\Omega} \{ Re\dot{\mathbf{u}} - \nabla [Re((\mathbf{u} - \dot{\mathbf{x}}) \otimes \mathbf{u}) + p\mathbf{I} - \underline{\tau}] \nabla\phi_i - St\mathbf{g}\phi_i \} d\Omega, \quad (3.31)$$

and $\mathcal{N}_i^{mom,fs}$ the integral over the boundary of the domain, Γ , can be derived via the free-surface boundary conditions, equation (3.22) and (3.23), giving:

$$\mathcal{N}_k^{mom,fs} = - \int_{\Gamma} (-p\mathbf{I} + \underline{\tau}) \mathbf{n}\phi_k d\Gamma = - \frac{1}{Ca} \int_{\Gamma} \kappa \mathbf{n}\phi_k d\Gamma. \quad (3.32)$$

Inflow/outflow conditions and no-slip at the substrate means $\mathcal{N}_i^{mom,fs}$ is only non-zero at the free-surface boundary. As the work is restricted to two-dimensional flow, equation (3.32) is a line integral and can be simplified by using an expression for line curvature, $\mathbf{n}\kappa = dt/d\Gamma$ (where \mathbf{t} is the tangent vector to the free-surface); using this and integrating by parts and applying the inflow/outflow boundary condition leads (Wilson *et al.*, 2006) to:

$$\mathcal{N}_k^{mom,fs} = \frac{1}{Ca} \int_{\Gamma} \mathbf{t} \frac{d\phi_k}{d\Gamma} d\Gamma. \quad (3.33)$$

Discrete forms of the continuity equation, (3.19), and the kinematic boundary con-

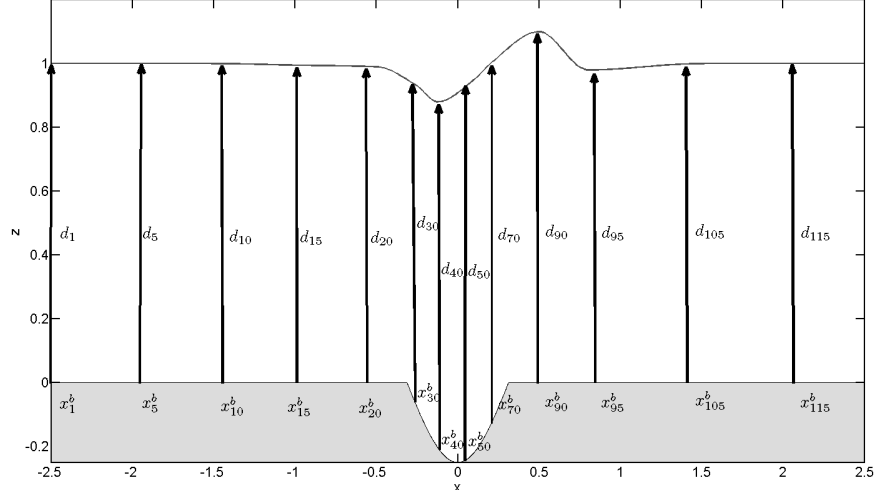


FIGURE 3.3: An illustration of spines used to track the free-surface. Each base node \mathbf{x}_k^b and direction vector \mathbf{d}_k is associated with a spine k .

dition, (3.22), are obtained in a similar manner:

$$\mathcal{N}_j^{cont} = \int_{\Omega} \nabla \cdot \mathbf{u} \psi_j d\Omega = 0, \quad (3.34)$$

$$\mathcal{N}_k^{kin} = \int_{\Gamma} [\mathbf{n} \cdot (\mathbf{u} - \dot{\mathbf{x}})] \phi_k d\Gamma = 0. \quad (3.35)$$

3.3.1.2 Free-surface spine method

The current system of equations (3.30), (3.34) and (3.35) is incomplete, currently the number of equations is $2n_e^i + n_e^j$ which is less than the number of unknown values, $2n_j^i + n_e^j + n_e^k$. To complete the problem it is necessary to define how the mesh evolves with the free-surface deformation via n_e^k free-surface parameters. This is achieved by the method of spines, Kistler and Schweizer (1997), that relates the mesh \mathbf{x} -nodes to a set of free-surface parameters, h_k , that must be solved for; the values of h_k determine the deformation of the mesh. The basis of the technique is to parameterise the free-surface location via a series of spines, each spine is defined by the location of a fixed base node, denoted by \mathbf{x}_k^n , and a direction vector \mathbf{d}_k . The nodes of the mesh are chosen so that each node lies on a spine.

The free-surface parameters, h_k , are defined as the distance along the spine from

base to free-surface. Therefore, for each \mathbf{x} -node, the position can be defined via:

$$\mathbf{x}_i = \mathbf{x}_i^b + \tilde{\Delta}_{i,k} h_k \mathbf{d}_i, \quad (3.36)$$

where $\tilde{\Delta}_{i,k}$ is unity if global node i lies on spine k and zero otherwise. Equation (3.36) defines that all nodes lie on some spine k intermediately between the free-surface node of the spine and the associated base node. In all cases here, the direction vectors only have z -direction and indicate the proportion along the spine that \mathbf{x}_i is located. An annotated example is shown in Figure 3.3 (note that the figure does not depict an actual numerical solution). As the free-surface deforms, the free-surface nodes are displaced and so all nodes on the associated spine have a displacement that depends on the free-surface parameters to be calculated, h_k . In the time-dependent case, the mesh therefore has a velocity $\dot{\mathbf{x}}$ which is accounted for within the time-dependent governing equations.

The number of free-surface parameters, n_e^k , is the same as the total number of spines and so the system of discretised equations is complete and can be written in the following form:

$$\mathcal{N}(\mathbf{z}) = \begin{pmatrix} \mathcal{N}_i^{mom} \\ \mathcal{N}_j^{cont} \\ \mathcal{N}_k^{kin} \end{pmatrix} \begin{pmatrix} \mathbf{u}_i \\ p_j \\ h_k \end{pmatrix} = \mathbf{0}. \quad (3.37)$$

3.3.1.3 Calculation of integrals

The computational domain, Ω , is split into n^e triangular elements with local domain Ω_e for element e ; the free-surface boundary Γ is divided into n^{fs} free-surface elements with local domain Γ_{fs} for free-surface element fs . The integral contributions of equations (3.31), (3.32), (3.34) and (3.35) over each element in the domain, Ω_e , or free-surface, Γ_{fs} , can be assembled to calculate the integrals over the whole problem domain. The number of local \mathbf{u}/\mathbf{x} -nodes on an element e is defined as n_e^α similarly there are n_e^β p -nodes and n_e^γ free-surface nodes on e .

Accordingly, the weighted-residual discretised equations must be written in terms of the local coordinates of each element as described in Section 3.3.1.1. The Jacobian of the transformation of the Cartesian coordinates of the element into local coordinates $\mathbf{x}(L_1, L_2, L_3)$ is denoted by J . The weighted-residual equation $\mathcal{N}_\alpha^{mom,d,e}$ on any element e , where α is a node on element e , can then be written as an integral over a unit orthogonal triangle and is defined as:

$$\begin{aligned} \mathcal{N}_\alpha^{mom,d,e} &= \int_{\Omega_e} \{ Re\dot{\mathbf{u}} - [(\mathbf{u} - \dot{\mathbf{x}}) \otimes \mathbf{u} + p\mathbf{I} - \underline{\underline{\tau}}] \nabla\phi_\alpha + St\mathbf{g}\phi_\alpha \} d\Omega_e \\ &= \int_0^1 \int_0^{1-L_1} \{ Re\dot{\mathbf{u}} - [Re(\mathbf{u} - \dot{\mathbf{x}}) \otimes \mathbf{u} + p\mathbf{I} - \underline{\underline{\tau}}] \nabla\phi_\alpha + St\mathbf{g}\phi_\alpha \} |J| dL_1 dL_2, \end{aligned} \quad (3.38)$$

where $|J|$ is the determinant of the Jacobian of the coordinate transformation, J :

$$J = \begin{pmatrix} 1 & 1 & 1 \\ \frac{\partial x}{\partial L_1} & \frac{\partial x}{\partial L_2} & \frac{\partial x}{\partial L_3} \\ \frac{\partial z}{\partial L_1} & \frac{\partial z}{\partial L_2} & \frac{\partial z}{\partial L_3} \end{pmatrix}, \quad (3.39)$$

and $\nabla\phi_\alpha$ is calculated via:

$$\nabla\phi_\alpha = \sum_{\beta=1}^{n_e^\beta} \frac{\partial\phi_\alpha}{\partial L_\beta} \frac{\partial L_\beta}{\partial \mathbf{x}} = \frac{1}{|J|} \sum_{\beta=1}^{n_e^\beta} \frac{\partial\phi_\alpha}{\partial L_\beta} [\mathbf{i}C_{\beta x}(J) + \mathbf{k}C_{\beta z}(J)], \quad (3.40)$$

where $\partial\phi_\alpha/\partial L_\beta$ values are calculated via equation (3.25). The derivatives $\partial L_\beta/\partial \mathbf{x}$ are the elements of J^{-1} , the inverse of the Jacobian matrix J , calculated via an expression in terms of the transpose of the matrix of cofactors, $C(J)$, and determinant $|J|$:

$$J^{-1} = \frac{1}{|J|} \begin{pmatrix} C_{11} & C_{1x} & C_{1z} \\ C_{21} & C_{2x} & C_{2z} \\ C_{31} & C_{3x} & C_{3z} \end{pmatrix}. \quad (3.41)$$

The rest of the integrals, (3.32), (3.34) and (3.35), are obtained similarly:

$$\begin{aligned}\mathcal{N}_\gamma^{mom,fs,e} &= \frac{1}{Ca} \int_\Gamma \mathbf{t} \frac{d\phi_k}{d\Gamma} d\Gamma \\ &= \frac{1}{Ca} \int_0^1 [\mathbf{i}(\mathbf{n} \cdot \mathbf{k}) - \mathbf{k}(\mathbf{n} \cdot \mathbf{i})] \left(\frac{\partial \phi_\gamma}{\partial L_2} - \frac{\partial \phi_\gamma}{\partial L_3} \right) \Big|_{L_1=0} dL_2\end{aligned}\quad (3.42)$$

$$\mathcal{N}_\beta^{cont,e} = \int_{\Omega_e} \nabla \cdot \mathbf{u} \psi_j d\Omega_e = \int_0^1 \int_0^{1-L_1} \nabla \cdot \mathbf{u} |J| \psi_\beta dL_1 dL_2, \quad (3.43)$$

$$\begin{aligned}\mathcal{N}_\gamma^{kin,e} &= \int_\Gamma [\mathbf{n} \cdot (\mathbf{u} - \dot{\mathbf{x}})] \phi_\gamma d\Gamma \\ &= \int_0^1 [\mathbf{N} \cdot (\mathbf{u} - \dot{\mathbf{x}})] \Big|_{L_1=0} \phi_\gamma dL_2,\end{aligned}\quad (3.44)$$

this is assuming, without loss of generality, that a natural coordinate that is equal to zero at the free-surface edge is L_1 so the location of a point on the free-surface is determined by L_2 and L_3 . \mathbf{N} is a vector normal to the free-surface defined by:

$$\mathbf{N} = \left(\frac{\partial \mathbf{x}}{\partial L_2} \times \frac{\partial \mathbf{x}}{\partial L_3} \right) \Big|_{L_1=0}, \quad (3.45)$$

where \times denotes the vector product and the unit normal vector $\mathbf{n} = \mathbf{N}/|\mathbf{N}|$.

3.3.1.4 Solution strategy

The Newton method is used to linearise the global system of discrete Navier-Stokes equations, (3.37), leading to:

$$\frac{\partial \mathcal{N}}{\partial \mathbf{z}} = -\mathcal{N} \Delta \mathbf{z}, \quad (3.46)$$

where $\partial \mathcal{N} / \partial \mathbf{z}$ is the global Jacobian matrix and $\Delta \mathbf{z}$ the solution increment, both of which are defined as

$$\frac{\partial \mathcal{N}}{\partial \mathbf{z}} = \begin{pmatrix} \frac{\partial \mathcal{N}_i^{mom}}{\partial \mathbf{u}_i} & \frac{\partial \mathcal{N}_i^{mom}}{\partial p_j} & \frac{\partial \mathcal{N}_i^{mom}}{\partial h_m} \\ \frac{\partial \mathcal{N}_j^{cont}}{\partial \mathbf{u}_i} & 0 & \frac{\partial \mathcal{N}_j^{cont}}{\partial h_m} \\ \frac{\partial \mathcal{N}_k^{kin}}{\partial \mathbf{u}_i} & 0 & \frac{\partial \mathcal{N}_k^{kin}}{\partial h_m} \end{pmatrix}, \Delta \mathbf{z} = \begin{pmatrix} \Delta \mathbf{u}_i \\ \Delta p_j \\ \Delta h_k \end{pmatrix}. \quad (3.47)$$

The solution increment is then used to update the solution, this process is repeated until the norm of the residual \mathcal{N} is reduced below a specified tolerance of 10^{-6} .

The integral contributions for each element are calculated numerically from equations (3.38), (3.42), (3.43) and (3.44) and appropriate derivatives of the same (needed to form the global Jacobian matrix) using Gaussian quadrature - a commonly used, accurate method adopted widely in finite element calculations, see for example Chung (2002); Veremieiev (2011). For illustration purposes, consider a function dependent on a set of local coordinates, i.e. $f(L_1, L_2, L_3)$, the value of the integral of the function over an interior element in the domain may be approximated as:

$$\int_0^1 \int_0^{1-L_1} f(L_1, L_2, L_3) dL_1 dL_2 \approx \sum_{p=1}^{n^p} w^p f(L_1^p, L_2^p, L_3^p), \quad (3.48)$$

where w^p are weight coefficients, (L_1^p, L_2^p, L_3^p) are quadrature points and n^p the number of integration points. The weight coefficients and quadrature points can be found by representing the function f as a polynomial of degree $2n^p$ or less, substituting into (3.48) and resolving the system of non-linear equations; results of weight coefficients and quadrature points (abscissae) can be found for triangular elements (integrals of order 2) in Rathod *et al.* (2004).

Chapter 4

Long-time rivulet formation on planar substrates

Contents

4.1	Long-time rivulet formation - results	73
4.1.1	Fully wetting fluid	74
4.1.1.1	Merger of neighbouring rivulets	74
4.1.1.2	Comparison to experimental data	79
4.1.1.3	Linear stability analysis	81
4.1.2	Partially wetting fluid	83
4.1.2.1	Influence of wetting properties on rivulets characteristics	83
4.1.2.2	Wavelength and width: comparison to experimental data	85
4.1.3	General expression for wavelength	91
4.1.4	Varying the inflow condition	94
4.2	Summary	97

	Density, ρ (kgm^{-3})	Dynamic viscosity, μ (Pa s)	Surface tension, σ (Pa m)	Contact angle, θ_c (degs)
Fluid A	1075	3.11×10^{-2}	0.069	38°
Fluid B	1210	8.349×10^{-2}	0.066	7°

TABLE 4.1: Table of the fluid properties that are utilised here. The two fluids were used in experiments in Johnson *et al.* (1999).

This chapter utilises the numerical procedure described in Chapter 3 to solve the lubrication equations for the problem of rivulet formation on an inclined planar substrate, with comparisons drawn to the experimental data of Johnson (Johnson, 1997) and Johnson *et al.* (1999). Three-dimensional free-surface plots reveal features of the long-time evolution such as merging of neighbouring rivulets. The incorporation of wetting properties forms a major part of the investigation with the differences between fully and partially wetting scenarios examined, again with comparisons drawn with experimental observations. The results obtained lead to the formulation of a general expression for the final, long-time wavelength of the rivulet structures with dependence on the wetting properties of the fluid; this is compared to the classical expression of Huppert (1982) and other subsequent models.

Many of the experimental investigations found in the literature are inconsistent with one another in terms of fluid properties, wetting properties and substrate material. A majority also employ a constant volume configuration; where a fixed volume of fluid is deposited on an inclined plane and allowed to develop. Comparisons are drawn here with the experimental results of Johnson (1997) and Johnson *et al.* (1999) who obtained data for several different fluids for experiments which had a constant inflow upstream. Numerical solutions are obtained using two fluids, ‘Fluid A’ and ‘Fluid B’ (see Table 4.1 for fluid properties), which are water-glycerin mixtures with different properties; ‘Fluid B’ is near fully wetting (treated as such in the numerical solutions) and ‘Fluid A’ has a larger equilibrium contact angle. The differing wettability of each fluid allows for comparisons to be drawn between partial and fully wetting fluids. Such a full set of data is rarely available in the literature and is used for validation of the results collected from numerical solutions.

For the interested reader, the performance of the fully adaptive multigrid method

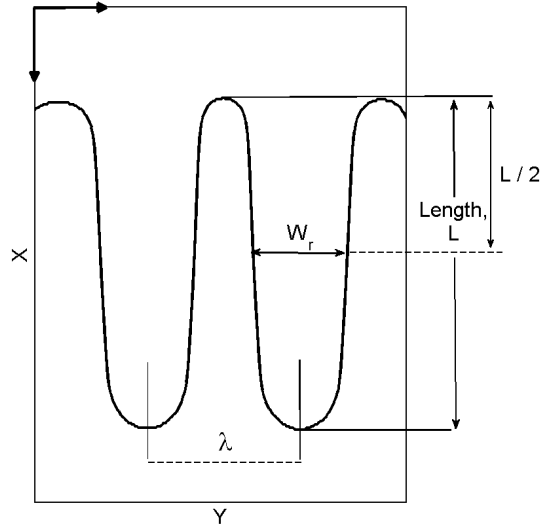


FIGURE 4.1: Definitions of width, W_r , length, L and wavelength, λ of the rivulets.

is demonstrated and compared in Appendix D. Also considered is the most appropriate approach to calculating the Jacobian of the problem, either numerically or analytically; in addition, a number of different smoothers are compared and the most efficient was adopted to obtain the numerical results presented below.

4.1 Long-time rivulet formation - results

The unstable advancing front evolves such that at long-times, a characteristic near-periodic rivulet pattern emerges; the associated wavelength together with the rivulet width and length are as indicated in Figure 4.1 and reported in the present work so as to be consistent with the same qualities as extracted from experiment. The wavelength, λ , is obtained by measuring the distance between the tips of the adjacent rivulets forming the system, Johnson (1997), the value quoted, λ_f , being the mean across the entire front and at a stage when the possibility of rivulets merging has long since passed. The corresponding mean rivulet width, W_r , is based on measurements taken half-way along the length of a rivulet, see Johnson *et al.* (1999).

4.1.1 Fully wetting fluid

Free-surface film thickness colour maps at long-times are depicted in Figure 4.2 for $\alpha = 13.9^\circ, 27.9^\circ, 60^\circ$ and 90° ; for flow rate $Q_0 = 8.87\text{mm}^2/\text{s}$, this gives $H_0 = 0.92$ mm, 0.74 mm, 0.62 mm and 0.57 mm respectively (Johnson, 1997). The profiles exhibit a number of characteristic features as α increases, these include a decrease of the final mean wavelength, λ_f , of the pattern that emerges at the advancing front, with a corresponding reduction in the width of the rivulets. The pattern develops straighter edged rivulets, in contrast to the saw-toothed shaped rivulets seen at lower values of α . The length of the fingers increases with inclination angle and the final, saturated length of the rivulets also increases in keeping with the findings of Kondic and Diez (2005). The free-surface profiles shown in Figure 4.2 may be compared directly with those of Figure 5.11 in Johnson (1997) which shows snapshots of experiments that are seen to exhibit very good agreement.

The finite difference solutions were obtained for long times and reveal the merging of neighbouring rivulets; this can be observed in Figure 4.3 which shows a progression of rivulet formation in time. The merger of rivulets affect their wavelength and thickness depending at what time in the evolution of the system an evaluation is conducted. This phenomena does not appear to have been considered in-depth before and is the subject of further investigation below.

4.1.1.1 Merger of neighbouring rivulets

Merging has been observed and commented on before; one such instance is in a numerical study where a heterogeneous striped substrate was used to directly influence the wavelength of the emerging pattern (Zhao and Marshall, 2006); the authors noticed that rivulets that were forced to grow near one another would merge to form a new, single rivulet. Johnson *et al.* (1999) observed the merger of rivulets in an experimental setting, concluding that coalescence of rivulets growing in close proximity was observed to happen in an apparent random fashion.

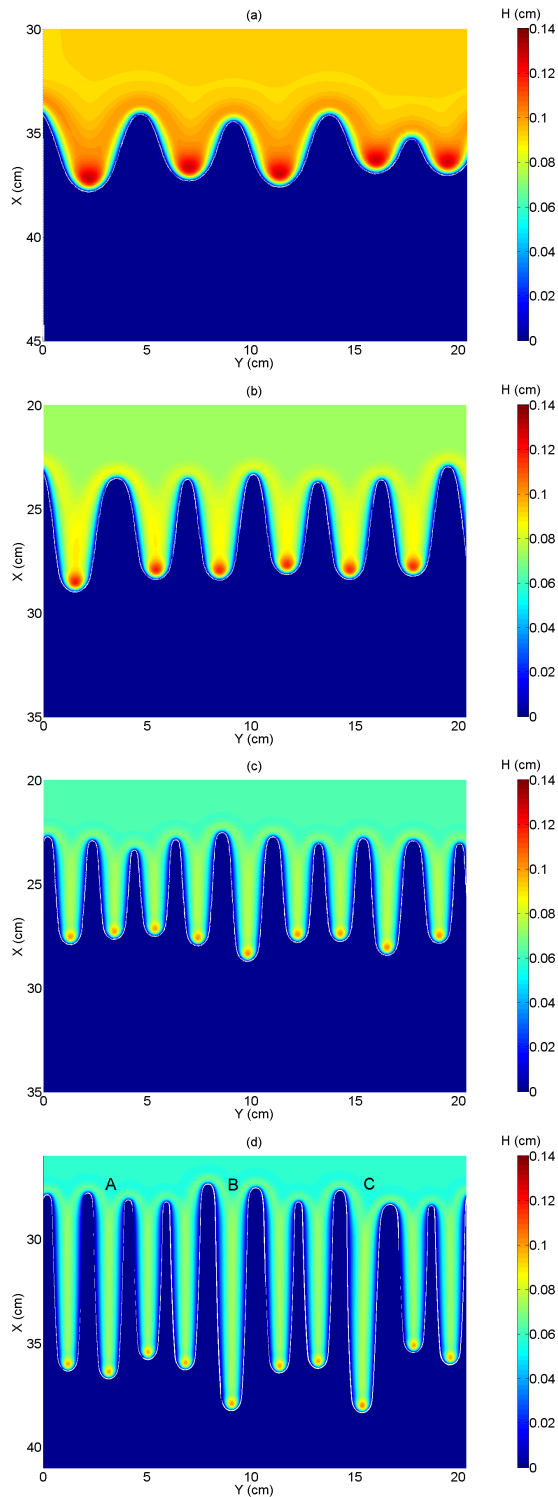


FIGURE 4.2: free-surface colour maps of film thickness for the flow of 'Fluid B' down an inclined planar substrate at long times; cf the experiments of Johnson, see Figure 5.11 in (Johnson, 1997); (a) $\alpha = 13.9^\circ$, (b) $\alpha = 27.9^\circ$, (c) $\alpha = 60^\circ$ and (d) $\alpha = 90^\circ$. Lengths and heights are given in centimetres. The vertical axis is shifted to keep the advancing front central.

This merging process can be observed in Figure 4.3 which shows the flow pattern in terms of colour maps of the film thickness at four different times in the case of a vertically aligned substrate. In Figure 4.3(a), there are three areas indicated; B and C, which show two sets of rivulets growing in close proximity to one another, and A which shows the early time merging of two rivulets. In the second snapshot, the rivulets at B have combined to form a new rivulet, while the rivulets at C are growing from a combined root at a slower rate. In the third colour map the combined root of the two rivulets at C is approaching the tips of the rivulets as the two structures fuse from the root towards the tips. All merging events are near completion in the fourth figure - the slower, less developed rivulet at C is drawn towards the side of the longer rivulet which merge to form a new, single rivulet. The single rivulet now found at B has continued to grow and is noticeably one of the longer rivulets in the system, similarly the merged rivulet at C also stretches ahead. The final wavelength is shown in Figure 4.2(d) where the rivulets formed by the joining of two or more original fingers are more advanced than the other structures which grew independently. The merging of neighbouring fingers observed here explains some of the characteristic patterns seen in experiments (see for example Figure 1 of Kondic and Diez (2001) or Figure 3 in Kondic and Diez (2004)) such as rivulets of uneven length and merging from a combined root.

When two rivulets amalgamate the root area of the rivulets combine and the merging continues up to the point when the tips of the rivulets coalesce into one, this leads to a steep rise in the height of the capillary ridge which creates an increase in velocity and extension of the merged rivulet. The change in capillary ridge height is revealed in Figure 4.4 which shows the evolution at successive times of the contact line and corresponding capillary ridge height for a film on a substrate inclined at $\alpha = 90^\circ$. At position I, the capillary ridge height starts to increase as the rivulets begin to merge, peaking at position II as the rivulet tips merge fully. The newly formed rivulet thereafter stretches in front of the neighbouring rivulets, as with the rivulets indicated at B and C in Figure 4.3. The capillary ridge then gradually reduces to

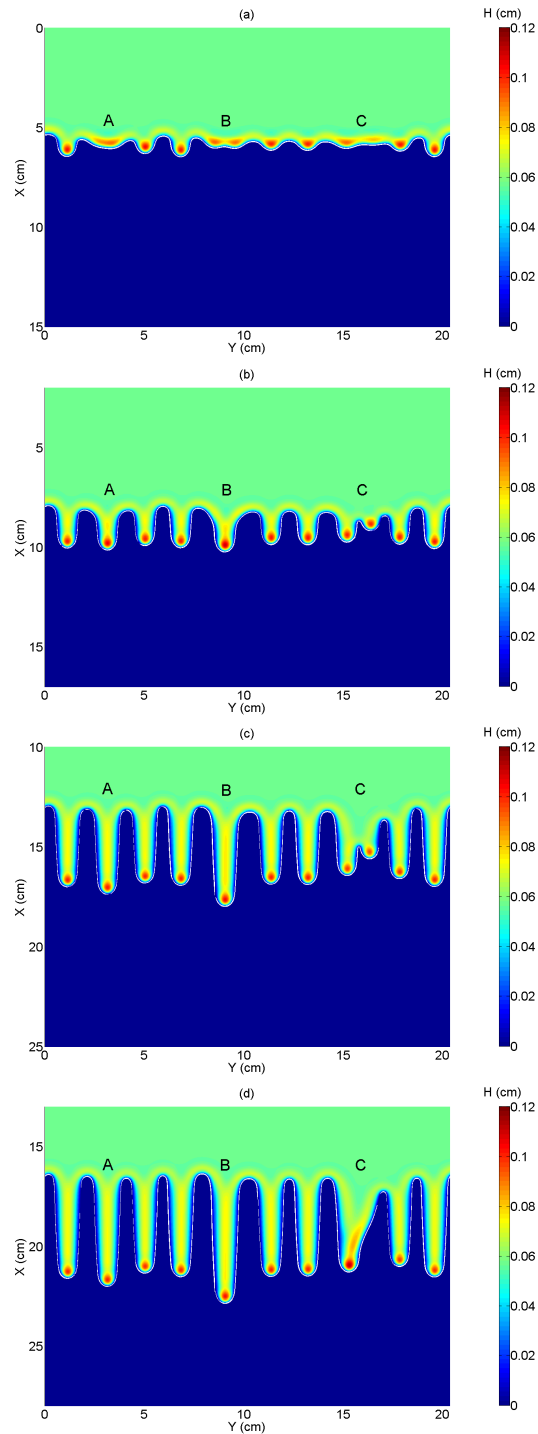


FIGURE 4.3: Colour maps of the evolution of the advancing front of ‘Fluid B’ on a substrate, with $\alpha = 90^\circ$, at four different increasing non-dimensional times showing the development and merging of rivulets - note that these snapshots are before the one shown in Figure 4.2(d). The ordinate in (b),(c) and (d) is shifted to keep the rivulets central to the plot.

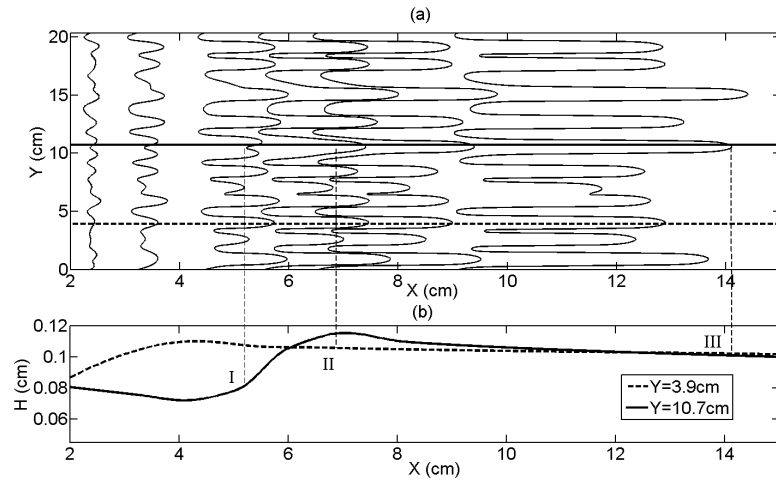


FIGURE 4.4: (a) Contact line evolution for a thin film of fully wetting ‘Fluid B’ on a substrate inclined at 90° plotted with $\Omega = (0, 150) \times (0, 200)$. (b) is the capillary ridge height for $Y = 3.9\text{cm}$ and $Y = 10.7\text{cm}$ (indicated on (a) by dotted lines). At $y = 39$ no merging takes place so the height is relatively steady, however at $y = 105$ there is merging between two neighbouring rivulets; when they merge the capillary ridge height exhibits a sharp increase before settling to a height slightly higher than before the merger process.

a height consistent with the surrounding rivulets at the advancing front of the film, correspondingly the rivulet’s relative elongation rate reduces to the same as the other rivulets, and indicated at III in Figure 4.4. As the number of rivulets decreases through rivulet merger, the capillary ridge height at the tips of the structures that are in the vicinity of merging rivulets increases and thus the elongation rate of these rivulets increases; this is a consequence of mass conservation as the volume of fluid ‘feeding’ each rivulet is increased.

The trajectory of the rivulets is influenced by the merging of the rivulets; for instance, considering the rivulets indicated by C in Figure 4.3 the smaller rivulet is drawn into the side of the larger one creating a meandering path as the two merge. The newly formed rivulet follows, almost exactly, the path the larger rivulet was directed along. Similarly, in Figure 4.4 (a), the rivulets, which are of a similar size, that merge along the solid line create a rivulet with a path directed almost directly down the centre of the two merged rivulets.

In both cases the merger creates a base wider than the newly formed rivulet, with the slanted path of the smaller rivulet still visible, for example point C of Figure 4.3

and along $Y = 15\text{cm}$ in Figure 4.4 (a). The large combined base with slanted path has been observed in experiments - see for example Figure 1(g) in Huppert (1982) and Figure 5.10 in Johnson (1997) - and can be seen in the free-surface colour maps and contact line outlines shown in the present work when two rivulets merge (being particularly obvious when one rivulet is drawn into the other).

4.1.1.2 Comparison to experimental data

The long-time, final wavelength, λ_f , is measured as the mean wavelength of the rivulet pattern at long-times when all merging processes have completed. Figure 4.5 (a) shows the wavelength when merging is complete, extracted from numerical solutions at the advancing front at these long times for a range of inclination angles between 0° and 90° . Plotted alongside the numerical results are the corresponding experimental data of Johnson *et al.* (1999) which show very good agreement. These results enable predictions as to whether two adjacent rivulets will merge as the flow evolves with time; for instance, if two rivulets are observed that have tips that are in closer proximity than the final long-time wavelength, λ_f , then they will merge at some point in the future. This is due to the interaction between the two rivulets that occurs if the two rivulets are within the critical wavelength of one another which leads to the eventual merger.

An example of how Figure 4.5 (a) may be interpreted is shown below the wavelength graph. If a film is allowed to develop to its final long-time pattern on a substrate inclined at 60° the wavelength will be as indicated by point A (the corresponding contact line pattern shown). Should the substrate inclination angle reduce instantaneously to 30° , point A', as time continues the rivulets become wider initiating merging. The wavelength then increases, past point B, until finally reaching λ_f at C. If the inclination angle is subsequently instantaneously increased back to 60° the number of rivulets remain constant with time, but grow longer and thinner. These observations show that if the wavelength of the advancing front is below λ_f in Figure 4.5 (a) then $\lambda \rightarrow \lambda_f$. However, if $\lambda > \lambda_f$ then the wavelength, λ_f , will

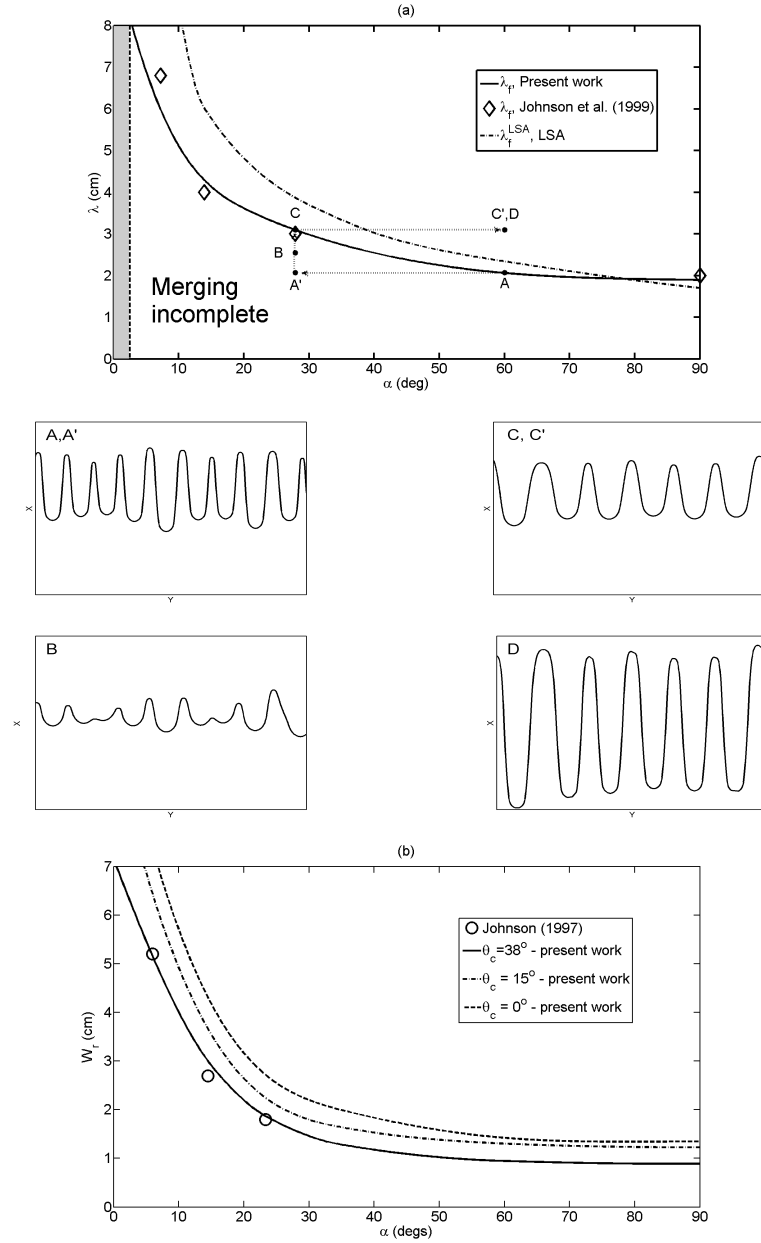


FIGURE 4.5: (a) The final, long-time wavelength, λ_f , of the rivulet pattern at the advancing front for ‘Fluid B’. Comparison is between the experiments of (Johnson *et al.*, 1999) and the present work. For comparison purposes predictions via linear stability analysis (LSA), λ_f^{LSA} , are also provided. The grey shaded area indicates predicted linear stability. (b) The width of the rivulets, W_r , for long times of ‘Fluid B’ plotted against inclination angle, results are from numerical solutions and the experiments of Johnson *et al.* (1999).

remain constant for all time.

Similarly, the results for the width of the rivulets are found to be in very good agreement with the data from the experiments of Johnson *et al.* (1999). Figure 4.5 (b) shows how the width decreases with inclination angle as the effect of gravity is reduced. The ratio of the rivulets width to wavelength gives a good indication of the shape of the rivulets that are forming. A small ratio implies the rivulets are straight edged, thin rivulets as opposed to the saw-tooth pattern that emerges at lower inclination angles; for instance at $\alpha = 13.9^\circ$ the ratio is 0.69 but at $\alpha = 90^\circ$ it is 0.42. The width of the rivulets when the inclination is changed spontaneously during growth is measured, see Figure 4.5 (b). As inclination angle is decreased the rivulets get wider. In contrast to the wavelength, when the inclination angle is returned to its original higher value the width does return to its initial size from C' to A, D .

4.1.1.3 Linear stability analysis

Linear stability analysis (LSA) is a widely used tool within the literature, see for example Troian *et al.* (1989); Spaid and Homsy (1996); Bertozzi and Brenner (1997); Davis and Troian (2003), to predict the behaviour of the advancing front of a thin film. The process is much less computationally demanding than obtaining three-dimensional numerical solutions; this has led to the relative sparseness of such results in the literature. In this thesis a LSA is utilised for comparison purposes against the numerical predictions obtained; the derivation of the equations (Appendix C) is also extended to include the disjoining pressure model incorporating wetting effects.

Solving the LSA equations, see Appendix C, has been found to produce reasonable predictions for the wavelength and growth rate of the instability at an advancing front (Kondic, 2003), for this reason the linear stability of the base states of ‘Fluid B’ are given for comparison with numerical and experimental results in Figure 4.5

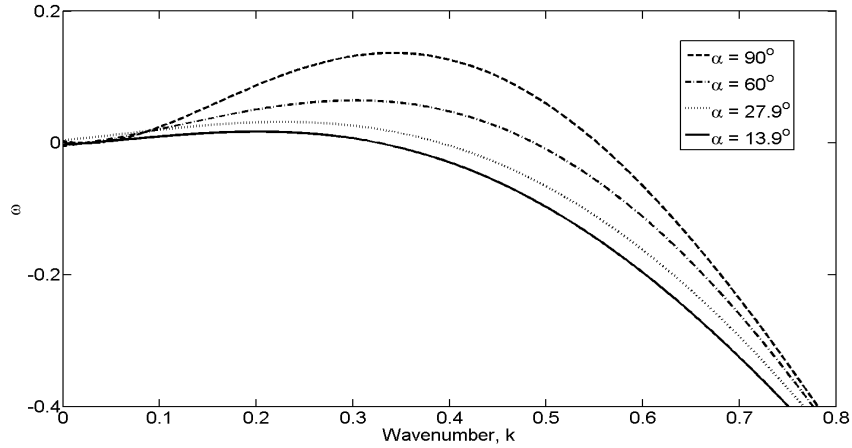


FIGURE 4.6: LSA growth rates, ω , computed for the base states of the problem modelled for comparison to experiments by Johnson *et al.*(1999) for ‘Fluid B’ and for $\alpha = 13.9^\circ, 27.9^\circ, 60^\circ$ and $\alpha = 90^\circ$.

(a). The eigenvalue problem given by equation (C.7) in Appendix C is solved using Matlab 7.9 via the *eig* function to yield the leading eigenvalue and corresponding eigenfunction. A spectrum of the growth rates, ω , at a range of wavenumbers, k , is assessed to determine the range of wavenumber for which the system is linearly unstable; the dispersion curves for $\alpha = 13.9^\circ, 27.9^\circ, 60^\circ$ and 90° are shown in Figure 4.6.

In keeping with observations and the numerical results, the growth rates decrease for smaller α and so does the most unstable wavenumber, k_{\max} . The most unstable wavenumber (the wavenumber with largest growth rate, ω) is the one that would be expected to emerge in an experimental setting (Kondic, 2003) and so the predicted wavelength, λ_f^{LSA} , is calculated via the associated wavelength $\lambda_f^{\text{LSA}} = 2\pi/k_{\max}$. The results are plotted in Figure 4.5 for comparison with the numerical results and experiments. LSA predicts a similar trend to that found from experiments and from numerical solutions; at high inclination angles the agreement is very good. However, it is clear that LSA over predicts the wavelength at most angles and is much less accurate compared with the full, non-linear numerical solutions. At low inclination angles the discrepancy between LSA and experiments is large and eventually linear stability is predicted at sufficiently small angles which have been observed to

yield unstable advancing fronts in experiments (Johnson *et al.*, 1999). This area of linear stability is indicated by the grey shaded region in Figure 4.5 (a).

4.1.2 Partially wetting fluid

4.1.2.1 Influence of wetting properties on rivulets characteristics

The wetting properties of a fluid coating an inclined substrate have been shown to affect the shape of the rivulets that emerge and contact angle hysteresis can determine the final coverage of the film on the substrate (Silvi and Dussan, 1985). Jerrett and Bruyn (1992) have also show that a high contact angle leads to a smaller wavelength of the instability appearing as well as causing thinner rivulets to develop. The ability to generate results numerically allows for the comparison of different value of θ_c for the same fluid and thus expose the effect its value has on the dynamics of the flow pattern; accurate control of such parameters would pose a significant challenge in an experimental procedure.

Three snapshots of the evolution of the advancing front of ‘Fluid A’ with $\theta_c = 38^\circ$ ($S_{\theta_c} = 5.5$) on a substrate inclined at 36° are shown in Figure 4.7; the evolution of the advancing front for ‘Fluid A’ with $\theta_c = 0^\circ$ ($S_{\theta_c} = 0.0$) and $\theta_c = 20^\circ$ ($S_{\theta_c} = 1.57$) are provided for comparison purposes. The flow rate is $Q_0 = 18.1\text{mm}^2/\text{s}$ which for inclination angle 36° gives $H_0 = 0.64$ mm.

There are a number of obvious and key differences between the three flow patterns. The capillary ridge height at the tips of the rivulets is larger when the fluid is partially wetting; for example in Figure 4.7 the capillary ridge height for $\theta_c = 38^\circ$ is 3.21mm while for $\theta_c = 0^\circ$ it is 2.02mm and $\theta_c = 20^\circ$ gives a value of 2.35mm. Thicker areas of fluid travel faster so the rivulets evolve at a faster rate for a high contact angle, clearly exhibited in Figure 4.7; in the final snapshot the rivulets are as much as 21cm in length for $\theta_c = 38^\circ$, while at the same time when $\theta_c = 0^\circ$ they are $< 4\text{cm}$ long and between 4cm and 8cm when $\theta_c = 20^\circ$.

When $S_{\theta_c} = 5.5$, the rivulets are particularly straight edged and thin, as S_{θ_c} decreases the rivulets become more saw-tooth shaped and wider - this is in keeping with the findings of experiments, see for example (Silvi and Dussan, 1985). As the rivulets are thinner more can form in a given area and so more rivulets are present at the front when the contact angle is large, thus the rivulet wavelength decreases. These differences are less exaggerated the nearer to zero the non-dimensional spreading coefficient, S_{θ_c} , is.

A second example is shown in Figure 4.8; the inclination angle in this case is larger, $\alpha = 60^\circ$ with the right hand column showing the partially wetting case when $\theta_c = 38^\circ$ and the left column the corresponding fully wetting scenario. The differences observed previously are similar, with obvious differences in length, shape, wavelength and evolution rate. The length of the rivulets in the final snapshot are as much as six times longer for this partially wetting case.

In both Figure 4.7 and Figure 4.8, when $S_{\theta_c} > 0$, the rivulets appear to bend and meander slightly during their evolution. This effect is exaggerated as S_{θ_c} increases in magnitude (an increase in contact angle). One hypothesis for this phenomena is as follows; small fluctuations in the height (and thus the flow rate) of the fluid feeding the rivulet from the bulk flow leads to one side of the rivulet growing at a faster rate than the other, this leads to a bend in the path of the finger. As the growth rate of the rivulets is much greater as S_{θ_c} increases and the rivulets are thinner, this effect is much more pronounced when the contact angle is large. The gradients in disjoining pressure in the vicinity of the contact line are also larger for high S_{θ_c} which means the effect of small fluctuations in film height along the width of the rivulet is amplified by the larger variations in pressure near the edge of the rivulets.

Meandering is also caused by the merger of rivulets; as observed earlier, the merging of rivulets can alter the path of the rivulets that merge, in the partial wetting case this can lead to slight meandering. A similar observation was made by Marshall and Wang (2005) where the merger of rivulets was forced by the random placement of contamination spots (areas of less wettability) in the substrate.

Plots of finger length against time are shown in Figure 4.9; the top plot shows an increase in rivulet length as inclination angle, α , increases due to the larger driving gravitational force behind the instability. At larger values of α the capillary ridge at the front is larger and so the tips of the rivulets move at a faster pace compared to the bulk flow. It is of note that the change in length is not always linear but may increase or decrease during the evolution of the front due to the merging of rivulets, as discussed previously.

The bottom plot of Figure 4.9 compares three values of S_{θ_c} with $\alpha = 36^\circ$; the evolution rate of the finger length increases with S_{θ_c} , again this can be linked to the increase in capillary ridge magnitude. The degree of increase in finger length is proportional to the ratio of non-dimensional spreading coefficient, i.e. the final finger length for $S_{\theta_c} = 5.5$ is over 3 times the size compared to the finger length when $S_{\theta_c} = 1.57$.

4.1.2.2 Wavelength and width: comparison to experimental data

Figure 4.10 shows the final long-time wavelength, λ_f , for ‘Fluid A’ extracted from numerical solutions when a disjoining pressure term was used with $\theta_c = 38^\circ$, as well as the experimental data points of Johnson (1997). The experimental data for ‘Fluid A’ correspond very well with the numerical solutions. Moreover, Figure 4.10 also shows the extracted numerical results when $\theta_c = 0^\circ$; as the contact angle increases the wavelength decreases. A fully wetting fluid will spread freely on the substrate and as such have wider rivulets and a greater tendency to merge thus leading to a larger wavelength. This clearly demonstrates the importance that the wetting properties of the fluid and substrate have on the emerging pattern at an advancing front.

The contact angle of the problem introduced via the disjoining pressure model is incorporated within the LSA formulation, see Appendix C, and the predicted wavelength is calculated for ‘Fluid A’ with large contact angle; the resultant λ_f^{LSA} is

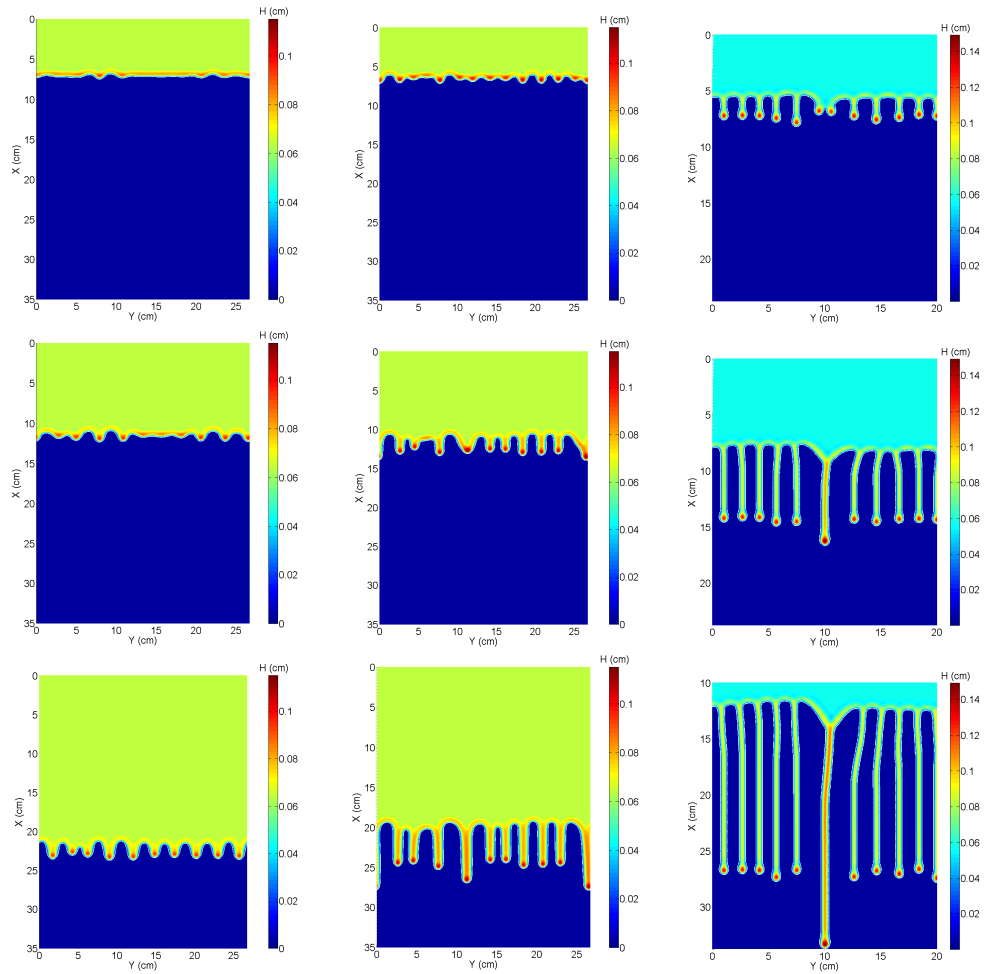


FIGURE 4.7: Colour maps of the long-time evolution of the advancing front of ‘Fluid A’ on a substrate, with $\alpha = 36^\circ$, at three different times where the equilibrium contact angle, θ_c , is 0° on the left hand column, 20° in the centre column and 38° on the right. Note: the ordinate in the right column is shifted to keep the rivulets central to the plot.

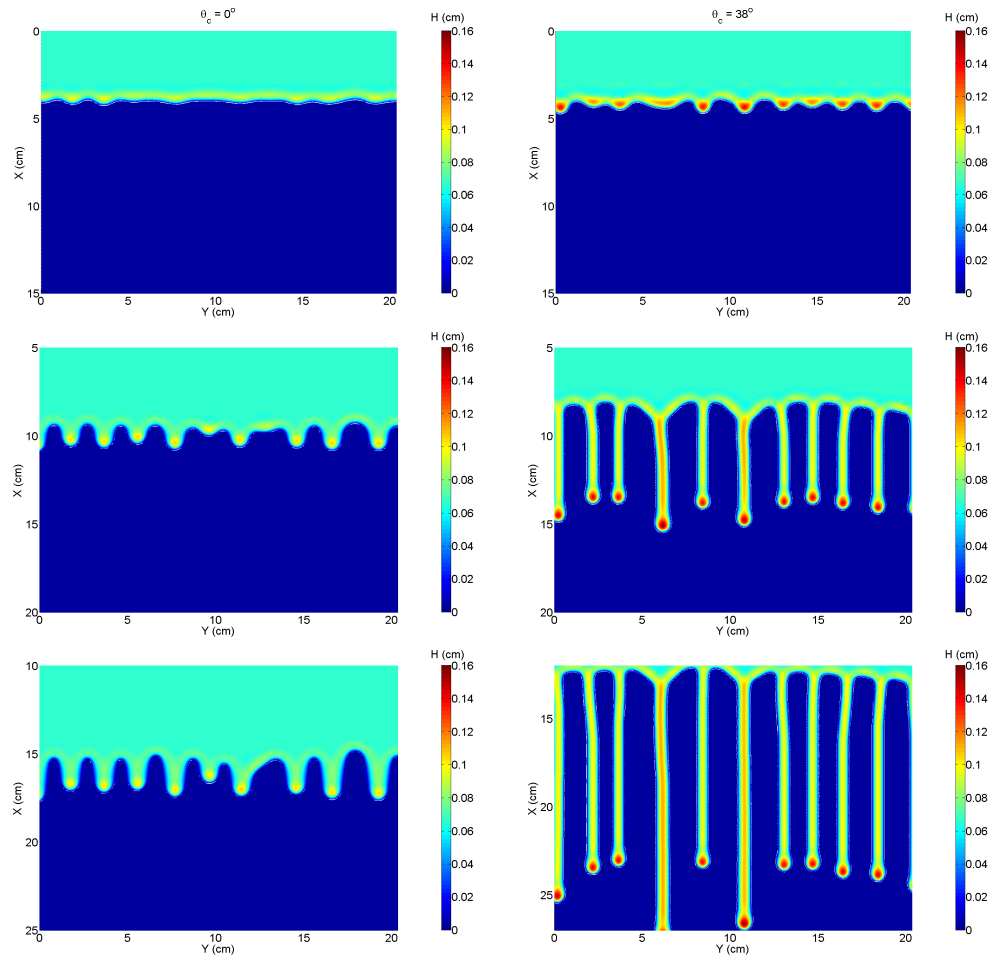


FIGURE 4.8: Colour maps of the long-time evolution of the advancing front of ‘Fluid A’ on a substrate, with $\alpha = 60^\circ$, at $t = 30$, $t = 100$ and $t = 180$ where the equilibrium contact angle, θ_c , is 0° on the left hand column and 38° on the right.

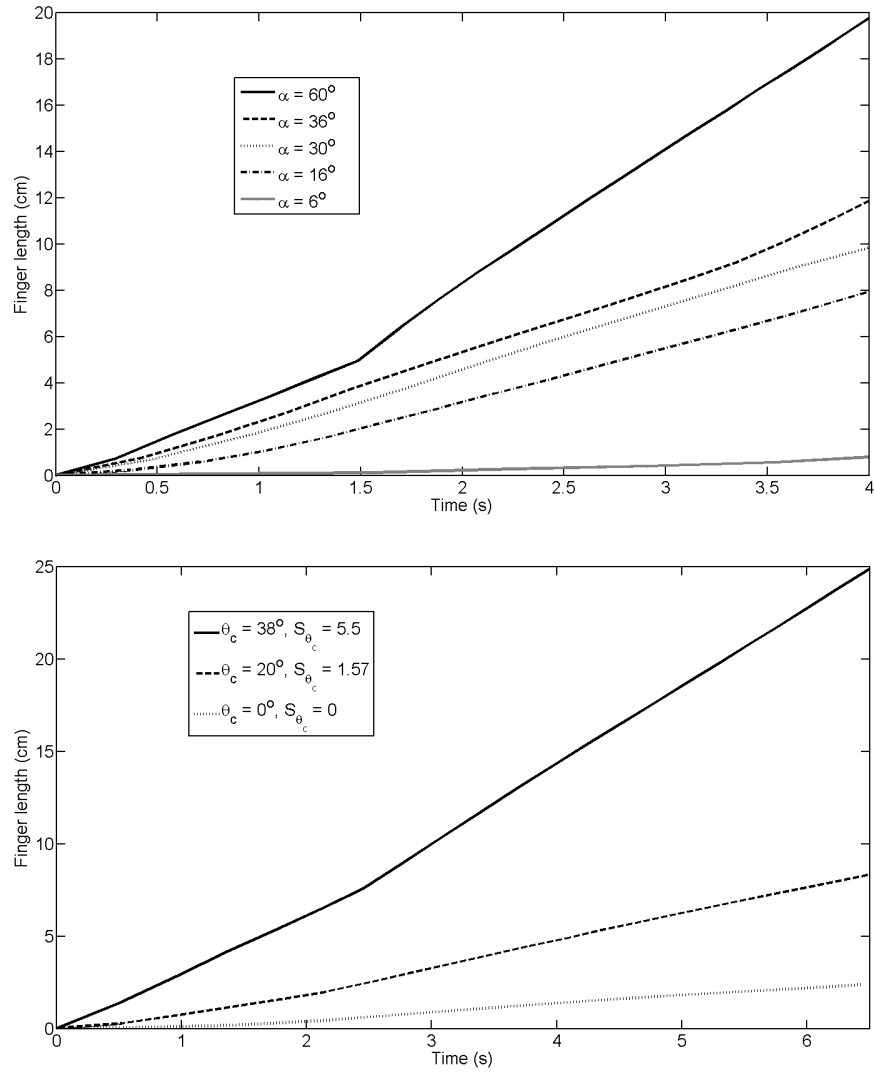


FIGURE 4.9: Finger growth at the advancing front of ‘Fluid A’ flowing on an inclined plane with (a) different values of α with $\theta_c = 38^\circ$; (b) different values of θ_c (and S_{θ_c}) at $\alpha = 36^\circ$.

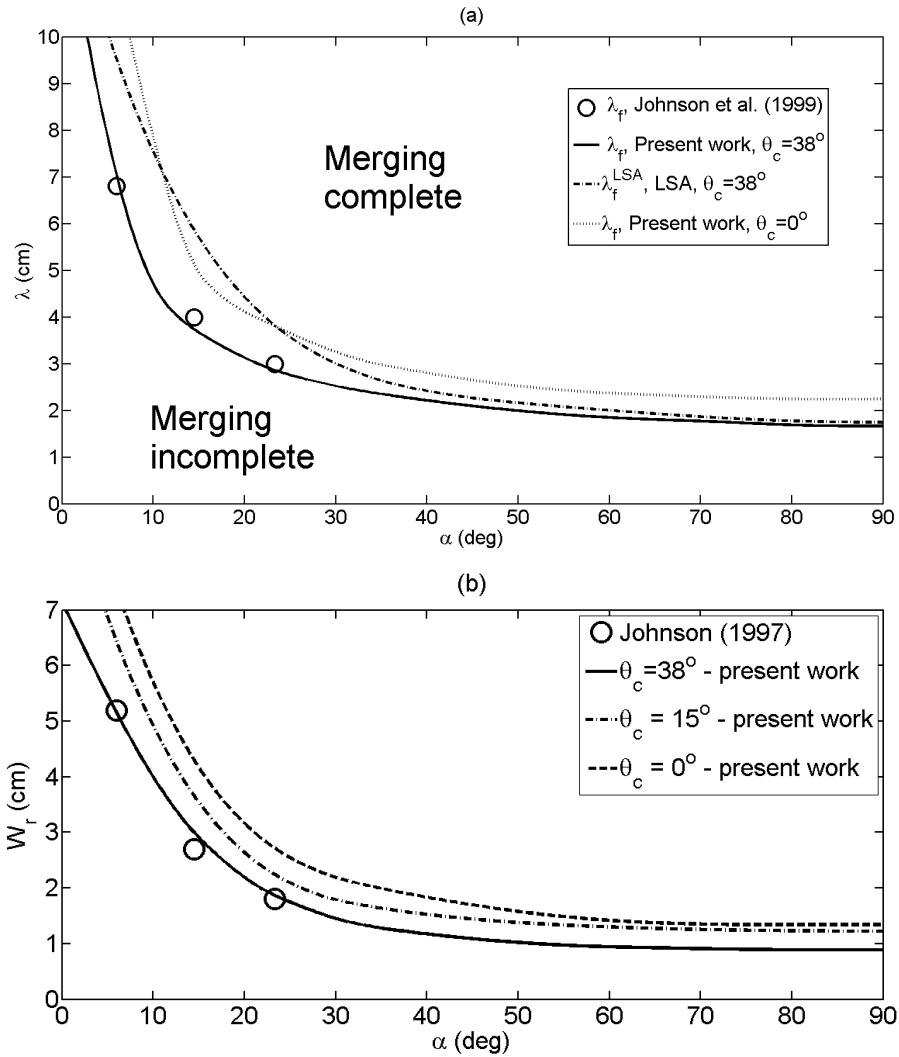


FIGURE 4.10: (a) The long-time wavelength, λ_f of the rivulet pattern at the advancing front of 'Fluid A' for a range of inclination angles. Comparison is between the experiments of (Johnson *et al.*, 1999) and the present work when $\theta_c = 38^\circ$ and 0° . LSA prediction is shown for comparison purposes. (b) The width of the rivulets that emerge at the advancing front of 'Fluid A', when $\theta_c = 0^\circ$, $\theta_c = 15^\circ$ and $\theta_c = 38^\circ$, plotted against the inclination angle, α . Plotted for comparison are the experimental results of Johnson (1997).

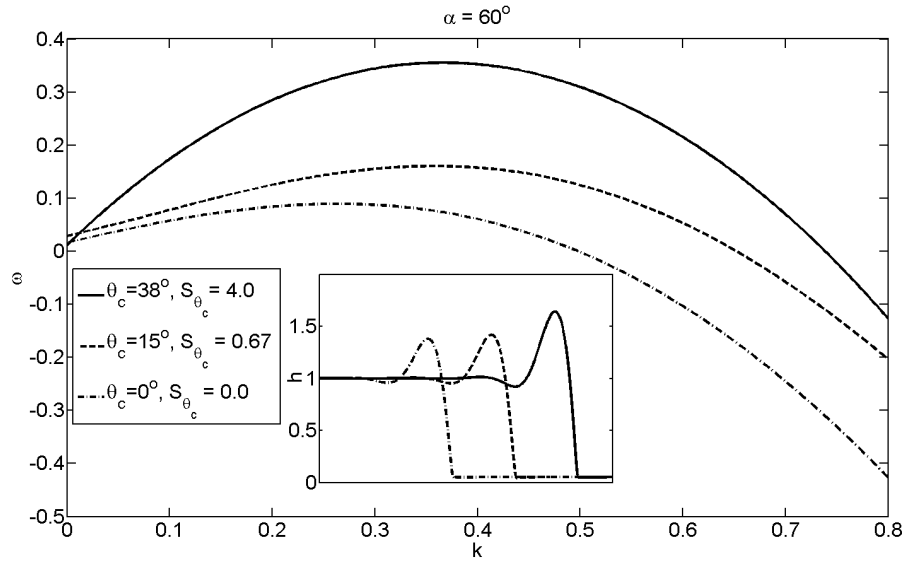


FIGURE 4.11: LSA growth rates, ω , computed for a range of wavenumbers, k , generated from a linear stability analysis of ‘Fluid A’ on an inclined substrate with $\alpha = 60^\circ$. The analysis was performed for three different contact angles, $\theta_c = 0^\circ, 15^\circ$ and 38° . The associated base states are shown inset demonstrating the change in the capillary ridge height with θ_c .

plotted in Figure 4.10 for comparison with experimental and numerical results. The disparity between predicted results and experimental and numerical solutions is, as with ‘Fluid B’, greater at low inclination angles. LSA predicts a shift in the critical wavelength with an increase of contact angle, see Figure 4.10, the same qualitative trend (but not as large quantitatively) as observed for the numerical data.

The critical inclination angle for a particular fluid, below which no rivulets will form, is very much dependent on the wetting properties; a highly wetting fluid will have a higher critical inclination angle, so the asymptotic of the curves are shifted in a positive direction of the ordinate in Figure 4.10 (a). A similar trend is observed for the LSA results, see Figure 4.10 (a). As contact angle (and so S_{θ_c}) increases LSA gives a larger predicted growth rate at all inclination angles and even predicts instability when, for the same case, linear stability is predicted at $\theta_c = 0^\circ$. The range of wavenumbers for which the problem is linearly unstable also increases with contact angle. Figure 4.11 shows the results for growth rate given by LSA over a range of wavenumbers, k , for ‘Fluid A’ on a substrate inclined at 60° for

three different values of S_{θ_c} .

The width of the rivulets are presented for ‘Fluid A’ with $\theta_c = 0^\circ, 15^\circ$ and 38° in Figure 4.10 (b). As observed earlier the fluid has much wider, saw-tooth shaped rivulets for a fully wetting fluid in contrast to a partially wetting one which has very thin, straight edged rivulets. The width of the rivulets is directly affected by the value of contact angle (as so value of S_{θ_c}). The results are presented alongside the experimental results of Johnson (1997) and correlate extremely accurately.

4.1.3 General expression for wavelength

Huppert (1982), Silvi and Dussan (1985) and Johnson *et al.* (1999) all found a linear relationship between the final wavelength of the rivulet pattern and the capillary length, i.e. $\lambda_f \propto L_0 = H_0/(6Ca)^{1/3}$, in reasonable agreement with one another even for different fluids. Jerrett and Bruyn (1992) found a similar relationship but noted a difference when the contact angle was large (60°) in comparison to the other fluids (contact angles of 14°). The data for fully wetting fluids here suggests a linear fit to the capillary length, L_0 , for higher inclination angles (small L_0) but this becomes inaccurate at low inclination angles (larger L_0). Johnson *et al.* (1999) suggest that the relationship may not be linear but in fact depend on a higher power of the capillary number; they find the relationship $\lambda_f = 9.2H_0/(2Ca)^{0.45}$ to be a good fit to the data. The contact angle of the fluid had not been considered to be a factor before and so data for different fluids were considered together when finding the best fit. Results here suggest that S_{θ_c} affects the wavelength of the rivulet pattern that emerges and so results with different θ_c should be treated separately.

In the present work the relationship found to best correspond to the numerical data for a fully wetting fluid is:

$$\lambda_f = \frac{20H_0}{(6Ca)^{0.4}}. \quad (4.1)$$

This is indicated in Figure 4.12 alongside experimental points for ‘Fluid B’ (con-

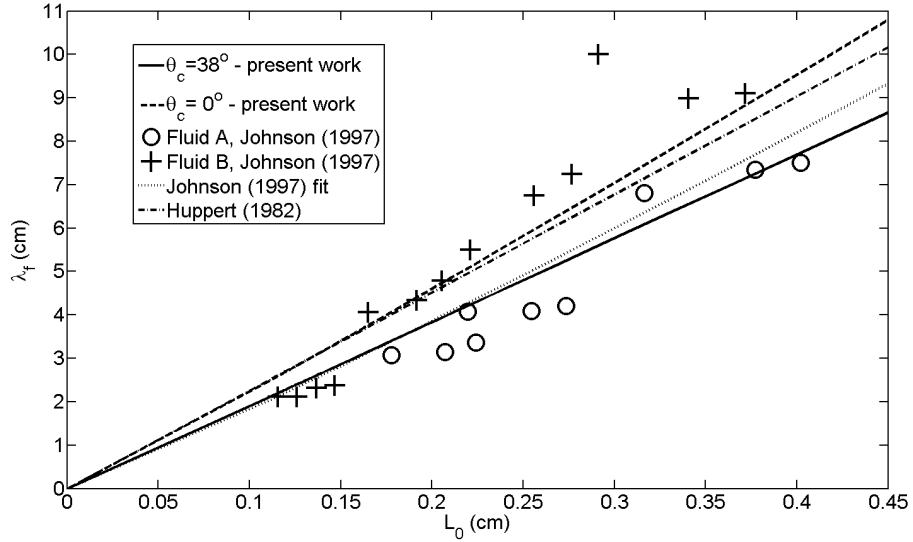


FIGURE 4.12: Relationships extracted from numerical data of current study, given by equation (4.2), shown for fully wetting fluid and when $\theta_c = 38^\circ$. The results of Johnson *et al.* (1999) are plotted for comparison; ‘Fluid A’ has a contact angle of 38° and ‘Fluid B’ is considered to be fully wetting. Also shown are the fits found by Huppert (1982) (interpreted by Troian *et al.* (1989)) and Johnson *et al.* (1999).

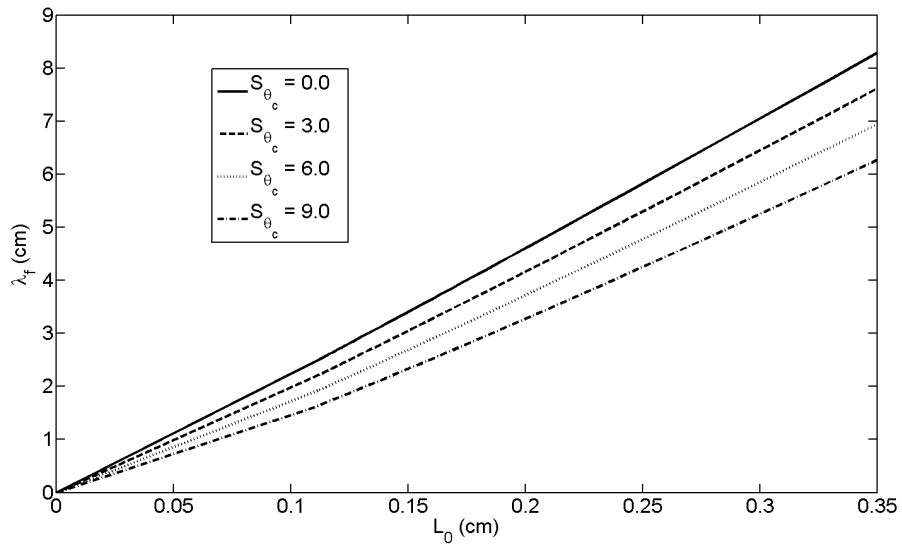


FIGURE 4.13: Results given by equation (4.2) for a range of spreading coefficient, S_{θ_c} .

sidered fully wetting). The line given by equation (4.1) is in good agreement with the experimental points of Johnson *et al.* (1999) and also correlates well with Huppert (1982) (also plotted in Figure 4.12), particularly at smaller L_0 ; the best linear fit for the data is given by $22H_0/(6Ca)^{1/3}$ which is not as accurate as the proposed relationship but is closer to that found by Huppert (1982) (as interpreted by Troian *et al.* (1989)).

The relative impact of the combined effect of the contact angle θ_c and the capillarity of the flow, can be evaluated by the value of the non-dimensional spreading coefficient $S_{\theta_c} = 6(6Ca)^{-2/3}(1 - \cos\theta_c)$. For instance, as witnessed by results discussed above, as θ_c increases so does S_{θ_c} and the change in the dynamics of the rivulet formation at the advancing front are more dramatic. The results for the long-time average wavelength, λ_f , generated with $\theta_c \neq 0$ are found to fit to:

$$\lambda_f = \frac{20H_0}{(6Ca)^{0.4}} - 1.51H_0S_{\theta_c} = H_0 [20(6Ca)^{-0.4} - 1.51S_{\theta_c}]. \quad (4.2)$$

The line generated by this equation for ‘Fluid A’ with $\theta_c = 38^\circ$ is shown in Figure 4.12. As can be seen as θ_c increases so does the impact of the contact angle on the corresponding wavelength, λ_f . The line for $\theta_c = 38^\circ$ gives very good agreement to the experimental points of Johnson *et al.* (1999) for ‘Fluid A’ and fits better than the nearest linear fit of $20L_0$.

Figure 4.13 shows the proposed relationship from equation (4.2) for a range of S_{θ_c} . Within the lubrication approximation S_{θ_c} can realistically range from 0 for fully wetting fluids to approximately 9.6 at low inclination angles (larger L_0) with a contact angle of 38° . As the partial wetting parameter S_{θ_c} increases λ_f decreases in a linear fashion. Note also that the fit (4.2) remains positive as long as Ca is larger than 3×10^{-5} which is well within the values considered in experiments.

4.1.4 Varying the inflow condition

Complete surface coverage is desirable in most applications or scenarios involving thin film flows whether industrial or biological - for instance, in the coating of televisions with non-reflective coating, complete uniform coverage of the screen is required for a highly-performing quality product. Rivulet formation can cause a non-even, non-complete coverage of the surface; in this section controlling the pattern of flow by temporally varying the inflow rate sinusoidally across the width of the domain is explored.

The inflow condition, $h(0, y) = 1$ for all t , is replaced by a travelling wave inflow condition, defined by:

$$h(0, y, t) = 1 + A_r \sin(2\pi ft) \sin\left(\frac{2\pi y}{\beta\lambda_f}\right), \quad (4.3)$$

where β controls the wavelength of the sinusoidal wave across the front, A_r is the amplitude of the variation, $f = 1/v_r$ the frequency of the fluctuations and λ_f , calculated from equation (4.2), the wavelength.

Figure 4.14 shows the free-surface colour map and corresponding contour plot for a constant inflow of 'Fluid B' on a vertically inclined substrate; parameters of the flow are the same as in Section 4.1.1. The amplitude of the fluctuations in inlet height is 0.5 with a wavelength of $3\lambda_f$, the frequency is set as $1/15$. As the areas of thicker fluid move faster than the rest of the film they approach the advancing contact line. Although the height of the pulse is damped as it travels along the film as it reaches the front rivulets are induced.

The pulses are channeled into rivulets that are already formed, this can be clearly seen in Figure 4.14 as there is an area of thick fluid half way along the long rivulets. The height of the rivulet increases and thus the growth rate increases; the longer rivulets have been extended via several pulses of fluid, whereas the shorter ones have experienced one less wave of thicker fluid.

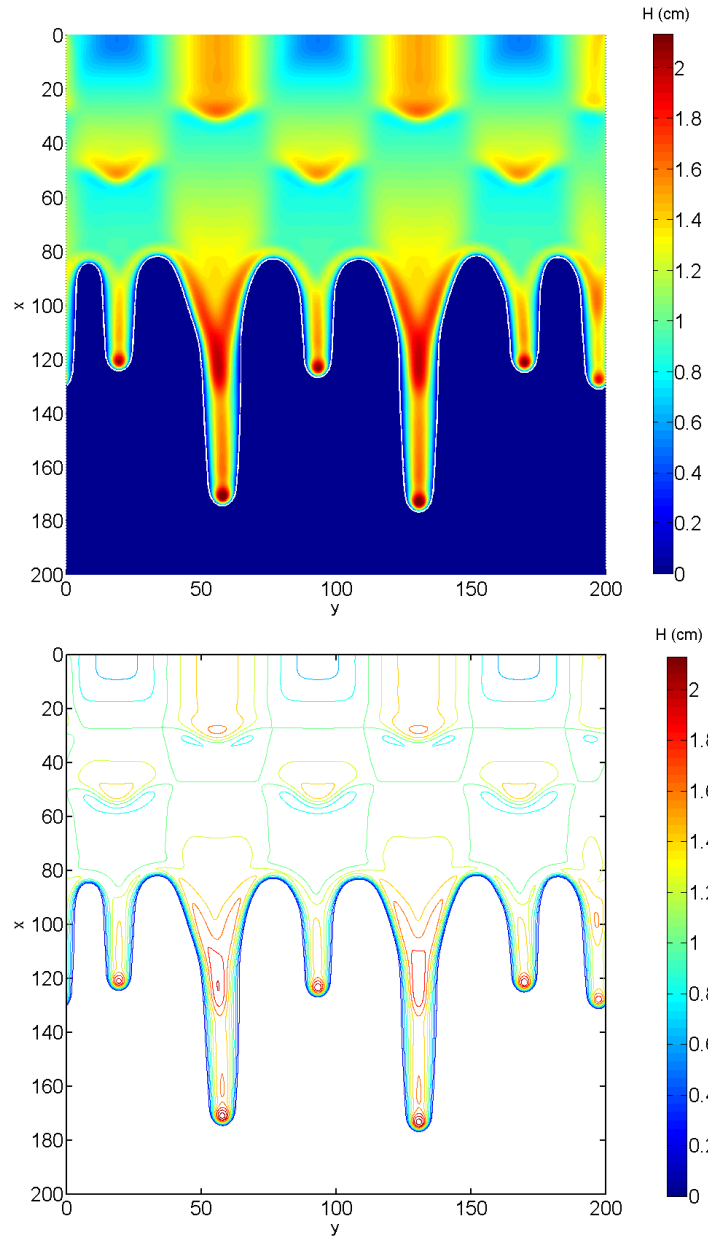


FIGURE 4.14: Free-surface colour map of ‘Fluid B’ flowing down a vertically inclined planar substrate with a temporally varying inlet given by equation (4.3) with amplitude fluctuation of $A_r = 0.5$, wavelength $3\lambda_f$ and frequency $f = 1/15$; also shown is the corresponding contour plot.

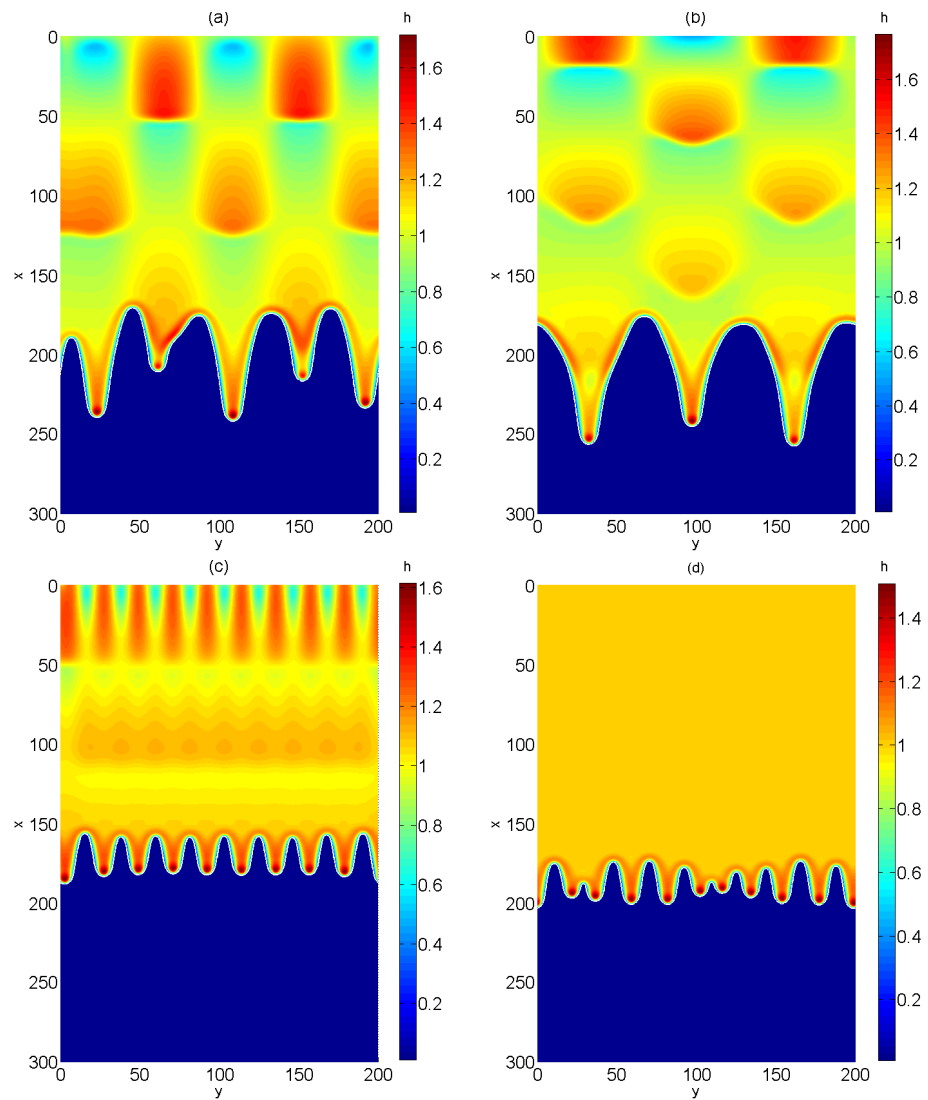


FIGURE 4.15: Free-surface colour maps of ‘Fluid B’ flowing down a planar substrate inclined at 27.9° with a temporally varying inlet controlled by parameters A_r (0.5 in all cases), wavelength $\beta\lambda_f$ and frequency f . (a) $\beta = 4$, $f = 1/60$; (b) $\beta = 6$, $f = 1/40$; (c) $\beta = 1$, $f = 1/60$; (d) no time dependence.

The wavelength of the rivulets is also controlled by the temporally dependent inlet flow; the width of the pulses is wider than the natural wavelength λ_f , thus when the first pulse reaches the front any rivulets that were forming are forced to unite with the newly created rivulet which then grows into a rivulet with the same width as the usual planar case. Figure 4.15 shows this feature; in (a) $\beta = 4$ and five rivulets form, when β is increased to 6 the number of rivulets drops to three as the width of the wavelength of the sinusoidal wave is increased.

If the forced wavelength is the same as λ_f , as in Fig 4.15 (c), then the maximum possible number of rivulets will be formed - in this case ten. There is a disparity between this case and (d) where there is no time dependence due to the regular pattern that is created by imposing a time-dependent inlet; in (d) there are eleven rivulets formed however two sets of neighbouring rivulets are growing in slightly closer proximity to the other rivulets and so are beginning to merge. This happens due to the near-periodic pattern that emerges, this is not observed when forcing the pattern to grow exactly periodic with a time-dependent inflow.

Although a time-varying inflow cannot be used to suppress the formation of rivulets it is certainly shown to give a limited amount of control in respect to the pattern of the flow. It is possible to change the number of rivulets that form or induce a more regular pattern and limit late merging that produces rivulets of varying length.

4.2 Summary

The classical problem of a thin liquid film spreading on a planar surface that is inclined has been revisited. The aim of the work was to link the wetting properties of the fluid to the global characteristic of wavelength thus consolidating work previously done since Huppert in 1982 (Huppert, 1982). Results are validated with the experimental data of Johnson (1997) showing excellent agreement for width and wavelength. A linear stability analysis proves to be reasonable in predicting

wavelength but not as accurate as full numerical solutions.

Dynamic computations revealed the merger of neighbouring rivulets in certain conditions, an interesting feature of rivulet formation that influences the final long-time rivulet pattern. Should two rivulets grow within a certain distance of one another they will merge; as they merge the paths can be altered and growth rate increase.

When the flow is partially wetting the rivulets grow in a very different pattern, in line with experimental observations. They become much thinner and straight edged, as opposed to the saw-tooth shape of fully wetting rivulets, they also evolve much faster leading to a decrease in surface coverage. As the partially wetting parameter increases these effects become more pronounced. The wavelength of the rivulet pattern was found to also decrease with decreasing wettability.

A general expression that allows the prediction of the wavelength of the rivulet pattern was extracted from the numerical data. This model, which encompasses the wetting properties of the liquid, was found to match well with existing experimental data and also tends to Huppert's expression when the film is fully wetting.

Chapter 5

Influence of surface tension gradient, substrate chemical heterogeneity and topographical features on rivulet formation

Contents

5.1	Constant surface tension gradient	100
5.1.1	Governing equations	100
5.1.2	Results	101
5.1.2.1	Marangoni forces	101
5.1.2.2	Topography	106
5.1.2.3	Climbing films	107
5.2	Chemical heterogeneity	110
5.2.1	Numerical results	111
5.2.1.1	Influence on rivulet formation	111
5.2.1.2	Influence on rivulet growth	117
5.3	Summary	121

In practice, substrates are rarely planar and may feature defects in the form of trench or mound topographies and/or areas of chemical heterogeneity; both will impact on the spreading of a liquid film over the surface. Additionally the flow may be subject to thermal gradients which can induce Marangoni stresses at the surface of the film.

This chapter investigates the impact such features may have on the rivulet instability including the formation, merger and long-time evolution of the fingering patterns that are formed. Chemical heterogeneity, modelled by introducing patches on the substrate where the fluid is more or less wetting (i.e has a smaller or larger contact angle than on the rest of the surface) is shown to promote rivulet formation as well as influence rivulets that have already formed. Topography and surface tension gradients can also introduce noticeable changes into the system.

First a surface tension gradient term is introduced into the lubrication approximation and the combined influence of surface tension gradient and topography on a gravity-driven film investigated. The ability of a film to climb against gravity, propelled by Marangoni stresses, has been investigated experimentally by Cazabat *et al.* (1990); Kataoka and Troian (1997, 1999). The mathematical model is able to capture this phenomena and shows good agreement with the experimental findings. Secondly, the influence of wettability changes on the surface of a substrate is considered, with the examples explored revealing how this feature can have a significant impact on the rivulet pattern that is formed.

5.1 Constant surface tension gradient

5.1.1 Governing equations

The lubrication equations, equations (2.23) and (2.24) in Section 2.1.1, are reformulated with the fluid now considered to have variable surface tension, σ , given by $\sigma = \sigma_0 \tilde{\sigma} = \sigma_0 + \tau X$, with σ_0 the value of surface tension at $X = 0$ and

$\tau (= \partial\sigma/\partial X)$ a constant surface tension gradient (Cazabat *et al.*, 1990); $\tilde{\sigma}$ is the non-dimensional surface tension. Re-deriving the lubrication equations, with the appropriate adjustments to the tangential free-surface boundary condition, leads to the following governing equation incorporating surface tension gradient:

$$\frac{\partial h}{\partial t} = \frac{\partial}{\partial x} \left[\frac{h^3}{3} \left(\frac{\partial p}{\partial x} - 2 \right) - \frac{\tilde{\tau} h^2}{2} \right] + \frac{\partial}{\partial y} \left[\frac{h^3}{3} \left(\frac{\partial p}{\partial y} \right) \right], \quad (5.1)$$

together with:

$$p = -\frac{\epsilon^3}{Ca} \hat{\sigma} \nabla^2 (h + s) + 2\epsilon (h + s - z) \cot \alpha - \Pi(h), \quad (5.2)$$

where $h, p, \tilde{\tau}$ ($= H_0 \tau / \mu U_0$) and s are the dimensionless film height, pressure, constant surface tension gradient and topography function, respectively.

The new term in equation (5.1), $\frac{1}{2} \frac{\partial \tilde{\tau} h^2}{\partial x}$, is discretised as follows:

$$\frac{\tilde{\tau}}{2} \left(\frac{h_{i+1,j}^2 - h_{i-1,j}^2}{2\Delta} \right). \quad (5.3)$$

Experimentally a heated substrate is used to induce the surface tension gradient. It was observed that fluctuations in viscosity and density were small when compared with changes in surface tension. Therefore, despite not taking thermo-viscosity or thermally-dependent density into account, this model is deemed suitable for recreating the conditions observed experimentally.

5.1.2 Results

5.1.2.1 Marangoni forces

The results presented below are for the case of the flow of a $100\mu\text{m}$ water film (density $\rho = 1000 \text{ kg m}^{-3}$, viscosity 0.001 Pa s and surface tension $\sigma_0 = 0.07 \text{ N m}^{-1}$) on a substrate inclined at 65° to the horizontal, this gives $Ca = 6.35 \times 10^{-4}$

and $\epsilon = 0.16$. The precursor film thickness is taken to be $h^* = 0.01$ ($H^* = 1 \mu\text{m}$), a value chosen to be consistent with the one used by Diez and Kondic (2001*b*), to facilitate comparison between the results generated, l_j and $\lambda_{0,j}$ were kept the same. When topographies are present, they are restricted to simple square peak and trench features with $\gamma = 0.01$; see expression (2.45) in Chapter 2.

The results shown in Figure 5.2 were obtained on a computational domain with $(l_p, w_p) = (200, 100)$; the adaptive multigrid method utilised five grid refinement levels, $0 \leq k \leq 4$, with the number of nodes on each level being $n_k = 278 \times 2^k + 1$ and $m_k = 139 \times 2^k + 1$ which equates to a finest mesh resolution of $\Delta = 0.045$. The value of $\tilde{\tau}$ is prescribed as indicated; surface tension gradients of similar magnitude have been achieved in an experimental setting using heated substrates (Cazabat *et al.*, 1990).

Comparing the left, middle and right columns of free-surface colour maps reveals the effect of the surface tension gradient, $\tilde{\tau}$, see equation (5.1), acting in the stream-wise direction. The main difference is the length of the rivulets formed: a value of $\tilde{\tau} > 0$ accelerates the lengthening of the rivulets with the spreading rate characterised by an increase in the maximum film height of the capillary ridge at their tips; for $\tilde{\tau} < 0$, the opposite effect is observed and there is a flattening/decrease in the capillary ridge at the tips suppressing lengthening. At later times, see the bottom row of colour maps, the difference in position and length is even more pronounced.

The merging of neighbouring rivulets is observed in Figure 5.2 and is clearly influenced by the presence of a surface tension gradient. In Figure 5.2(d), where $\tilde{\tau} < 0$, the merger of two rivulets has just occurred with their tips coalescing to form a new, single rivulet; the retarded lengthening of these rivulets mean they interact at an earlier stage and coalesce. The same rivulets in Figure 5.2 (e), $\tilde{\tau} = 0$, and (f), $\tilde{\tau} \geq 0$, have yet to merge fully but have begun to do so from their common root; they will eventually merge but at a later time. This is seen to have happened in Figure 5.2(h), for $\tilde{\tau} = 0$; however, with $\tilde{\tau} = 0.25$, Figure 5.2(i), the rivulet tips remain distinct. The rivulet formed by the merging process, see Figure 5.2(g), has moved

ahead of its neighbours due to the increase in capillary ridge height which accompanies merging and which in turn leads to accelerated lengthening of the combined rivulet. A negative surface tension gradient promotes earlier merger of neighbouring rivulets, whereas a positive one delays the time at which merger occurs.

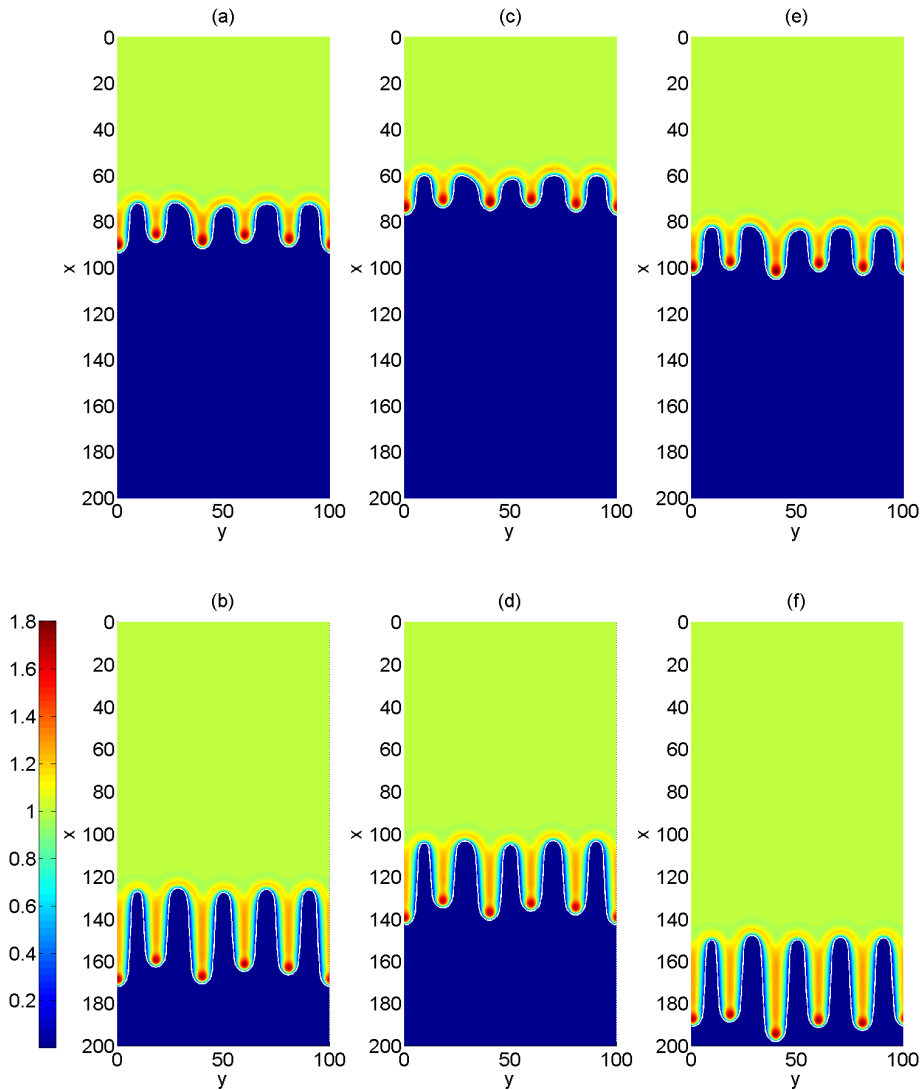


FIGURE 5.1: Color maps of free-surface profile for a water film spreading on a planar substrate inclined at 65° . The left profiles are for flow with no surface tension gradient, the middle column is flow when $\tilde{\tau} = -0.25$ and the right hand side is when $\tilde{\tau} = 0.25$. The top profiles are at $t = 100$ and the bottom profiles are at $t = 200$.

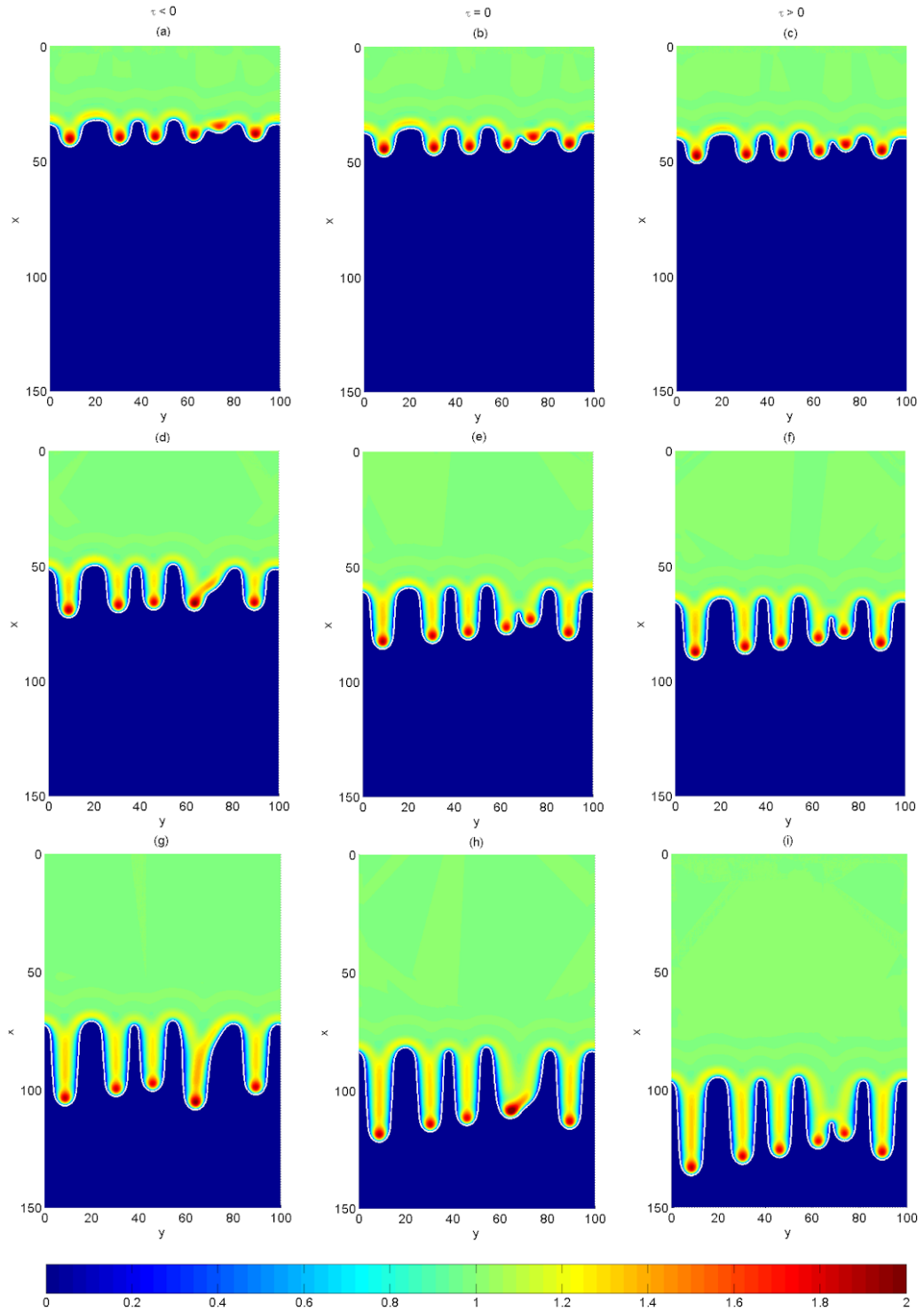


FIGURE 5.2: Colour maps of the free-surface height, $h + s$, for gravity-driven flow over a planar substrate, $s_0 = 0$, and $\alpha = 65^\circ$: the rivulet pattern formed corresponds to $t = 50$ (top), $t = 100$ (middle) and $t = 150$ (bottom) when $\tilde{\tau} = -0.25$ (left), $\tilde{\tau} = 0.0$ (centre) and $\tilde{\tau} = 0.25$ (right), respectively. The streamwise direction of flow is from top to bottom in each sequence.

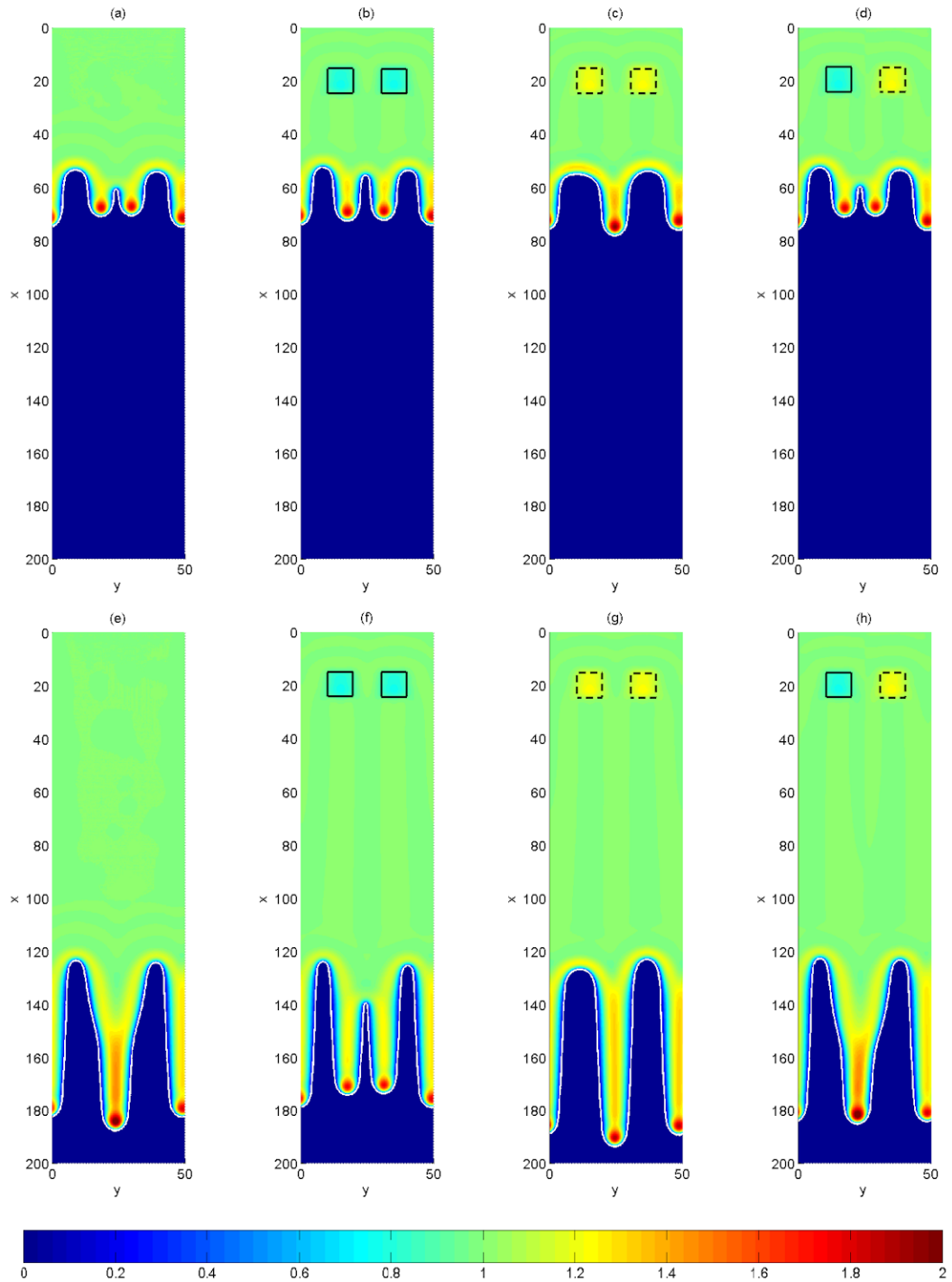


FIGURE 5.3: Colour maps of the free-surface, $h + s$, showing rivulet formation for flow over substrate containing different topographical heterogeneities, $|s_0| = 0.2$ and $\theta = 65^\circ$; top row $t = 100$, bottom row $t = 258$ (bottom). The substrate contains (from left to right) no topography; two square trench topographies; two peak topographies (dashed outline); and a square trench and a square peak topography. $\tilde{\tau} = -0.25$ in all cases. The streamwise direction of flow is from top to bottom in each sequence.

5.1.2.2 Topography

Similarly the presence of topography can, in addition, have a dramatic influence on the formation of rivulet patterns. An example of this is shown in Figure 5.3 for an advancing front moving down different planar substrates, one containing two identical trenches, another with two identical peaks, a third containing equal but opposite trench and peak topographies and one completely planar. The advancing front starts from the same position upstream of the topographical features in each case, at $x = 10$. All topographies have height/depth $s_0 = |0.2|$ and length and width $l_t = w_t = 10$. The domain size for these solutions is $(l_p, w_p) = (250, 50)$ with, in this case, the number of nodes on level k given by $n_k = 348 \times 2^k + 1$ and $m_k = 70 \times 2^k + 1$, the surface tension gradient is $\tilde{\tau} = -0.25$; the case when no topographical features are present is shown as a comparative solution.

The upper set of plots in Figure 5.3 shows the rivulet structures at $t = 100$; the various combinations of topographical features clearly affect the position and growth of the rivulets differently. When twin trenches are present, Figure 5.3(b), the two inner most rivulets formed are slightly longer and slightly more advanced relative to their planar substrate counterparts, Figure 5.3(a). Figure 5.3(c), for the case of twin peaks, shows a very different pattern emerging; the inner most rivulets have already merged at an earlier time after being directed towards one another. Their merger is accompanied by a sharp increase in the height of the capillary ridge at the tip of the newly formed single rivulet which leads to an acceleration in the lengthening process.

At later times, see the bottom set of colour maps at $t = 258$, the influence of the topography persists. The inner most rivulets have merged in all cases apart from that in which the front encountered twin trenches; this suggests that the increased lengthening experienced in the latter case delays the merging of these rivulets. The middle rivulet in Figure 5.3 (h) is skewed to the left slightly (towards the trench topography side of the domain) compared to the ones in Figures 5.3 (e) and (g) due

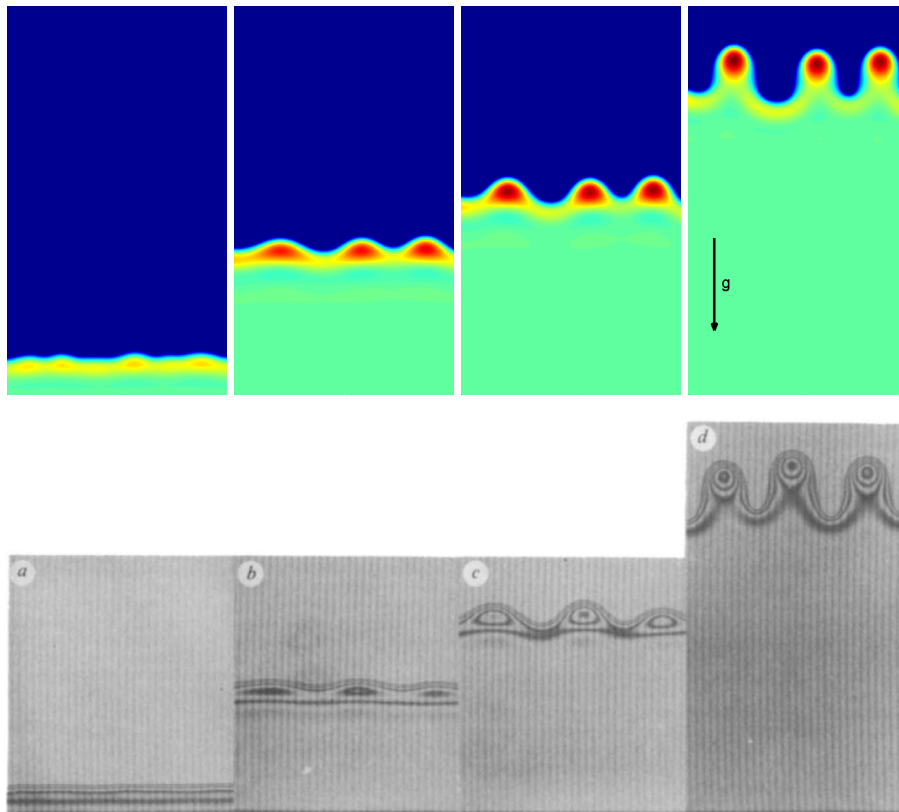


FIGURE 5.4: *Top*: Colour maps of free-surface film height for the case of a thin film climbing up a vertically inclined substrate due to Marangoni stress, $\tilde{\tau} = 1.6$ in this case. The direction gravity is acting is shown in (d) for clarity. *Bottom*: A typical evolution of a Marangoni driven advancing front from the experiments of Cazabat *et al.* (1990).

to the predominant deflection effect of the peak. The centre rivulet in the twin peak topography case, Figure 5.3 (g), results from the merging that occurred at much earlier times so has the usual, elongated shape. The other newly formed, single, centre rivulet, in Figures 5.3 (e) and (h), has a wider, V-shaped base due to it being fed from the two combined sources of the now merged rivulets. As time progresses, the increase in ridge height at the tip leads to an acceleration of the rivulet front which elongates the structure.

5.1.2.3 Climbing films

By introducing a temperature gradient along the substrate a surface tension gradient may be induced. If the Marangoni forces are larger than the opposing gravitational

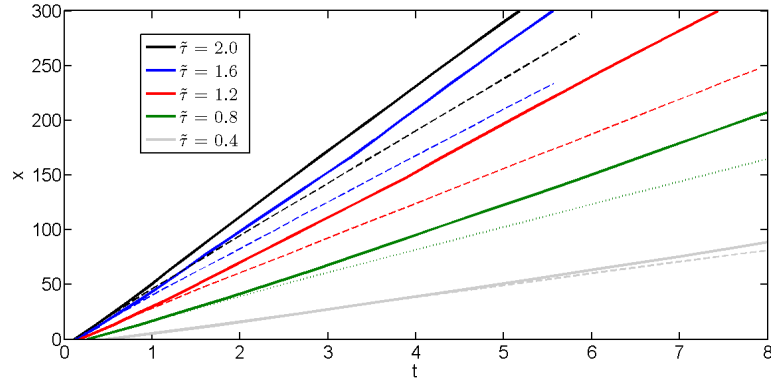


FIGURE 5.5: The position of the tip of the longest rivulet formed at the advancing front of a $0.86\mu\text{m}$ thick film rising up a vertically aligned plate under the influence of a surface tension gradient of $\tilde{\tau}$. The dashed line indicates the corresponding trough position.

τ, Nm^{-2}	$H_0, \mu\text{m}$	$L_0, \mu\text{m}$	$\lambda, \mu\text{m}$	$\lambda_{\text{caz}}, \mu\text{m}$	$\tilde{\lambda} = \lambda/L_0$
0.5	0.86	21.4	514	600	24
0.27	0.65	21.4	514	610	24
0.21	0.54	19.8	436	480	22
0.1	0.27	15.9	366	370	23
0.054	0.17	14.3	329	340	23
0.21	0.65	22.2	533	580	24
0.21	0.33	14.3	329	340	23

TABLE 5.1: Table of wavelength, λ , of the advancing front of a climbing film for a range of parameters obtained from numerical solutions and compared with the experimentally measured values in Cazabat *et al.* (1990), λ_{caz} .

effects then the advancing front of the thin film may begin to climb an inclined substrate against gravity. A similar instability seen in gravity-driven flows occurs and rivulets form. There have been a number of studies into this Marangoni driven fingering phenomena such as that of Kataoka and Troian (1997) and Cazabat *et al.* (1990).

Cazabat *et al.* (1990) considered the above problem using a light silicone oil polydimethylsiloxane (PDMS) as a working fluid and film thicknesses between $0.17\mu\text{m}$ and $0.86\mu\text{m}$. A temperature gradient was applied to a vertically inclined plate which had one end submerged in a bath of the fluid. Here the same range of parameters is considered; the lubrication model described previously is modified in that the term that encompasses the gravity term changes sign due to the reversal of perspective (i.e. the positive x -direction now goes up), therefore equation (5.1) becomes:

$$\frac{\partial h}{\partial t} = \frac{\partial}{\partial x} \left[\frac{h^3}{3} \left(\frac{\partial p}{\partial x} + 2 \right) - \frac{\tilde{\tau} h^2}{2} \right] + \frac{\partial}{\partial y} \left[\frac{h^3}{3} \left(\frac{\partial p}{\partial y} \right) \right]. \quad (5.4)$$

The advancing liquid front will only climb if the film is thin enough. By considering the governing lubrication equations, equations (5.4) and (5.2), and comparing the terms encompassing gravitational forces, $2h^3/3$, and those arising from the surface tension gradient, $\tilde{\tau}h^2/2$, it can be shown that the film will only climb if:

$$\frac{2h^3}{3} - \frac{\tilde{\tau}h^2}{2} < 0 \Rightarrow \tilde{\tau} > \frac{4h}{3}.$$

Substituting $U_0 = \rho g \sin \alpha / 2\mu$ into the inequality and noting that the film thickness is of the same order as H_0 gives the condition for the advancing front to climb as:

$$\tau > \frac{2}{3} \rho g H_0 \sin \alpha. \quad (5.5)$$

Figure 5.4 shows the typical progression of the advancing front of a climbing film as colour maps of film thickness; the case shown is for a film thickness $0.86\mu\text{m}$ and an applied surface tension gradient of $\tilde{\tau} = 2$. As in the case of gravity-driven

rivulet formation, the advancing front develops a capillary ridge, areas of thicker fluid stretch out in front of the bulk of the fluid forming the rivulet pattern observed; the predicted evolution of the pattern is compared with the corresponding experimentally observed pattern presented by Cazabat *et al.* (1990) - their Figure 2 - which shows very good qualitative agreement.

The width of the rivulets depends on the surface tension gradient, $\tilde{\tau}$; the larger the magnitude of $\tilde{\tau}$ the thinner and more elongated the rivulets are, as seen in gravity-driven flow with increasing inclination angle. This is shown in Figure 5.5 where the size of τ is varied and the positions of the tips of the rivulets and the corresponding troughs are plotted. It shows that the finger lengthening is enhanced (indicated by the gap between tip and trough) as τ increases.

The wavelength, λ , of the rivulet pattern is the distance between the tips of neighbouring rivulets. Cazabat *et al.* (1990) find that the non-dimensional wavelength, $\tilde{\lambda} = \lambda/L_0$, lie in the range from 22 to 27 (similar to values found in experiments for gravity-driven flow Troian *et al.* (1989), Kondic and Diez (2001)). Here the non-dimensional wavelength (taken as the average of $\tilde{\lambda}$ across the whole front) was found to range from 22 to 24 for the range of parameters used by Cazabat *et al.* (1990) showing good agreement with their experimental study and giving similar results to that of gravity-driven rivulet growth, see Table 5.1.

5.2 Chemical heterogeneity

Substrates made up of different materials/chemicals or with varying surface properties may contain regions exhibiting differing wettability. Chemically striped substrates have been shown to influence the wavelength of emerging rivulets in gravitationally driven films (Kondic and Diez, 2002; Zhao and Marshall, 2006) as well as in the case of thermally driven climbing films (Kataoka and Troian, 1997, 1999). When a random pattern of heterogeneous patches with differing wettability is de-

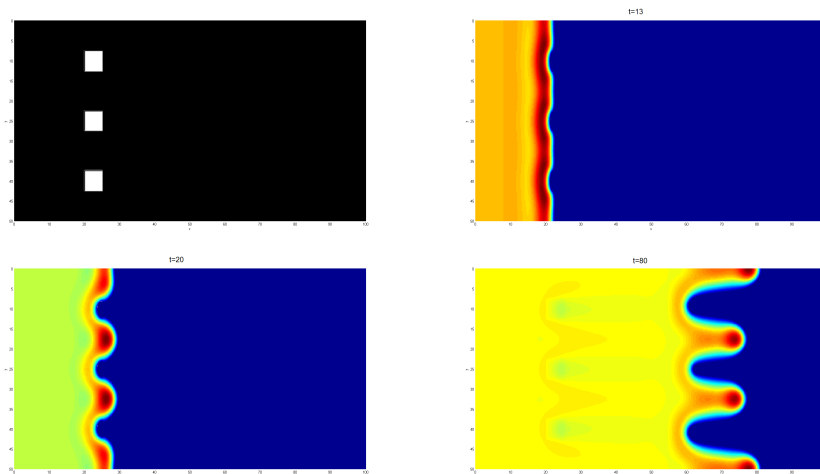


FIGURE 5.6: The low wettability patch pattern is shown in the top left figure. Free-surface contour maps showing the progression of the contact line of a thin film flowing down an inclined plane tilted at 30° onto a substrate with 5 equally spaced low wettability patches of equilibrium contact angle $\theta_c = 10.0$ and $S_{\theta_c} = 3.5$.

fined on the substrate the wavelength that emerges is similar to the planar case; however, there is a significantly higher variation of wavelength to the mean (Zhao and Marshall, 2006).

In this section the formation of rivulets on a chemically heterogeneous substrate is investigated by introducing areas of high/low wettability across the surface. The influence with regard to the features observed in Chapter 4 are recorded and discussed.

5.2.1 Numerical results

5.2.1.1 Influence on rivulet formation

Figure 5.6 and 5.7 show the evolution of a $100\mu\text{m}$ thick water film on a substrate inclined at 30° approaching three and five equally spaced low wetting patches on the substrate. In the first case four rivulets are created by the spacing and these grow unabated down the substrate. In the second case, as in the first, the spacing induces the same number of rivulets as spaces between the patches (i.e. 4 in Figure 5.6 and

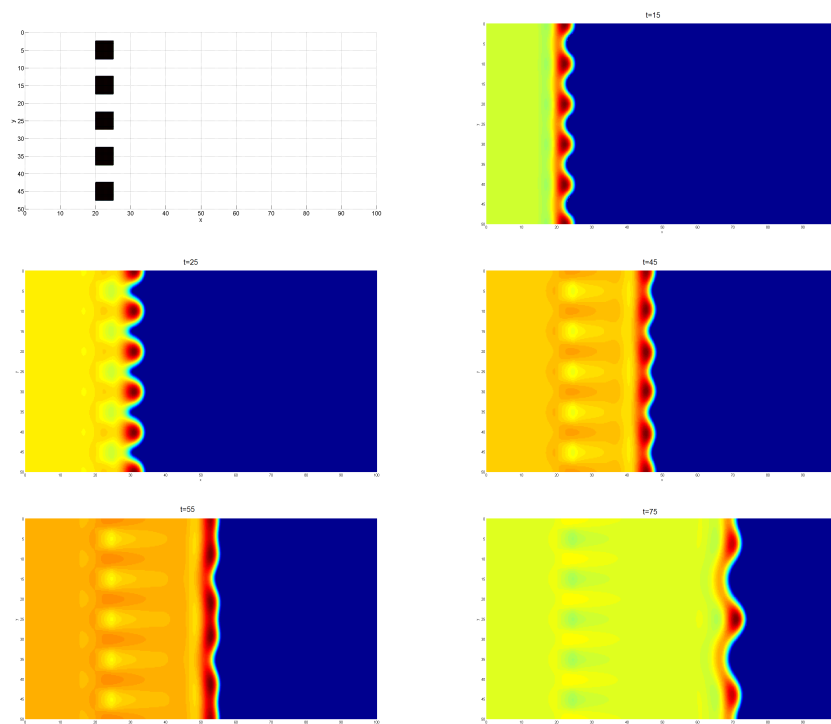


FIGURE 5.7: Free-surface contour maps showing the progression of the contact line of thin film flowing down an inclined plane tilted at 30° onto a substrate with 5 equally spaced low wettability patches of equilibrium contact angle $\theta_c = 10.0$ and $S_{\theta_c} = 3.5$.

6 in Figure 5.7). However, this time the narrower spacing causes the rivulets to grow in closer proximity to one another - the rivulets then coalesce; this takes place between neighbouring rivulets leaving only three rivulets after the merger process.

The spacing between the patches directly determines the number of rivulets formed; one patch induces two rivulets, two induces three and so on. As the liquid front meets the patches, fluid is channelled into the spaces between the patterns; this creates areas of thicker fluid, with a higher capillary ridge at the contact line, which grow faster than the bulk flow thus exaggerating the instability. If the spacing becomes too small, smaller than λ_f as determined in Chapter 4, merging takes place and can lead to fewer rivulets for a greater number of patches. These findings are analogous to the finding of Kondic and Diez (2002) who introduced small trough topographies ahead of an advancing front and found that if the spacing between the troughs is larger than the critical wavelength, λ_f , then the number of rivulets to emerge is the same as the number of troughs. If the spacing is smaller than the critical value rivulets are formed that grow in close proximity to one another, this in turn means - see Chapter 4 - that merging is promoted - the final wavelength after merging is complete can then be larger than λ_f . Zhao and Marshall (2006) also found this when the substrate was chemically striped (different wettability stripes).

Figure 5.8 (a) and (b) depicts the same case but with two different patterns of chemically different patches. In (a), the three patches have a small spacing between them so, although four rivulets are initially induced, the two centre rivulets merge leaving two outer rivulets and one central rivulet. The central rivulet, created from the merging of the two rivulets created by the spacing of patches, has formed directly in the centre of the trajectories of its two 'parent' fingers. As the front then meets a complex of four more patches, with the same spacing as the first set of patches, the three rivulets are directed down fully wetting areas as they are repelled from the low wetting area. The existing rivulets are squeezed in the spacing between patches, as the spacing is smaller than the natural width of the fingers; this leads to an increase in film thickness between the patches, as the fluid exits the spacing the rivulets re-

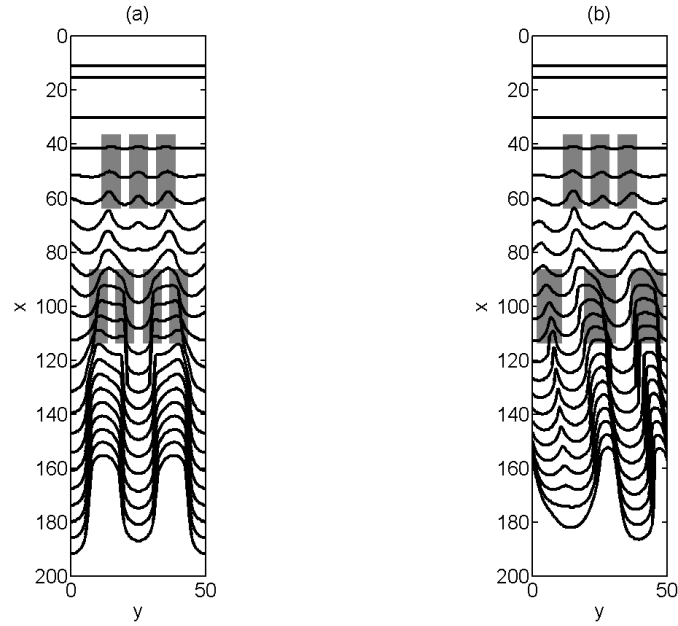


FIGURE 5.8: Contact line plots of a thin water film flowing down an inclined plane tilted at 30° on a substrate containing areas of low wettability, indicated by grey patches, where $\theta_c = 10^\circ$ and $S_{\theta_c} = 3.5$.

lax and becomes wider again. In the area between patches where no rivulets are directed the beginnings of two new rivulets can be seen, as they grow in close proximity to the large central rivulet, with a spacing smaller than λ_f , they get drawn into the side of the longer finger. This type of merging, where a smaller rivulet is drawn into the side of a larger one, was observed in the planar case in Chapter 4. Three rivulets then grow in the expected straight manner after the patches.

Now considering Figure 5.8 (b), the process is initially the same as (a), this time however there are only three patches in the second set and they are wider than their counterparts in (a) and the one nearest the $y = 0$ boundary is slightly thinner than the other two. The central rivulet's path directs it towards the middle, low wetting patch. The rivulet is deflected down the left of the patch, due to its low wetting nature, creating a slanted trajectory. Rivulets travel preferentially towards the 'easiest' spreading route with most wettability and thus least resistance; due to this, the rivulet at the top boundary is squeezed towards the top spanwise boundary. The bottom rivulet is also deflected, there is also a new rivulet near the $y = 0$

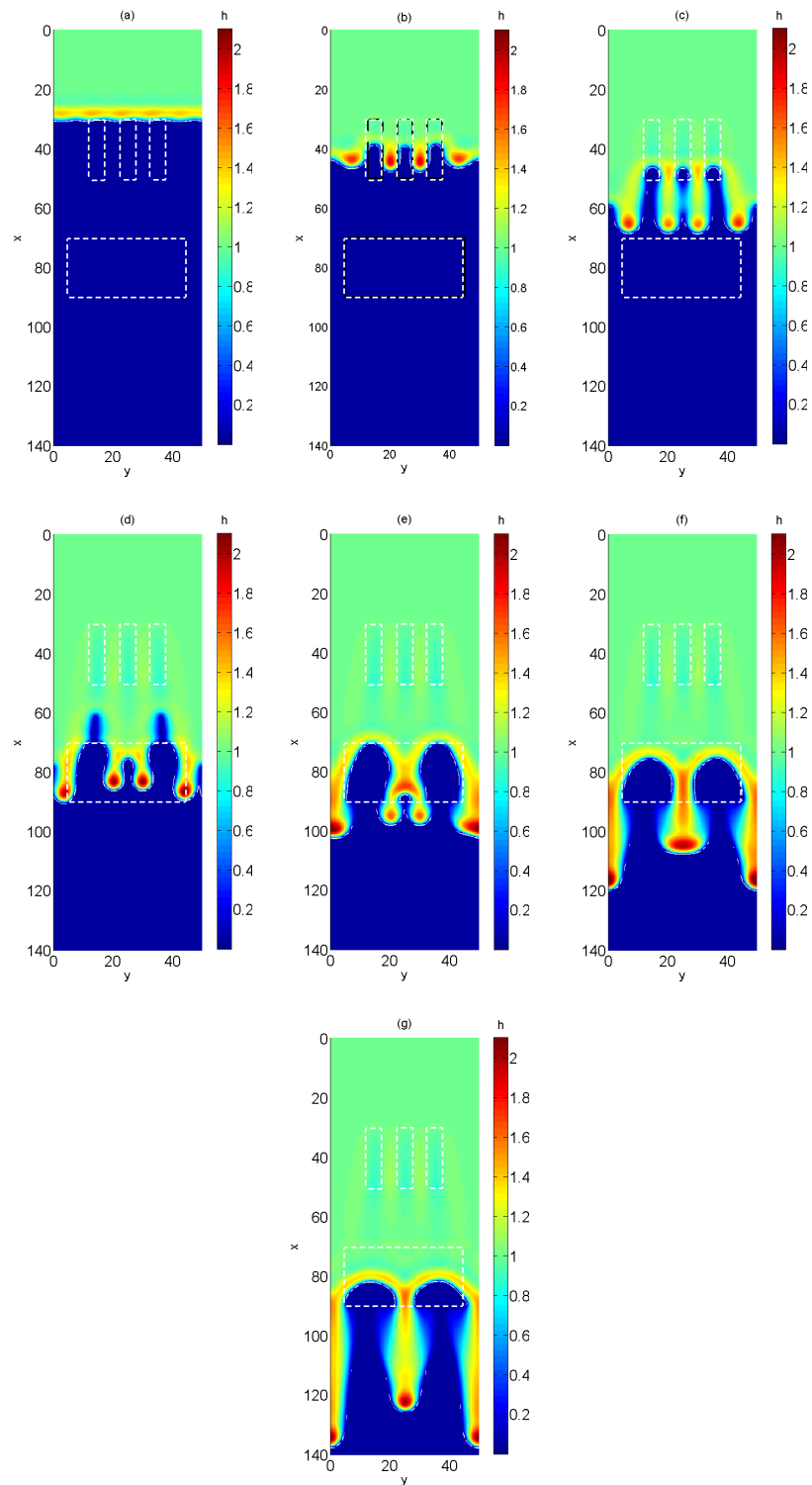


FIGURE 5.9: Three-dimensional free-surface plots to demonstrate the dramatic effect on rivulet formation of large areas of substrate heterogeneity. The fluid is a $100\mu\text{m}$ thick water film flowing down a substrate inclined at 65° with contact angle $\theta_c = 0^\circ$ on the majority of the substrate. The outline of the patches of low wettability are indicated with a white dashed line; on the patches $\theta_c = 10^\circ$.

spanwise boundary that is formed by the wetting patches. As the spacing between these rivulets is small they merge while continuing on their slanted, deflected paths. The asymmetry of the wetting patches introduces asymmetry to the advancing front pattern.

A similar situation is encountered in the film thickness contours shown in Figure 5.9, with $\alpha = 65^\circ$. Instead of having a second row of low wetting patches, these have been replaced by a single large patch. The location of the low wetting regions are indicated by dashed white outlines. This means all four rivulets, seen in Figure 5.9 (b) and (c), resulting from the presence of three low wetting patches meet another area, the large rectangular region downstream, of low wettability. The two rivulets at the spanwise boundaries are deflected around the edges of the patch creating a curving rivulet, see Figure 5.9 (d) and (e). The two centre rivulets begin to merge after the first set of patches, as the merger process begins the half-coalesced structure meets the second region of low wettability, observed in Figure 5.9 (c) and (d). The merging process continues and the tips are close to merging in Figure 5.9 (e) as the tips exit the low wetting region. The half merged base is advancing at a faster rate as it is on the low wetting region and also due to the larger film thickness caused by the merging, this in turn leads to the completion of merger as the base catches the tips of the rivulets - Figure 5.9 (f). As the rivulet leaves the low wetting area, it grows down the centre of the substrate, along with the two side rivulets in Figure 5.9 (g).

The results show that surface heterogeneity can heavily influence the number of rivulets that are formed. The film preferentially spreads along trajectories of least resistance, that is, with highest wettability. This can lead to interesting dynamics and patterns which may be induced by chemical heterogeneity or surface topography including the merger of rivulets and the ‘squeezing’ of rivulets between surface features.

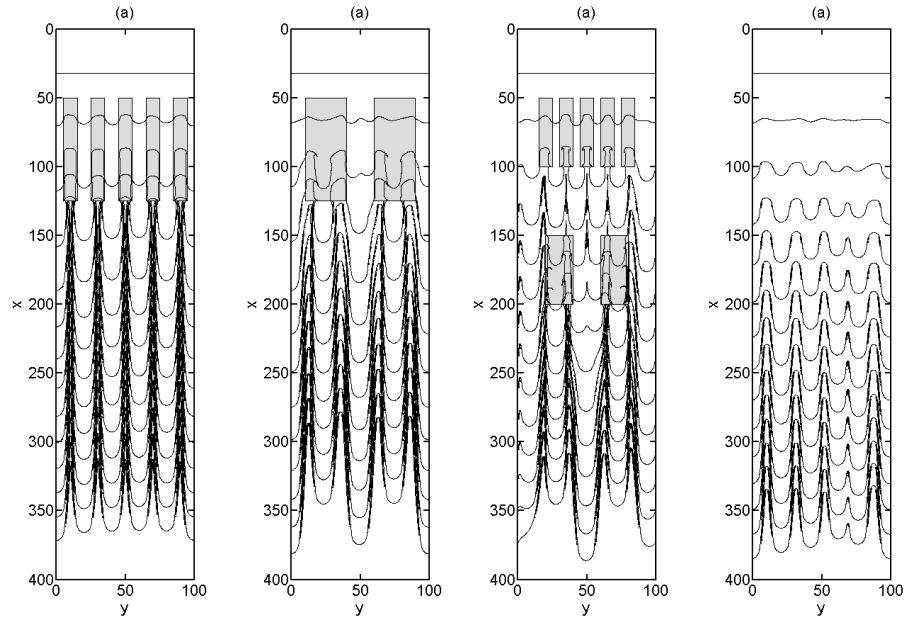


FIGURE 5.10: Rivulet formation and evolution for the flow of a thin film of ‘Fluid A’ on a vertically aligned substrate containing a variety of chemical heterogeneous patterned regions. The plots show the outline of the contact line as it progresses with time. Grey areas indicate areas where $\theta_c = 35^\circ$; the white areas denote fully wetting regions, $\theta_c = 0^\circ$.

5.2.1.2 Influence on rivulet growth

In this section the influence of surface chemical heterogeneity is considered on rivulets that are already growing. The initial front is perturbed as in Chapter 4 so the natural, expected wavelength will emerge if left unimpeded.

The developing contact line is depicted in Figure 5.10 and 5.11 for the same flow as investigated in Figure 4.2 (d) (‘Fluid A’ on a vertically inclined substrate) on a substrate with a variety of different heterogeneous patchwork scenarios; the grey areas denote parts on the substrate where the liquid behaves as if partially wetting, with $\theta_c = 35^\circ$, and the white areas indicate where it is fully wetting, $\theta_c = 0^\circ$. The outline of the contact line is shown as it spreads along the substrate, this allows for the visualisation of the evolution of the rivulet pattern without requiring many contour plots.

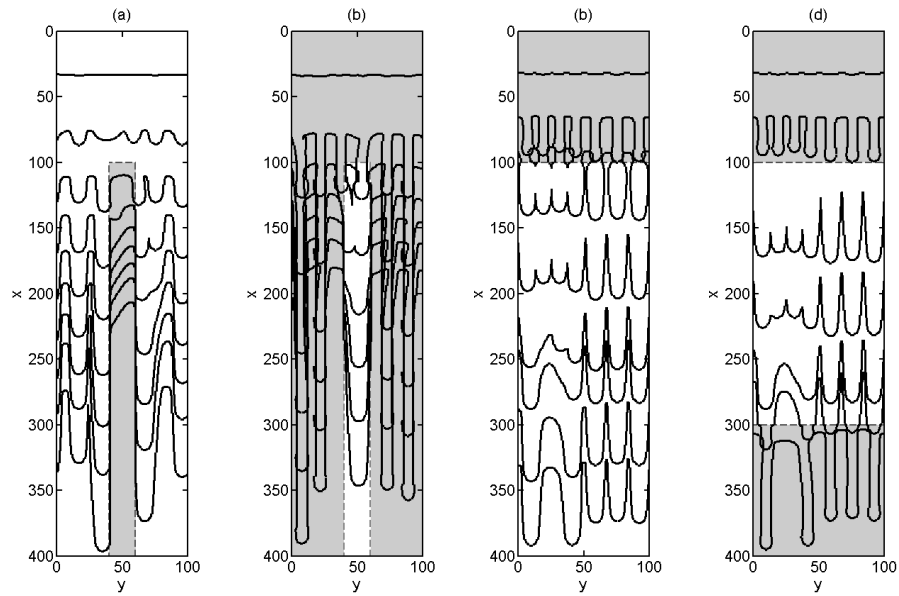


FIGURE 5.11: Rivulet formation and evolution for the flow of a thin film of ‘Fluid A’ on a vertically aligned substrate containing a variety of chemical heterogeneous patterned regions. The plots show the outline of the contact line as it progresses with time. Grey areas indicate areas where $\theta_c = 35^\circ$; the white areas denote fully wetting regions, $\theta_c = 0^\circ$.

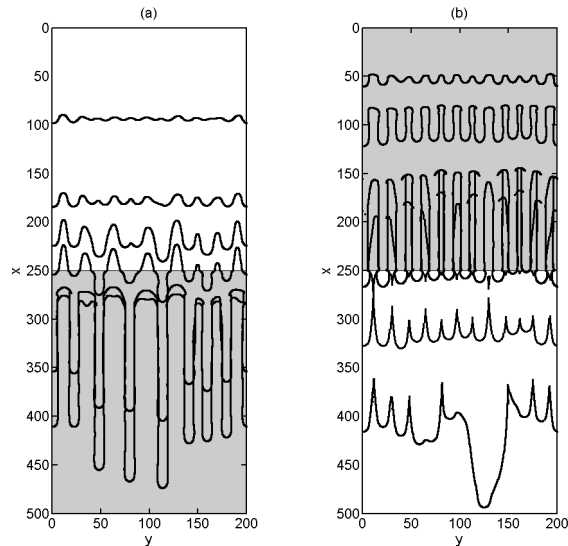


FIGURE 5.12: Contact line outline plots for a thin film of ‘Fluid A’ spreading on a substrate inclined at $\alpha = 36^\circ$ to the horizontal. (a) shows the development of the film on a fully wetting area before crossing onto an area of low wettability where the equilibrium contact angle is $\theta_c = 30^\circ$ (indicated by greyed areas); (b) shows the opposite arrangement.

Five, thin patches near the top of the substrate are seen in Figure 5.10 (a); as the flow evolves the film is channelled between the patches creating six equally spaced rivulets. The emerging periodic rivulet pattern remains the same as it flows down the rest of the substrate. In contrast, when there are no chemical heterogeneities present, in Figure 5.10 (d), six rivulets are again formed. However, as the pattern emerges from the random initial condition it is not completely periodic; due to this two rivulets grow in close enough proximity to begin merging - this can be seen in the final contact line outline in Figure 5.10 (d). Figure 5.10 (b) shows how the contact line develops in the presence of two large heterogeneous patches; the spacing causes the merger of two initial rivulets in the centre of the plot, two rivulets grow down the domain boundaries and a single rivulet grows over each low wetting region. Five, very thinly spaced patches are seen in Figure 5.10 (c) creating four very thinly-spaced rivulets in the centre of the substrate and two rivulets by the spanwise boundaries. Before these thinly-spaced rivulets can merge two more patches are encountered forcing the middle two rivulets to merge and increasing the wavelength as such that the other two rivulets enough space to grow independently.

Figure 5.11 (a) shows the case of a thin partially wetting patch located at the centre of the substrate, initially ahead of the advancing front; it is clear that as the flow evolves the front preferentially avoids this central section and flows onto the fully wetting region. This has two consequences; the first is an increase in film thickness around the edges of the low wetting patch, this causes an increase in the capillary ridge height of the rivulets adjacent to the patch creating an enhanced lengthening effect, the second is a repositioning of the rivulets whose edges overlap the patch as they are redirected, marginally, away from the patch. This change in trajectory can direct such a rivulet into the proximity of its neighbour, the two rivulets may then coalesce, a process that would have not occurred had the substrate remained uniformly homogeneous. In the contrasting case, when the wettability is reversed and the central patch is fully wetting, see Figure 5.11 (b), the rivulets preferably spread onto this region leading to faster and fuller coverage of the patch.

The configuration demonstrated in Figure 5.11 (c), is for the case of an advancing front that begins to evolve on a region of the substrate that is partially wetting before spreading onto one that is fully wetting there-on in. As the advancing front crosses onto the fully wetting region the rivulets widen. Rivulets that were sufficiently far apart beforehand now grow in closer proximity to one another and so merge. The number of rivulets on the fully wetting region in Figure 5.11 (c), once the merging processes are complete, is five; this represents a reduction from the corresponding partial wetting case where seven rivulets form. Interestingly, as shown in Figure 5.11 (d), if the advancing front develops on a fully wetting region before encountering an area of low wettability the rivulets do not increase/decrease in number as their wavelength remains above the critical wavelength λ_f - as shown in Chapter 4, wavelengths only increase due to merger, they do not decrease. The only alteration is in the shape; as seen previously, when spreading on a low wetting substrate the rivulets become much thinner.

The situations displayed in Figure 5.10 and 5.11 demonstrate how the rivulet pattern can be forced to be completely periodic and thus grow the maximum number of rivulets possible, similar to when the problem has a time-dependent inlet with a wavelength the same as λ_f - see Section 4.1.4. If the spacing between chemical heterogeneous areas is small then rivulets may be created that evolve close to one another which leads to their merger. The film preferentially spreads onto areas of high wettability, this results in the ability to direct the film into regions of choice; see in Figure 5.11 (a) where the low wetting stripe is mostly uncovered or Figure 5.11 (b) where the patch is highly wetting and so is preferentially covered.

Should a film spread and rivulets form on a partially wetting substrate, 5.11 (d) and 5.12 (b), initially before crossing onto a highly or fully wetting area then the rivulets relax and widen as they spread onto the fully wetting area. The associated critical wavelength, λ_f with the fully wetting region is larger than that associated with the low wetting area, see equation (4.2), therefore merger is observed between those rivulets evolving within this critical distance of each other. In the reverse

situation, Figure 5.12 (b), the wavelength does not decrease as the film crosses from a region of high wettability to low wettability as the associated λ_f decreases; the rivulets merely become thinner with larger capillary ridge heights at the tips and so lengthening is enhanced.

5.3 Summary

The approach taken for considering a planar inclined substrate is extended in this chapter to include a number of new features including the influence of surface tension gradients, substrate topography and chemical heterogeneities on rivulet formation.

A surface tension gradient applied across the film is incorporated into the lubrication approximation and shown to be able to either enhance or suppress the progress of rivulet formation. This can also delay or promote the onset of merger between two rivulets. If the film is thin enough, the Marangoni stresses may be large enough, if obeying equation (5.3), to force the liquid front to climb on a vertically aligned plane. Numerical results presented in this chapter agree well with the experimental observations of Cazabat *et al.* (1990) and exhibit the robustness of the method of formulation, via the lubrication approximation, and method of solution, adaptive multigrid, adopted to investigate thin film flows.

An approach to investigating rivulet flow on real surfaces was utilised by specifying the presence of substrate topographies in the form of mounds and trenches. These features were shown to influence the paths of the rivulets during formation by both deflection and enhancement via the known free-surface deformations that the topographies create. The surge that occurs after a trench topography was seen to create an enhancement of rivulet length after the advancing front has passed due to the increase in film thickness.

Finally, the effect that areas of differing wettability have on the advancing front

instability is uncovered. Such regions have a direct influence on the number of rivulets that form at the advancing front. The film front preferably flows down the area with highest wettability thus creating areas of relatively thick film compared to the film flowing over the low wetting areas. The patches of chemical heterogeneity can have a significant influence on the pattern that emerges by inducing merging between rivulets due to the small distance between evolving rivulets that can be enforced. This can also happen when the front moves from an area of low wettability to high wettability as the critical wavelength, as uncovered in Chapter 4, associated with the highly wetting region is larger than that of the low wetting region and so neighbouring rivulets merge until at or above the critical value. If the liquid then spreads back to an area of high wettability the wavelength will not decrease but continue at this larger value as the critical wavelength has decreased again. The number of rivulets may only decrease and not increase without physically inducing new rivulets through means of topography or patterned differing wetting patches.

Chapter 6

Rivulet flow on the surface of a vertically aligned cylinder

Contents

6.1	Background	124
6.2	Governing equations of rivulet flow on a vertically aligned cylinder	125
6.2.1	Cylindrical substrate LSA	127
6.3	Results : Three-dimensional numerical solutions	128
6.3.1	Fully wetting fluid	128
6.3.2	Partially wetting	138
6.3.3	Regime model for wavelength	147
6.3.4	Flow down the inner surface of a vertically aligned cylinder	148
6.4	Summary and Discussion	154

6.1 Background

Realistically, in industrial, medical and natural processes, substrates of interest are rarely flat planes. One complication that arises is the presence of topography or chemical heterogeneity as dealt with in Chapter 5, the other is where the shape of the substrate is non-planar and curved in one or more directions. In the context of lubrication theory and non-planar, curvy geometry, some attention has been given to free-surface flow on a arbitrarily curved substrate (Roy *et al.*, 2002) but much more emphasis has been placed on flow over a horizontally aligned cylinder, such investigatory reports can be found in Duffy and Wilson (1999), Evans *et al.* (2004), Takagi and Huppert (2010) and Leslie *et al.* (2011). In the work presented here, the affect that the geometry of a vertically aligned cylinder has on rivulet formation is explored.

The work presented in this chapter was inspired by a recent experimental study by Smolka and SeGall (2011) who investigated the flow of thin films down the outer surface of a vertically aligned cylinder. Comparisons with linear stability analysis of the governing equations, a first order long-wave approximation reminiscent of the equations of lubrication theory, were found to be favourable. The scenario is reminiscent of liquid coating a fibre, see for example Kalliadasis and Chang (1994) or Craster and Matar (2006), and the recent work of Takagi and Huppert (2010) who considered flow on a sphere and a horizontally aligned cylinder.

Full three-dimensional numerical solutions are generated for a range of cylinder radii using the parameters provided in Smolka and SeGall (2011). The disjoining pressure model is incorporated into the derivation of the governing equations, which differ from those presented in Chapter 2 due to the long-wave approach adopted, and used to compare the results obtained for a fully wetting fluid (silicone oil) and a partially wetting one (glycerin). The numerical solutions are also contrasted against a recent numerical study by Mayo *et al.* (2013), which appeared as this thesis was being written, who modelled the cylindrical case using the usual lubrication ap-

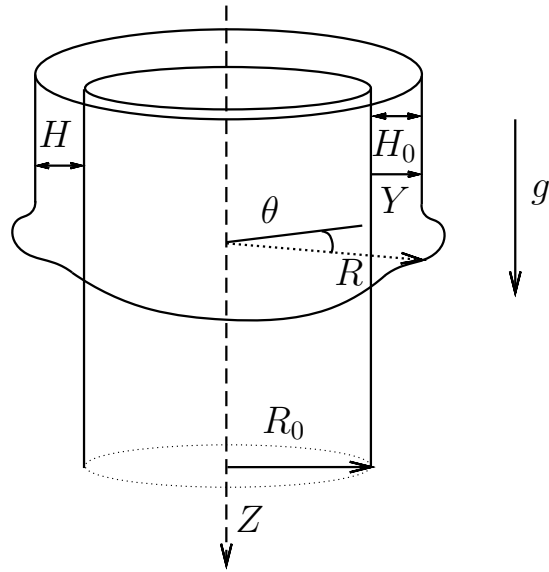


FIGURE 6.1: Schematic view of thin film flow down a vertically inclined cylinder (circumference, C_R and length, L_R). The film is fed by a constant inflow at the upstream boundary and H_0 denotes the asymptotic film thickness. The radius to any arbitrary point in the Y direction is denoted by R . Note: the film thickness is exaggerated for clarity.

proach; from their numerical data they concluded that the curvature of the substrate was an insignificant factor in the formation of rivulets and asserted that the flow behaved like that on an inverted, inclined substrate.

Furthermore, comparisons are drawn with the results of Chapter 4 and a regime model suggested to predict wavelength; the model also predicts the cut off parameters that determine when the curvature of the cylinder becomes negligible, and so the film acts as if on a vertical plane, and when the cylindrical surface area is so small that only one rivulet is formed.

6.2 Governing equations of rivulet flow on a vertically aligned cylinder

Consider the scenario of a thin film flowing down a smooth, vertically aligned cylinder of radius R_0 and height L_R , as shown schematically in Figures 6.1 and 6.2. The

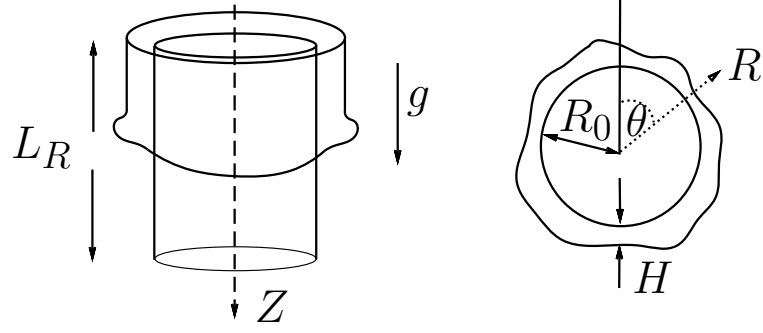


FIGURE 6.2: Schematic view, three-dimensional (left) and cross-sectional (right), of thin film flow down a vertical cylinder (circumference, C_R and length, L_R). The film is fed by a constant inflow at the upstream boundary and H_0 denotes the asymptotic film thickness.

Note: the film thickness height has been exaggerated for the sake of clarity.

circumference of the cylinder is denoted by $C_R = 2\pi R_0$. The film is fed by a constant inflow at the upstream boundary and the fully developed film thickness is denoted by H_0 . Surface tension, σ , dynamic viscosity, μ , and density, ρ , are considered to be constant.

By scaling the film thickness by H_0 and substrate dimensions by R_0 , introducing the non-dimensional variables into the cylindrical Navier-Stokes and continuity equations, as well as boundary conditions (2.3)-(2.6) together with the assumption that $\epsilon_R = H_0/R_0 \ll 1$, then the governing lubrication equations for the cylindrical flow are:

$$(1 + \epsilon_R h) \frac{\partial h}{\partial t} = \frac{\partial}{\partial z} \left[\frac{\epsilon_R h^3}{3} \left(\frac{\partial p}{\partial z} - \frac{1}{\epsilon_R} - h \right) \right] + \frac{\partial}{\partial \theta} \left[\frac{\epsilon_R h^3}{3} \left(\frac{\partial p}{\partial \theta} \right) \right], \quad (6.1)$$

$$p = -\frac{1}{Bo_R} (h + \nabla^2 h) - \Pi(h), \quad (6.2)$$

where $Bo_R = \rho g R_0^2 / \sigma$ is the Bond number, ∇ is $(\frac{\partial}{\partial \theta}, \frac{\partial}{\partial z})$ and the non-dimensional disjoining pressure, denoted by $\Pi(h)$, in this case is given by:

$$\Pi(h) = \frac{(1 - \cos \theta_c) (n - 1) (m - 1)}{\epsilon_R^2 Bo_R h^* (n - m)} \left[\left(\frac{h^*}{h} \right)^n - \left(\frac{h^*}{h} \right)^m \right]. \quad (6.3)$$

Terms without analogous forms in equations (2.23) and (2.24) represent conservation of mass across the cross-sectional area of an angular ring. The spanwise computational boundary conditions accounting for the nature of the problem are taken as being periodic.

A more comprehensive derivation of the above is provided in Appendix B.

6.2.1 Cylindrical substrate LSA

A similar method to that used for the planar case enables the LSA equations for an advancing front on a vertically aligned cylinder to be obtained. The fourth order equation for a perturbation h_1 of the solution is:

$$(1 + \epsilon_R h_0) \frac{\partial h_1(\xi, k, t)}{\partial t} = \left(h_0^2 h_1 p_{0\xi} + \frac{h_0^3}{3} p_{1\xi} \right)_\xi - \frac{1}{3} (3h_0^2 h_1 + 4\epsilon_R h_0^3 h_1)_\xi + [U_w (1 + \epsilon_R h_0) h_1]_\xi + \frac{\epsilon_R k^2}{3B_{OR}} [(1 + k^2) h_0^3 h_1 + 2h_0^3 h_{1\xi\xi} + 3h_0^2 h_{1\xi}], \quad (6.4)$$

which is solved as in the planar case, see Section 2.1.6 of Chapter 2. In the cylinder case the wave speed is given by:

$$U_w = \frac{1 + h^* + h^{*2} + \epsilon_R (1 + h^* + h^{*2} + h^{*3})}{3 \left(1 + \frac{\epsilon_R}{2} + \frac{\epsilon_R h^*}{2} \right)}, \quad (6.5)$$

where $\xi = z - U_w t$.

Appendix C provides a thorough derivation of the LSA equations for both the planar and cylindrical case.

6.3 Results : Three-dimensional numerical solutions

6.3.1 Fully wetting fluid

Results are generated using two films of differing fluid properties taken from Smolka and SeGall (2011). The fully wetting liquid is a silicone oil, density 986 kg m^{-3} and surface tension 0.0219 Pa m ; the partially wetting liquid is glycerin, density 1260 kg m^{-3} and surface tension 0.0584 Pa m . The contact angle for glycerin, although not reported, is estimated, using the results within their paper and the findings in Chapter 4, to be approximately 40° giving S_{θ_c} as 2.35. Other contact angles may be used for comparison purposes, clearly stated for all of the cases considered. The film thickness, H_0 , is taken to be 0.085 cm as reported in the same set of experiments (Smolka and SeGall, 2011). The inflow rate is kept constant for all radii of cylinder employed.

Since the spanwise boundaries are clearly periodic, the computational boundary conditions are written appropriately to include the continuous nature of the geometry.

A fully wetting film coating the surface of a vertically aligned cylinder is considered first. In Figure 6.3 and 6.4 the progress of a thin silicone oil film spreading on a cylinder of radius 1.27 cm is revealed. The rivulets emerge to form a near periodic pattern at the advancing front and grow length wise as time progresses.

Figure 6.5 shows a number of free-surface colour maps in the form of an unfolded cylinder for ease of interpretation, L_θ denotes the distance around the circumference calculated as $L_\theta = \theta R_0$. Their three-dimensional counterparts are shown in Figure 6.6 for visualisation purposes. As is clear, as the radius, and so circumference, of the cylinder increases so does the number of rivulets that may form on the surface as would be expected intuitively. If the circumference is small enough only one rivulet forms, see Figure 6.6 (d), due to the restriction of the surface area compared to the width of the rivulet. If two rivulets were to form in the confined space then

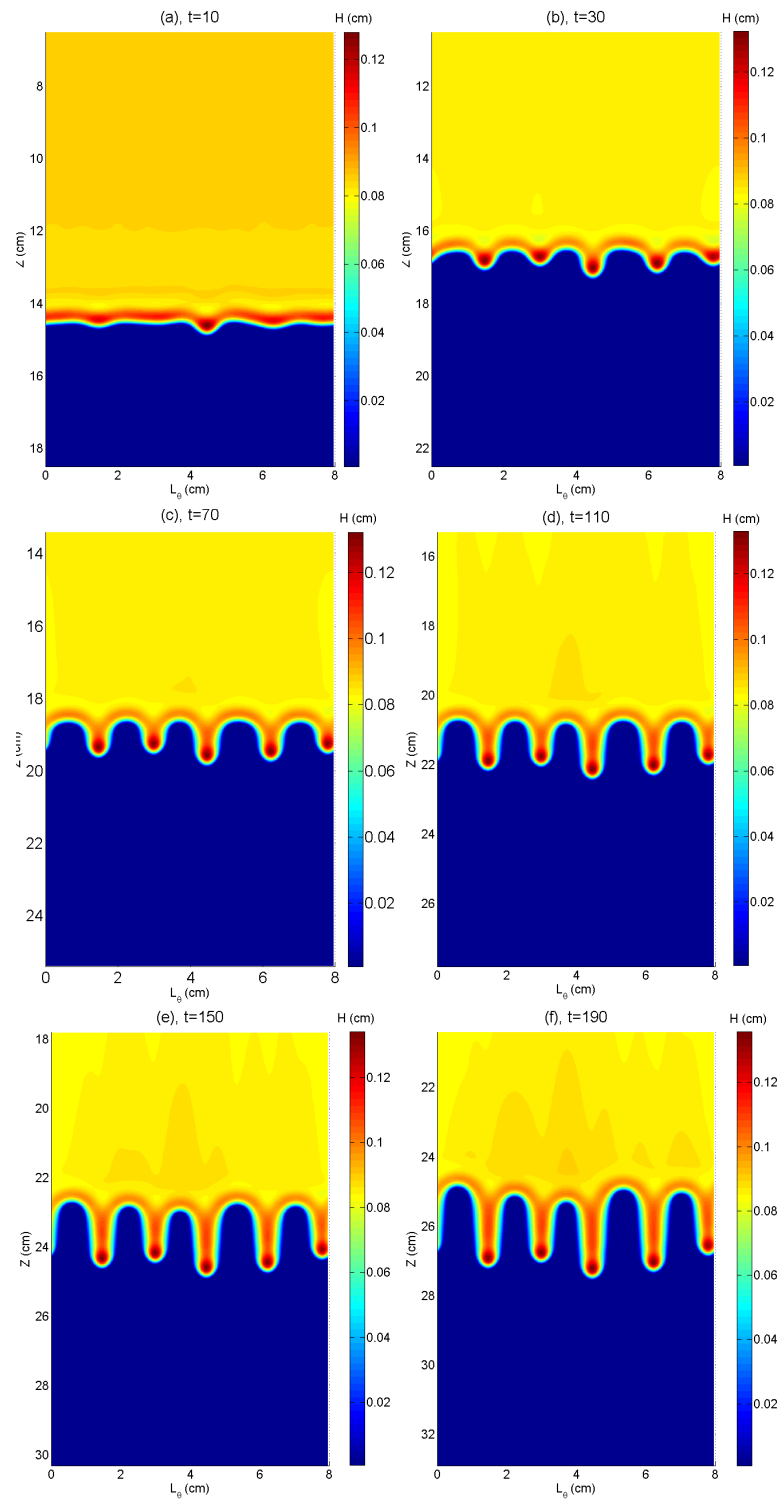


FIGURE 6.3: Unfolded free-surface colour maps showing rivulet formation at the advancing front of a film of fully wetting silicone oil on the outside surface of a cylinder with radius 1.27cm.

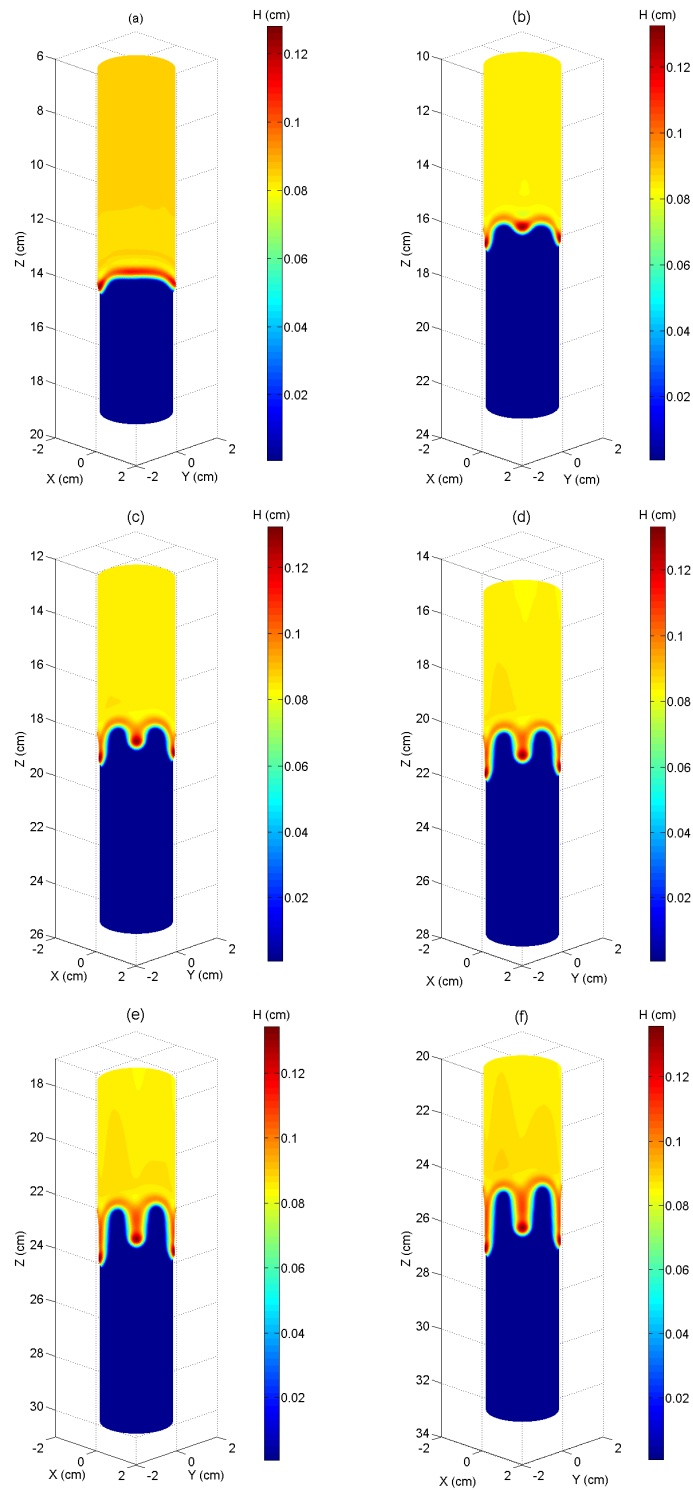


FIGURE 6.4: Free-surface colour maps showing rivulet formation at the advancing front of a film of fully wetting silicone oil spreading down the outside surface of a cylinder of radius 1.27cm plotted on a three-dimensional representation of the cylinder.

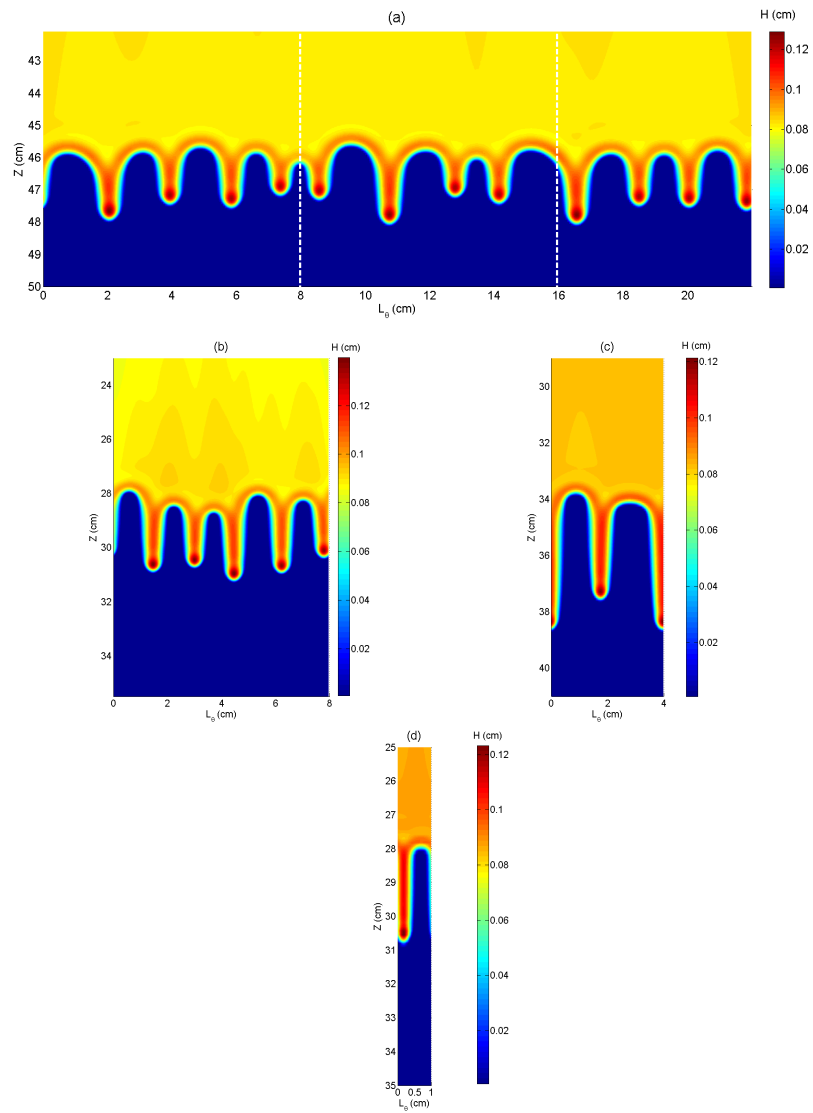


FIGURE 6.5: Unfolded free-surface colour maps - a three-dimensional representation - for the flow of silicone oil down the surface of a cylinder with four different radii; (a) 3.5cm, (b) 1.27cm, (c) 0.635cm and (d) 0.159cm. C.f. Figure 6.4.

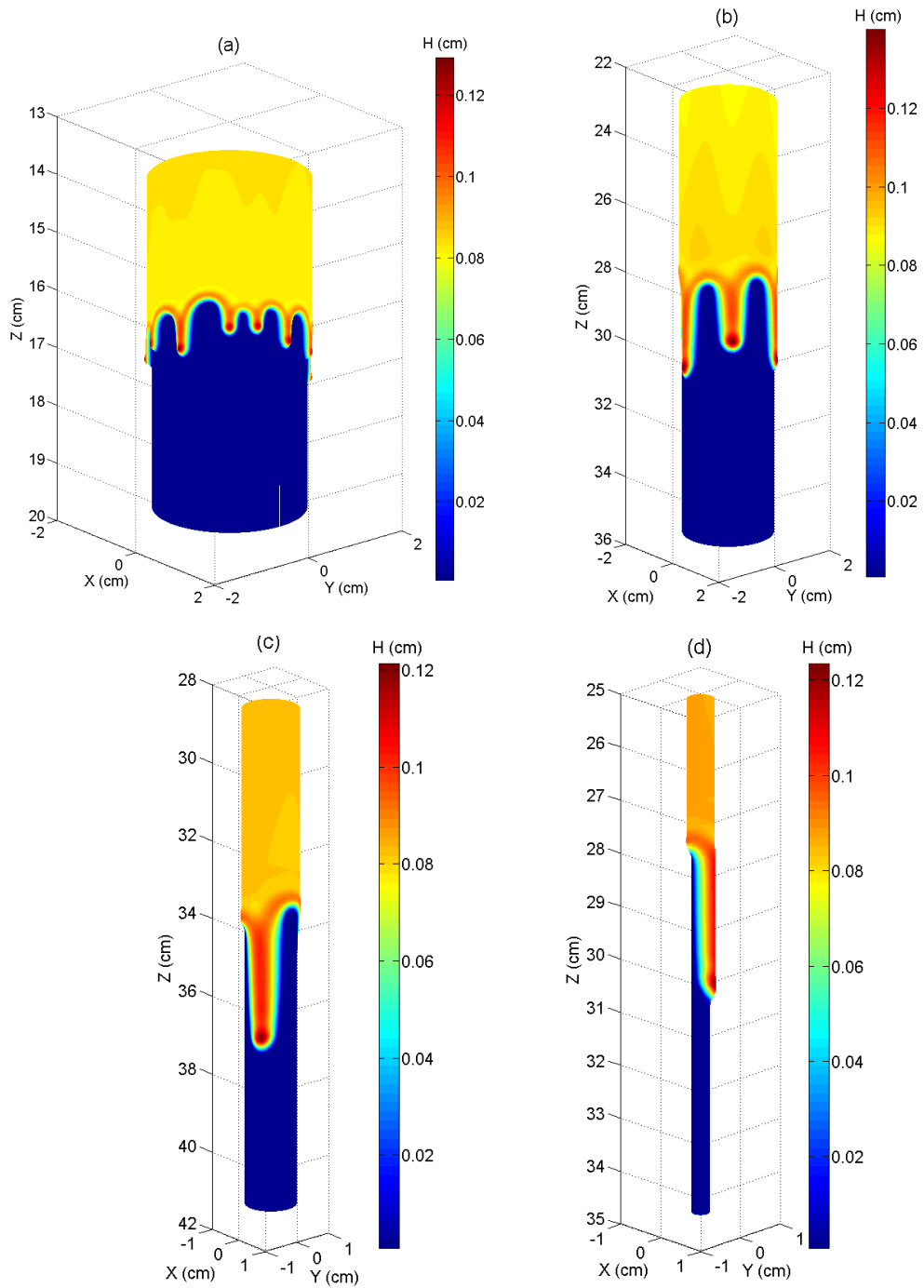


FIGURE 6.6: Free-surface colour maps of Figure 6.5 transferred onto the corresponding cylinder for visualisation purposes.

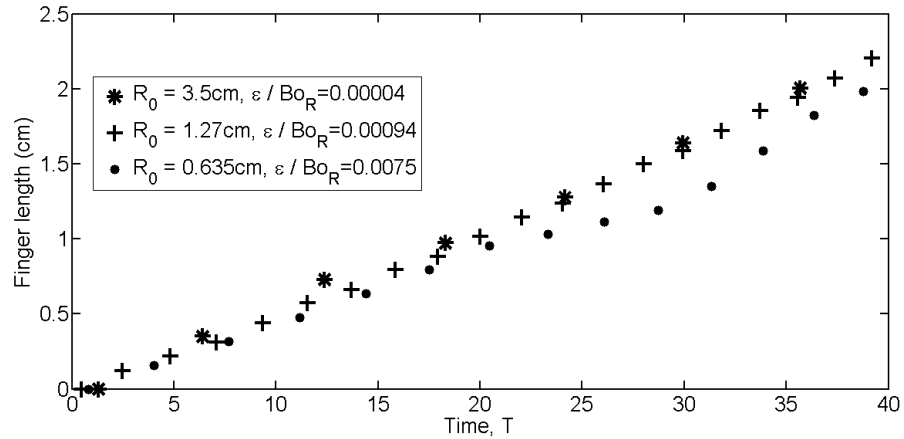


FIGURE 6.7: This figure shows dimensional rivulet length against scaled time for flow on three different cylinders with radii $R_0 = 3.5, 1.27,$ and 0.635cm .

they would interact with one another and merge together to form a single rivulet.

The change in length of the rivulets is showcased in Figure 6.7 where the dimensional length of the fingers is shown for $R_0 = 3.5, 1.27$ and 0.635cm against time T . The finger lengths stay reasonably consistent for all time for the range of R_0 shown, this suggests that the curvature of the cylinder plays only a minor role with respect to the inhibition of the lengthening of the rivulets.

As the curvature increases the rivulets ‘wrap’ around the cylinder, that is become wider with respect to θ or cover a more significant proportion of the cylinder circumference; this can be seen in the cylinder plot in Figure 6.6. For the largest radius the rivulets that form look like those on a flat plane. When growing on the smallest radius it is observed that the rivulet covers half the circumference of the cylinder. The surface tension of the fluid keeps the width of the rivulet consistent across the cylinders. The capillary ridge height decreases slightly at smaller radii due to the smaller wavelength meaning that the flux feeding each rivulet decreases slightly.

Although not immediately apparent from Figure 6.5 & 6.6, the cylindrical geometry has a subtle influence on the wavelength of the pattern that emerges. The wavelength associated with the maximum number of rivulets that may grow on the cylinder surface is not always the wavelength that appears due to non-linearity and

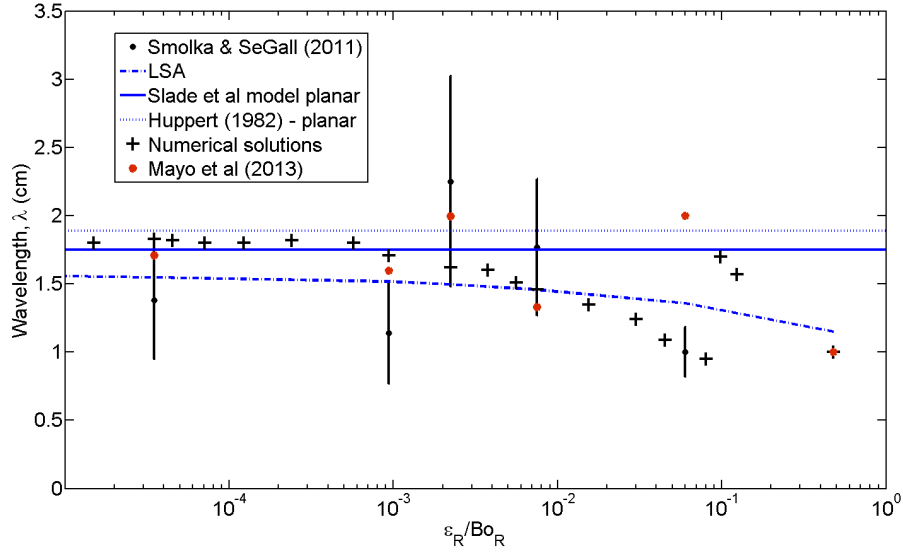


FIGURE 6.8: Wavelength of the rivulet pattern that emerges at the advancing front of a silicone oil film. Also plotted are the findings of Huppert (Huppert, 1982) and the current author for predicting the wavelength on a vertically inclined plane. Experimental data points for silicone oil of Smolka and SeGall (Smolka and SeGall, 2011) are also provided.

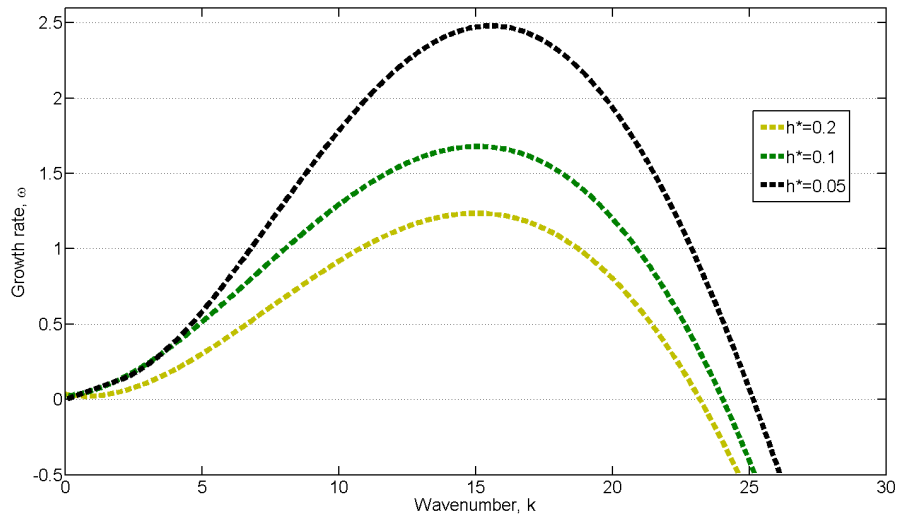


FIGURE 6.9: Results of linear stability analysis for flow of silicone oil coating a cylinder of radius 3.81cm performed for different values of precursor film thickness, h^* .

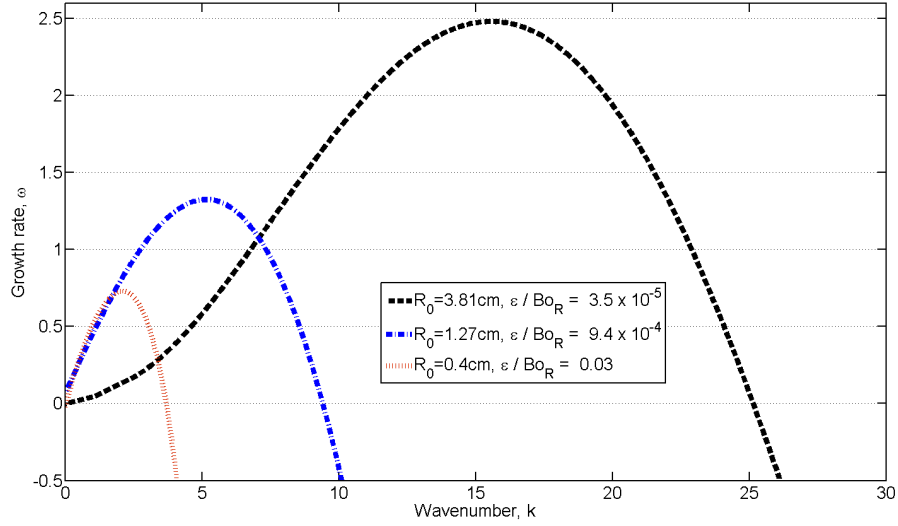


FIGURE 6.10: Results of linear stability analysis for flow of silicone oil coating a cylinder of radius 3.81cm and 1.27cm, the values of ϵ/Bo_R are indicated on the figure.

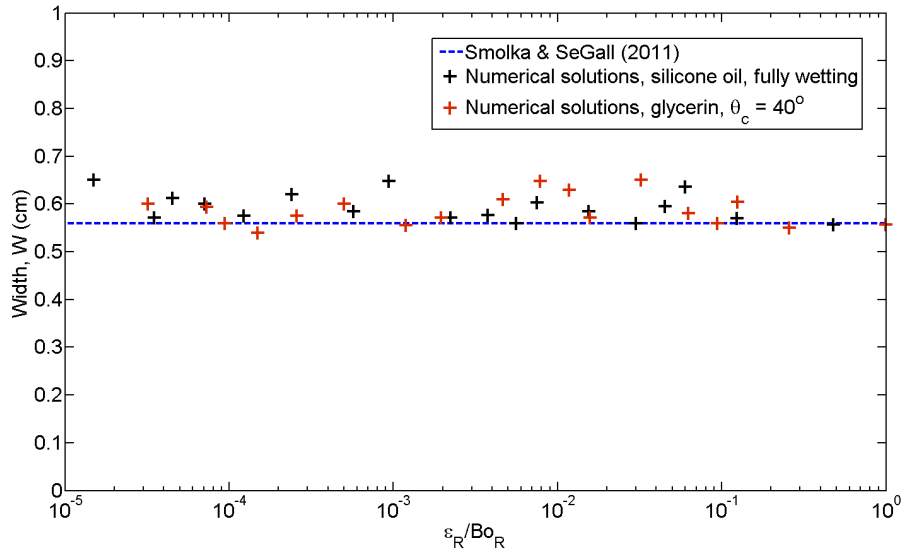


FIGURE 6.11: The average width of the rivulets for a range of ϵ_R/Bo_R plotted with the experimental value of Smolka and SeGall (2011). Results here are for silicone oil (fully wetting) and glycerin (partially wetting, $S_{\theta_c} = 2.35$).

the random perturbations applied at the contact line. The wavelength reported here is the averaged wavelength over the rivulet pattern for a number of simulations; this is done due to the random nature of the emerging instability meaning the number of rivulets is not always the same. This observation is also seen within experiments and can be explained by the interaction and amalgamation of rivulets that grow within close proximity of one another. Figure 6.8 shows the wavelength, λ , of the rivulet pattern emerging at the advancing front of a silicone oil film for a range of cylinder radii. Also plotted is the prediction for the analogous scenario on a vertically inclined plane calculated from the results of Huppert (1982) (as interpreted by Troian *et al.* (1989)), $22H_0/(6Ca)^{1/3}$ and equation (6.6), $20H_0/(6Ca)^{0.4}$. The wavelength is compared against the value of ϵ_R/Bo_R as this is a measure of the importance of the curvature in the governing equations; a co-efficient analogous to the gravitational parameter in the planar case - $N = Ca^{1/3} \cot \alpha$ (Gaskell, Jimack, Sellier, Thompson and Wilson, 2004) - that measures the relative importance of the gravitational component. The results here are consistent with the observations of Smolka and SeGall, following a similar trend, see Figure 6.8.

Below a certain critical value of ϵ_R/Bo_R the wavelength that emerges is consistent with that observed on a flat plane, this value is approximately $crit_\theta = 5 \times 10^{-3}$ or $\hat{R} = 12.6$ where $\hat{R} = (\rho g / \sigma H_0)^{1/3}$ is the scaled radius as defined by Mayo *et al.* Mayo *et al.* (2013). The value reported in Mayo *et al.* (2013) is $\hat{R} = 2.56$, a smaller value, indicating that the cylinder must be much smaller before curvature effects influence rivulet formation. Above the critical value, $crit_\theta$, the wavelength decreases as the value of ϵ_R/Bo_R increases. This effect of curvature is demonstrated in Figure 6.5 (a); the white dashed line indicates the circumference of a 1.27cm radius cylinder which is 7.98cm. The number of rivulets that grow per 7.98cm is four in the larger radius ($R_0 = 3.5\text{cm}$) case, whereas in the 1.27cm radius cylinder case five rivulets grow per 7.98cm. As the radius decreases the circumference of the cylinder becomes a counter-acting restrictive factor on the number of rivulets formed, when the circumference is sufficiently small only one rivulet can develop

- this happens at $\epsilon_R/B_{OR} \approx 0.06$ or $\hat{R} = 2.55$ (the value in Mayo *et al.* (2013) was given as 3.05). Due to the random nature of the initial condition in some cases although more than one rivulet may grow only one emerges and survives at longer times due to enforced merger of the neighbouring rivulets. The critical value of cylinder circumference below which only one rivulet may grow occurs approximately when $C_R \lesssim 3W_r$, where W_r is the width of the rivulet.

A majority of work in the area of thin films considers linear stability analysis, see for instance Troian *et al.* (1989); Bertozzi and Brenner (1997). For comparison a linear stability analysis is performed with the highest growing wavenumber used to calculate the predicted wavelength that will appear. Smolka and SeGall found reasonable agreement between linear stability and experiments. A sample of stability curves is plotted in Figure 6.9 for different values of the precursor film. As the precursor film thickness decreases the most unstable wavenumber does not change but the growth rate increases, a result first reported by Bertozzi and Brenner (1997) for flow on a planar substrate. As the radius of the cylinder decreases so does the band of unstable wavenumbers and growth rates, see Figure 6.10. The predicted wavelength from LSA is plotted in Figure 6.8 and matches reasonably well with both the numerical solutions and experiments. The under prediction at low values of ϵ/B_{OR} is due to the fact that LSA cannot take into account interactions and merging between rivulets which increases the wavelength. At larger values of ϵ/B_{OR} the stability calculations also does not take into account the restrictive size of the geometry circumference and so under predicts somewhat the wavelength. It also of note that in reality it is not necessarily just the most unstable wavelength that becomes evident but an interplay between unstable modes which is why the pattern observed is not exactly periodic.

The width of the rivulets, W_r , stays consistent for the range of cylinders investigated here. There is some variation in width due to the non-periodic nature of the pattern leading to varying degrees of flux feeding each rivulet, which also partly accounts for rivulets of different length, but the results match well with the value reported by

Smolka and SeGall (2011) which is also plotted.

6.3.2 Partially wetting

When a contact angle, θ_c , greater than zero is introduced into the problem, representing the case of partial wetting, the value of the disjoining pressure $\Pi(h)$ becomes non-zero. A partially wetting fluid compared to a fully wetting one is known to alter some of the observations at an advancing front (Silvi and Dussan, 1985). As in the case of rivulet formation on an inclined plane it is convenient to consider things in terms of a ‘non-dimensional spreading coefficient’, $S_{\theta_c} = 6(6Ca)^{-2/3}(1 - \cos\theta_c)$ where Ca is the capillary number of the flow. In Chapter 4 it was found that the long-time wavelength of the rivulet pattern on an inclined plane, λ_f for a partially wetting fluid could be expressed as and well represented by:

$$\lambda_f = \frac{20H_0}{(6Ca)^{0.4}} - 1.51H_0S_{\theta_c}. \quad (6.6)$$

The progress of a glycerin film coating a cylinder of radius $R_0 = 0.953\text{cm}$ is shown as unfolded colour maps of the free-surface in Figure 6.12 (the three-dimensional visualisations of the same are shown in Figure 6.13). The rivulets evolve in a near periodic pattern with very straight-edges. The differences in flow pattern evolution for fluids of different wettability can be observed in Figure 6.14 where results for contact angles of 0° , 20° and 40° are shown (that is $S_{\theta_c} = 0.0, 0.6$ and 2.35); the radius of the cylinder in this case being 0.953cm . As the contact angle, and so S_{θ_c} , increases so does the magnitude of the effect on the rivulet formation process, the rivulets becoming thinner and more straight edged. Due to a decrease in their width the number of rivulets increases with a corresponding decrease in the wavelength. Another feature of note is the increase in elongation with S_{θ_c} , the bulk of the fluid spreads at a slower rate but the rivulets extend at a faster one which is associated with the observed increase in capillary ridge height. This is demonstrated clearly in Figure 6.16. The finger length increases at a much greater rate as S_{θ_c} increases.

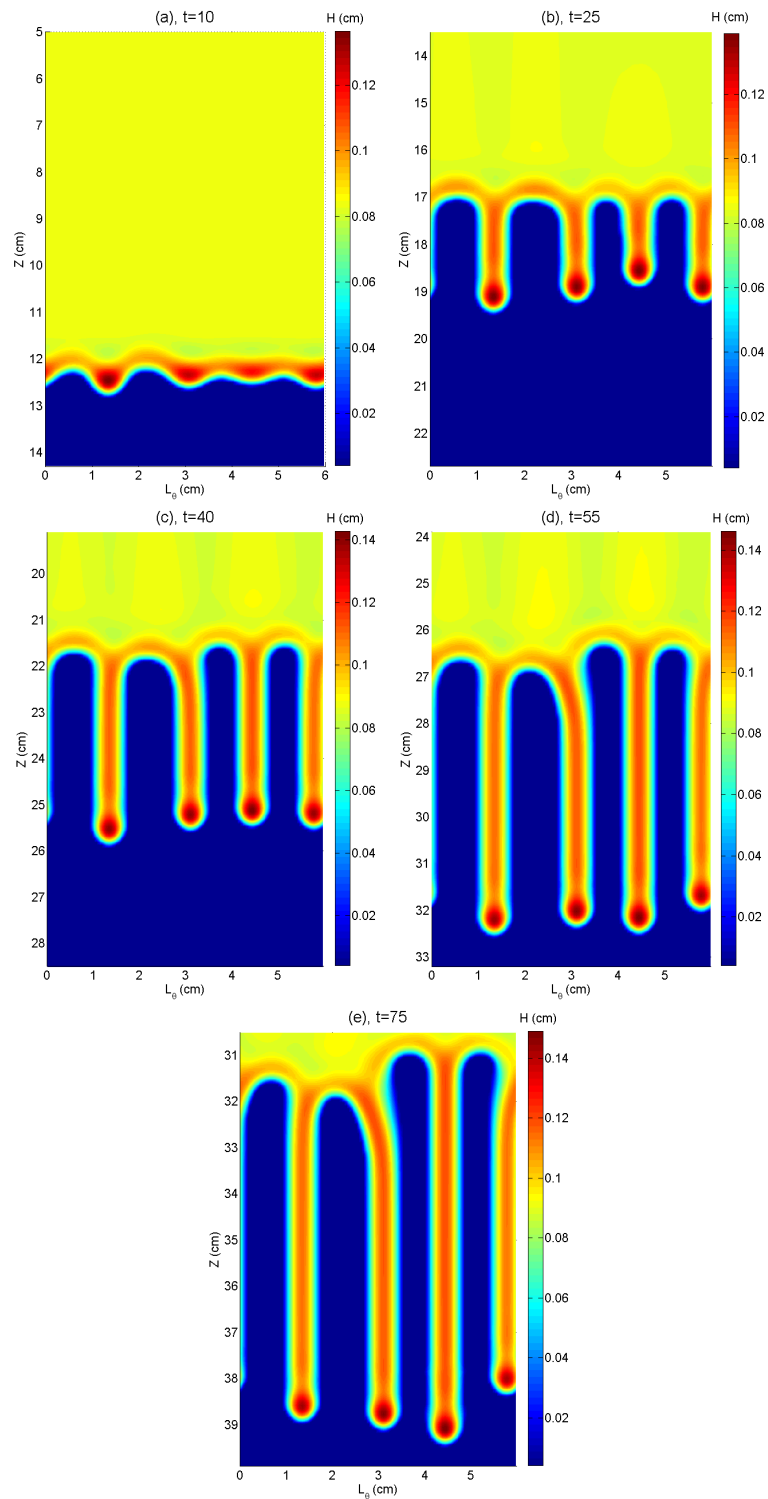


FIGURE 6.12: Unfolded free-surface colour maps visualising the formation of rivulets at the contact line of a glycerin film flowing down the outer surface of a cylinder with radius 0.953cm plotted on a three-dimensional cylinder with $S_{\theta_c} = 2.35$ ($\theta_c = 40^\circ$).

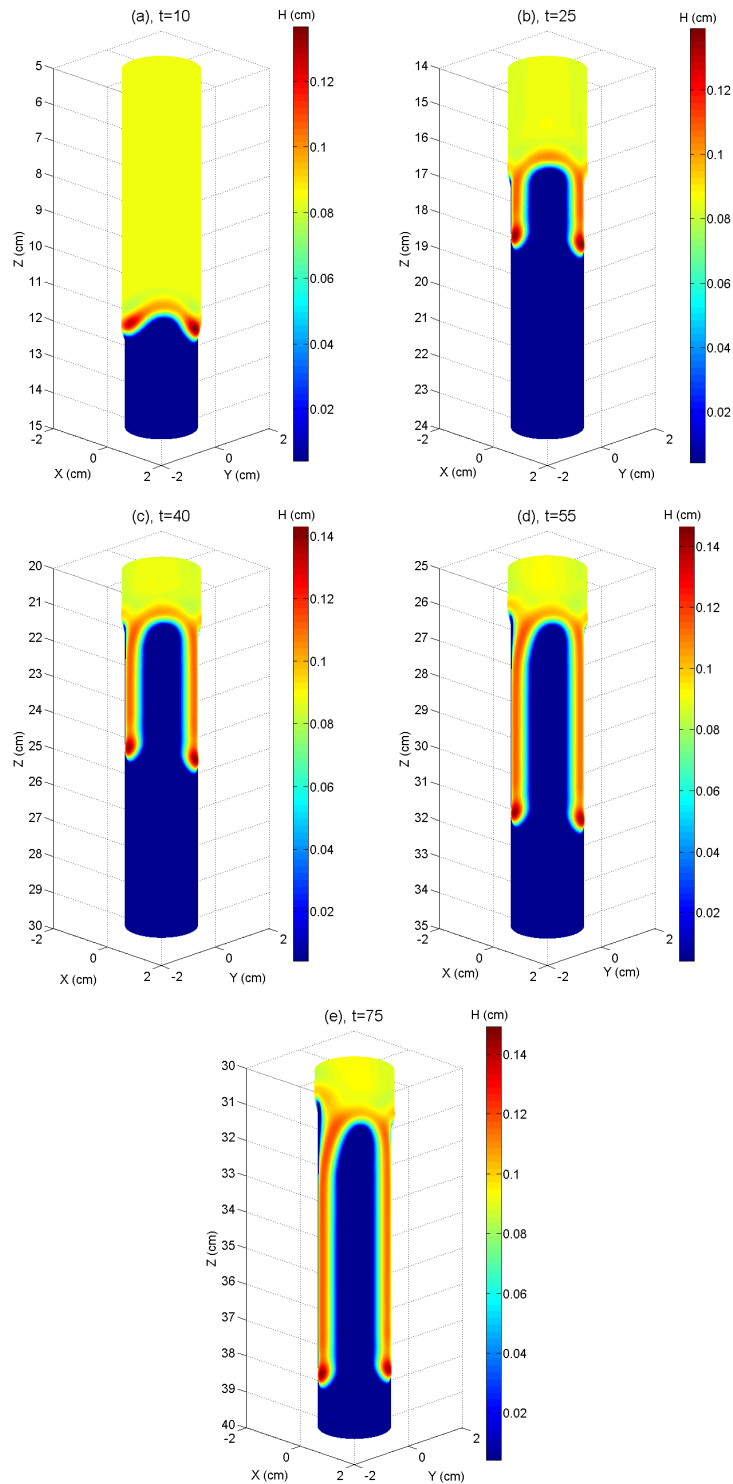


FIGURE 6.13: Free-surface colour maps visualising the formation of rivulets at the contact line of a glycerin film flowing down the outer surface of a cylinder with radius 0.953cm plotted on a three-dimensional cylinder with $S_{\theta_c} = 2.35$ ($\theta_c = 40^\circ$). Plotted on the cylinder to visualise the reality of the flow.

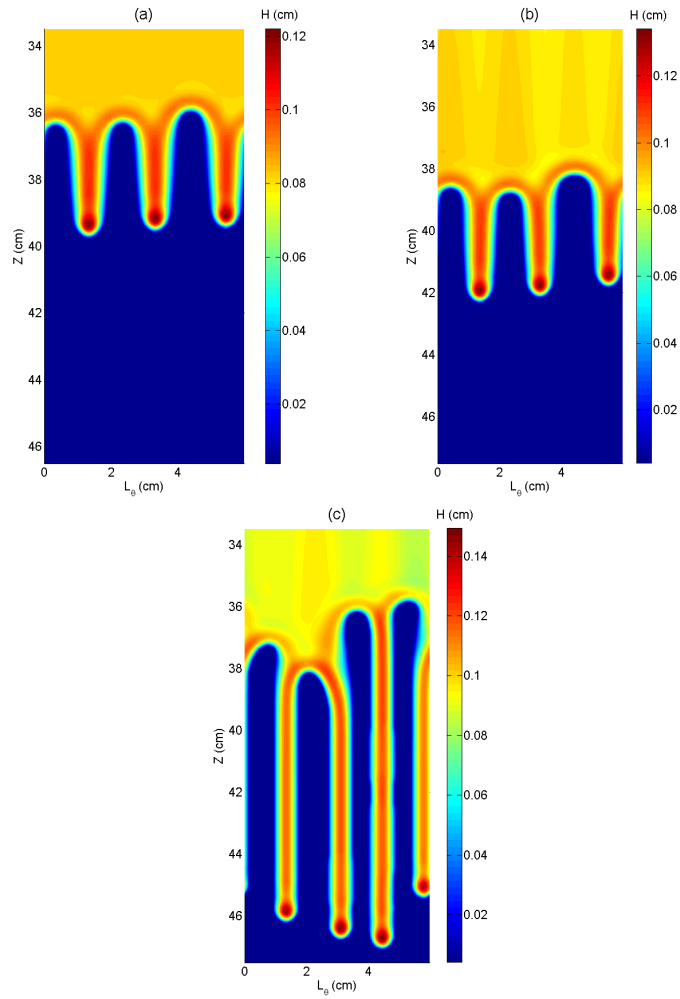


FIGURE 6.14: Unfolded free-surface colour maps for the flow of glycerin down the surface of a cylinder with radius 0.953cm plotted on a three-dimensional cylinder. The flows are identical except for the contact angle. The range of spreading coefficient is $S_{\theta_c} =$ (a) 0.0, (b) 0.61 and (c) 2.35, corresponding to $\theta_c = 0^\circ, 20^\circ$ and 40° .

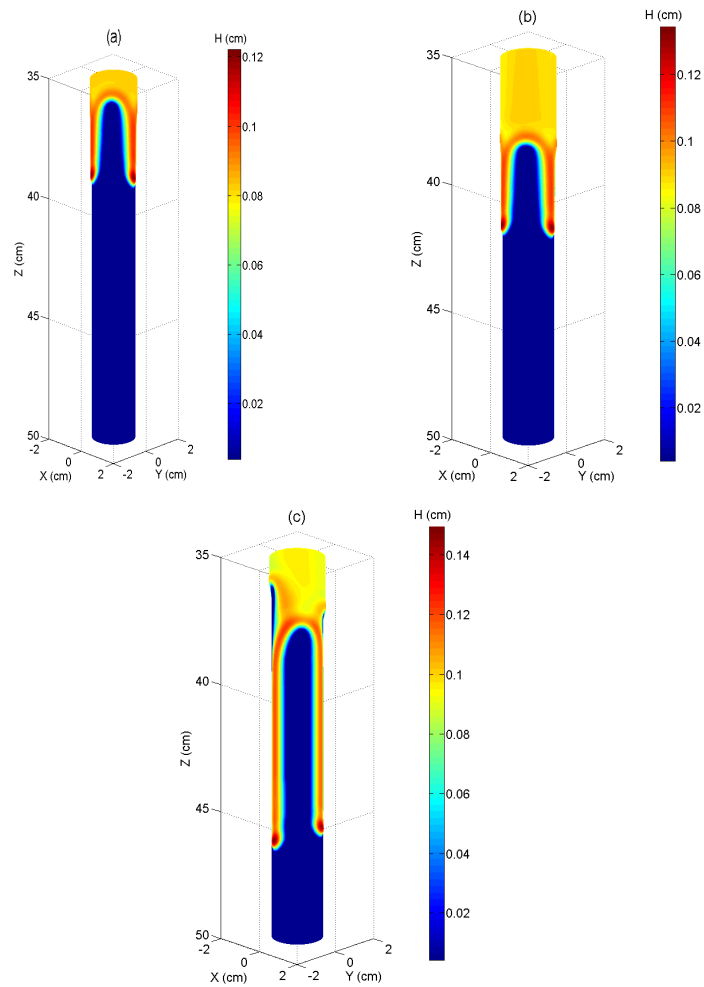


FIGURE 6.15: Free-surface colour maps for the flow of glycerin down the surface of a cylinder with radius 0.953cm plotted on a three-dimensional cylinder. The flows are identical except for the contact angle. The range of spreading coefficient is $S_{\theta_c} =$ (a) 0.0, (b) 0.61 and (c) 2.35, corresponding to $\theta_c = 0^\circ$, 20° and 40° . Flows plotted on the cylinder.

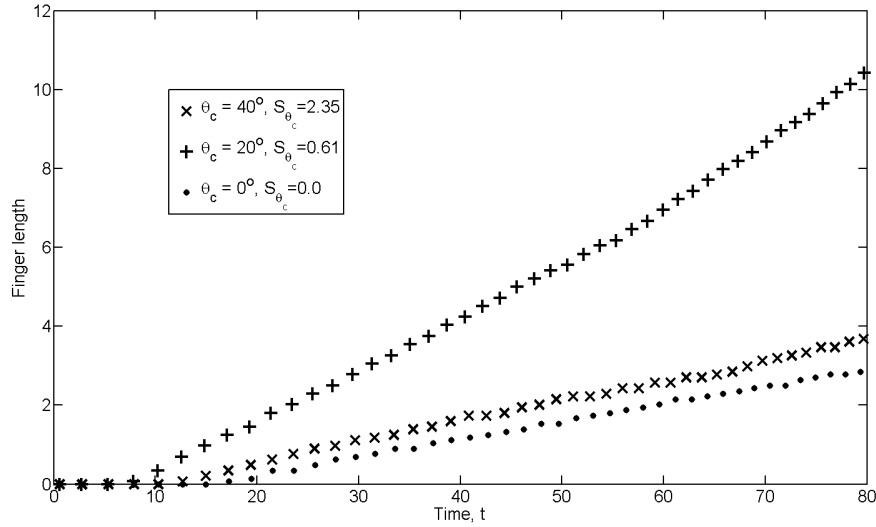


FIGURE 6.16: Rivulet length against time for glycerin coating a cylinder of radius 0.953cm. Four different non-dimensional spreading coefficients are compared with one fully wetting and two partially wetting films - $S_{\theta_c} = 0.0, 0.61, \text{ and } 2.35$.

As the cylinder radius is decreased, as in Figures 6.17 and 6.18, with $S_{\theta_c} = 2.35$, the results obtained for the case of a fully wetting fluid, section 6.3.1, hold true for a partially wetting one. The wavelength of rivulets for the flow of a glycerin film over a range of cylinders of different radius is shown in Figure 6.19 for both $S_{\theta_c} = 0.0$ and $S_{\theta_c} = 2.35$. Also plotted are the predictions for wavelength on an inclined plane as given by equation (4.2). The critical value of ϵ/BOR at which the wavelength becomes that for the equivalent planar case appears to be the same in both the fully wetting and partially wetting case having a value of approximately 5×10^{-3} . However, as the width of the rivulets is greater for a fully wetting fluid, the critical value, $crit_{\theta}$, of ϵ/BOR at which only one rivulet can grow is shifted to a larger one, that is a smaller value of R_0 , for the partially wetting case - for the fully wetting case the critical value is $\epsilon_R/BOR \approx 0.06$ or $\hat{R} \approx 2.55$, and in the partially wetting case $\epsilon_R/BOR \approx 0.1$ or $\hat{R} \approx 2.15$. This is because the transition to a single rivulet is dictated by the circumference of the geometry, C_R , and less dependent on the curvature or the value of ϵ_R/BOR .

The wavelength results correspond well to the experimental values reported by Smolka and SeGall (2011). Mayo *et al.* (2013) also attempted to assess the crit-

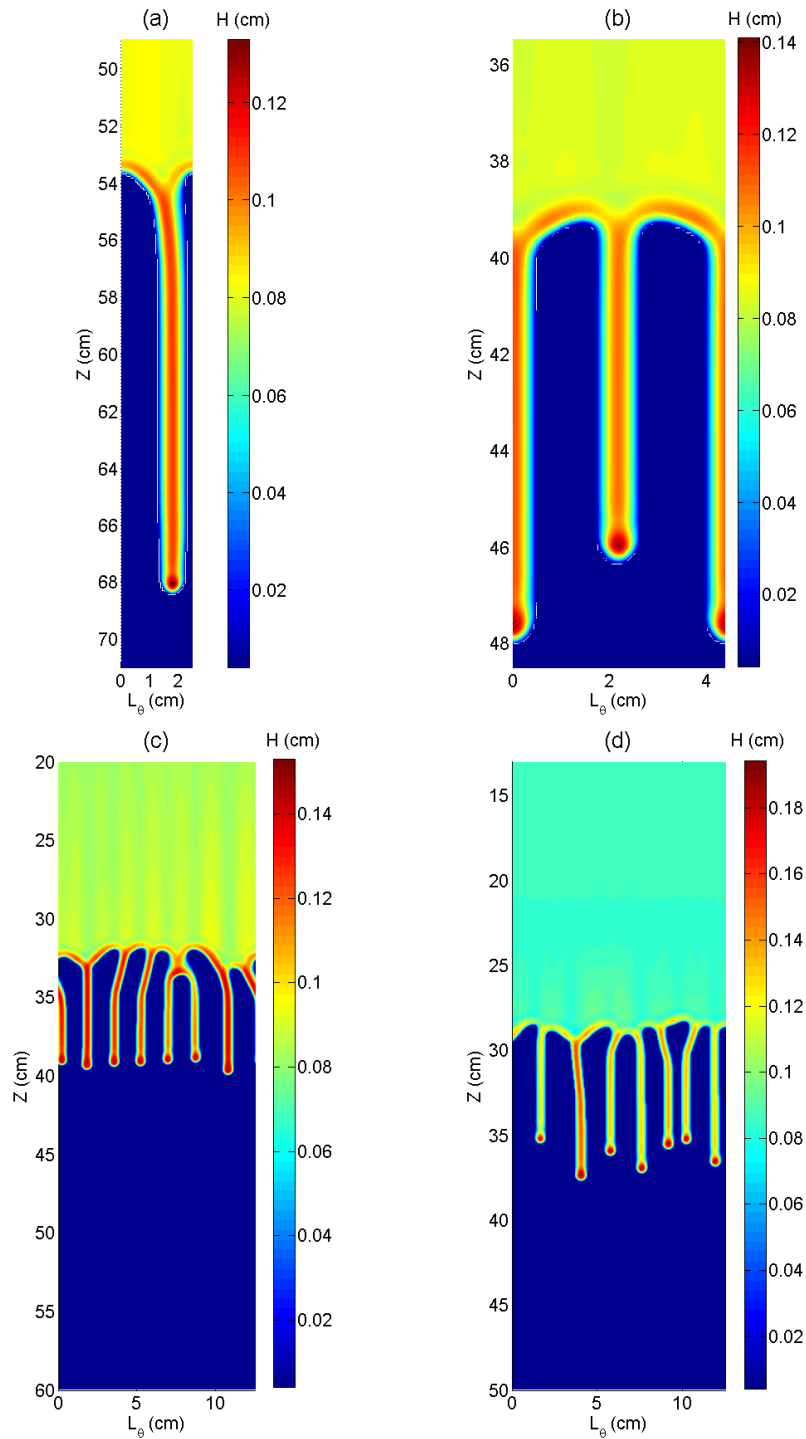


FIGURE 6.17: Unfolded free-surface visualisations of glycerin coating a cylinder with varying radii but constant contact angle, 40° and $S_{\theta_c} = 2.35$. The four radii shown are (a) 0.4cm, (b) 0.7cm, (c) 2cm and (d) 2.5cm respectively.

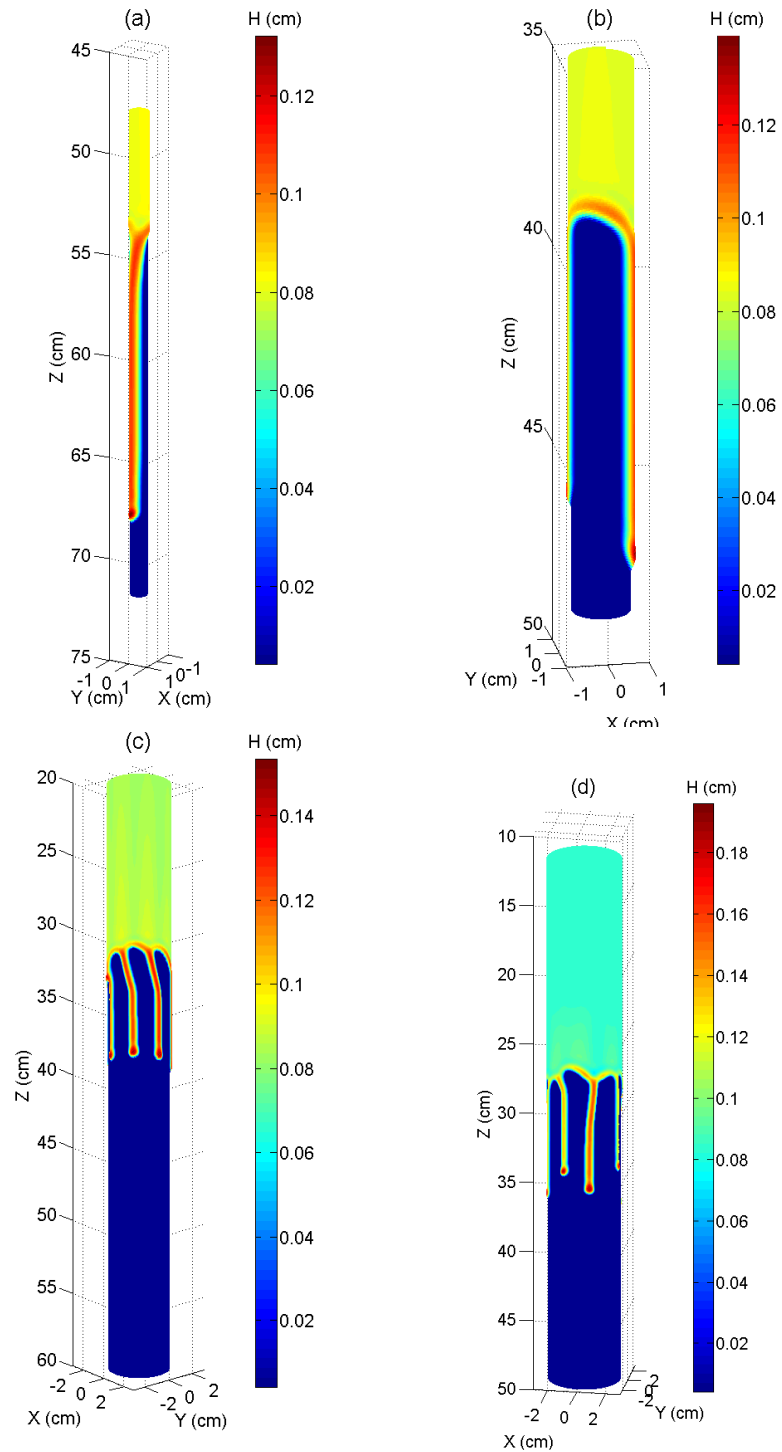


FIGURE 6.18: Free-surface visualisations of glycerin coating a cylinder with varying radii but constant contact angle, 40° and $S_{\theta_c} = 2.35$. The four radii shown are (a) 0.4cm, (b) 0.7cm, (c) 2cm and (d) 2.5cm respectively.

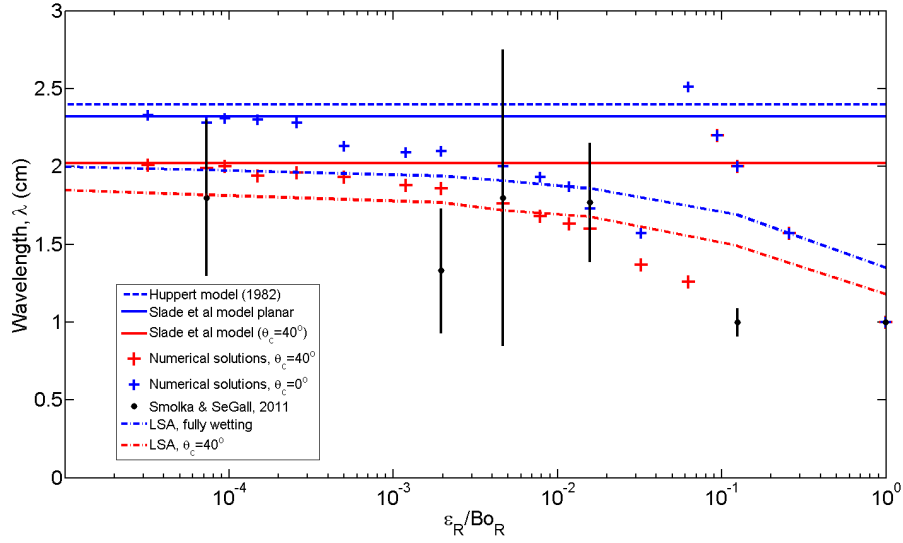


FIGURE 6.19: Wavelength of the rivulet pattern that emerges at the advancing front of a glycerin film. Also plotted are the findings of Huppert (1982) and the current author for predicting the wavelength on a vertically inclined plane. Experimental data points for silicone oil of Smolka and SeGall (2011) are also provided.

ical values where curvature and circumference became important influences; their findings do not correlate with those obtained here. The value of $crit_\theta$ they obtained was larger than their value for a single rivulet to form, i.e. curvature only becomes important once only a single rivulet is able to evolve. Their critical value above which only one rivulet can form is also much smaller (at much larger radii) than the one obtained in the current study. The differences in the reported results here and those of Mayo *et al.* (2013) can be explained by the different approaches adopted in formulating the governing equations; in the case here the equations contain higher order terms that capture the curvature effects - these are discarded in Mayo *et al.* (2013). The random nature of the initial condition and the averaging calculation used to determine the wavelength may also account for disparities in both sets of reported data.

The predicted width of the rivulets for a glycerin film with $S_{\theta_c} = 2.35$ (estimated to be approximately the physically representative value) are in reasonable agreement with the value of Smolka and SeGall (2011), see Figure 6.11. As the curvature effects increase the surface tension forces at play are strong enough to resist spreading

around the circumference of the cylinder and creating a wider rivulet.

6.3.3 Regime model for wavelength

From the results presented thus far it is evident that there are three regimes in which the instability, that manifests as rivulets at the advancing front of a thin film, evolves. There is the planar regime where the curvature of the cylinder has little effect on the formation and growth of the rivulets and the wavelength is identical to that for the equivalent flow on a planar surface. The critical value of ϵ_R/Bo_R at which there is a transition to the next regime, $crit_\theta$, appears to be constant in all cases. This is because below this value indicates when the importance of the extra terms that appear in the governing equations due to the geometric effect of the substrate becomes negligible, this critical value is found to be $crit_\theta = \epsilon_R/Bo_R \approx 0.0005$.

For values of ϵ_R/Bo_R above C_{crit_p} the curvature of the geometry becomes an influencing factor. The regime where the wavelength of the emerging pattern is smaller than that seen on an inclined plane is named the cylinder regime. This happens since the curvature of the cylinder acts against the capillary pressure allowing for a larger curvature (steepness of rivulet edge) to appear between rivulets without merging taking place. The rivulets are confined to this regime until the circumference of the cylinder is approximately three times the width of the rivulets, $3W_r$. At this point transition is made into the single rivulet regime, where only one rivulet is able to grow due to the restrictions of the size of the rivulet. If more than one rivulet develops then they are forced to merge to form just a single rivulet.

A general regime model for the rivulet wavelength can then be written as:

$$\lambda = \begin{cases} \lambda_f - \frac{2.47}{R_0} \frac{H_0}{6Ca^{0.4}} & \text{if } C_R \geq 3W_r \\ 2\pi R_0 & \text{otherwise} \end{cases} \quad (6.7)$$

where λ_f is given by equation (4.2). The results of the regime model are plotted against numerical solutions for both silicone oil, Figure 6.20 (a), glycerin when fully wetting and glycerin when partially wetting, Figure 6.20 (b), as well as the experimental points of Smolka and SeGall (2011). The model fits the numerical data well and also fits with the trend of the experimental data (taking into account the large error bars associated with experiments).

6.3.4 Flow down the inner surface of a vertically aligned cylinder

To complete the story, the flow down the inside surface of a vertically aligned cylinder is considered. It is simple to re-derive the governing equations for flow on the inner surface of the cylinder, equation (6.1) becomes:

$$(1 - \epsilon_R h) \frac{\partial h}{\partial t} = \frac{\partial}{\partial z} \left[\frac{\epsilon_R h^3}{3} \left(\frac{\partial p}{\partial z} - \frac{1}{\epsilon_R} + h \right) \right] + \frac{\partial}{\partial \theta} \left[\frac{\epsilon_R h^3}{3} \left(\frac{\partial p}{\partial \theta} \right) \right], \quad (6.8)$$

noting the change in sign of some of the terms.

Figures 6.22 and 6.23 show the developing flow for a fully wetting silicone oil on the inner surface of a cylinder with radius 0.635cm and that of a film of glycerin coating the inside of a cylinder of radius 2cm, respectively. The formation and evolution of the rivulets are similar to that seen on the outer surface and on a plane surface; the merger of neighbouring rivulets is observed in Figure 6.22, while the partially wetting rivulets that form are straight-edged, thin and meander compared with the corrugated saw-tooth pattern that emerges in the fully wetting case.

An example of how flow down the inside of a cylinder compares with its outer surface counterpart is shown in Figure 6.24 for a fully wetting silicone oil fluid and $R_0 = 1.27\text{cm}$. The rivulets take on differing shapes; the rivulets that form on the inner surface are less pointed, more square ended and have larger roots.

The width of the two cases, inner and outer, are quite similar however the inner

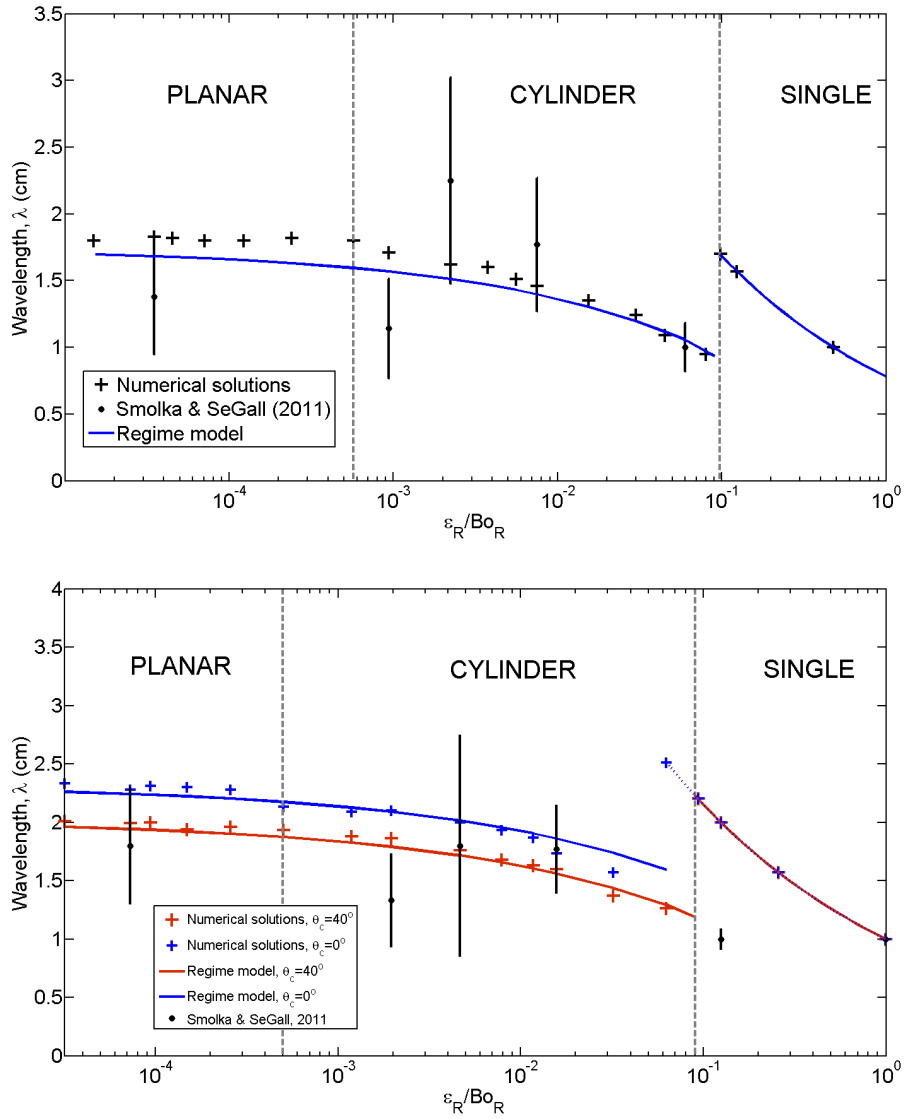


FIGURE 6.20: Regime model plotted against numerical solutions for silicone oil (top) and glycerin (bottom). Experimental points are provided for reference, and critical values of ϵ_R/Bo_R are indicated by grey dashed lines. The regimes are indicated as ‘Planar’, ‘Cylinder’ and ‘Single’.

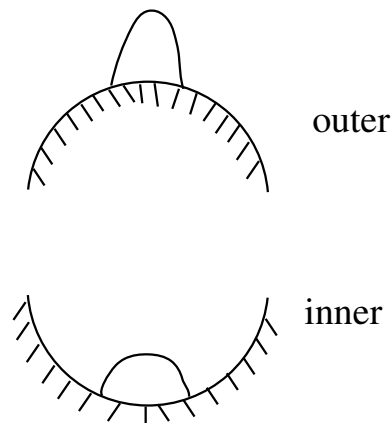


FIGURE 6.21: Illustration of the curvature of the inner and outer surfaces of the cylinder and how this affects the shape of the rivulet.

rivulets are very slightly wider. This has small implications on the wavelength of the pattern and the critical value of $\epsilon/B\sigma_R$ at which only a single rivulet will emerge.

The differences in shape, the inner cylinder rivulets having a thicker front end, can be explained in terms of the difference in surface curvature experienced by the flow. The curvature of the inside of the cylinder supports the outer edge region of the rivulets increasing their height, creating the square-ended shape - the appearance is like a squashed, stretched tip of the outer surface rivulets. The curvature of the outside of the cylinder encourages a more domed shape with a peak in the centre of the finger. For clarity of this explanation please see the illustration shown in Figure 6.21. As the curvature decreases, i.e. the radius of the cylinder increases, the differences ease and both tend to the case of flow on a vertically inclined plane.

In the partially wetting scenario the differences are less pronounced. The tip of the rivulet is less round and more square as in the fully wetting case, however the shape and width of the rivulets are very similar. See Figure 6.25 which shows an example of rivulets developing on the inside of a cylinder of radius 1.5cm at the advancing front of a glycerin film with $\theta_c = 40^\circ$.

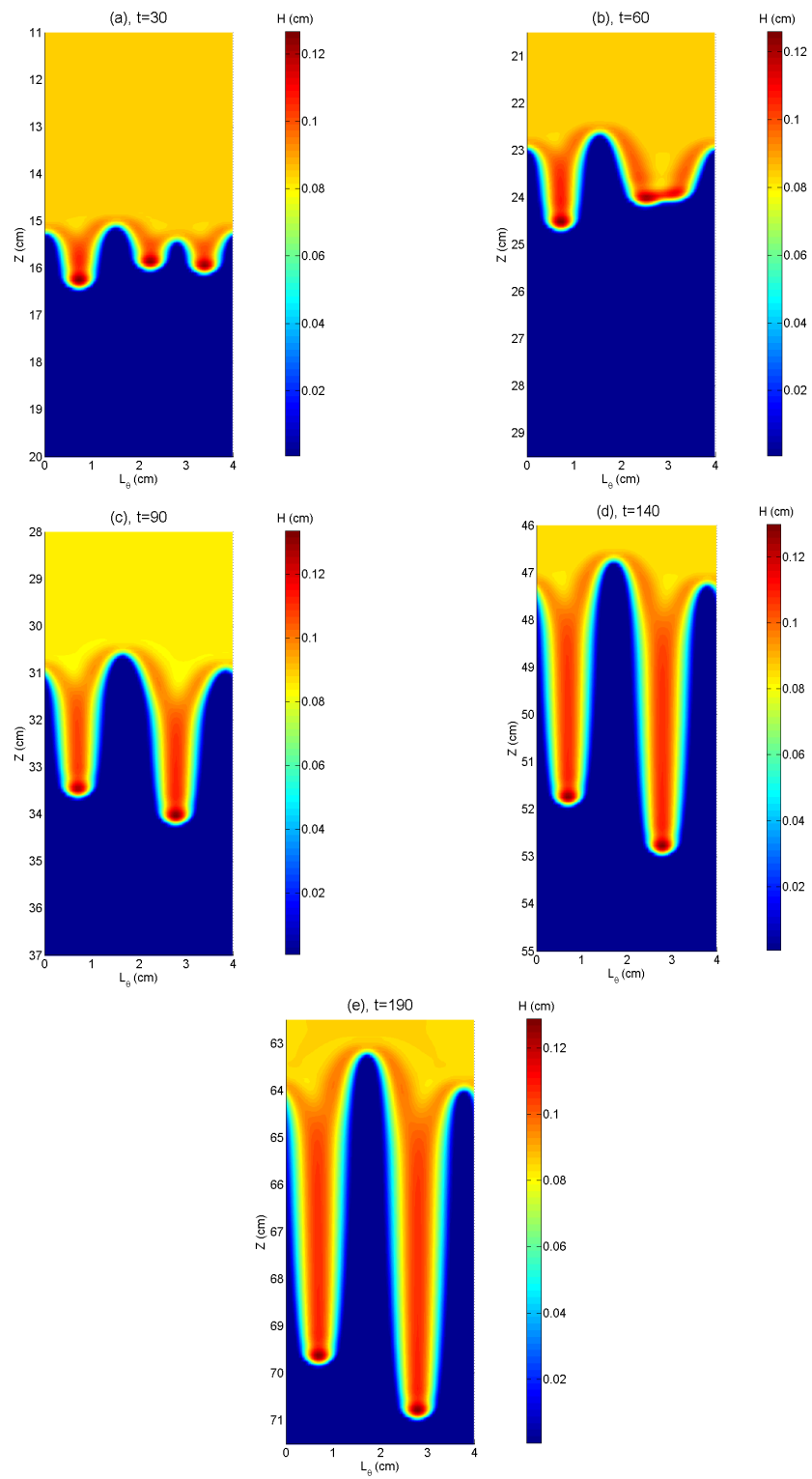


FIGURE 6.22: Free-surface visualisations of fully wetting silicone oil coating the inside surface of a cylinder of radius 0.635cm.

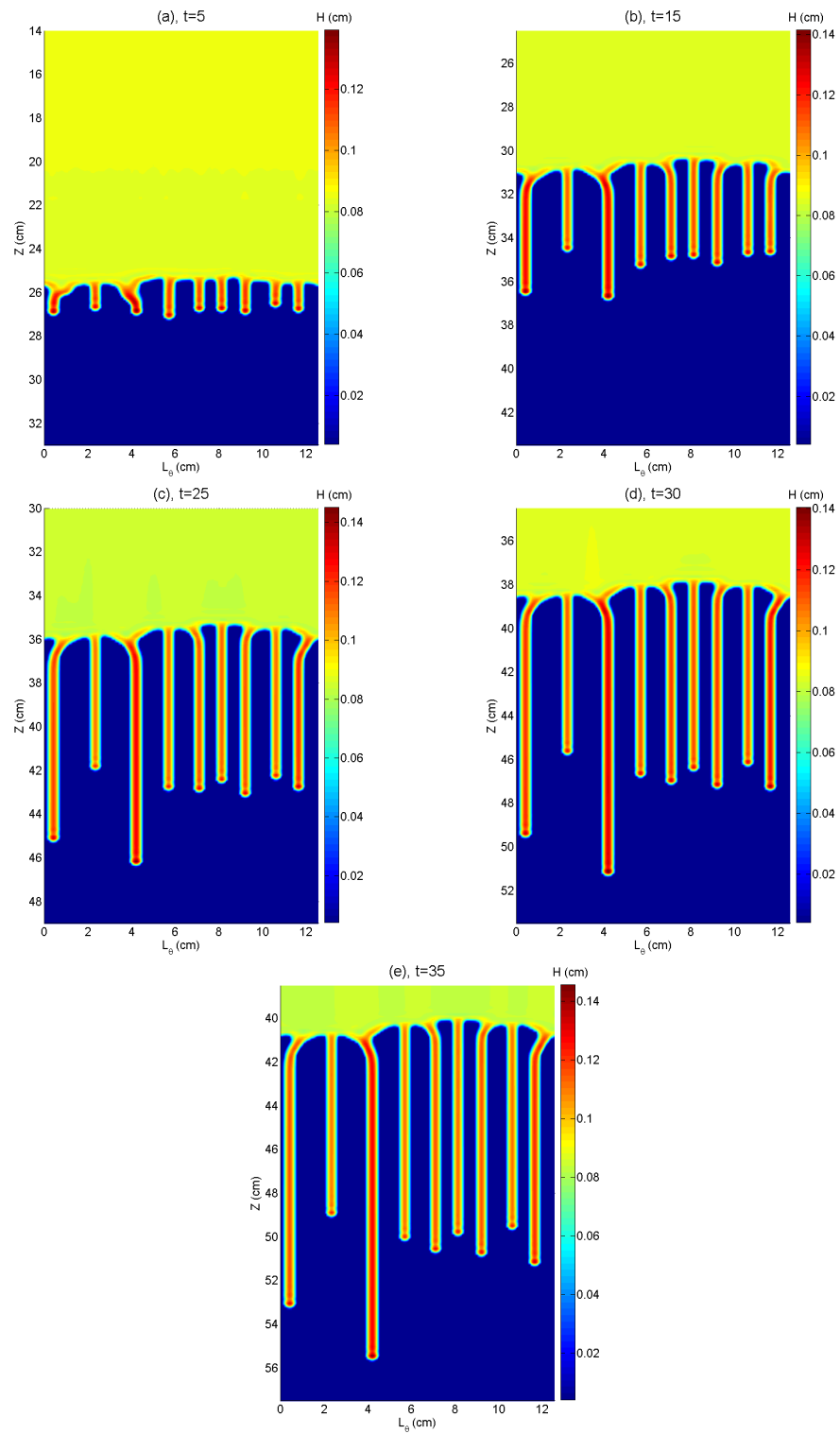


FIGURE 6.23: Unfolded free-surface visualisations of partially wetting glycerin ($S_{\theta_c} = 2.35$) coating the inside surface of a cylinder of radius 2.0cm.

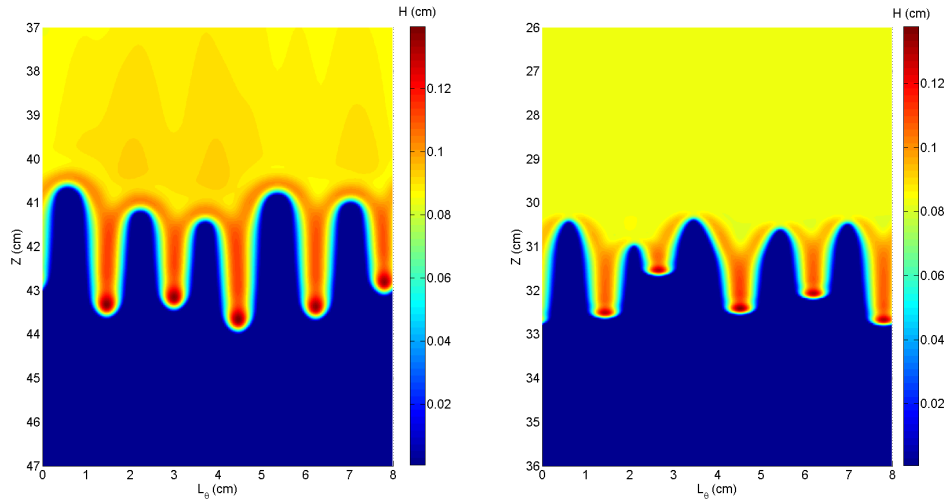


FIGURE 6.24: Unfolded free-surface visualisations of fully wetting silicone oil coating the outside (left) and inside (right) surface of a cylinder of radius 1.27cm.

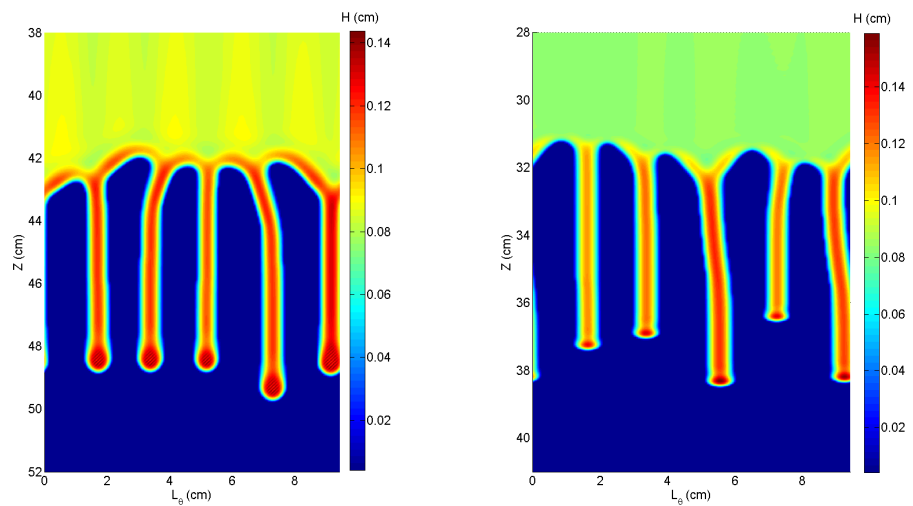


FIGURE 6.25: Unfolded free-surface visualisations of a partially wetting ($\theta_c = 40^\circ$, $S_{\theta_c} = 2.35$) glycerin film coating the outside (left) and inside (right) surface of a cylinder with radius 1.5cm.

6.4 Summary and Discussion

In this chapter lubrication models based on the long-wave approximation have been used to explore gravity-driven thin film flow on the outer and inner surface of a vertically aligned cylinder. The models, derived in a different manner to the usual lubrication approach to rivulet formation in thin films (Kondic and Diez, 2001), retains terms that embody the effect of the curvature of the cylinder. Three-dimensional numerical solutions are achieved by solving the transient coupled governing equation set via a state-of-the-art fully adaptive multigrid method taking advantage of local mesh refinement, automatic error-controlled variable time-stepping and grid devolution to efficiently achieve long-time solutions. These results, with comparison made to corresponding experimental data and numerical results for flow on a planar substrate, allow a regime model for wavelength to be developed that describes the effect of curvature on the emerging wavelength pattern.

The results obtained prove to be consistent with the experimental observations of Smolka and SeGall (2011). At larger enough cylinder radius, or small enough curvature, the evolution of the rivulets is identical to that on an inclined plane with width equivalent to the circumference of the cylinder. This happens when the value of ϵ_R/Bo_R is small and the curvature terms become negligible - this regime occurs for values of ϵ_R/Bo_R less than the critical value of 0.0005.

As R_0 is decreased the wavelength of the emerging rivulet pattern reduces since the curvature of the substrate opposes the surface tension forces of the free-surface allowing for rivulets to grow in closer proximity to one another without interacting and merging. This effect is opposed by the decreasing circumference of the cylinder; as the circumference decreases the number of rivulets that are able to form and evolve also decreases. Eventually, the effect of the circumference prevails and only one rivulet can form on the cylinder surface at $C_R \approx 3W_r$. From these observations a regime model has been developed that accurately predicts the wavelength that will occur at the advancing front.

A linear stability analysis allows reasonable predictions on the wavelength of the pattern when compared with numerical simulations and experimental data however it fails to capture fully the effect of curvature and the restriction the circumference of the cylinder has at smaller values of radius. The LSA predicted growth rate decreases with cylinder radius suggesting the curvature inhibits the growth of the instability.

By incorporating a disjoining pressure term into the mathematical formulation partially wetting is introduced into the problem, allowing direct comparison with results for a fully wetting one. As in the planar case, as the contact angle increases the width of the rivulets formed decreases and so does the wavelength. Although this does not shift the critical value at which the planar regime persists, it does shift the critical value at which only one rivulet can grow due to the decrease in width.

The recent work of Mayo *et al.* (2013) comes to similar conclusions concerning fully wetting fluids (they did not consider a partially wetting liquid). The parameter that determines which controls the effect of the curvature is essentially the same for both sets of work, however there are some disparities between their work and the results presented here. For instance, the critical values at which the regimes become active are different, this could be due to the differing governing equations and the terms that are neglected if derived via a usual lubrication approach which define the impact of the surface curvature on the film. To pin point the critical values is difficult to accurately define due to the random nature of the instabilities that emerge and the interaction between neighbouring rivulets.

Flow down the inner surface of a cylinder is also considered. The reversal of the curvature effects has an impact on the shape and width of the rivulets that form particularly in the case of a fully wetting liquid. The differences are minimal and only have small implications on the predicted behaviour from the outer surface flow, the growth rate stays similar and the wavelength remains almost identical to that on the outer surface.

Mayo *et al.* (2013) assert that there is a critical value at which no rivulets grow. This has not been observed in the present work, even for very small cylinder radii. The capillary ridge associated with the instability is present for all radii indicating instability at all values. In a physical sense, as the radius reaches small values the rivulet that emerges fills more and more of the circumference and so eventually it will appear as a single rivulet. This does not necessarily mean the flow is stable as there are still modes of small enough wavelength that are associated with instability. The restriction on observing these may well be theoretical as the derivation of the governing equations depend on the restriction that $H_0/R_0 \ll 1$ which at very small R_0 is not necessarily the case, therefore a higher order model should be considered when ϵ_R/Bo_R becomes of $O(1)$.

Chapter 7

Preliminary investigations of material transport enhancement in film flows over wavy substrate

Contents

7.1	Turnstile lobes - transport enhancement	158
7.2	Flow visualisation	161
7.2.1	Streamlines	162
7.2.2	Eddy centre	162
7.2.3	Particle tracking	162
7.2.4	Stable and unstable manifolds	163
7.3	Results: material transport enhancement	163
7.3.1	Inner flow structures	164
7.3.2	Turnstile lobe transport: pulsed flow	169
7.3.2.1	Geometric effects	178
7.3.3	Inertially induced eddy	182
7.4	Summary	183

In this chapter numerical solutions of the full Navier-Stokes and continuity equations are sought via the method described in section 3.3 of Chapter 3. The problem of interest being the inner flow structure present within the valleys of a wavy substrate over which is flowing a continuous liquid film and the enhancement of material transport from such valleys to the overlying flow as the film thickness varies with time. The flow domain of interest is shown in Figure 7.1. Wavy or undulating substrates are of particular interest due to their extensive use within industry, for example in heat exchangers or evaporators (Szulczewska *et al.*, 2003).

In practice the presence of isolated or repeating topographical features on a functional substrate can lead to trapped debris and stagnant flow in the separated flow regions which result in the formation of a closed eddy structure. Wierschem and Aksel (2004) observed the transfer mechanism of material from such eddies to the bulk flow; here the turnstile lobe mechanism, discussed in depth in Horner *et al.* (2002), is investigated as the vehicle for this by pulsing the flow at the inlet creating a wave that induces material transport. The effect of the size of the pulse on the transport of material is investigated, as well as the effect of the periodicity of the pulses. Turnstile lobes are visualised by plotting the stable and unstable manifolds of the problem and material transport quantified by employing a fourth-order Runge-Kutta method to track inert particles.

7.1 Turnstile lobes - transport enhancement

In their experiments of steady film flow over undulating substrate, Wierschem and Aksel (2004) observed the transport of inert tracers from fluid in the valleys of a sinusoidal topography, when surface waves were present, enabled via a turnstile lobe mechanism. Horner *et al.* (2002) present a comprehensive overview of this mechanism for modulated flow over a square cavity and Wilson *et al.* (2006) investigated the enhancement of transport and stirring between two rollers via lobe dynamics.

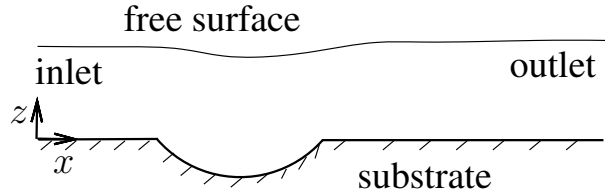


FIGURE 7.1: Schematic diagram of the domain of interest, the wave topography is located nearer the upstream inlet boundary to allow the pulse to pass downstream to the outlet boundary condition. The domain is also subject to an inclination angle, α .

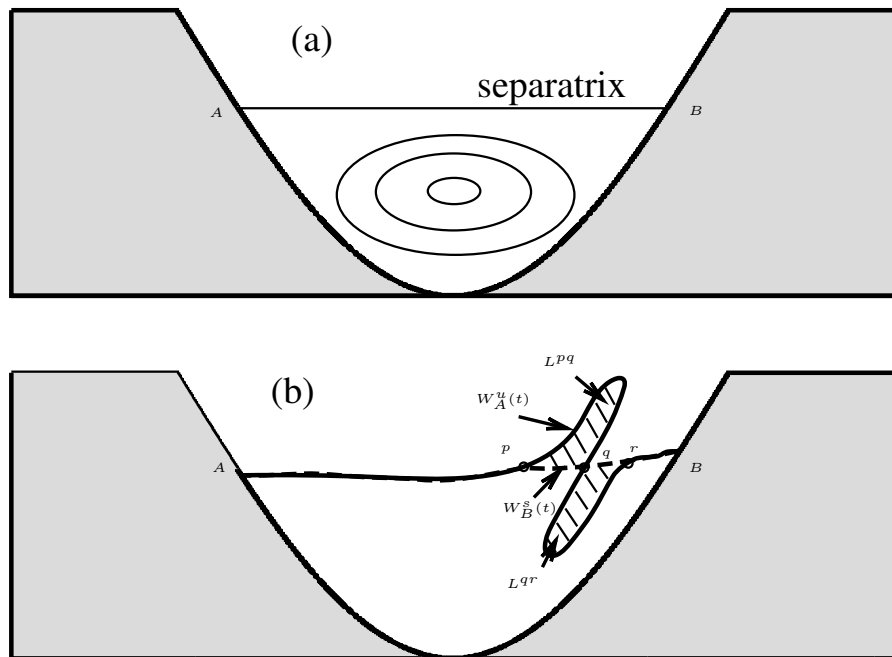


FIGURE 7.2: (a) A schematic diagram of the unstable and stable invariant manifolds, $W_A^u(t)$ and $W_B^s(t)$, of the upstream and downstream hyperbolic separation points, A and B . The intersection of the manifolds, at points p, q , and r , create two lobes, L^{pq} and L^{qr} , that facilitate the transport of material across the boundary between overlying bulk flow and encapsulated eddy flow. (b) Steady-state schematic of the same flow showing the eddy region separated from the overlying bulk flow by the separatrix.

Figure 7.2 (a) shows an illustration of how a typical inner flow structure might look at steady state; an eddy is present separated from the bulk flow by the separatrix which is connected to the wall at points A and B . Considering Figure 7.2 (b), at a time t there are two hyperbolic separation points at the upstream and downstream boundary between the overlying flow, the eddy and the substrate - these are denoted in the figure as $A(t)$ (upstream) and $B(t)$ (downstream). Physically, at these points fluid separates off the wall and moves in a vertical direction away from it reminiscent of a saddle point seen in dynamical systems theory. Manifolds are invariant curves meaning particles that start trajectories on these curves remain on them for all time; hence no trajectories can cross them and thus they are barriers to material transport. All points making up the stable (unstable) manifold approach the stable (unstable) fixed point as time tends to ∞ ($-\infty$). Hyperbolic saddle points possess both stable and unstable manifolds; when the flow is steady the unstable manifold of A , denoted $W_A^u(t)$, and the stable manifold of B , denoted $W_B^s(t)$, coincide to form the separatrix shown in Figure 7.2 (a).

When an appropriate forcing is applied to the flow, $W_A^u(t)$ and $W_B^s(t)$ separate and intersect to create a tangle. Regions enclosed by portions of both the unstable and stable manifolds are called lobes and determine transport between the bulk flow and the entrapped flow in the topography. In Figure 7.2 (b) there are three intersection points of the invariant manifolds, p , q and r ; the regions enclosed between unstable and stable manifold portions connected by these points, the lobes, are denoted L^{pq} and L^{qr} . The time-dependent motion of the lobes determines the material transport from the bulk region to the eddy region and vice versa.

Figure 7.3 is a diagrammatic sketch of how the exchange of material is achieved. At time $t = t_{n-1}$ the intersection of the manifolds, $W_B^s(t_{n-1})$ and $W_A^u(t_{n-1})$, creates the lobes L_{out}^{n-1} and L_{in}^{n-1} , respectively; these are the turnstile lobes at $t = t_{n-1}$. The motion of the manifolds means that the material enclosed in L_{out}^{n-1} is moved from R_e^{n-1} to R_b^n in the lobe L_{out}^n ; similarly the material encapsulated in L_{in}^{n-1} in the bulk region, R_b^{n-1} , is moved into the eddy region R_e^n within lobe L_{in}^n . Another

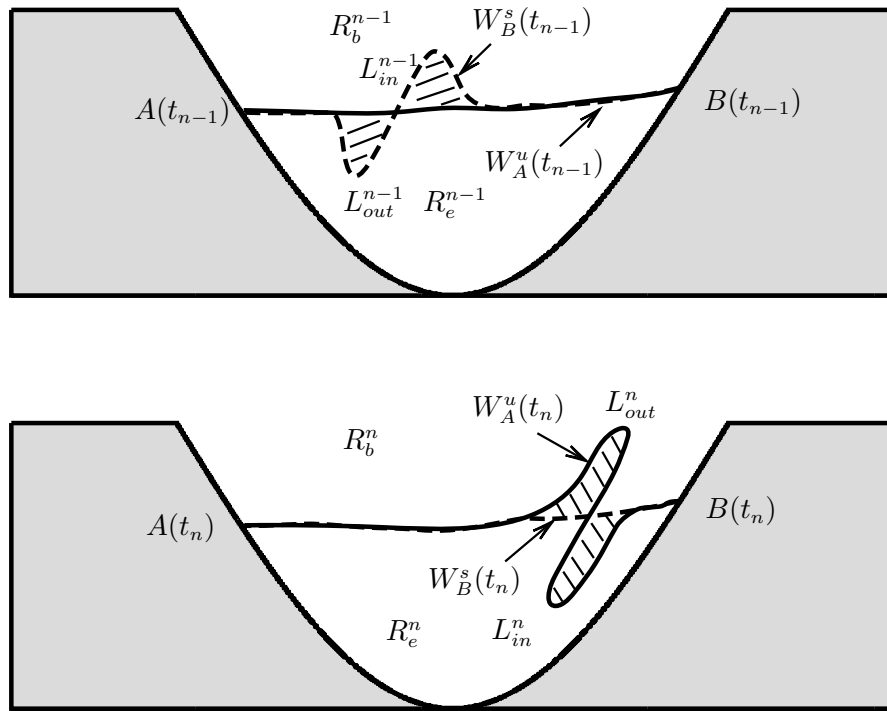


FIGURE 7.3: A sketch to demonstrate the turnstile lobe mechanism between time t_{n-1} and t_n .

way to describe the motion is by defining the movement of the points in the flow from position \mathbf{x}^{n-1} to \mathbf{x}^n between $t = t_{n-1}$ and $t = t_n$ via a mapping function f_{n-1} ; therefore $L_{out}^n = f_{n-1}(L_{out}^{n-1})$ and similarly for the other lobe. The motion of the lobes through time is reminiscent of a turnstile rotating, hence the name.

Due to the invariance of the manifolds the only material that can be exchanged across the boundary between R_b^{n-1} and R_e^{n-1} is that contained within the boundaries of L_{out}^{n-1} and L_{in}^{n-1} under the motion of the mapping function f_{n-1} . A rigorous overview of the rules governing the turnstile lobe material transport mechanism can be found in Horner *et al.* (2002).

7.2 Flow visualisation

To visualise the flow structures within topographies a number of plotting tools are utilised and parameters calculated.

7.2.1 Streamlines

The instantaneous streamlines of the flow reveal the presence and shape of an eddy. Streamlines are found by solving:

$$\nabla^2\Psi = \frac{\partial u}{\partial y} - \frac{\partial v}{\partial x}, \quad (7.1)$$

where Ψ is the stream function and is zero along the substrate boundaries. The stream function equation is solved in weighted residual form, represented bi-quadratically on the standard element.

7.2.2 Eddy centre

Eddy centres are found by sweeping the domain element by element and finding the maximum and minimum values of velocity to determine whether an eddy centre lies within the element. If it is determined that an eddy centre is present the corresponding simultaneous equations in the local co-ordinates are solved to pinpoint exactly the co-ordinates of the centre.

7.2.3 Particle tracking

Integral to the visualisation of transport in time-dependent flows are the trajectories of passive tracer particles, which provide a means of observing fluid motion without influencing the flow. The trajectory, $\mathbf{x}(t)$, of a tracer whose global position is $\mathbf{x} = (x, z)$, is found by integrating the advection equation:

$$\frac{d\mathbf{x}}{dt} = u(\mathbf{x}, t) \quad (7.2)$$

which is achieved using a fourth-order RungeKutta scheme.

7.2.4 Stable and unstable manifolds

The transport of material via the turnstile lobe mechanism can be visualised by plotting the invariant manifolds, both stable and unstable. To do this, a new inert tracer is inserted at a point on the relevant trajectory at each new time step and then advected forward (for unstable) or backwards (for stable) in time to construct these manifolds.

7.3 Results: material transport enhancement

A sketch of the domain of interest is shown in Figure 7.1; the usual approach to model an undulating substrate is to consider one undulation and apply periodic boundary conditions at the inlet and outlet of the computational domain, see for example Scholle, Haas, Aksel, Thompson, Hewson and Gaskell (2009). In the current work, the interest in pulsing the inlet flow requires a different approach - here a longer domain is used with a single wave topography present. This is to allow the free-surface wave that is induced to develop and travel along the domain, passing over the topography and thus reveal the symmetry-breaking effects that are induced.

Two-dimensional results are sought of the discretised Navier-Stokes and continuity equations described in Chapter 3 using the freely available Multifrontal Massively Parallel sparse direct solver (MUMPS) (Amestoy *et al.*, 2000, 2001). Simulations are run using 8GB of memory spread evenly across 8 processors using the memory efficient method of storing matrix cofactors ‘out-of-core’ on the hard drive.

The number of elements making up the mesh utilised in the x -direction are 300 and in the z -direction 150, a total of 45,000. That is, the number of \mathbf{u}/\mathbf{x} -nodes $n_e^i = 190,901$, the number of p -nodes $n_e^j = 45,451$ and number of free-surface \mathbf{u}/\mathbf{x} -nodes $n_e^k = 601$. The total degrees of freedom (DOF) is given by $2 \times n_e^i + n_e^j + n_e^k$ and in this case is 407,854. The mesh is constructed to have much higher resolution

around the topography where the flow is re-circulating.

The non-dimensional parameters employed to generate results are: substrate length in the x -direction defined as $110 + \lambda_t$, $Re = 0.5$, $Ca = 4 \times 10^{-4}$ and $\alpha = 45^\circ$. The topography is defined via $\lambda_t = 0.625$ and $A_t = 0.25$.

The inlet condition is pulsed by amplifying the inlet velocity condition, i.e. $u|_{x=0} = F_a z(2 - z)$ where F_a is a scalar term controlling the amplitude of the pulse.

7.3.1 Inner flow structures

The non-perturbed flow streamlines around the topography are visualised in Figure 7.4. A symmetrical eddy is clear visible at the bottom of the wave topography. The eddy is a geometrically induced structure (Scholle *et al.*, 2008), meaning that it persists at all values of global Reynolds number. An inertially induced eddy would not exist at low Reynolds numbers but becomes visible as the Reynolds number is increased. The eddy centre is very slightly skewed away from the centre line of the topography due to the small effect of inertia and has co-ordinates $(x_c, z_c) = (-0.00024, -0.19637)$. The eddy depth, D_e , is defined as $D_e = |z_c|$.

The inlet condition is pulsed to create a free-surface wave, the size of which depends on the value of F_a and the time duration of the pulse, taken as $\Delta t = 0.5$. The wave dissipates as it travels down the substrate, becoming elongated with a smaller amplitude. The maximum free-surface disturbance induced above the wave topography centre line at $x = 0$ by the pulse depends on the value of F_a , as shown in Figure 7.5.

As the wave traverses the topography, the shift in the film height disturbs the eddy, separatrix and centre. To indicate the vertical shift in the eddy structure the depth of the eddy relative to the bulk flow is considered by taking the modulus of the centre vertical co-ordinate z_c . The eddy increases in depth and decreases in size as the pulse passes over before then decreasing in depth and increasing in size as the pulse

peaks and passes fully over to the downstream; this effect is shown in Figure 7.6 where both the eddy depth and film surface height at $x = 0$ is shown. The motion of the eddy corresponds to the wave passing over the topography and an increase in the local film thickness.

If $F_a < 1$ the motion is opposite, the eddy first decreasing in depth before increasing in depth as the film height is lowered above the topography. To induce a large change in local film thickness and create a large motion of the inner flow structure by decreasing the flow rate, the inlet velocity must either be severely reduced or, more realistically maybe, reduced for a longer period of time to get the same impact as increasing the flow rate.

As the free-surface deforms there is also a shift in the longitudinal position, that is the x -coordinate, see Figure 7.7 for the maximum shift during the time evolution of the flow. If $F_a > 1$ the shift is in the negative direction, as seen in Scholle *et al.* (2008) for increasing inertia. Similarly if $F_a < 1$ the shift is in the positive direction towards the downstream edge. This motion is relatively small, even for large Reynolds numbers; Scholle *et al.* (2008) found the shift to be at most 0.015.

The magnitude of the eddy depth shifts as the amplitude in the film height above the topography changes - the thicker the film the larger the eddy and change in eddy depth. Figure 7.8 shows how the minimum and maximum depth of the eddy depth depends on the value of F_a and therefore the local film height above the wave topography. These findings are consistent with that of Scholle *et al.* (2004, 2006, 2008), where the depth of the eddy was found to depend on a combination of geometric (wavelength and amplitude of the topography) and inertial (global Reynolds number) effects. By increasing the film thickness the eddy depth decreases (moving closer to the free-surface) before vanishing, and vice versa for decreasing film thickness. Manipulation and creation of eddies could also be achieved by altering the wavelength or amplitude of the substrate undulations (Scholle *et al.*, 2008).

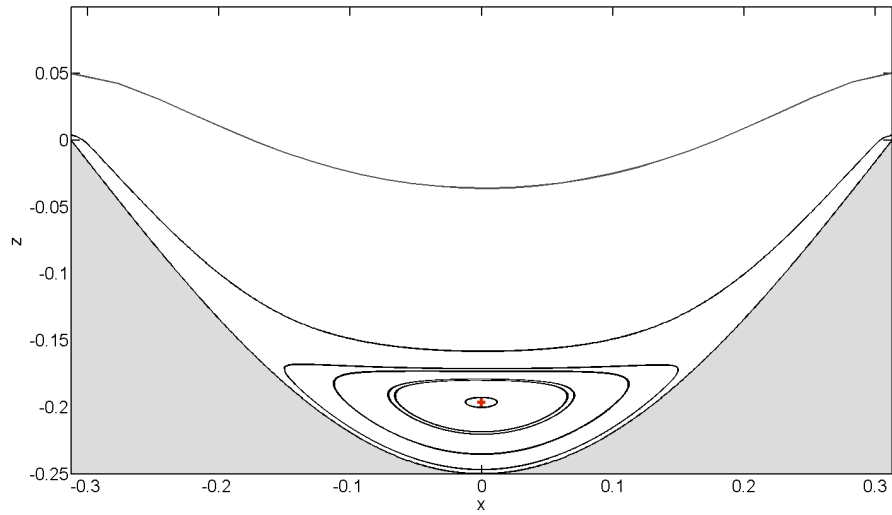


FIGURE 7.4: Streamlines of the unperturbed flow depicting the eddy in the topography of the substrate below the bulk flow.

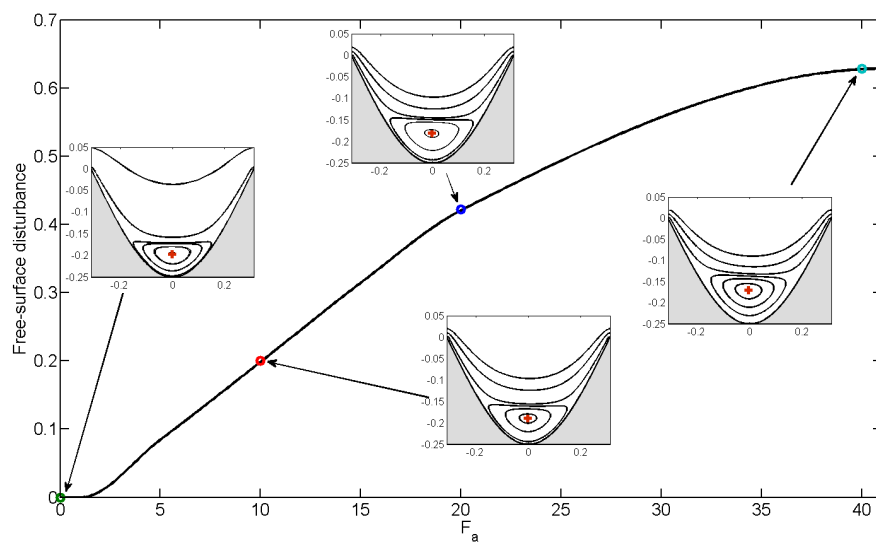


FIGURE 7.5: Maximum free-surface disturbance above the centreline of the valley of the topography with increasing strength of the pulsed inlet via an increase in F_a .

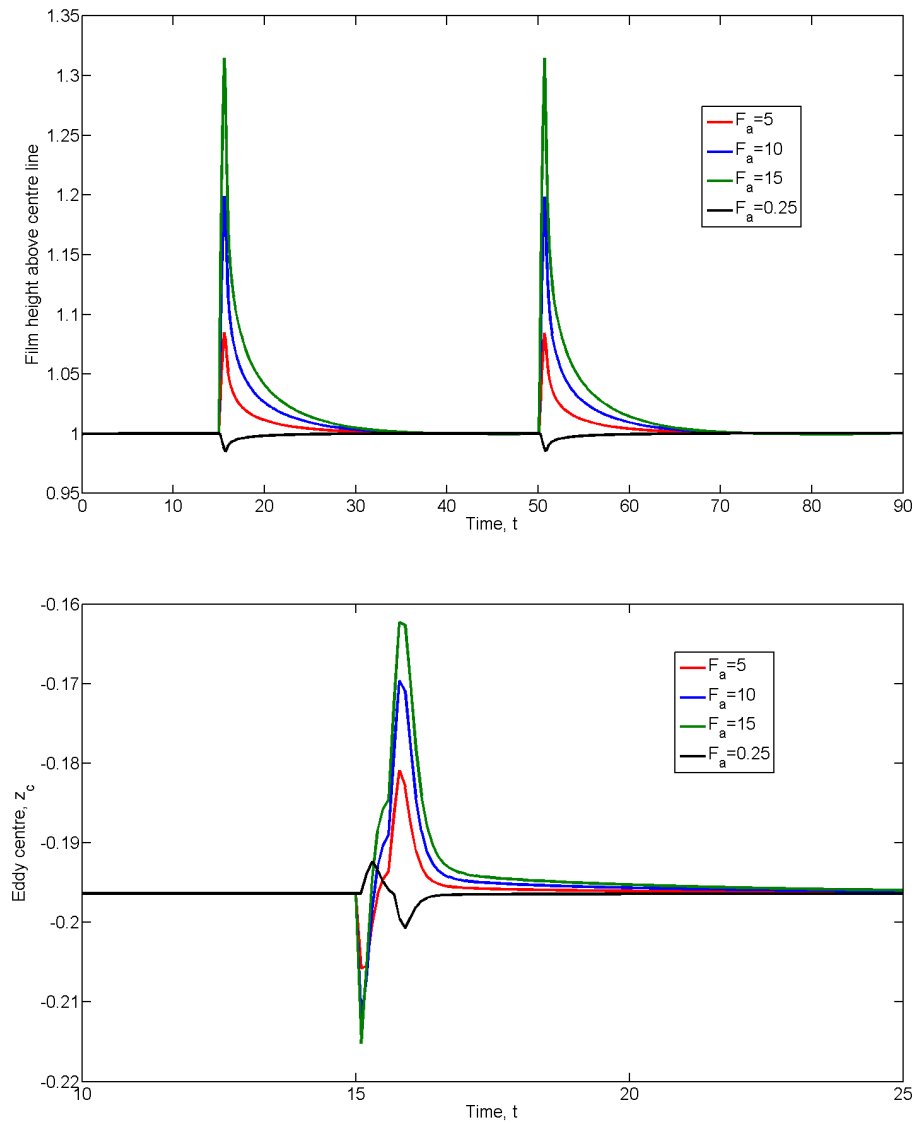


FIGURE 7.6: The time evolution of the film height above the centre-line of the topography and the change in associated eddy depth co-ordinate z_c .

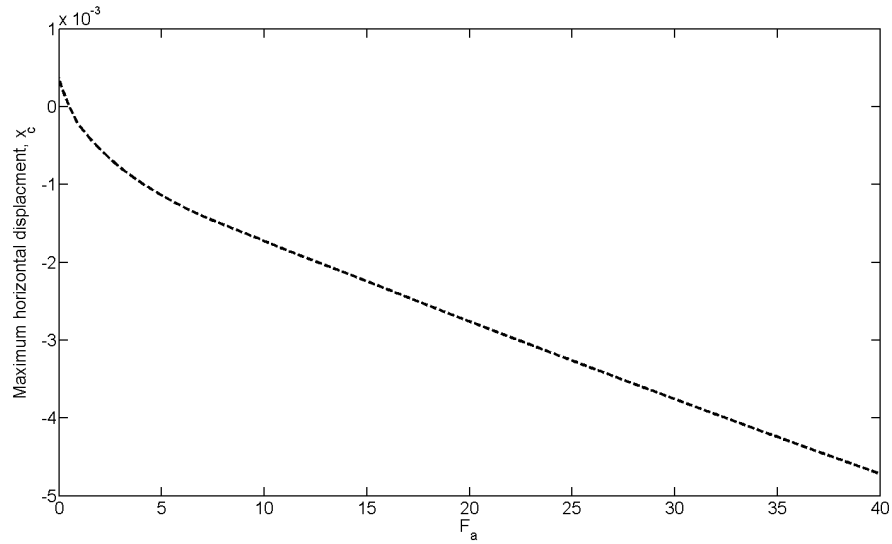


FIGURE 7.7: The maximum shift in the eddy centre in the x -direction during the pulsed flow.

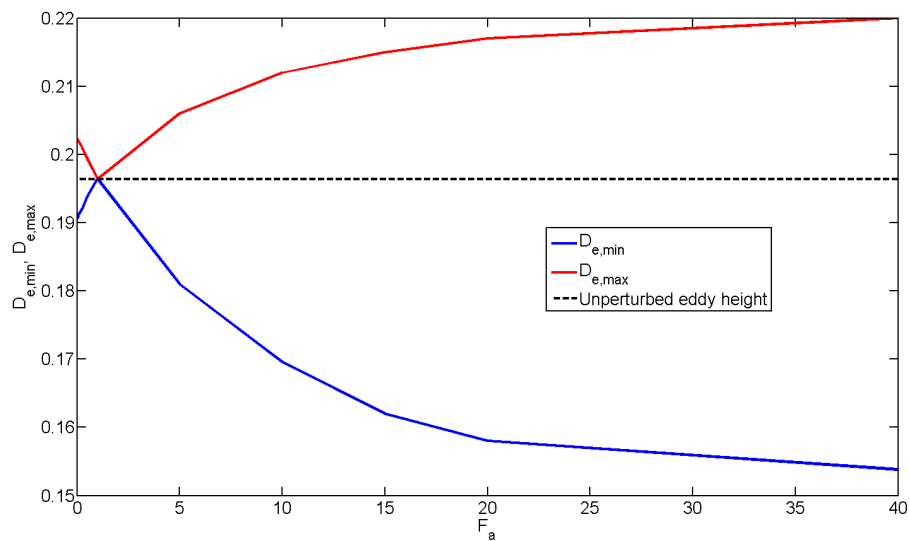


FIGURE 7.8: The maximum and minimum eddy depth co-ordinate, D_e , as a pulse crosses above the topography for a range of F_a .

7.3.2 Turnstile lobe transport: pulsed flow

The free-surface wave induced creates changes in the local film thickness over the sinusoidal topography, the thickening and subsequent thinning of the film impact on the underlying eddy structures, generating the turnstile lobe dynamics that drive material exchange between the bulk flow that exits the domain and the re-circulating region.

In Figure 7.9 inert particle trajectories are used to visualise the flow in the topography. Here, $F_a = 20$ and there are two pulses - each last for $\Delta t = 0.5$ at $t = 15$ and $t = 50$. At $t = 15$ the particles visualise the folding of the invariant manifolds to form lobes. The entraining lobe pulls fluid into the eddy from the bulk flow, this is pictured by the white swirl that appears in the eddy as time progresses. The lobe that removes material from the eddy can be similarly visualised as the escaping particles that can be seen leaving the topography. The second pulse has a similar effect, creating a new inner white swirl and further particles are released into the bulk flow. The motion of the inner flow structures also induces mixing as can be seen from the swirling pattern, and the particles swirl towards the centre. The trail of particles near the substrate wall that are leaving the topography seemingly persist due to the slow velocity near the walls, at very long times these tracers exit the topography; in Figure 7.9 (j) the inner flow structures are back to steady state status even though particles can be seen travelling out of the topography.

In Figure 7.10 the effect of increasing F_a to 40 is shown. The dynamics are the same but the turnstile lobes have a larger area and thus the amount of material transported is increased. The long-time particle positions are shown in Figure 7.12 for a range of F_a . A larger magnitude of pulse leads to an increased flux of material in and out of the re-circulation area.

The work of Wierschem and Aksel (2004) briefly discussed the feature of turnstile lobe transport enhancement after observing the mechanism in process during their experiments. Videos of the experiments in question were shared by these authors,

the receipt of which is gratefully acknowledged by the candidate. A snapshot is shown in Figure 7.11 of a fluid of $Re = 15$ flowing over a wavy topography. The visual agreement with the particle tracking plots shown in Figures 7.9 and 7.10 is excellent, even capturing the asymmetric shape of the lobes moving material in and out of the eddy.

Portions of the stable and unstable manifolds are plotted in Figure 7.13 to depict the turnstile lobes responsible for material transport. The intersection of the two invariant manifolds, W_A^u and W_B^s , associated with the upstream and downstream wall attachment points, A and B , create the lobe mechanism; the portions of W_A^u and W_B^s between the intersection points p and q encapsulates the lobe L_{out} which contains fluid that moves across the separatrix boundary into the bulk flow during the evolution of the flow. Similarly the entraining lobe, L_{in} , is bordered by the sections of manifolds between intersection points q and r . The material contained within L_{in} is moved from the bulk flow into the separated flow region and can be visualised in the particle track figures as the white swirl that evolves. The effect on the size of the lobes by increasing F_a can be observed; lobe areas are noticeably larger for an increase in amplitude of the impulse. For an example of how the manifolds appear at longer times see Figure 7.18.

The percentage of particles remaining in the topography as time progresses is shown in Figure 7.14, the time of the pulses are indicated using grey dashed lines. There is a delay between the inlet pulse and the removal of particles, this delay is larger for small F_a . It is clear that as F_a increases the number of particles removed also increases due to the larger motion of the inner flow structures. The lines on Figure 7.14 are not completely smooth and appear to contain ‘steps’ due to the calculation method; when the tracer’s x and or y position is not within the topography then it is discounted, this means that although a stream will give a smooth line due to the lobe structures ‘clumps’ of tracers leave over one time step. The area of the lobe moving material out of the eddy is directly proportional to the number of particles transferred into the bulk flow above the topography; the lobe size increases with F_a ,

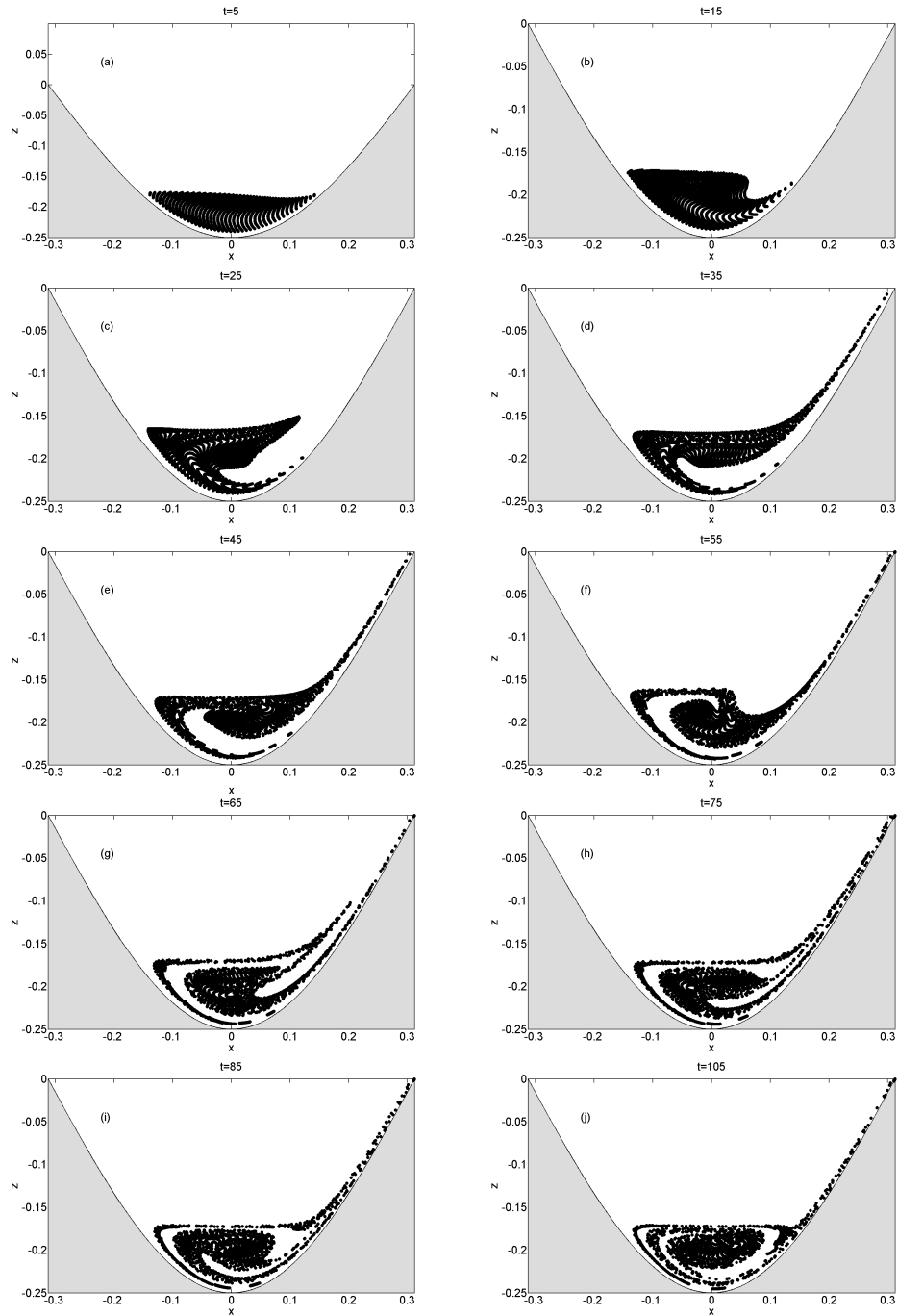


FIGURE 7.9: Time evolution of particles entrapped within the eddy found in the valley of the substrate geometry, showcasing the enhancement of transport of material into the overlying flow. Here, the pulse strength is $F_a = 20$ and the inlet is pulsed at $t = 15$ and $t = 50$.

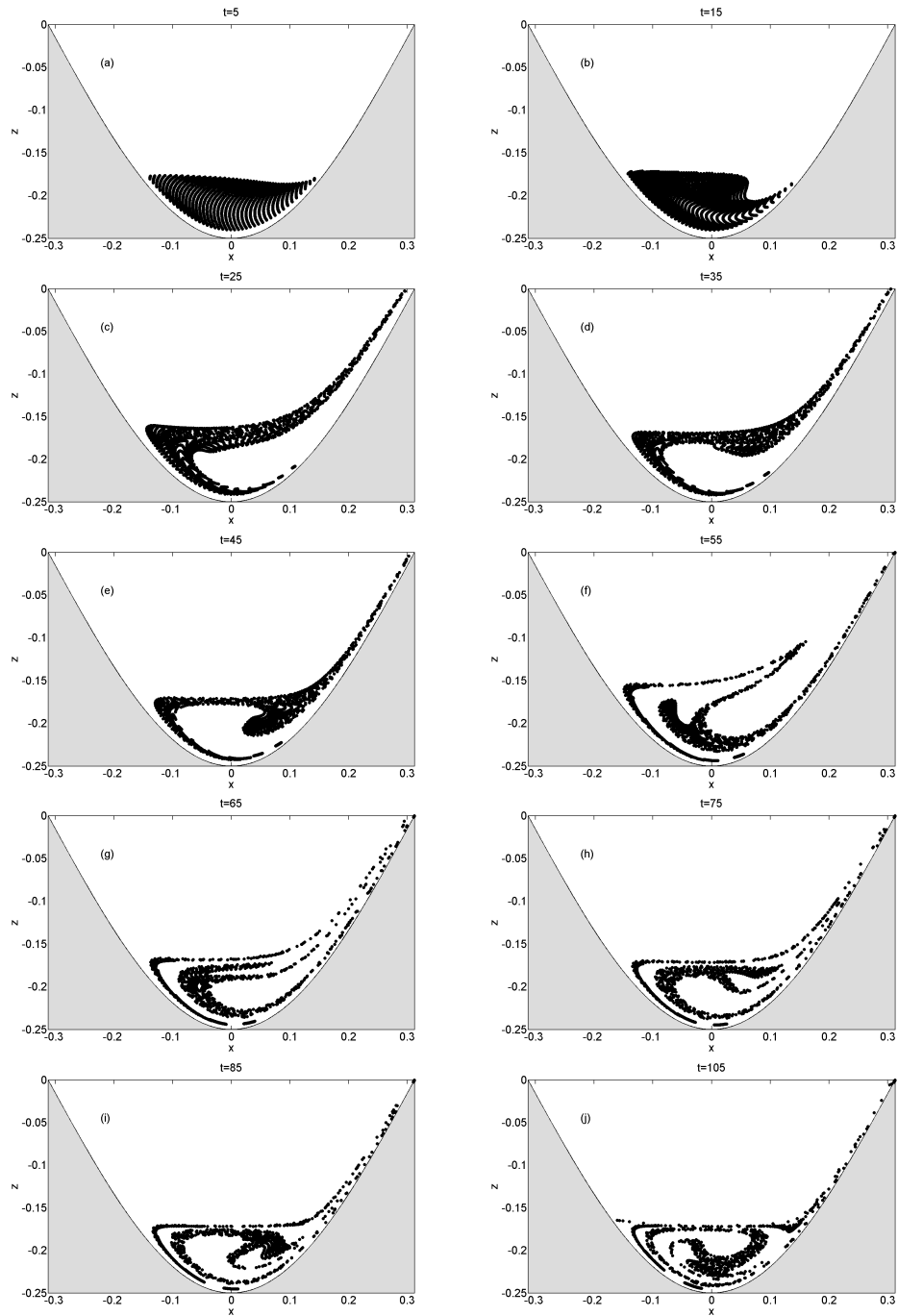


FIGURE 7.10: Time evolution of particles as in Figure 7.9 but with a stronger pulse, $F_a = 40$.

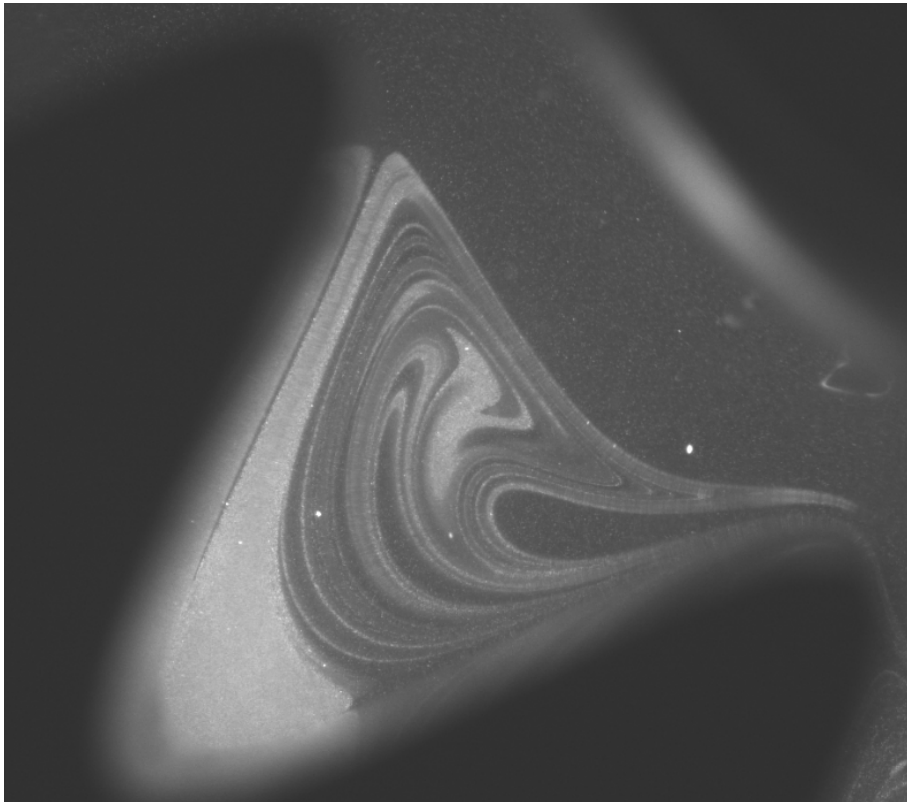


FIGURE 7.11: A snapshot from the experiments of Wierschem and Aksel (2004) showing the turnstile lobe mechanism for a film of liquid with $Re = 15$ flowing over a wavy topography. The candidate gratefully acknowledges the generosity of Andreas Wierschem and Markus Scholle in sharing the fascinating videos of their experimental work.

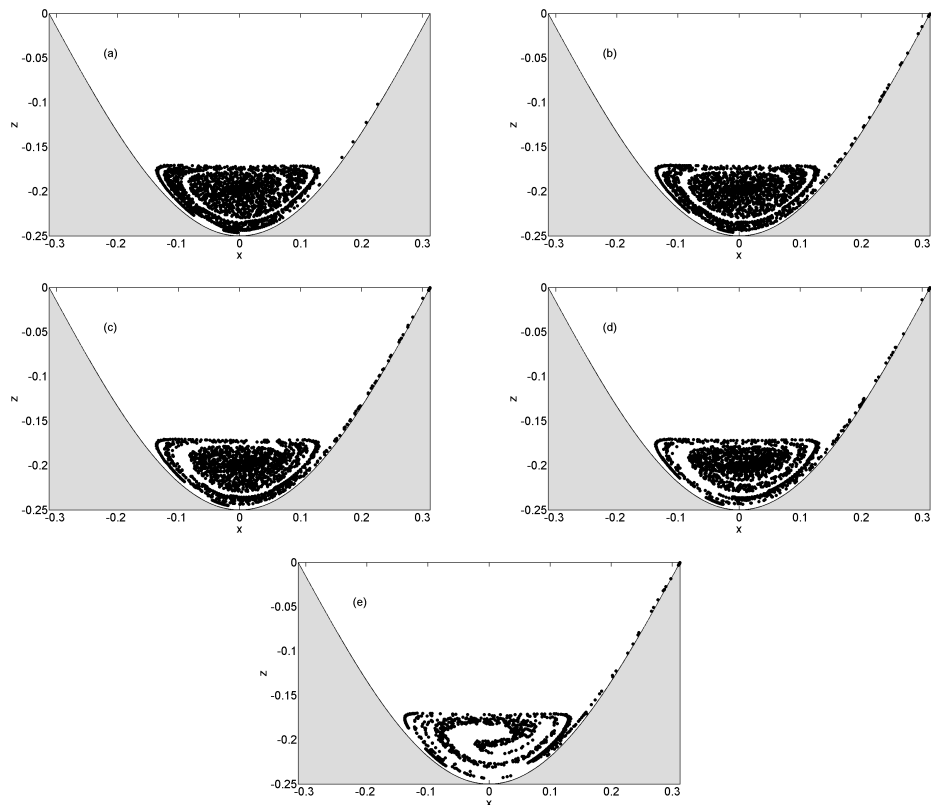


FIGURE 7.12: Long-time particle positions, $t = 145$, after experiencing two pulses of the same strength for a range of F_a ; (a) 5, (b) 10, (c) 15, (d) 20 and (e) 40.

see Figure 7.16.

When $F_a < 1$ the motion is very small leading to very little fluid transport; by increasing the time length of the pulse it is possible to induce a large enough surface deformation to enhance the lobe area and hence the transport of material to the bulk flow.

If the number of pulses is increased from two to five at $t = 15$, $t = 25$, $t = 35$, $t = 45$ and $t = 50$ fluid transfer is enhanced. The percentage of particles present within the valley of the wave topography when $F_a = 20$ for two and five pulses is shown in Figure 7.15; there is a much larger movement of particles out of the eddy when there are more pulses, in a more continuous fashion. The delay that occurs is due to the travelling time of the pulse, the time for the lobe mechanism to transition the particles and the time for the particles to travel out of the topography. The time-

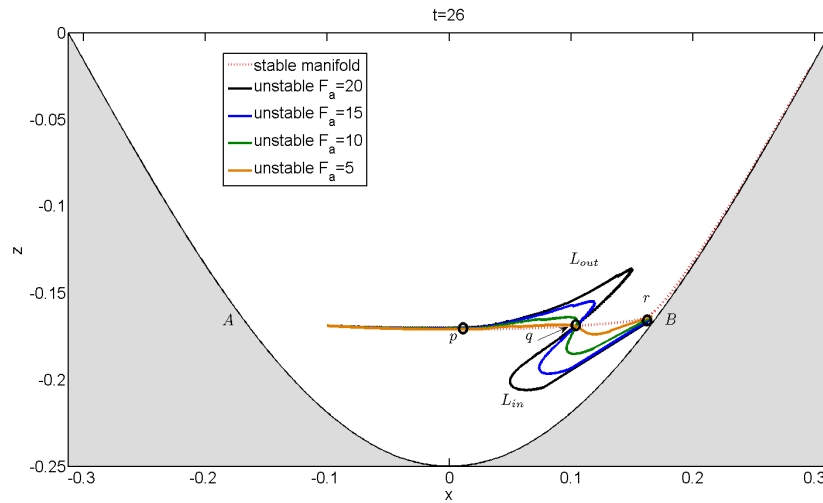


FIGURE 7.13: Portions of the unstable and stable manifolds demonstrating the turnstile lobes that are formed by the pulsed inlet condition.

progressing particle positions are also shown in Figure 7.17 for multiple pulses, it is possible to visualise the outline of the unstable manifold due to the swirls created by the particles - the stable and unstable manifolds are shown in full in Figure 7.18 at $t = 45$, revealing the beginnings of mixing and swirling created by the first three pulses.

The most effective way of enhancing material transport in a geometrically induced eddy is to create large waves with large intervals between each pulse, this strips large quantities of material out of the eddy via a turnstile lobe mechanism. The changes in local film thickness induce changes in the inner flow structures and invariant manifolds to exchange material. Another option, to reduce the magnitude of the free-surface disturbance created by the wave, is to pulse with small amplitude but at much more frequent intervals or increase the inlet velocity at a smaller amplitude but for a longer time period. By inducing the tangling of the stable and unstable manifolds associated with the upstream and downstream triple points, transport enhancement can be achieved via a turnstile lobe mechanism.

Note, from the results of Scholle *et al.* (2008) and those seen here, it is not possible to completely suppress the eddy region in a geometrically induced eddy using this

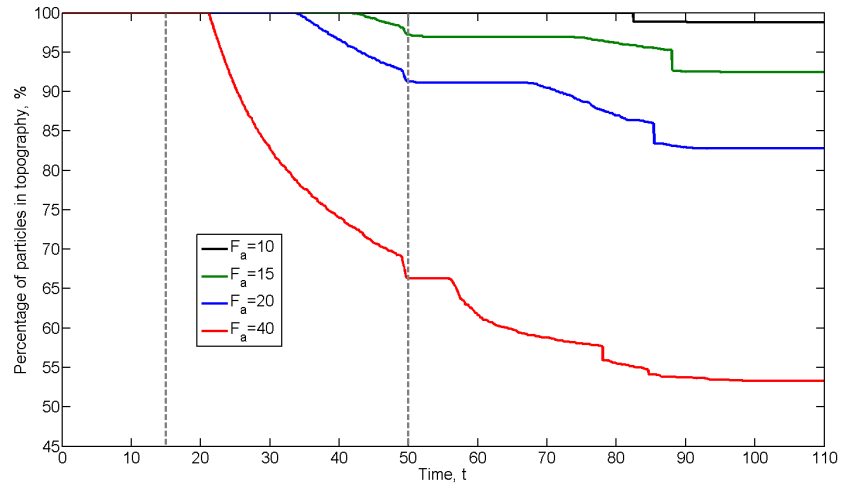


FIGURE 7.14: Percentage of particles remaining in the topography as time evolves for a range of strength of pulse (time of pulse indicated by dashed lines).

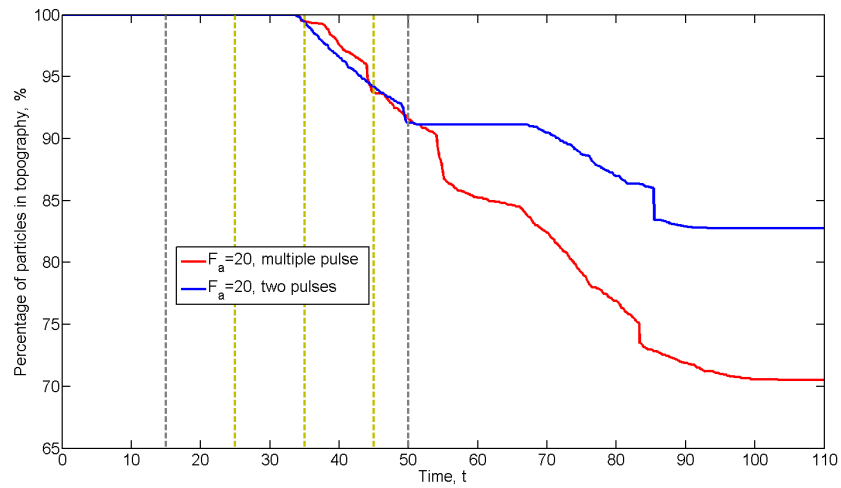


FIGURE 7.15: Percentage of particles remaining in the topography as time evolves when $F_a = 20$ for two pulses and five pulses (time of pulse indicated by dashed line).

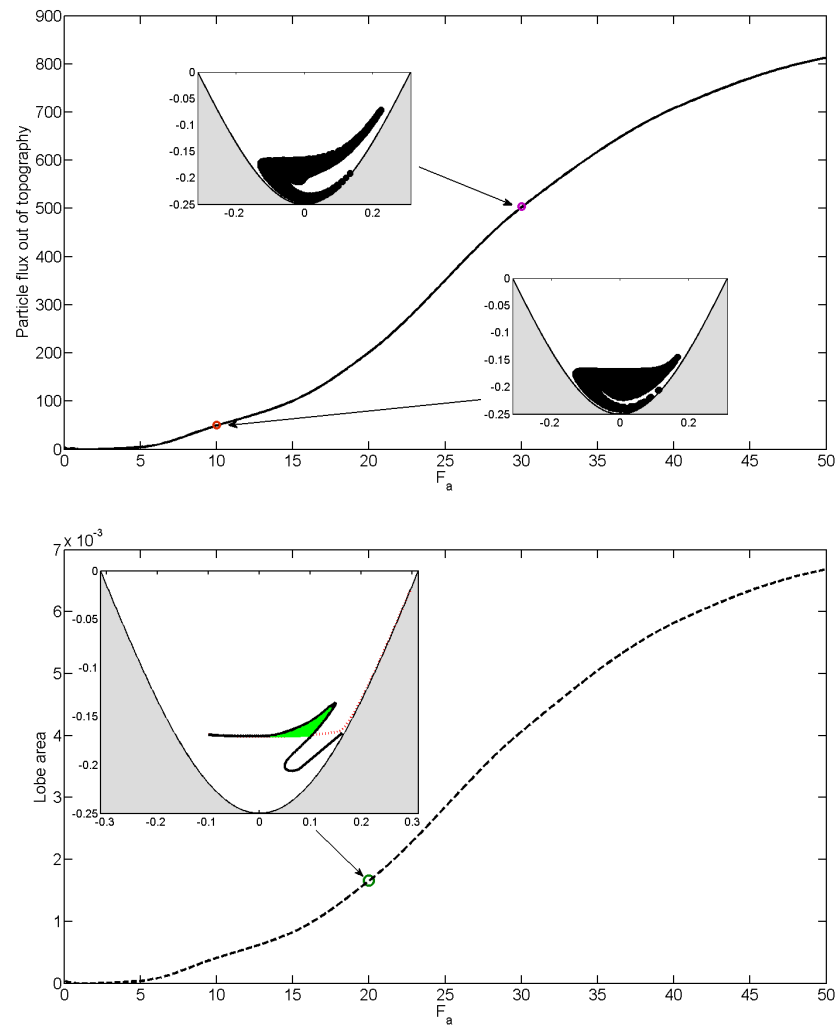


FIGURE 7.16: *Top*: Number of particles removed via one pulse as the pulse strength increases. The two examples visualised show the particle tracers been transported in lobes for $F_a = 10$ and $F_a = 30$. *Bottom*: Estimated area of the outward moving turnstile lobe. Visualised are portions of the stable and unstable manifolds forming lobes for $F_a = 20$.

The lobe area is shaded in green.

method. This is because the eddy structure will always persist for a geometrically induced eddy at all film thickness.

In a situation where the undulations and Reynolds number are such that no eddy is present, one may be induced by surface waves created by a pulsed inlet (or instability). This would create a local, temporary eddy in the topography inducing mixing of particles in the flow, when the flow settles/stabilises these particles would be released from the topography. This is illustrated in Figure 7.19 where a film with Reynolds number $Re = 10$ flows over a wave topography with amplitude 0.2. The substrate geometry and film inertia are such that no eddy is present. When the film inlet is pulsed, with $F_a = 5$, a free-surface disturbance is created and an inertially induced eddy is observed; the eddy increases in size and decreases in depth - minimum depth $|z_c| = 0.144$. The skewness of the eddy is a result of inertial effects as $Re = 10$ (Wierschem and Aksel, 2004; Scholle *et al.*, 2008). As the film disturbance decreases in size the eddy is forced down towards the substrate before disappearing as the pulse passes away downstream, see Figure 7.20. Note how there is no eddy present until the free-surface disturbance reaches approximately 1.05 and the eddy disappears at this level as the pulse passes over the topography. Note too, the critical Reynolds number for the appearance of an eddy in the steady state analogous scenario is $Re \approx 26$. For maximum mixing/stirring of the particles a longer pulse is required to maintain separated, re-circulating flow for a longer period of time.

7.3.2.1 Geometric effects

If the amplitude of the substrate topography is increased the eddy size (i.e. the surface area of the eddy) increases although the eddy centre stays relatively stationary. In this case if the film is pulsed the magnitude of motion of the eddy is the same; this means that although the same amount of material will be transported in or out of the separated flow area the proportion of material that is moved will decrease.

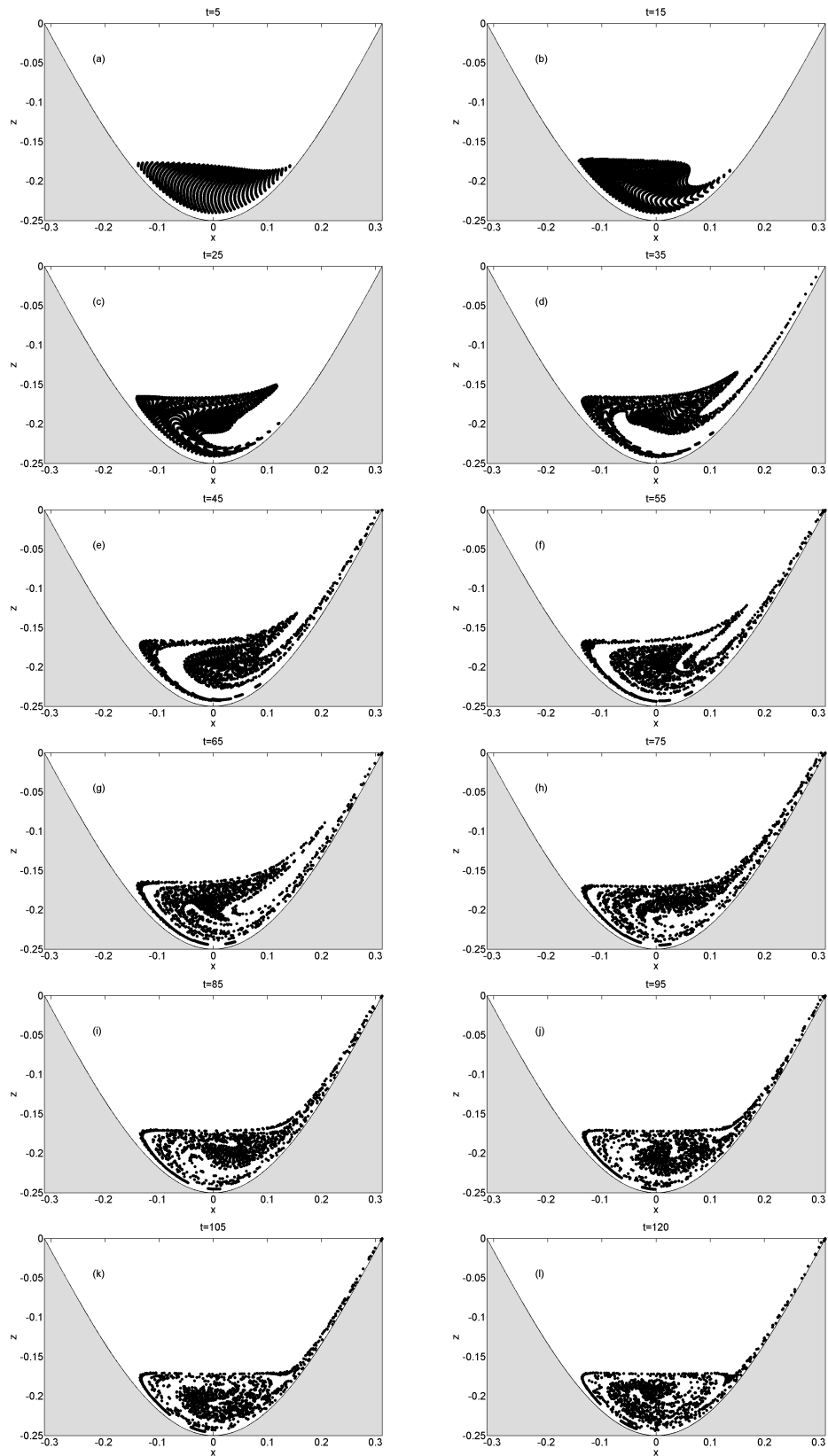


FIGURE 7.17: Particle tracking showing the stirring and transport enhancement created by pulsing the inlet condition multiple times.

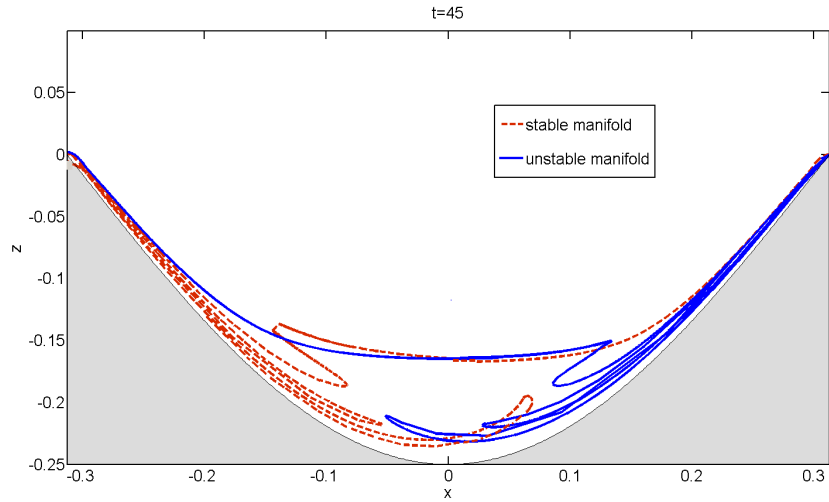


FIGURE 7.18: Unstable and stable manifolds for multiply pulsed situation demonstrating the transport enhancement via turnstile lobe mechanism and the increased mixing.

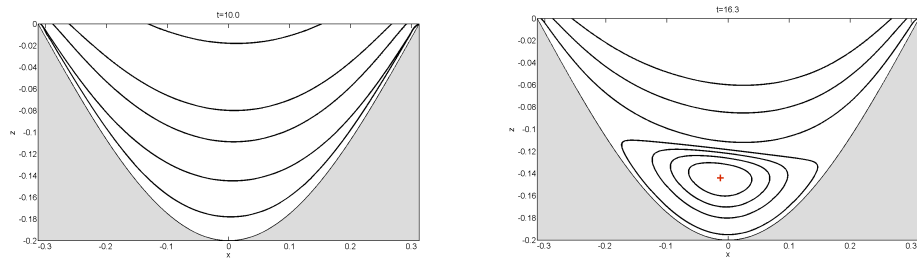


FIGURE 7.19: *Left:* Streamlines of the steady flow of a film flowing over a wave topography with $Re = 10$, no eddy is present at $t = 10$. *Right:* Streamlines at $t = 16.3$ as the free-surface disturbance created by pulsing the inlet velocity with $F_a = 5$ reaches the topography - an inertially induced eddy is created.

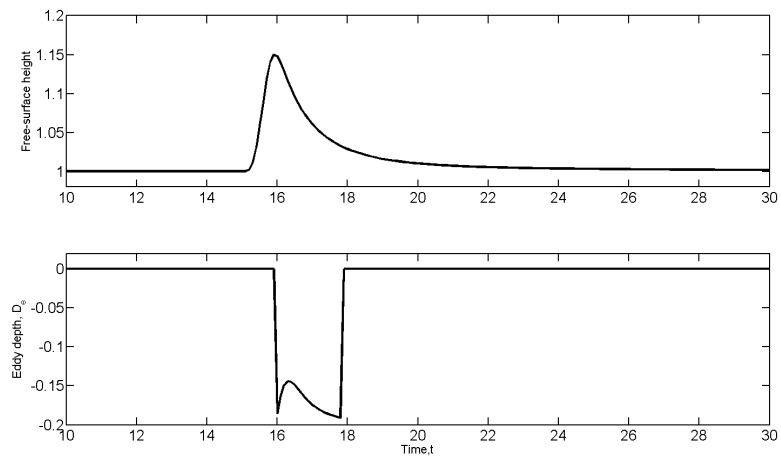


FIGURE 7.20: The free-surface height above the topography and the eddy height, D_e . $D_e = 0$ indicates no eddy present.

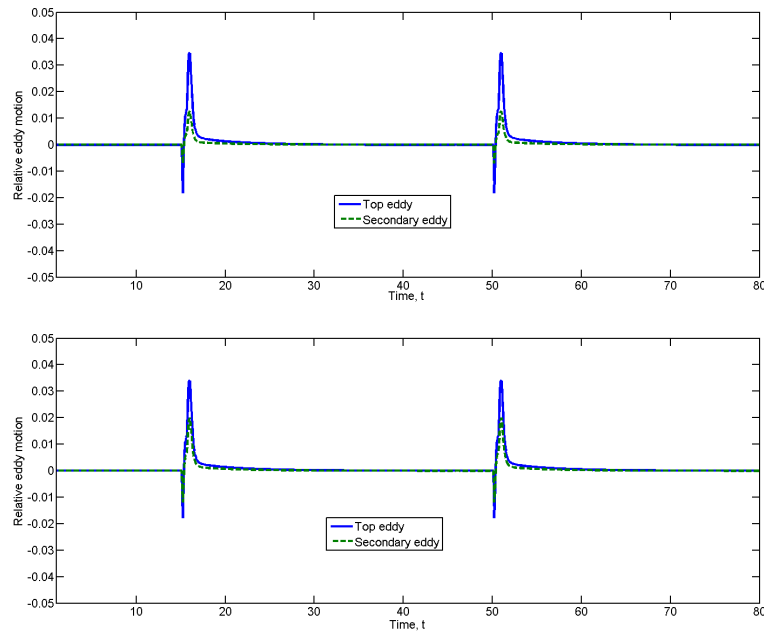


FIGURE 7.21: The relative eddy motion of the two eddies present in topography with (left) $A_t = 0.7$ and (right) $A_t = 1$.

A nested sequence of eddies were found to be present by Moffatt (1964) in wedge geometries, the number present being dependent on the specification of the geometry. In the case of wave topography, if the ratio of depth to wavelength of the topography increases to a large enough magnitude then a second eddy will form. In this case there are two layers of separated flow. The motion of the deeper eddy is less affected by the wave formed by the pulsed inlet condition as demonstrated in Figure 7.21 which shows the relative eddy motion of the two eddies present (that is the position relative to the steady state position). There are two sets of lobe dynamics induced; the usual motion between the overlying flow and the separated flow. The other is between the two areas of separated flow. The deeper the eddy the smaller the lobes that are formed meaning there is less transport between the regions of separated flow than the overlying flow and top separated flow region. An example of this is shown in Figure 7.22; note how the transport mechanism in the deeper eddy is also suppressed by the near stagnant velocity of the fluid near the bottom of the topography.

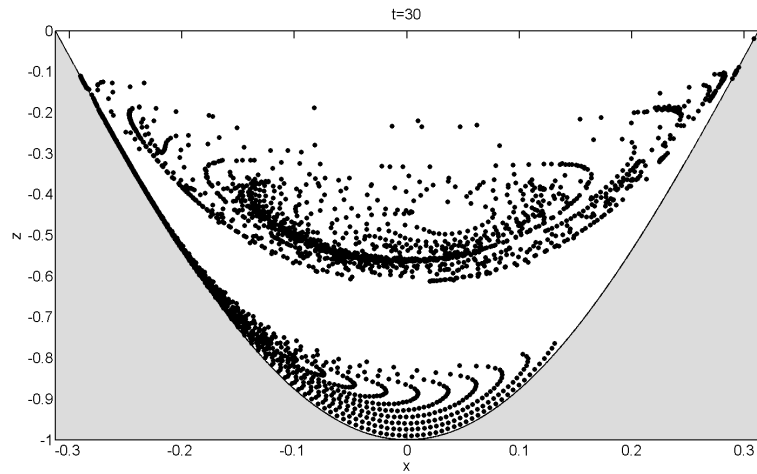


FIGURE 7.22: Illustrative particle tracking showing the two areas of separated flow within a topography of amplitude, $A_t = 1$.

7.3.3 Inertially induced eddy

In the previous section, manipulation and transport enhancement from an eddy induced by the geometry of the substrate is considered. Inertially induced eddies react the same as their geometrically induced counterparts when a deformation in the free-surface is induced by pulsing the inlet flow.

As noted previously, it is impossible to completely remove trapped particles from the separated flow caused by geometric factors due to the nature of the eddy. Following from this logic it is conceivable that this can be achieved when considering the situation of an inertially induced eddy by temporarily reducing the film thickness above the topography. In theory, if one pulses the inflow rate a suitable amount for a long enough period of time the local reduction in film thickness will lead to the temporary disappearance of the eddy. One can also justify this thought process by considering the topographies that do not contain geometrically induced eddies; those that have larger wavelength and smaller amplitude.

Similar to the previous scenario but with Reynolds number set to 30, the inflow rate was reduced with $F_a = 0.2$. Streamlines for the flow in its 'steady' state are shown in Figure 7.23. A small eddy is located near the base of the wave topography, the

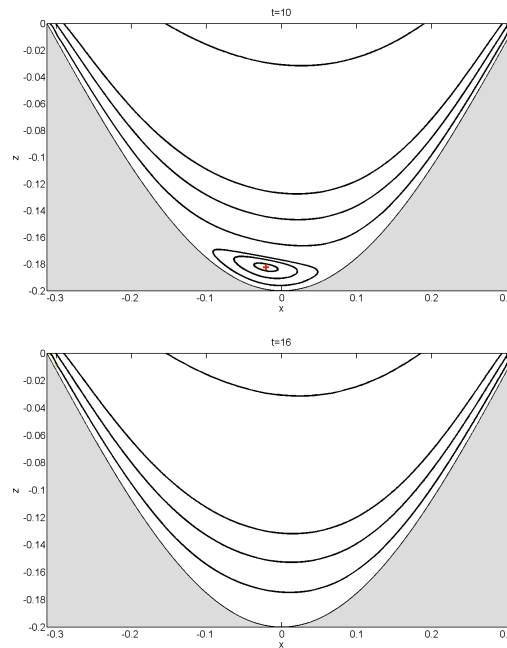


FIGURE 7.23: *Left:* Streamlines of the steady flow of a film flowing over a wave topography with $Re = 30$, no eddy is present at $t = 10$. *Right:* Streamlines at $t = 16.3$ as the free-surface disturbance created by pulsing the inlet velocity with $F_a = 0.2$ reaches the topography - the eddy is suppressed.

skewed separated flow area is due to inertial effects. This hasn't been seen, to such an extent, in previous results due to the lower values of Re employed. After the inlet condition is altered the separated flow is reconnected to the bulk flow, see the streamlines in the second figure in Figure 7.23.

7.4 Summary

This chapter used a Bubnov-Galerkin finite element method to discretise the full, time-dependent Navier-Stokes and continuity equations in two-dimensions to investigate flow over wavy topography. Within wavy topography an eddy, that is an area of separated flow, can form trapping liquid in the topography valley.

By pulsing the inlet condition of velocity it is possible to induce a surface wave. As the wave passes over the topography the increase in local film thickness induces

a motion in the position of the eddy structure that forms. This motion creates a transport of liquid across the separatrix via a turnstile lobe mechanism. The larger the pulse the larger the amount of liquid that is transported. The lobes are visualised using particle tracking calculations and by plotting the unstable and stable manifolds.

An increase in the depth of the valley of the topography leads to an increase in the size of the separated flow area. The proportion of liquid transported in and out of the region is thus decreased. If the valley depth is increased a secondary eddy can be induced. In this case the motion of the deeper eddy is damped so only a small amount of liquid is transported between regions of separated flow.

It is shown that by using the knowledge of how eddies respond to changes in inertia (Scholle *et al.*, 2008) that an eddy can either be suppressed, briefly, or induced where before there was no eddy. This is an interesting feature that could be exploited to either increase mixing of a fluid or release a majority of material that is trapped within a separated flow region.

The results here match up with the theory developed by Scholle *et al.* (2008) and form a preliminary investigation into the turnstile lobe mechanism in this free-surface scenario. The main issue with the work conducted in this chapter is the need for extensive computational resources to obtain solutions; should one wish to extend the work to three-dimensions these requirements may become insurmountable.

Chapter 8

Conclusion and Further Work

Contents

8.1	Conclusions of current study	186
8.2	Suggested future work	191

8.1 Conclusions of current study

The work presented within this thesis contributes to existing knowledge within the field of gravity-driven thin films, in a number of areas:

1. The development of efficient numerical procedures, finite difference and finite element based, to solve different governing equation sets (a lubrication model and the full Navier-Stokes equations) to enable the long-time investigation of the flows of interest.
2. The addition of new and important understanding in relation to the rivulet instability synonymous with an advancing liquid front from a number of different stand points - the classical problem of flow down a planar substrate, wetting properties, the presence of heterogeneities (chemical and/or topographical features) on the substrate, flow down curved substrates namely cylinders; a key feature of the work is consideration of the phenomena of both complete and partially wetting liquids.
3. The undertaking of the first numerical investigation of transport enhancement via symmetry breaking of film flow over a wavy trench topography, and exploration of the mechanism affecting the removal of fluid trapped within closed eddies, located in valleys, by pulsing the flow.

The long-wave (lubrication) approximation facilitates the reduction of order of the problem while still revealing important aspects of the flow, in particular the free-surface disturbance and associated dynamics. The nature of the equations are particularly well suited to approximation via a finite-difference methodology and solution using a multigrid technique. The addition of adaptive features, including error-controlled local mesh refinement and automatic, variable time-stepping, increases the efficiency of the latter further still. For the problem of rivulet flow a new feature called grid devolution is introduced, which in conjunction with the former refinements, allows for the rapid generation of long-time three-dimensional

solutions; efficiency is found to be at worst of $O(N)$ for N unknowns, with even greater improvements in efficiency obtained with high levels of mesh adaptivity.

The Navier-Stokes equations are solved using a Bubnov-Galerkin finite element approximation which involves mixed interpolation for the flow variables and free-surface parametrisation based on the Arbitrary Lagrangian-Eulerian method of spines. Unlike the lubrication equations, this approach is well suited to revealing simultaneously both the inner flow features and the shape of the unbounded free-surface. Utilising parallel computational methods along with an out-of-core approach for storing matrix cofactors on the hard drive, results are generated in the most memory efficient route possible.

The solutions obtained for rivulet formation on an inclined planar substrate are compared with existing experimental data, revealing excellent agreement between the two. The results obtained via a complementary linear stability analysis are also found to agree well at high inclination angles but less so at lower inclination angles. Long-time solutions reveal the merger of rivulets that evolve in close proximity to each other, restricting the critical wavelength of the instability to a minimum size, i.e. a maximum number of fingers per unit width of the substrate. Surface tension forces limit the possible curvature between rivulets (that is the steepness of the sides of the rivulets directly effecting the width), if this limit is exceeded then the rivulets will merge. The incorporation of wetting effects, via a disjoining pressure model, unveils the impact low wettability has on the formation of rivulets; the rate of elongation is increased and their width decreases which in turn leads to a reduction in wavelength due to the possibility of more rivulets growing in close proximity to one another. Plots of three-dimensional free-surface data reveal the large differences that arise in the rivulet patterns formed for fully wetting and partially wetting fluids. These differences become exaggerated as the wettability of the fluid decreases, that is as the contact angle between the liquid film and the substrate.

By systematically generating a large data set, a new general model formula for predicting the wavelength of rivulets formed on an inclined plane, incorporating

the effects of partial wetting, has been developed. While the classical model of Huppert predicts a linear proportionality between the wavelength and the capillary length regardless of whether the liquid is fully or partially wetting, the new model includes a slightly larger power for the capillary number while accounting for the wetting characteristics; it is the first of its kind to do so.

While flow on a planar uniformly homogeneous surface is important from a general engineering perspective, in practice surfaces tend to contain heterogeneities which are topographical and/or chemical in nature. Rivulet flow over square trench and peak topography is considered, revealing the subtle effects resulting from small surface imperfections. A trench topography has previously been observed to create a surge in the continuous film case; this surge effects rivulet flow by enhancing the elongation of the rivulets directly downstream of the trench. A peak topography can deflect a rivulet that meets it, altering its previous trajectory. These influences can lead to merging as the rivulets are forced to evolve within a certain proximity (the critical wavelength from Chapter 4) of one another.

Chemical heterogeneities are also found to influence the evolution of rivulets; they can induce a rivulet instability. Should a flow of rivulets meet a set of patches the rivulets travel preferentially along the highest wetting areas. This can lead to a number of different scenarios; a deflection in the trajectory as the edge of a rivulet is slowed by the low wetting region while the remainder of the rivulet flows freely through the fully wetting area. A rivulet can also thin if the spacing between low wetting regions is smaller than the rivulet width, the finger height increases as the liquid is squeezed into a smaller area - once past the patches the rivulet relaxes to its usual width. Two rivulets can be forced to merge due to alteration in their trajectories as described above. The effect of the wetting regions can lead to a decrease in the number of rivulets; if an evolving advancing front spreads from a low wetting area onto a high wetting one the critical wavelength increases and so neighbouring rivulets merge. In the opposite scenario the number of rivulets stays constant but they become thinner. The number of rivulets can decrease but can

never increase without an external influence inducing more rivulets.

The influence of a surface tension gradient and accompanying Marangoni stresses is also considered. A positive surface tension gradient promotes the elongation of rivulets in gravity-driven rivulet flow, and the opposite effect is observed for a negative gradient. The decrease in elongation leads to an earlier onset of merging, and an increase in elongation rate delays merger when compared to the corresponding zero surface tension gradient case. Slowing the rate of rivulet growth could be of practical use to facilitate more complete surface coverage. The same model is used to explore climbing films, yielding reasonable qualitative agreement to experimental data. In the climbing film case, the Marangoni stresses counteract gravity to pull the liquid up a vertical substrate. The size of the gradient controls the width and wavelength - much the same as the size of inclination angle does in the gravity driven case.

Continuing the above theme of modelling film flow over real surfaces, the problem of flow down a vertically-aligned cylinder is investigated. The problem is formulated using a long-wave approximation that is not based on the lubrication parameter but a new parameter that measures the disparity between asymptotic film thickness and the cylinder radius. By mapping the cylinder onto a rectangular computational mesh it is possible to apply the same multigrid solution methodology used in the plane case. Results are compared with recent experimental data and, again, show very good agreement. The correlation of experimental data and numerical results is good for both fully and partially wetting films with similar observations of the differences between the two as in the inclined plane case. The findings of the numerical investigation for a wide range of different sized cylinders reveal the subtle interplay of curvature effects and the restriction of the cylinder circumference. At large radii, i.e. small curvature, the behaviour of the instability mirrors that on a vertical plane. As the radius of the cylinders is decreased curvature becomes increasingly important in counteracting the capillary forces that limit the space between rivulets and thus result in merging, leading to a decrease in wavelength compared

to that observed in the equivalent plane case. As the radii is decreased further still, the circumference becomes too small to accommodate more than one rivulet; if two or more start to form they are forced to coalesce. These observations are captured in an extension of the wavelength model developed for the plane case. By adding an additional term based on the relative curvature of the cylinder to the term found for wavelength in the planar case, it is possible to reproduce results of numerical simulations and experiments.

The second, very different, problem considered in this thesis required the generation of solutions to the full Navier-Stokes and continuity equations in order to visualise the eddies/separated flow present within the valleys formed by a wavy topography supporting the flow of a continuous liquid film. By pulsing the inlet condition, and thus creating either a surface wave or depression, induces symmetry breaking of the previously steady eddy centre, separatrix and size of separated flow region. The motion of this inner flow exhibits a transport enhancement mechanism via turnstile lobe structures. As the film thickness changes as the wave flows over the topography, the eddy shrinks and becomes located deeper in the valley before enlarging again, resuming eventually its steady position prior to the pulse. The motion that is triggered is elucidated by seeding the region with tracer particles and then observing their trajectories as the flow evolves. The lobes formed by the transient motion can be visualised by either tracking inert particles in the flow or plotting the stable and unstable manifolds associated with the wall attachment points. The transfer of fluid from the eddy region is a function of the free-surface deformation. To increase the transfer the pulse should be either large or, if a large deformation of the free-surface is undesirable, applied for a longer time. Geometrically induced eddies persist at all Reynolds numbers and so can't be suppressed; however, for inertially induced eddies it is possible to enforce a temporary disappearance of the separated flow - leading to a large increase in transport of fluid to the bulk flow. If the topography is such that no eddy is present, by increasing the local inertia by pulsing the inlet flow an eddy can be temporarily induced. These findings are preliminary and should be

extended to fully undulating substrates.

8.2 Suggested future work

The problem formulations, models and solution methodologies are adaptable and can be extended to further investigations of rivulet flow. While a thorough investigation of gravity-driven rivulet formation has been conducted for both fully and partially wetting fluids there are still other practical scenarios that require attention. One such problem is that of spin coating; while there has been some research garnered on such flow, the area would benefit from a similar investigation as conducted here including partial wetting and substrate heterogeneities.

Extensions of the inclined plane case to reveal further the interplay of other physical effects with the advancing front instability would be of interest, for instance, flow on a porous or flexible surface or the effect of an insoluble surfactant. As an extension to the current work the implementation of an evaporation model alongside the surface tension gradient model would certainly offer further insights. By understanding the effects of these influences it may be possible to develop a realistic methodology to control the formation of rivulets or, further still, suppress the instability completely.

Inertial effects on rivulet flow could also be explored via the Depth Average Form (DAF) of the governing equations (Veremieiev *et al.*, 2010). Le Grand-Piteira *et al.* (2006) found that the meandering of a single rivulet could be explained via a balance between inertia and capillarity, it would be of interest to observe whether this meandering occurs in a inertial regime for a spreading film. Obviously this has an enormous effect on the efficiency of surface coverage.

An interesting related problem to flow on a cylindrical substrate relates to the flow down the inner surface of such a tube like structure. The filling of tubes can be found in a number of situations, for instance in the medical world, and so an investigation

into the optimal flow rate required for the tube to be filled with liquid would reveal results of interest.

The continued investigation of the coating of real surfaces is required from an application point of view. Flow on a cone for instance would be a fascinating extension of the cylinder problem. The increasing size of the radius of the substrate would introduce thinning into the problem. Whether this would affect the growth rate and number of rivulets is still unknown. Such a scenario could be extended to simulate the flow of lava on the side of a volcano amongst other situations.

The enhancement of transport within wavy topography has been carried out in a two-dimensional framework. Shear-driven flow and flow over other shaped substrates is also easily possible - the specification of the problem can be readily adapted to the required application. These preliminary investigations for flow over a half-period sinusoidal wave topography provide an insight into expected behaviour in a full period sinusoidally undulating type substrate. The work will thus be extended to reveal the exchange of material within the eddies formed in the valleys of an undulating substrate and the overlying bulk flow. Shear-driven flow may be considered to separate the effects at work; in the free-surface case the film thickness deforms inducing a motion in the eddy, by using a shear driven flow to induce lobe dynamics this effect would be quelled. Transferring liquid trapped in eddies between successive topographies could be of interest together with how the number of such topographical features effects the residence time of the liquid in the substrate and would form a natural extension of the work. The results obtained here provide an insight into the breadth of possible investigations; the desired final outcome would be to develop a full three-dimensional model for a large domain of undulating substrate. This would require the use of prohibitive computational resources which can only be found at specialist facilities.

While the current study is carried out using numerical strategies due to the complicated and difficult challenges facing an experimentalist, it is important to confirm the findings of numerical simulations where possible, as well as add important

findings to challenge further numerical studies. An in depth study of the effect of wettability on rivulet formation concentrating on the wetting properties of the fluid would add much needed data and knowledge to the area, while also being a good starting point of further experimental studies.

Appendix A

Long-wave approximation

Contents

A.1	Governing equations	195
-----	-------------------------------	-----

The lubrication equations (2.23) and (2.24) can be thought of as a first-order long-wave approximation of the non-dimensional Navier-Stokes equations, (2.50) and (2.51), and boundary conditions (2.3) - (2.6). The long-wave approximation essentially reduces the dimensionality of the problem by one (Oron *et al.*, 1997) by assuming that the long-wave ratio $\epsilon = H_0/L_0$, that is the ratio of characteristic film thickness and the associated length scale (in the lubrication approach this is the capillary length), is small, i.e. $\epsilon \ll 1$.

A.1 Governing equations

To formulate the Navier-Stokes and continuity equations for thin film flow under gravity down a planar surface inclined at α to the horizontal as shown in Figure 2.1, employing a Cartesian coordinate system, in terms of L_0 the variables are shifted via:

$$(x, y, l_t, w_t, t, p) \rightarrow (x, y, l_t, w_t, t, p) / \epsilon, \quad w \rightarrow \epsilon w,$$

giving:

$$\begin{aligned} \epsilon Re \left(\frac{\partial u}{\partial t} + u \frac{\partial u}{\partial x} + v \frac{\partial u}{\partial y} + w \frac{\partial u}{\partial z} \right) &= -\frac{\partial p}{\partial x} + \epsilon^2 \left(\frac{\partial^2 u}{\partial x^2} + \frac{\partial^2 u}{\partial y^2} \right) + \frac{\partial^2 u}{\partial z^2} + 2, \\ \epsilon Re \left(\frac{\partial v}{\partial t} + u \frac{\partial v}{\partial x} + v \frac{\partial v}{\partial y} + w \frac{\partial v}{\partial z} \right) &= -\frac{\partial p}{\partial x} + \epsilon^2 \left(\frac{\partial^2 v}{\partial x^2} + \frac{\partial^2 v}{\partial y^2} \right) + \frac{\partial^2 v}{\partial z^2}, \\ \epsilon^3 Re \left(\frac{\partial w}{\partial t} + u \frac{\partial w}{\partial x} + v \frac{\partial w}{\partial y} + w \frac{\partial w}{\partial z} \right) &= \\ &= -\frac{\partial p}{\partial z} + \epsilon^4 \left(\frac{\partial^2 w}{\partial x^2} + \frac{\partial^2 w}{\partial y^2} \right) + \epsilon^2 \frac{\partial^2 w}{\partial z^2} - 2\epsilon \cot \alpha, \\ \frac{\partial u}{\partial x} + \frac{\partial v}{\partial y} + \frac{\partial w}{\partial z} &= 0. \end{aligned}$$

The normal vector, tangential vector components, viscous stress tensor and free-surface curvature terms (noting that f_x represents the partial derivative of f with respect to x , etc.);

$$\mathbf{n} = \frac{(-\epsilon f_x, -\epsilon f_y, 1)}{[\epsilon^2 (f_x^2 + f_y^2) + 1]^{\frac{1}{2}}}, \quad (\text{A.1})$$

$$\mathbf{t}_x = \frac{(1, 0, \epsilon f_x)}{(1 + \epsilon^2 f_x^2)^{\frac{1}{2}}}, \quad (\text{A.2})$$

$$\mathbf{t}_y = \frac{(0, 1, \epsilon f_y)}{(1 + \epsilon^2 f_y^2)^{\frac{1}{2}}}, \quad (\text{A.3})$$

$$\underline{\underline{\tau}} = \begin{pmatrix} 2\epsilon u_x & \epsilon(u_y + v_x) & u_z + \epsilon^2 w_x \\ \epsilon(u_y + v_x) & 2\epsilon v_y & v_z + \epsilon^2 w_y \\ u_z + \epsilon^2 w_x & v_z + \epsilon^2 w_y & 2\epsilon w_z \end{pmatrix} \quad (\text{A.4})$$

$$\kappa = \epsilon^2 \frac{f_{xx} + f_{yy} + \epsilon^2 [f_{xx}f_y^2 + f_{yy}f_x^2 - 2f_{xy}f_xf_y]}{[1 + \epsilon^2 (f_x^2 + f_y^2)^{\frac{3}{2}}]}. \quad (\text{A.5})$$

The boundary conditions at $z = f = h(x, y, t) + s(x, y)$ for the normal and tangential stress can then be written as:

$$-p + 2\epsilon^2 \left[\frac{-u_z f_x - v_z f_y + w_z}{1 + \epsilon^2 f_x^2 + \epsilon^2 f_y^2} + \epsilon^2 \frac{(u_x f_x^2 + u_y f_y^2 + (u_y + v_x) f_x f_y - w_x f_x - w_y f_y)}{1 + \epsilon^2 f_x^2 + \epsilon^2 f_y^2} \right] = \frac{\epsilon \kappa}{Ca}, \quad (\text{A.6})$$

$$u_z + \epsilon^2 [f_x (-u_z f_x - v_z f_y + 2w_z) - 2u_x f_x - (u_y + v_x) f_y + w_x - \epsilon^2 (w_x f_x + w_y f_y)] = 0, \quad (\text{A.7})$$

$$v_z + \epsilon^2 [f_y (-u_z f_x - v_z f_y + 2w_z) - 2v_y f_y - (u_y + v_x) f_x + w_y - \epsilon^2 (w_x f_x + w_y f_y)] = 0. \quad (\text{A.8})$$

If only leading order terms in ϵ are retained and boundary conditions applied, it

follows that long-wave equations reduce to:

$$\frac{\partial h}{\partial t} = \frac{\partial}{\partial x} \left[\frac{h^3}{3} \left(\frac{\partial p}{\partial x} - 2 \right) \right] + \frac{\partial}{\partial y} \left[\frac{h^3}{3} \left(\frac{\partial p}{\partial y} \right) \right], \quad (\text{A.9})$$

$$p = -\frac{\epsilon^3}{Ca} \nabla^2 (h + s) + 2\epsilon (h + s - z) \cot \alpha, \quad (\text{A.10})$$

as given in Chapter 2.

Appendix B

Governing equations of rivulet formation on a vertically aligned cylinder

Contents

B.1 Long-wave approximation	199
B.2 Discretisation	204
B.2.1 Spatial discretisation	204
B.2.2 Temporal discretisation	205

B.1 Long-wave approximation

Consider the case of a thin film flowing down a vertically aligned cylinder of radius R_0 and height L_R , as shown schematically in Figure 6.1. The circumference of the cylinder is denoted by $C_R = 2\pi R_0$. The film is fed by a constant inflow at the upstream boundary, the fully developed film thickness is denoted by H_0 . Surface tension, σ , dynamic viscosity, μ , and density, ρ , are assumed constant. In cylindrical coordinates, any point has position (Y, θ, Z) , the radius to the free-surface, R , is given by $R_H = R_0 + H(\theta, Z, T)$ where H is the film thickness and T is the time. In the cylindrical co-ordinate system the fluid velocity is denoted by (U, V, W) .

Following Smolka and SeGall (2011), a long-wave model is derived based on the assumption that $\epsilon_R = H_0/R_0 \ll 1$. Non-dimensional variables are introduced in a similar manner seen when deriving similar equations for thin film flow down a inclined, flat substrate, namely;

$$(y, h, h^*) = \frac{(Y, H, H^*)}{\epsilon_R R_0}, \quad (z, r, l_r) = \frac{(Z, R, L_r)}{R_0}, \quad t = \frac{T}{T_0}, \quad \kappa = R_0 \tilde{\kappa},$$

$$p = \frac{P}{\rho g H_0}, \quad (u, v, w) = \left(\frac{U}{\epsilon_R U_0}, \frac{V}{U_0}, \frac{W}{U_0} \right), \quad T_0 = \frac{R_0}{U_0};$$

giving the non-dimensional radius as $r = 1 + \epsilon_R y$.

Introducing the non-dimensional variables into the cylindrical Navier-Stokes and

continuity equations leads to:

$$\begin{aligned}
& \epsilon_R^2 Re \left(\epsilon_R \frac{\partial u}{\partial t} + \epsilon_R u \frac{\partial u}{\partial y} + \epsilon_R \frac{v}{r} \frac{\partial u}{\partial \theta} + \epsilon_R w \frac{\partial u}{\partial z} - \frac{v^2}{r} \right) = \\
& \quad - \frac{\partial p}{\partial y} + \epsilon_R \Delta_r u - \epsilon_R^3 \frac{u}{r^2} - \frac{2\epsilon_R^2}{r^2} \frac{\partial v}{\partial \theta}, \\
& \epsilon_R^2 Re \left(\frac{\partial v}{\partial t} + u \frac{\partial v}{\partial y} + \frac{v}{r} \frac{\partial v}{\partial \theta} + w \frac{\partial v}{\partial z} + \frac{\epsilon_R u v}{r} \right) = \\
& \quad - \frac{\epsilon_R}{r} \frac{\partial p}{\partial \theta} + \Delta_r v - \epsilon_R^2 \frac{v}{r^2} + \frac{2\epsilon_R^3}{r^2} \frac{\partial u}{\partial \theta}, \\
& \epsilon_R^2 Re \left(\frac{\partial w}{\partial t} + u \frac{\partial w}{\partial y} + \frac{v}{r} \frac{\partial w}{\partial \theta} + w \frac{\partial w}{\partial z} + \frac{\epsilon_R u v}{r} \right) = -\epsilon_R \frac{\partial p}{\partial z} + \Delta_r v + 1, \\
& \quad \frac{1}{r} \frac{\partial (ru)}{\partial y} + \frac{1}{r} \frac{\partial v}{\partial \theta} + \frac{\partial w}{\partial z} = 0,
\end{aligned}$$

where the Reynolds number is given by $Re = \rho R U_0 / \mu$; Δ_r is the cylindrical version of the usual Laplace second derivative operator calculated via:

$$\Delta_r = \frac{1}{r} \frac{\partial (r \frac{\partial}{\partial y})}{\partial y} + \frac{\epsilon_R^2}{r^2} \frac{\partial^2}{\partial \theta^2} + \epsilon_R^2 \frac{\partial^2}{\partial z^2}. \quad (\text{B.1})$$

As in Appendix A, the above equations are simplified by assuming higher order terms are small and only terms larger than $O(\epsilon_R^2 Re)$ are retained.

The usual no-slip condition is applied at the surface of the cylinder. At the free-surface boundary, kinematic, tangential and normal stress conditions given by:

$$\frac{\partial h}{\partial t} + v \frac{\partial h}{\partial \theta} + w \frac{\partial h}{\partial z} = u, \quad (\text{B.2})$$

$$\mathbf{t} \cdot (-p \mathbf{I} + \underline{\underline{\tau}}) \cdot \mathbf{n} = 0, \quad (\text{B.3})$$

$$\mathbf{n} \cdot (-p \mathbf{I} + \underline{\underline{\tau}}) \cdot \mathbf{n} = \sigma \tilde{\kappa} + \Pi(h), \quad (\text{B.4})$$

are applied where $\underline{\underline{\tau}}$ represents the viscous stress tensor, \mathbf{n} denotes the normal to the free-surface and \mathbf{t} is the tangential to the free-surface which can be split into

two components, \mathbf{t}_θ and \mathbf{t}_y (Evans *et al.*, 2004). In non-dimensionalised cylindrical coordinates the normal to the free-surface (excluding terms of higher order) is:

$$\mathbf{n} = \left(1, -\epsilon_R \frac{\partial h}{\partial \theta}, -\epsilon_R \frac{\partial h}{\partial z} \right). \quad (\text{B.5})$$

Similarly, the two tangents to the free-surface are given by

$$\mathbf{t}_\theta = \left(\epsilon_R \frac{\partial h}{\partial \theta}, 1, 0 \right), \quad (\text{B.6})$$

$$\mathbf{t}_y = \left(\epsilon_R \frac{\partial h}{\partial z}, 0, 1 \right). \quad (\text{B.7})$$

An approximation to the free-surface, κ , is found via:

$$\tilde{\kappa} = R_0 \kappa = R_0 \nabla \cdot \mathbf{n} = 1 - \epsilon_R h - \epsilon_R \nabla^2 h + O(\epsilon_R^2), \quad (\text{B.8})$$

here ∇ denotes the dimensionless gradient operator in cylindrical terms, i.e. $\nabla = \left(\frac{\partial}{\partial z}, \frac{\partial}{\partial \theta} \right)$. Substituting it into the normal stress boundary condition and neglecting higher order terms, it can be shown that at the free-surface:

$$-p = -\frac{\tilde{\kappa}}{\epsilon_R B_{OR}} + \Pi(h), \quad (\text{B.9})$$

where $B_{OR} = \rho g R_0^2 / \sigma$ is the Bond number, closely linked to the Bond number used in modelling gravity driven films on a flat, inclined substrate which is given by $Bo = \rho g H_0^2 / \sigma = \epsilon_R^2 B_{OR}$ (Gaskell, Jimack, Sellier and Thompson, 2004).

The tangential stress and kinematic conditions are also reduced to

$$\frac{\partial v}{\partial y} - \epsilon_R v + O(\epsilon_R^2) = 0, \quad (\text{B.10})$$

$$\frac{\partial w}{\partial y} + O(\epsilon_R^2) = 0, \quad (\text{B.11})$$

$$\frac{\partial h}{\partial t} + \frac{v}{r} \frac{\partial h}{\partial \theta} + w \frac{\partial h}{\partial z} = u, \quad (\text{B.12})$$

respectively.

Terms for velocity are found via equations (B.9) - (B.12); at first order the relevant velocity terms are:

$$\mathbf{u}^{(0)}(y, \theta, z, t) = (u^{(0)}, v^{(0)}, w^{(0)}) = \left(-\frac{1}{2}y^2 \frac{\partial h}{\partial z}, 0, -\frac{1}{2}y^2 + hy \right), \quad (\text{B.13})$$

and at $O(\epsilon_R)$, $u^{(1)} = 0$ and

$$v^{(1)} = \left(\frac{y^2}{2} - hy \right) \frac{\partial p}{\partial \theta}, \quad (\text{B.14})$$

$$w^{(1)} = \left(\frac{y^2}{2} - hy \right) \frac{\partial p}{\partial z} + \frac{1}{6} (y^3 - 3y^2h + 3yh^2). \quad (\text{B.15})$$

Making use of the kinematic boundary condition (B.12), in combination with conservation of mass and the no-slip condition, the relationship representing the required governing equations is obtained as:

$$(1 + \epsilon_R h) \frac{\partial h}{\partial t} + \frac{\partial}{\partial \theta} \int_0^h (v^{(0)} + \epsilon_R v^{(1)}) dy + \frac{\partial}{\partial z} \int_0^h (1 + \epsilon_R y) (w^{(0)} + \epsilon_R w^{(1)}) dy = 0. \quad (\text{B.16})$$

By substituting the velocity and pressure terms (B.9), (B.14) and (B.15), respectively, into equation (B.16) and solving, a coupled set of governing lubrication equations is obtained in terms of non-dimensional film thickness, h , and pressure, p , for thin film flow down a vertically aligned cylinder:

$$(1 + \epsilon_R h) \frac{\partial h}{\partial t} = \frac{\partial}{\partial z} \left[\frac{\epsilon_R h^3}{3} \left(\frac{\partial p}{\partial z} - \frac{1}{\epsilon_R} - h \right) \right] + \frac{\partial}{\partial \theta} \left[\frac{\epsilon_R h^3}{3} \left(\frac{\partial p}{\partial \theta} \right) \right], \quad (\text{B.17})$$

$$p = -\frac{1}{Bo_R} (h + \nabla^2 h) - \Pi(h). \quad (\text{B.18})$$

As only pressure gradients affect the flow the term $(\epsilon_R Bo_R)^{-1}$ is neglected. In

addition, the disjoining pressure, $\Pi(h)$ is calculated via the term

$$\Pi(h) = \frac{(1 - \cos \theta_c)(n-1)(m-1)}{\epsilon_R^2 B o_R (n-m)} \left[\left(\frac{h^*}{h} \right)^n - \left(\frac{h^*}{h} \right)^m \right]. \quad (\text{B.19})$$

The spanwise boundary conditions are adjusted to account for the geometry, as such they become periodic, namely:

$$h(0, z, t) = h(2\pi, z, t) \quad p(0, z, t) = p(2\pi, z, t). \quad (\text{B.20})$$

The film height is specified as fully developed at the inlet, $h(\theta, 0, t) = 1$, and to be equal to the precursor film downstream of an advancing front extending to the bottom end of the cylinder, $h(\theta, l_r, t) = h^*$.

The profile of the front is taken initially to be a flat front perturbed in the spanwise direction with a superposition of M modes with random length, $l_j \in [-0.2, 0.2]$, and differing wavelength, $\lambda_{0,j} = 2w_p/j$ for $j = 1, \dots, N$, in the same manner as in Kondic and Diez (2001), given by the following equations:

$$h(\theta, z, 0) = 0.5 \left\{ 1 + h^* - (1 - h^*) \tanh \left[\frac{(x - x_f(\theta))}{\delta} \right] \right\} \quad (\text{B.21})$$

$$x_f(\theta) = x_u - \sum_{j=1}^M l_j \cos(2\pi\theta/\lambda_{0,j}) \quad (\text{B.22})$$

with δ controlling the steepness, taken here to be 0.1, and x_u is the position of the unperturbed front (taken to be 30). Its subsequent evolution is independent of the initial condition imposed provided M is sufficiently large.

B.2 Discretisation

B.2.1 Spatial discretisation

Equations (B.17) and (B.18) are discretised via central-differencing Lee *et al.* (2007), leading to second order accurate spatial analogues of the form:

$$(1 + \epsilon_R h) \frac{\partial h_{i,j}}{\partial t} = \frac{1}{\Delta_{cyl}^2} \left[\frac{\epsilon_R h^3}{3} \Big|_{i+\frac{1}{2},j} (p_{i+1,j} - p_{i,j}) - \frac{\epsilon_R h^3}{3} \Big|_{i-\frac{1}{2},j} (p_{i,j} - p_{i-1,j}) \right. \\ \left. + \frac{\epsilon_R h^3}{3} \Big|_{i,j+\frac{1}{2}} (p_{i,j+1} - p_{i,j}) - \frac{\epsilon_R h^3}{3} \Big|_{i,j-\frac{1}{2}} (p_{i,j} - p_{i,j-1}) \right] \\ - \frac{1}{\Delta_{cyl}} \left(\frac{h^3}{3} \Big|_{i+\frac{1}{2},j} - \frac{h^3}{3} \Big|_{i-\frac{1}{2},j} + \frac{\epsilon_R h^4}{3} \Big|_{i+\frac{1}{2},j} - \frac{\epsilon_R h^4}{3} \Big|_{i-\frac{1}{2},j} \right), \quad (\text{B.23})$$

$$p_{i,j} + \frac{1}{B_{OR} \Delta_{cyl}^2} [h_{i+1,j} + h_{i-1,j} + h_{i,j+1} + h_{i,j-1} - 4h_{i,j}] + \frac{h_{i,j}}{B_{OR}} + \Pi(h_{i,j}) = 0, \quad (\text{B.24})$$

for all points (i, j) in the computational domain, $\Omega = (0, l_r) \times (0, 2\pi)$; with Δ_{cyl} the size of the grid cells (for simplicity the discretisation using a square mesh is shown). The curved surface of the cylinder is mapped to a square or rectangular grid by considering the problem in terms of cylindrical co-ordinates; to map onto a three-dimensional cylinder in Cartesian co-ordinates one can use:

$$x = h \cos \theta, \quad (\text{B.25})$$

$$y = h \sin \theta, \quad (\text{B.26})$$

$$z = z. \quad (\text{B.27})$$

The prefactors in equation (B.23) are obtained using linear interpolation between neighbouring grid points and are given by, for example,

$$\frac{h^3}{3} \Big|_{i+\frac{1}{2},j} = \frac{1}{2} \left(\frac{1}{3} h_{i+1,j}^3 + \frac{1}{3} h_{i,j}^3 \right),$$

and similarly defined for the other prefactors.

B.2.2 Temporal discretisation

The temporal derivative in equation (B.17) is approximated using the implicit, second-order accurate Crank-Nicolson method. Writing the spatial discretisation as a function of $h_{i,j}, p_{i,j}, h_{i\pm 1,j}$ and $p_{i\pm 1,j}$ allows the discretised time-dependent term for film height, h , to be expressed conveniently in the form:

$$(1 + \epsilon_R h_{i,j}^n) \frac{\partial h_{i,j}}{\partial t} = F(h_{i,j}^n, p_{i,j}^n, h_{i\pm 1,j}^n, p_{i\pm 1,j}^n, h_{i,j\pm 1}^n, p_{i,j\pm 1}^n), \quad (\text{B.28})$$

for all $(i, j) \in \Omega$. Employing the Crank-Nicolson method yields an equation for the variables h and p at $t = t^{n+1}$ (denoted by superscript $n + 1$) in terms of the calculated values at $t = t^n$ (denoted by superscript n) as:

$$\begin{aligned} h_{i,j}^{n+1} - \frac{\Delta t^{n+1}}{2(1 + \epsilon_R h_{i,j}^{n+1})} F(h_{i,j}^{n+1}, p_{i,j}^{n+1}, h_{i\pm 1,j}^{n+1}, p_{i\pm 1,j}^{n+1}, h_{i,j\pm 1}^{n+1}, p_{i,j\pm 1}^{n+1}) \\ = h_{i,j}^n + \frac{\Delta t^{n+1}}{2(1 + \epsilon_R h_{i,j}^n)} F(h_{i,j}^n, p_{i,j}^n, h_{i\pm 1,j}^n, p_{i\pm 1,j}^n, h_{i,j\pm 1}^n, p_{i,j\pm 1}^n), \end{aligned} \quad (\text{B.29})$$

with $\Delta t^{n+1} = t^{n+1} - t^n$.

Appendix C

Linear stability analysis

Contents

C.1 Planar, inclined substrate	207
C.1.1 Travelling wave solution	207
C.1.2 Perturbation Analysis and Eigenvalue Problem	208
C.2 Analysis of vertically aligned cylinder	209
C.2.1 Travelling wave solution	209
C.2.2 Perturbation Analysis	210

C.1 Planar, inclined substrate

The linear hydrodynamic stability of the gravity-driven thin film flow has been explored by a number of authors, including Davis and Troian (2003), Troian *et al.* (1989) and Kondic (2003); the traditional approach, as adopted here, determines the travelling wave solution and the governing equation is then linearised to obtain the associated eigenvalue problem (Craster and Matar, 2009). The equations are also adapted to incorporate the effects of a non-zero equilibrium contact angle.

C.1.1 Travelling wave solution

The analysis proceeds by combining equations (2.23) and (2.24) to form a fourth order partial differential equation in h :

$$\begin{aligned} \frac{\partial h}{\partial t} = \frac{\partial}{\partial x} & \left[\frac{h^3}{3} \left(\frac{-\epsilon^3}{Ca} \left(\frac{\partial^3 h}{\partial x^3} + \frac{\partial^3 h}{\partial xy^2} \right) + 2\epsilon \frac{\partial h}{\partial x} \cot \alpha - \frac{\partial \Pi(h)}{\partial x} - 2 \right) \right] \\ & + \frac{\partial}{\partial y} \left[\frac{h^3}{3} \left(\frac{-\epsilon^3}{Ca} \left(\frac{\partial^3 h}{\partial y^3} + \frac{\partial^3 h}{\partial yx^2} \right) + 2\epsilon \frac{\partial h}{\partial y} \cot \alpha - \frac{\partial \Pi(h)}{\partial y} \right) \right]. \end{aligned} \quad (\text{C.1})$$

The base state is a travelling wave solution such that $h(x, y, t) = h_0(x - U_w t)$ (Troian *et al.* (1989)); substituting this into equation (C.1), with $p_0 = p(h_0)$ (see Equation (2.24)), and integrating once yields the governing equation for $h_0(\xi)$ as

$$-U_w h_0 + \frac{2h_0^3}{3} - \frac{h_0^3}{3} \frac{\partial p_0}{\partial \xi} = c, \quad (\text{C.2})$$

where U_w is the travelling wave velocity and c is a constant of integration. These constants are fixed by the condition that as $\xi \rightarrow -\infty$ the film thickness is fully developed, i.e. $h_0 \rightarrow 1$. The other necessary condition is that the film height must match onto the precursor film height h^* , so as $\xi \rightarrow \infty$ then $h_0 \rightarrow h^*$. This returns U_w and c as

$$U_w = \frac{2}{3} \frac{1 - h^{*3}}{1 - h^*}, \quad c = -\frac{2h^*}{3} \frac{1 - h^{*2}}{1 - h^*}. \quad (\text{C.3})$$

C.1.2 Perturbation Analysis and Eigenvalue Problem

Consider a reference frame travelling with velocity U_w of the travelling wave (Troian *et al.*, 1989), given above, and a perturbation $\varsigma h_1(\xi, y, t)$ applied to the front given by the base state solution h_0 , where $\varsigma \ll 1$, which gives $p = p_0 + \varsigma p_1$ with $p_1 = -\frac{\epsilon^3}{Ca} \nabla^2 h_1 + 2\epsilon h_1 \cot \alpha - h_1 \frac{\partial \Pi(h_0)}{\partial h}$, where only the first term of the associated Taylor expansion is kept. Substituting the perturbed solution into equation (2.23) and keeping terms of $O(\varsigma)$ only, a fourth order equation for the perturbation h_1 emerges:

$$\frac{\partial h_1(\xi, y, t)}{\partial t} = \nabla \left(h_0^2 h_1 \nabla p_0 + \frac{h_0^3}{3} \nabla p_1 \right) - (2h_0^2 h_1)_\xi + U_w h_{1\xi}. \quad (\text{C.4})$$

Note that subscripts of ξ denote the partial derivative of the same. Following Bertozzi and Brenner (1997), as the travelling wave solution h_0 does not depend on y the Fourier transform of (C.4), $h_1(\xi, y, t) = \int_{-\infty}^0 h_1(\xi, k, t) e^{iky} dk$, gives:

$$\begin{aligned} \frac{\partial h_1(\xi, k, t)}{\partial t} = & \left(h_0^2 h_1 p_{0\xi} + \frac{h_0^3}{3} p_{1\xi} \right)_\xi - (2h_0^2 h_1)_\xi + U_w h_{1\xi} - \frac{k^2 h_0^3}{3} p_1 \\ & + \frac{k^2 \epsilon^3}{Ca} \left[\left(\frac{h_0^3}{3} h_{1\xi} \right)_\xi - \frac{k^2 h_0^3}{3} h_1 \right], \quad (\text{C.5}) \end{aligned}$$

where k is the wavenumber of the spanwise perturbation. The equation is subject to decay conditions so that $h_1, h_{1\xi}, h_{1\xi\xi\xi} \rightarrow 0$ as $\xi \rightarrow \pm\infty$. If the equation is discretised spatially with central differences of second order then a system of equations that determines the growth of the perturbation \mathbf{h}_1 is found, having the form:

$$\frac{\partial \mathbf{h}_1}{\partial t} = \mathbf{A}(\xi, k) \mathbf{h}_1, \quad (\text{C.6})$$

where $\mathbf{A}(\xi, k)$ is a linear autonomous matrix (Davis and Troian, 2003) acting on \mathbf{h}_1 , that is the discretised elements of the perturbation. The solution $h_1(\xi, k, t)$ has exponential dependence on t (Kondic, 2003) and so may be written in the form

$h_1(\xi, k, t) = \phi(\xi) e^{\omega(k)t}$ giving:

$$\omega(k) \phi = \mathbf{A}(\xi, k) \phi. \quad (\text{C.7})$$

This is an eigenvalue problem for the linear operator defined in \mathbf{A} . The values of ω that satisfy the problem are the eigenvalues which are the growth rates of the corresponding eigenfunctions ϕ . If $\omega > 0$ then the perturbations are unstable and increase with time, if $\omega < 0$ the perturbations are stable and decay with time.

C.2 Analysis of vertically aligned cylinder

The analysis for rivulet flow on a vertically aligned cylinder follows a very similar route.

C.2.1 Travelling wave solution

Considering the governing equations for thin film flow down a vertical cylinder, equations (B.17) and (B.18), and searching for a travelling wave solution $h_0(\xi)$, similarly to the planar substrate case, the governing equations are given by:

$$-U_w \left(h_0 + \frac{\epsilon_R h_0^2}{2} \right) + \frac{1}{3} (h_0^3 + \epsilon_R h_0^4) + \frac{\epsilon_R h_0^3}{3} \frac{\partial p_0}{\partial \xi} = c. \quad (\text{C.8})$$

Applying the boundary conditions as above fixes the travelling wave velocity and constant of integration. The wave velocity, U_w is given by:

$$U_w = \frac{1 + h^* + h^{*2} + \epsilon_R (1 + h^* + h^{*2} + h^{*3})}{3 \left(1 + \frac{\epsilon_R}{2} + \frac{\epsilon_R h^*}{2} \right)}. \quad (\text{C.9})$$

C.2.2 Perturbation Analysis

Applying a small perturbation via $h = h_0(\xi) + \varsigma h_1(\xi, \theta, t)$ and $p = p_0 + \varsigma p_1$, the perturbed pressure term is given by

$$p_1 = -\frac{1}{Bo_R} (h_1 + \nabla^2 h_1) - h_1 \frac{\partial \Pi(h_0)}{\partial h}. \quad (\text{C.10})$$

Substituting (C.10) into equation (B.17) and only retaining terms of $O(\varsigma)$, a fourth order equation in h_1 is obtained as:

$$(1 + \epsilon_R h_0) \frac{\partial h_1(\xi, \theta, t)}{\partial t} = \nabla \left(h_0^2 h_1 \nabla p_0 + \frac{h_0^3}{3} \nabla p_1 \right) - \frac{1}{3} (3h_0^2 h_1 + 4\epsilon_R h_0^3 h_1)_\xi + [U_w (1 + \epsilon_R h_0) h_1]_\xi, \quad (\text{C.11})$$

here ∇ denotes the dimensionless gradient operator in cylindrical terms, i.e. $\nabla = \left(\frac{\partial}{\partial z}, \frac{\partial}{\partial \theta} \right)$.

Performing the same Fourier transform as previously shown, the stability equation in terms of wavenumber k is:

$$(1 + \epsilon_R h_0) \frac{\partial h_1(\xi, k, t)}{\partial t} = \left(h_0^2 h_1 p_{0\xi} + \frac{h_0^3}{3} p_{1\xi} \right)_\xi - \frac{1}{3} (3h_0^2 h_1 + 4\epsilon_R h_0^3 h_1)_\xi + [U_w (1 + \epsilon_R h_0) h_1]_\xi + \frac{\epsilon_R k^2}{3Bo_R} [(1 + k^2) h_0^3 h_1 + 2h_0^3 h_{1\xi\xi} + 3h_0^2 h_{1\xi}], \quad (\text{C.12})$$

where k is the wavenumber in the θ -direction. The problem is solved, as in the planar case, with the associated growth rates determining the stability of the perturbation.

Appendix D

Adaptive multigrid performance

Contents

D.1	Efficiency of multigrid procedure	212
D.2	Jacobian calculation: Numerical vs Analytical	219
D.2.1	Numerical Jacobians	219
D.2.2	Analytical form of the Jacobian	219
D.2.3	Comparison of the two approaches	220
D.3	Relaxation schemes	222
D.3.1	Newtonian relaxation	222
D.3.2	Broyden's secant method	224
D.3.3	Conjugate gradient method	225
D.3.3.1	Line search	226
D.3.3.2	Brent's method	227
D.3.3.3	Preconditioning	228
D.4	Comparison of iterative smoother efficiency	229
D.4.1	Two-dimensional problem	229
D.4.2	Three-dimensional flow	233

In this section the efficiency of the multigrid method of solution described in Chapter 3 is demonstrated which together with the concept of grid devolution is shown to give an increase in efficiency compared to other multigrid strategies. Also shown is a selection of relaxation methods that may be utilised in the smoothing procedure. Numerical and analytical methods of determining the Jacobian associated with the governing lubrication equations are compared in terms of accuracy and efficiency. The results shaped which form of multigrid method was used in the results presented in Chapters 4 to 6, since in a detailed dynamic process like rivulet formation computational efficiency is key.

D.1 Efficiency of multigrid procedure

The adaptive multigrid method described in Chapter 3 utilises local mesh refinement and grid devolution to improve computational efficiency at each time step iteration. Automatic, error-controlled variable time-stepping is employed additionally to improve the efficiency still further when generating long-time solutions. Here the difference in efficiency between multigrid methods with three different levels of adaption are investigated, namely; non-adaptive multigrid (A), multigrid with local mesh refinement (LMR) (B) and , finally, multigrid with both LMR and grid devolution (C). Implementing multigridding strategies to solve the lubrication equations has already been shown to be substantially preferential to the use of time-splitting methods (Cowling *et al.*, 2011).

The results generated and compared are for the case of film flow down a flat substrate inclined at 60° to the horizontal with a constant inflow of ‘Fluid A’ (see Chapter 4) having zero equilibrium contact angle. The coarsest grid, \mathcal{G}_0 , consists of 257×65 nodes spanning a computational domain of $(0, 400) \times (0, 100)$. The choice of grid level, D , on which to employ grid devolution depends on the resolution of the coarsest mesh; in this case the coarsest mesh, \mathcal{G}_0 , is suitably fine and provides a reasonably accurate initial solution on which to base grid devolution.

The number of active nodes on the refined grid with finest level K , at $t = 50$, is shown in Figure D.1(a); the number of nodes reduces when using strategy B compared to strategy A but stays similar when, additionally, grid devolution is activated, strategy C. This is because the number of nodes removed from the hybrid-mesh is small, as only nodes from the coarsest grid are removed; nevertheless the amount of calculations and work performed on the coarse level during a full multigrid iteration is reduced significantly with a corresponding reduction in the CPU time required.

The efficiency of introducing both local mesh refinement and grid devolution is demonstrated in Figure D.1 (b), showing an example of the CPU time required for a single time iteration at $t = 50$. The reduction in CPU time is large when local mesh refinement and grid devolution are employed, compared to a non-adaptive approach; in some cases as much as an order of magnitude difference is seen. The saving from the LMR only case compared to strategy C appears less impressive; however, over a long-time simulation these savings can be significant - as demonstrated subsequently.

Essential to the incorporation of grid devolution is that the solution is not affected; all solutions produced identical results with the same truncation error at each point. To optimise the use of devolution, a range of values of TOL_d were used (flow conditions the same as above); if the number of nodes making up the finest grid level, K , are equal for both adaptive multigrid strategies (strategies B and C) then level of error in the solution is indicated to be the same. When TOL_d is not too large there are more nodes on level K as the truncation error is higher on the lower grid levels due to the removal of nodes in areas of high film height/pressure gradient on the coarse grid. These nodes do not then get refined and smoothed and thus the truncation error is very high in the given area of the computational domain and so more nodes are refined via local mesh refinement to the finest grid level. Figure D.2 shows how as TOL_d decreases the number of nodes for strategy C approaches that of strategy B and the optimal value of TOL_d is found to be 0.0001; at this value, areas of local mesh refinement and grid devolution do not intersect at any point, as

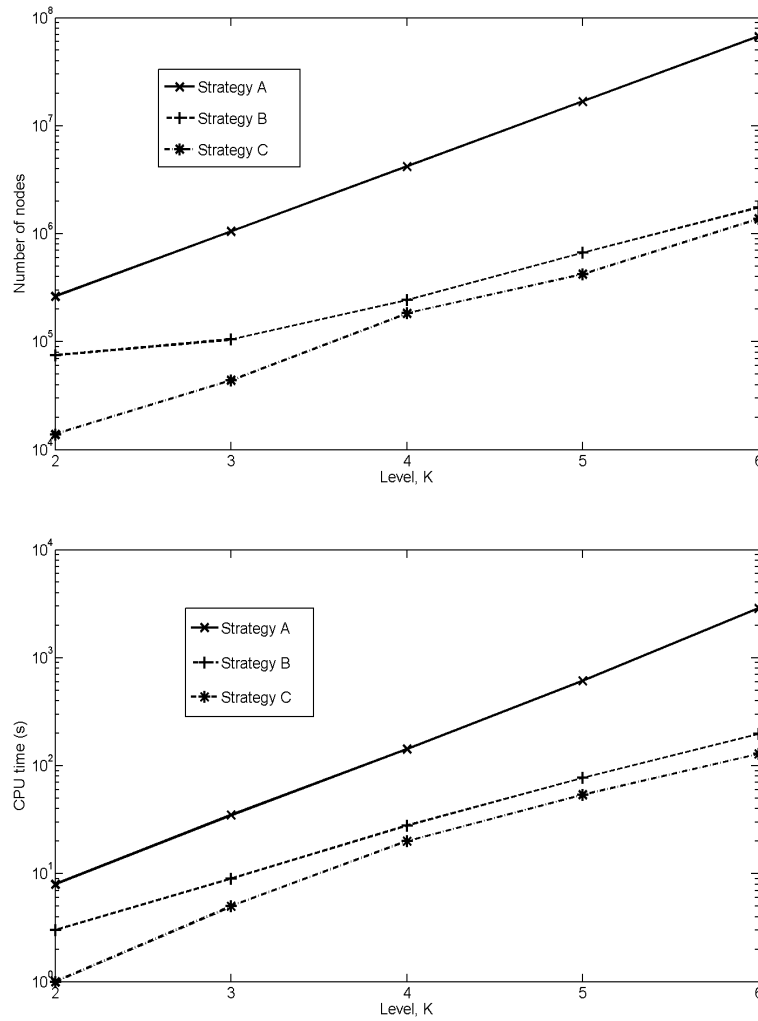


FIGURE D.1: The number of nodes on the specified finest level, K , is shown in (a) for three different variations of the multigrid method; strategies A,B and C. The corresponding CPU time for each K is then presented in (b). This is for the case of a thin film of 'Fluid A' on a substrate inclined at 60° where the coarsest grid is 257×65 nodes and the computational domain is $(0, 400) \times (0, 100)$.

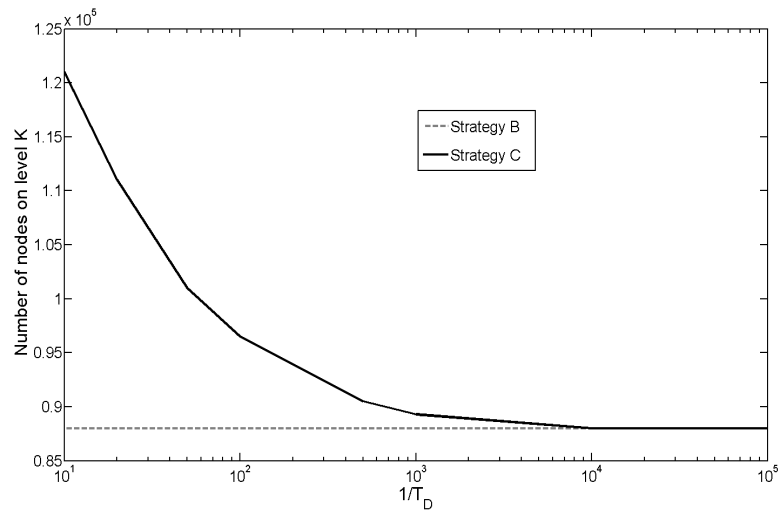


FIGURE D.2: Plot to show how the number of nodes on the finest grid level, K , changes with the tolerance value for grid devolution, TOL_d .

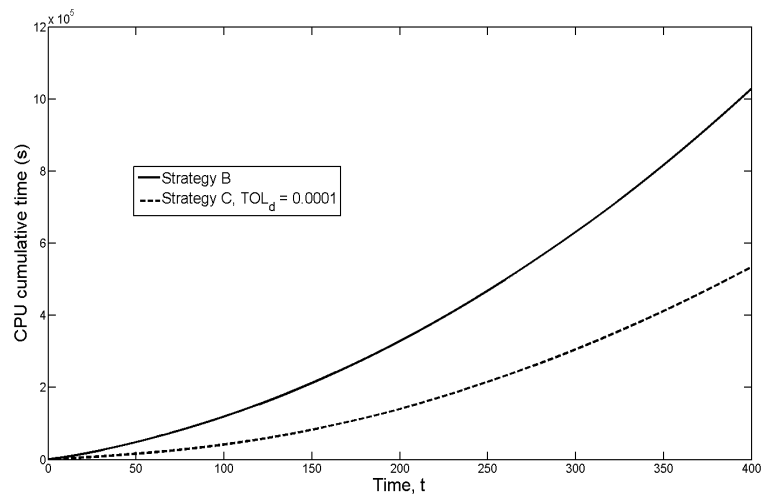


FIGURE D.3: Graph showing the significant decrease in CPU time required when devolution is employed compared to when only mesh refinement is active in the multigrid algorithm. The solution is for identical initial conditions of a film of 'Fluid A', considered as fully wetting, flowing down a substrate inclined at 60° to the horizontal. The CPU time increases per iteration as the number of nodes increases due to the growth of rivulets at the advancing front area.

required.

Figure D.3 shows the cumulative CPU time for the generation of the numerical solution of the lubrication equations for the flow under consideration, up to $t = 400$. Two multigrid strategies are considered, B and C, revealing the difference when grid devolution is added to the algorithm. The overall improvement of efficiency between the two strategies is clear; at $t = 400$ the total CPU time used is approximately twice that when devolution is not employed than when it is utilised. This large improvement in efficiency is very valuable when calculating transient, memory intensive processes such as rivulet formation; the method thus allows for the efficient calculation of long-time solutions on large substrates which can then be used for direct comparison with experimental data. Note that the increase in CPU time is not linear due to the increase in the effective grid size since the rivulets, that represent the domain of interest, are lengthening.

Examples of how the active, refined computational mesh evolves through the formation of the rivulets is shown in Figures D.4 and D.5. In Figure D.4, free-surface colour maps of the film thickness are shown alongside the corresponding computational mesh at three different times for flow on a wide substrate. Figure D.5 shows a close-up of the same setup, with the contact line indicated in white. A grid generated without devolution is shown in Figure D.5 (a), demonstrating the disparity in the number of nodes active when strategies B and C are employed. The dynamic, evolving mesh is dense and refined only around the advancing front area, becoming coarser further away until the point at which the film is flat, either fully developed or equal to the precursor film thickness, where the appropriate value of h is assigned and the nodes removed from subsequent calculations in the given time iteration.

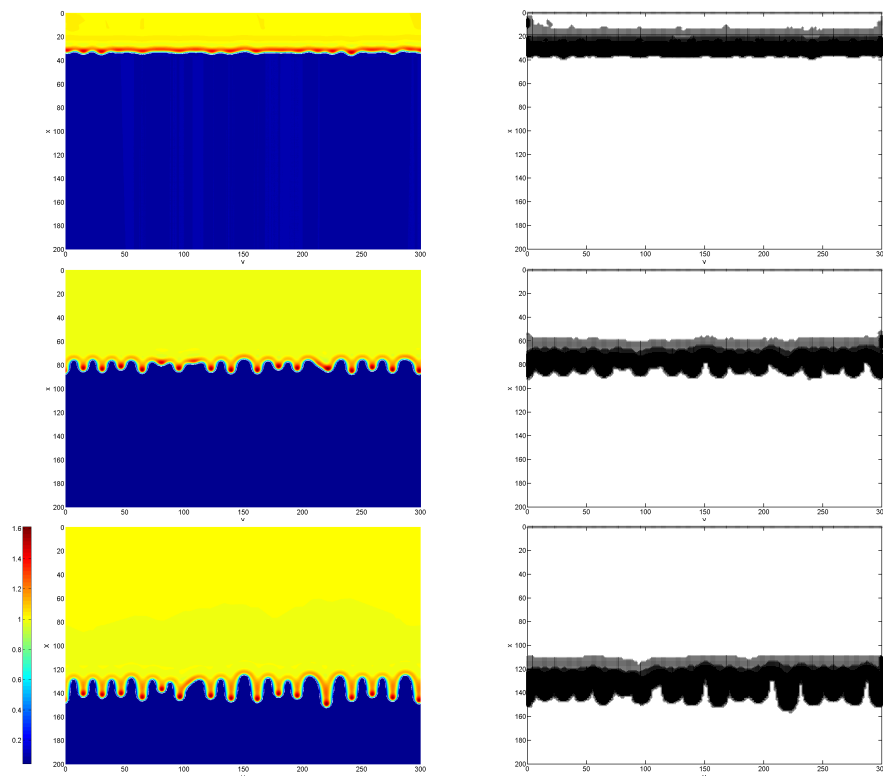


FIGURE D.4: Left hand side figures show colour maps of the free-surface profiles of the advancing front of a water-glycerin film spreading on a substrate inclined at 60° at $t = 50, 100$ and 200 . The associated composite, finest multigrid levels are shown on the right hand side exhibiting grid refinement and coarse grid devolution.

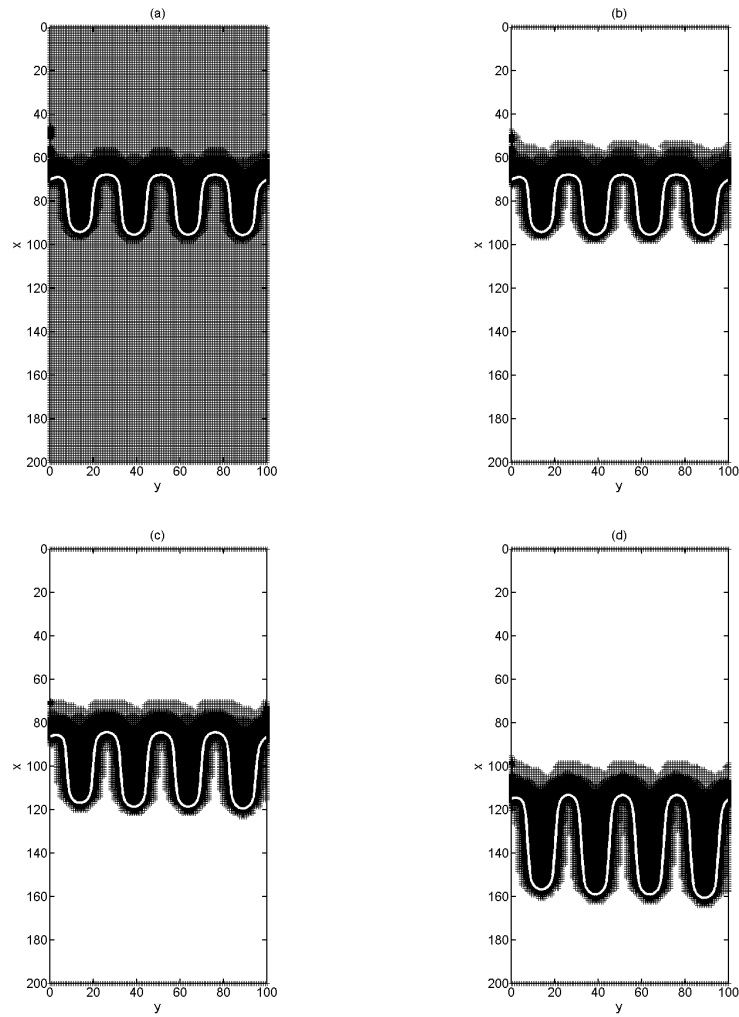


FIGURE D.5: The refined grid structure used in the multigrid solution of thin film flow for a fully wetting liquid spreading on an inclined substrate with $\alpha = 60^\circ$ when adaption strategies B), shown in (a), and C), shown in (b), (c) and (d), are utilised. The contact line is indicated in white and develops in (b), (c) and (d) which show subsequent times.

D.2 Jacobian calculation: Numerical vs Analytical

When utilising the Newtonian method described in Appendix D.3 the Jacobian of the equation set is required to compute corrections to the solution. There are two ways of computing the required matrix, the first is analytical, the second numerical. The analytical method is the most accurate and so can reduce error and thus computing time. However, the analytical approach requires the analytical form of the Jacobian to be derived every time one or more new equations or new physics are introduced into the problem. Evaluating the Jacobian numerically is much more general and simple to implement via a finite difference method; however, due to the approximate nature of the process more iterations of the smoothing method may be required leading to a small increase in computing time - see Gaskell *et al.* (2010).

D.2.1 Numerical Jacobians

If equations (2.23) and (2.24) are written as a discretised vector function as in equation (3.7) then:

$$\mathbf{F}(\mathbf{u}_{i,j}^{n+1}) = \mathbf{N}\mathbf{u}_{i,j}^{n+1} - \mathbf{f}(\mathbf{u}_{i,j}^n) \quad (\text{D.1})$$

where $\mathbf{u}_{i,j}^n = (h_{i,j}^n, p_{i,j}^n)$ for all $(i, j) \in \Omega$, the computational domain.

The numerical Jacobian at each computational node is then calculated as

$$\mathbf{J}_{i,j} = \frac{\mathbf{F}(\mathbf{u}_{i,j}^{n+1} + \delta) - \mathbf{F}(\mathbf{u}_{i,j}^{n+1})}{\delta}.$$

D.2.2 Analytical form of the Jacobian

The Jacobian matrix of the discretised equations, expressed analytically, is:

$$\mathbf{J}_{i,j,k,l} = \begin{pmatrix} \frac{\partial \mathcal{N}_{i,j}^h}{\partial h_{k,l}^{n+1}} & \frac{\partial \mathcal{N}_{i,j}^h}{\partial p_{k,l}^{n+1}} \\ \frac{\partial \mathcal{N}_{i,j}^p}{\partial h_{k,l}^{n+1}} & \frac{\partial \mathcal{N}_{i,j}^p}{\partial p_{k,l}^{n+1}} \end{pmatrix} \quad (\text{D.2})$$

where

$$\frac{\partial \mathcal{N}_{i,j}^h}{\partial h_{k,l}^{n+1}} = \left\{ \delta_{i,k} \delta_{j,l} - \frac{\Delta t}{4\Delta^2} \left[\delta_{i,k} \delta_{j,l} h_{i,j}^{n+1^2} + \delta_{i+1,k} \delta_{j,l} h_{i+1,j}^{n+1^2} - \delta_{i-1,k} \delta_{j,l} h_{i-1,j}^{n+1^2} \right. \right. \\ \left. \left. + \delta_{i,k} \delta_{j+1,l} h_{i,j+1}^{n+1^2} - \delta_{i,k} \delta_{j-1,l} h_{i,j-1}^{n+1^2} \right] \right. \\ \left. [p_{i+1,j}^{n+1} + p_{i-1,j}^{n+1} + p_{i,j+1}^{n+1} + p_{i,j-1}^{n+1} - 4p_{i,j}^{n+1}] - \frac{\Delta t}{2\Delta} \left[\delta_{i+1,k} \delta_{j,l} h_{i+1,j}^{n+1^2} - \delta_{i-1,k} \delta_{j,l} h_{i-1,j}^{n+1^2} \right] \right\},$$

$$\frac{\partial \mathcal{N}_{i,j}^h}{\partial p_{k,l}^{n+1}} = \left\{ \frac{\Delta t}{2\Delta^2} \left[\frac{h^3}{3} \Big|_{i+\frac{1}{2},j} (\delta_{i+1,k} \delta_{j,l} - \delta_{i,k} \delta_{j,l}) - \frac{h^3}{3} \Big|_{i-\frac{1}{2},j} (\delta_{i-1,k} \delta_{j,l} - \delta_{i,k} \delta_{j,l}) \right. \right. \\ \left. \left. + \frac{h^3}{3} \Big|_{i,j+\frac{1}{2}} (\delta_{i,k} \delta_{j+1,l} - \delta_{i,k} \delta_{j,l}) - \frac{h^3}{3} \Big|_{i,j-\frac{1}{2}} (\delta_{i,k} \delta_{j-1,l} - \delta_{i,k} \delta_{j,l}) \right] \right\},$$

$$\frac{\partial \mathcal{N}_{i,j}^p}{\partial h_{k,l}^{n+1}} = \frac{2\epsilon^3}{Ca\Delta^2} [\delta_{i+1,k} \delta_{j,l} + \delta_{i-1,k} \delta_{j,l} + \delta_{i,k} \delta_{j+1,l} + \delta_{i,k} \delta_{j-1,l} \\ - 4\delta_{i,k} \delta_{j,l}] - 2\delta_{i,k} \delta_{j,l} \epsilon \cot \alpha,$$

$$\frac{\partial \mathcal{N}_{i,j}^p}{\partial p_{k,l}^{n+1}} = \delta_{i,k} \delta_{j,l},$$

with Dirac-delta functions $\delta_{i,k}, \delta_{j,l}$ equating to unity when the subscripts intersect, and zero otherwise.

D.2.3 Comparison of the two approaches

Both methods of calculating the Jacobian (numerical and analytical) are compared for the case of continuous thin film flow over a trench topography, where the topography's non-dimensional width and length are set as 0.01 and depth to 0.2. The fluid properties are set to those of water, the asymptotic film thickness is defined as $100\mu\text{m}$ and inclination angle 65° . The resulting free-surface colour maps of the free-surface disturbance are shown in Figure D.6, the difference between them being indiscernible. The percentage difference, calculated via $Err =$

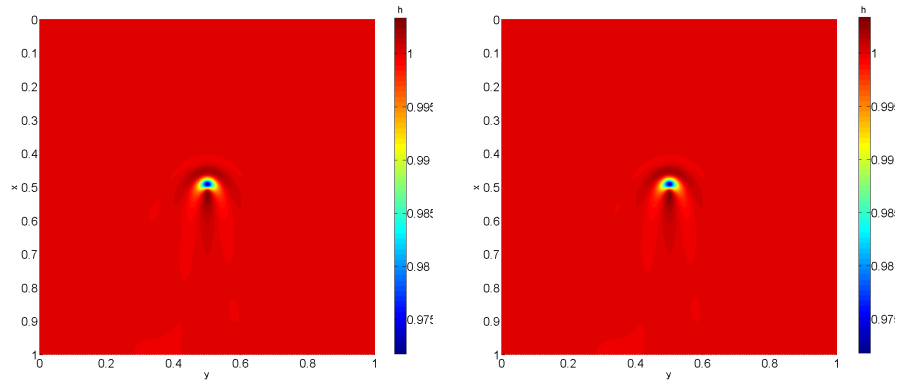


FIGURE D.6: Free-surface profiles for continuous thin film flow over a trench topography; the left hand side is the profile found when using an analytical Jacobian, the right hand side the corresponding profile when a numerical approach is utilised. Flow direction is from top to bottom.

$100|h_{i,j}^{analytical} - h_{i,j}^{numerical}|/h_{i,j}^{analytical}$, is shown in Figure D.7, the maximum difference being 0.006% only. Therefore, either method can be utilised with confidence.

The CPU times for both methods are very similar. It was found that when a multigrid method employs only variable time-stepping as an adaptive feature the total CPU time required for the solution to $t = 10$ is 78 seconds when the Jacobian is calculated analytically while it is 79 seconds when the Jacobian is obtained numerically. For a non-adaptive multigrid method, to complete 130,000 time steps the CPU time used is 56,266 seconds and 56,534 seconds for the analytical and numerical approaches, respectively - a percentage difference of just 0.5% in CPU time. Results are found to be similar for other solutions obtained with different topographies.

The above findings suggest that the performance of the multigrid method of solution when solving the Jacobian either numerically or analytically is incredibly similar in terms of efficiency and accuracy. However, the simplicity of implementation of the numerical scheme make it the more attractive prospect of the two.

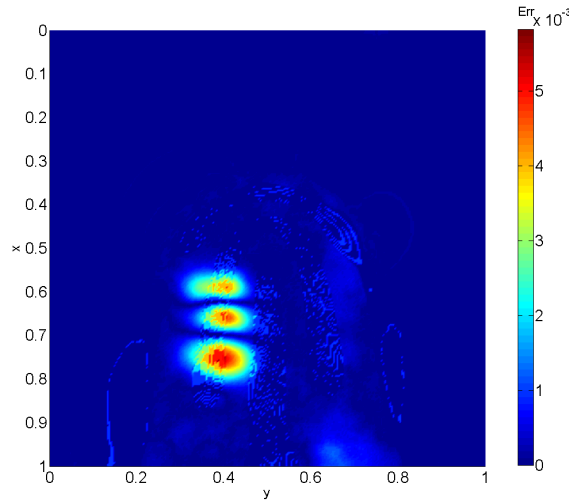


FIGURE D.7: Colour maps of the percentage change of film height between the two solutions shown in Figure D.6 over the computational domain.

D.3 Relaxation schemes

In the course of obtaining the solutions presented in Chapters 4 to 7 a number of different relaxation schemes were explored in relation to their efficiency for use with the multigrid methodology.

D.3.1 Newtonian relaxation

Consider a non-linear function $\mathbf{F}(\mathbf{x}) : \mathbb{R}^N \rightarrow \mathbb{R}^N$; a solution vector $\mathbf{x} \in \mathbb{R}^N$ is required such that $\mathbf{F}(\mathbf{x}) = 0$. From an approximate solution vector \mathbf{x}_n , the desire is to find a step $\delta\mathbf{x}$ in order to achieve:

$$\mathbf{F}(\mathbf{x}_n + \delta\mathbf{x}) = 0. \quad (\text{D.3})$$

Expanding \mathbf{F} in Taylor series gives:

$$\mathbf{F}(\mathbf{x}_n + \delta\mathbf{x}) = \mathbf{F}(\mathbf{x}) + \mathbf{J}.\delta\mathbf{x} + O(\delta\mathbf{x}^2), \quad (\text{D.4})$$

and thus setting $\mathbf{F}(\mathbf{x}_n + \delta\mathbf{x}) = 0$ and neglecting terms of order $\delta\mathbf{x}^2$ and higher leads to the Newton step, $\delta\mathbf{x}$, as:

$$\delta\mathbf{x} = -\mathbf{J}^{-1} \cdot \mathbf{F}, \quad (\text{D.5})$$

where \mathbf{J} is the Jacobian matrix of \mathbf{F} and \mathbf{J}^{-1} its inverse.

A new solution vector is then obtained as $\mathbf{x}_{n+1} = \mathbf{x}_n + \delta\mathbf{x}$, this iterative process is continued until satisfactory convergence is achieved.

In the context of the problem under consideration there are two residuals at each node (i, j) for $h_{i,j}$ and $p_{i,j}$. Thus the function considered is $\mathbf{F}(h_{i,j}, p_{i,j}) = 0$. However, in practice it may not be possible to find the zeroes of this function; so instead the aim is to find the best possible approximate solution at the node. To do this another function is considered,

$$f = \frac{1}{2} \mathbf{F} \cdot \mathbf{F}$$

and its minimum is found as this gives the nearest approximation possible of $\mathbf{F} = 0$.

The algorithm involves a line search in the direction of the Newton step. At first the full Newton step is tested, if this does not meet the criteria for a sufficient decrease in the function, f , then a backtracking algorithm is employed until the function decreases a sufficient amount in the direction of the Newton step. This process is repeated until $\mathbf{F}(h_{i,j}, p_{i,j})$ is sufficiently small ($< 1 \times 10^{-8}$ for a two dimensional problem).

This method is successful and efficient and is easily adapted to other problems. The main problem that can occur is if the Jacobian becomes singular and thus the Newton step cannot be calculated. This did not prove a problem during tests within the current work. Calculating the Newton step can also be computationally expensive as it is a requirement to calculate the Jacobian matrix or an approximation to it, this is especially true if $\mathbf{F} : \mathbb{R}^N \rightarrow \mathbb{R}^N$ where N is large.

The Newton method is presented and discussed in some depth by Gaskell *et al.* (2010). Here, the benefits of using a general, globally convergent Newton solver are demonstrated in full.

D.3.2 Broyden's secant method

Secant methods use less computationally expensive approximations of the Jacobian for zero finding or the Hessian matrix for minimisation. Broyden's method is such a method.

If the approximation to the Jacobian \mathbf{J} of \mathbf{F} is given by \mathbf{B}_n then it is imposed that the following equation, Kelley (2003), is satisfied:

$$\mathbf{B}_n (\mathbf{x}_n - \mathbf{x}_{n-1}) = \mathbf{F}(\mathbf{x}_n) - \mathbf{F}(\mathbf{x}_{n-1}), \quad (\text{D.6})$$

where \mathbf{x}_n is the current approximate solution vector and \mathbf{x}_{n-1} the approximate solution vector from the previous iterate.

The solution vector is updated via:

$$\mathbf{x}_{n+1} = \mathbf{x}_n - \lambda_n \mathbf{B}_n^{-1} \mathbf{F}(\mathbf{x}_n), \quad (\text{D.7})$$

where λ_n is the step length in the Broyden direction $\mathbf{d}_n = -\mathbf{B}_n^{-1} \mathbf{F}$.

After this update, the approximation to \mathbf{J} , that is \mathbf{B}_n , is updated (Press *et al.*, 2002) via:

$$\mathbf{B}_{n+1} = \mathbf{B}_n + \frac{((\mathbf{F}(\mathbf{x}_{n+1}) - \mathbf{F}(\mathbf{x}_n)) - \mathbf{B}_n \lambda_n \mathbf{d}_n) \lambda_n \mathbf{d}_n}{(\lambda_n \mathbf{d}_n)^T (\lambda_n \mathbf{d}_n)}. \quad (\text{D.8})$$

The main issue with Broyden's method is that the search direction is not necessarily a descent direction for \mathbf{F} , as \mathbf{B}_n is only an approximation. For this reason Newton-Krylov methods are more popular, this is where a Krylov solver is used to find a good approximation for the Newton step, and is especially useful for large N

(Kelley, 2003).

D.3.3 Conjugate gradient method

The non-linear conjugate gradient method considered and utilised is a line search descent method for solving the optimisation problem :

$$\min_{\mathbf{x} \in \mathbb{R}^N} f(\mathbf{x}). \quad (\text{D.9})$$

The process creates a sequence of conjugate search directions via the Gram-Schmidt process, each conjugate coming from the previous one, and a line search is carried out in the direction generated to find a step length, α , in the search direction that minimises f along this direction. In this case consider f , as in the Newtonian relaxation section, as $f = \mathbf{F} \cdot \mathbf{F}$. The process generates a sequence of approximate solution vectors \mathbf{x}_n , the starting vector is \mathbf{x}_0 , a sequence of gradient vectors for each \mathbf{x}_n namely \mathbf{g}_n and the search directions \mathbf{h}_n . The algorithm is as follows:
From a starting vector \mathbf{x}_0 the search direction vector \mathbf{h}_0 is set equal to $-\mathbf{g}_0$. Then for iteration n :

- Perform a line minimisation to find α that minimises f in the search direction \mathbf{h}_n .
- If f has suitably converged stop.
- Set $\mathbf{x}_{n+1} = \mathbf{x}_n + \alpha \mathbf{h}_n$, \mathbf{g}_{n+1} set to the gradient vector at \mathbf{x}_{n+1} .
- Calculate $\gamma_n = \frac{(\mathbf{g}_{n+1} - \mathbf{g}_n) \mathbf{g}_{n+1}}{\mathbf{g}_n^T \mathbf{g}_n}$ - Polak-Riberie term.
- Generate a new search direction $\mathbf{h}_{n+1} = -\mathbf{g}_{n+1} + \gamma_n \mathbf{h}_n$.

The method is computationally cheap and relatively simple to apply. The area that can be important for efficiency is the line search to minimise f in the direction of \mathbf{h}_n . Two methods were investigated; one is a line search, used by Charalambous

(Charalambous, 1992), the other Brent's method (Press *et al.*, 2002) that initially brackets the minimum between three points and then uses bisection and the secant method to find the minimum to within a prescribed tolerance (Press *et al.*, 2002).

D.3.3.1 Line search

The line search, Charalambous (1992), is useful as one can specify how exact the line search needs to be. If a function $\Phi(\alpha) = f(\mathbf{x}_n + \alpha\mathbf{h}_n)$ is introduced then the line search will search for a value α_{\min} such that $\Phi(\alpha)$ has decreased sufficiently from $\Phi(0)$.

The line search is continued until the Wolfe line search conditions are satisfied (Dai and Yuan, 2002):

$$f(\mathbf{x}_n + \alpha\mathbf{h}_n) \leq f(\mathbf{x}_n) + \mu\alpha\mathbf{g}_n^T\mathbf{h}_n, \quad (\text{D.10})$$

$$|\mathbf{g}_{n+1}\mathbf{h}_n| \leq -\sigma\mathbf{g}_n\mathbf{h}_n, \quad (\text{D.11})$$

where $0 < \mu < \sigma < 1$. The gradient vector at the sequence of approximate solution vectors \mathbf{x}_n is denoted by \mathbf{g}_n , recalling that $\mathbf{x}_{n+1} = \mathbf{x}_n + \alpha\mathbf{h}_n$.

The line search is as follows: Start at $\Phi(\alpha)$ and take a positive step size $\bar{\alpha}$ and evaluate $\Phi(\alpha + \bar{\alpha})$, there are then four possibilities to describe the new location:

1. The conditions are satisfied and thus line search is complete.
2. $\Phi(\alpha) \leq \Phi(\alpha + \bar{\alpha})$ and the new point has negative gradient. The step $\bar{\alpha}$ is then too large, thus set $\bar{\alpha} = 0.1\bar{\alpha}$ and repeat.
3. $\Phi(\alpha) > \Phi(\alpha + \bar{\alpha})$ and the new point has negative gradient. The step size can then be considered too small so repeat with $\bar{\alpha} = 10\bar{\alpha}$.
4. The other possibility is to be at a point with positive slopes but still one or both conditions are violated. In this case $(\alpha, \alpha + \bar{\alpha})$ brackets the minimum α_{\min} . At this point cubic interpolation is employed.

Having bracketed the minimum, consider the cubic function $C(\alpha)$ that passes through $(0, \Phi(\alpha))$ and $(\bar{\alpha}, \Phi(\alpha + \bar{\alpha}))$ and has minimum $\bar{\alpha}_c$. At α the cubic has gradient:

$$\mathbf{h}_n^T \nabla f(\mathbf{x}_n + \alpha \mathbf{h}_n),$$

and at $\alpha + \bar{\alpha}$

$$\mathbf{h}_n^T \nabla f(\mathbf{x}_n + (\alpha + \bar{\alpha}) \mathbf{h}_n).$$

This allows one to perform simple cubic interpolation to find $\bar{\alpha}_c$. The next $\bar{\alpha}$ is chosen from:

$$\bar{\alpha} = \max[\eta \bar{\alpha}, \min(\bar{\alpha}_c, (1 - \eta) \bar{\alpha})], \quad (\text{D.12})$$

to make sure that very small reductions to Φ are carried out.

The initial step size α is calculated from the minimum of the quadratic function that passes through $(0, \Phi(0))$ with gradient at $\alpha = 0$ given by $\mathbf{h}_n \mathbf{g}_n$ and whose minimum function value is $(\Phi(0) - \Delta f)$ where $\Delta f = f(\mathbf{x}_{n-1}) - f(\mathbf{x}_n)$. This gives a minimum of the quadratic function, α_q , as:

$$\alpha_q = -\frac{2\Delta f}{\mathbf{h}_n \mathbf{g}_n},$$

and to avoid a step size that is too small one applies:

$$\alpha = \max(\alpha_{n-1}, \alpha_q),$$

where α_{n-1} is the value of α from the previous line search.

D.3.3.2 Brent's method

The following method is an adaptation of Brent's method (Press *et al.*, 2002). The minimum of a function f is bracketed between three points, a , b and c , such that $a < b < c$, $f(a) > f(b)$ and $f(c) > f(a)$. The method then follows the iterative procedure:

- The secant method is used with both a and c to find two step sizes d_1 and d_2 via $(a - b) \frac{db}{db-da}$ where db is the derivative of the function at b , similarly using c . Two new coordinates are defined by $u_1 = b + d_1$ and $u_2 = b + d_2$, to be acceptable they must be closer to b than the other coordinates are initially, if both are acceptable then the smallest one is used as the step size, d .
- If neither are acceptable then bisection is used to find the step size d .
- Once the step size is determined then a new coordinate $u = b + d$ is tested, if $f(u) < f(b)$ then if $u > b$ set $a = b$, else set $c = b$, and put $b = u$ giving a new bracketing triple.
- If $f(u) > f(b)$ then bracket the minimum by setting $a = u$ if $u < b$, otherwise put $c = u$.
- Continue until a small movement from b in a downhill direction takes the function value to a higher value.

The aim of any iterative procedure is to be as fast and efficient as possible, one way to improve conjugate gradient methods is to precondition them. The idea of preconditioning is explained in the next section and results show that it can dramatically improve the performance of the conjugate gradient method.

D.3.3.3 Preconditioning

A preconditioning matrix transforms the problem in a manner to reduce the convergence time of the conjugate gradient method (Hager and Zhang, 2006), in the non-linear conjugate gradient method the ideal preconditioning matrix is the Hessian matrix or a good approximation to the Hessian matrix (Pytlak and Tarnawski, 2006; Pytlak, 2009; Grossman *et al.*, 2007; Al-Baali and Fletcher, 1996). Introducing this method gives the following algorithm for the Preconditioned Conjugate Gradient (PCG) method:

1. From a starting approximation solution vector \mathbf{x}_0 with gradient vector \mathbf{g}_0 set
 - Preconditioning matrix \mathbf{M}_0 as the Hessian matrix of $f(\mathbf{x}_0)$
 - Search direction $\mathbf{h}_0 = -\mathbf{M}_0^{-1}\mathbf{g}_0$
2. At iteration n : Perform a line minimisation search to find α that minimises f in the direction \mathbf{h}_n
3. If f is suitably converged then stop
4. Set $\mathbf{x}_{n+1} = \mathbf{x}_n + \alpha\mathbf{h}_n$, \mathbf{g}_{n+1} set to the gradient vector at \mathbf{x}_{n+1}
5. Let \mathbf{M}_{n+1} be the Hessian matrix of $f(\mathbf{x}_{n+1})$
6. Calculate $\gamma_n = \frac{(\mathbf{g}_{n+1} - \mathbf{g}_n)\mathbf{M}_{n+1}^{-1}\mathbf{g}_{n+1}}{\mathbf{g}_n^T\mathbf{M}_n^{-1}\mathbf{g}_n}$ - Polak-Riberie term (Al-Baali and Fletcher, 1996).
7. Generate a new search direction $\mathbf{h}_{n+1} = -\mathbf{M}_{n+1}^{-1}\mathbf{g}_{n+1} + \gamma_n\mathbf{h}_n$, return to step 2.

As in this case $N = 2$ it is straight forward to calculate the exact Hessian and its inverse for f without computational expense. If N is large then it is computationally expensive to calculate the Hessian and in some cases it may not be possible to analytically calculate the Hessian. In this case just the diagonal elements may be calculated and that matrix used as preconditioning matrix effectively.

D.4 Comparison of iterative smoother efficiency

D.4.1 Two-dimensional problem

The methods described above are used as the relaxation procedure used in the FAS and FMG algorithm described in Chapter 3, time adaptivity and mesh adaptivity are disabled. The lubrication equations for continuous flow over topography are solved

in the same way as in Gaskell, Jimack, Sellier, Thompson and Wilson (2004). The numerical simulations are run over 50 seconds and a time step of 0.01 seconds employed. The coarsest grid has 9 nodes; there are 4 levels including the coarsest. The tests were done over three different topographies described below. Variants of the conjugate gradient method are tested, namely:

- Conjugate Gradient Method with Polak-Riberie update (CGPR)
- Conjugate Gradient Method with Fletcher-Reeves update (CGFR)
- Preconditioned Conjugate Gradient Method with Polak-Riberie update (PCGPR)
- Preconditioned Conjugate Gradient Method with Fletcher-Reeves update (PCGFR)
- Conjugate Gradient Method using Charalambous line search method (CGlnsrch)
- Broyden Secant Method (Broyden)
- Newton Method (Newt)

Another variation of the conjugate gradient method is to restart the iteration process every N iterations (in our case every two), the reasoning behind this is that only N conjugate directions can be created (even though each direction is conjugate to the previous search direction) in an N -dimensional space. This is indicated in Table D.1 under the column 'restart'.

Time Taken (secs)						
Method	Case 1	Restart	Case 2	Restart	Case 3	Restart
CGPR	127	138	134	132	-	-
CGFR	FAIL	443	FAIL	447	-	-
PCGPR	56	60	61	62	60	60
PCGFR	56	60	61	62	59	61
Newt	49	-	54	-	49	-
Broyden	82	-	87	-	-	-
CGlnsrch	3178	-	2863	-	-	-

TABLE D.1: Time taken to complete a full numerical simulation involving 5002 time steps for two-dimensional thin film flow over various topographies.

Flow Parameters	
Flow rate	$2.85 \times 10^{-7} \text{m}^3/\text{s}$
Viscosity, μ	0.001Pa.s
Density, ρ	1000kg/m ³
Scaling height, H_0	0.0001m
Scaling velocity, U_0	0.004275 m/s
Capillarity number, Ca	6.10714×10^{-5}
Substrate length, L_0	$6.99 \times 10^{-4} \text{m} = 0.5L_0$

TABLE D.2: Parameters of the numerical simulation of flow over topography.

Three trenches with differing length and depth are used as the topographies. Case 1 has length $l_t = 0.1$ and depth $|s_0| = 0.1$, Case 2 has $l_t = 1.1$ and $|s_0| = 0.2$ and Case 3 has $l_t = 10.0$ and $|s_0| = 0.4$. The various flow parameters and fluid properties are displayed in Table D.2 and typical free-surface profiles produced are shown in Figure D.8.

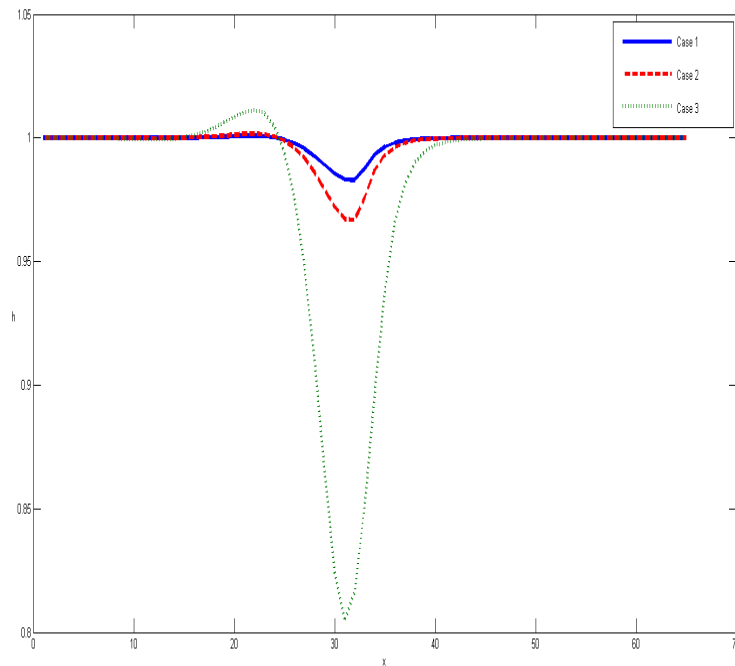


FIGURE D.8: Free-surface profiles for two-dimensional thin film flow over different spanwise topographies.

The results show a number of interesting features. The first point to make is the apparent ineffectiveness of the Charalambous line search (CGlnsrch), this may be due to the nature of the function being minimised and may not be suited to the problem. The next observation is that restarting the conjugate gradient iteration has little to no effect on the speed of the iterations; however, for CGFR it is necessary to prevent failure at some point of the conjugate gradient method within the specified number of maximum iterations.

Preconditioning is a very effective way of reducing convergence time as seen from the results. Using the exact inverse of the Hessian matrix at each point, for Polak-Riberie update it leads to a convergence rate that is more than twice as fast. This reflects an incredible reduction in computation time especially for finer grids with a significant number of nodes. An even greater improvement is seen with Fletcher-Reeves update, reducing the time of convergence to that of the PCGPR, to over 7 times faster than when CGFR is implemented. These results indicate the vital component that preconditioning is to iterative procedures. Should N be much larger it is possible to use an estimate of the Hessian, or even just to calculate the diagonal elements and use this matrix as the preconditioning matrix. Broyden's Secant method results in faster iteration times than both the CGFR and CGPR; however, is found to be slower than the preconditioned versions of these two methods.

The fastest method appears to be the Newtonian method, confirming Al-Baali and Fletcher's (Al-Baali and Fletcher, 1996) work where Newton's method is shown to be preferable to certain preconditioned versions of conjugate gradient methods. However the difference in practice is very small, and further refinement of the line search used by the conjugate gradient methods could lead to faster times when utilised in conjunction with the preconditioning methods described.

The problem being solved also appears to have only a small effect on the time taken for a full solution to be completed. As the size of the trench increases, and with it the disturbance of the film surface, the time for a full solution to reach convergence increases very slightly as would be expected.

Other investigations were carried out, including how the number of nodes effects the solution time and enabling time step adaptivity to effect the solution time. The same pattern of results is observed, obviously with more nodes the run time is significantly larger.

D.4.2 Three-dimensional flow

A similar investigation was carried out for three-dimensional film flow. In these investigations time adaptivity and mesh adaptivity are enabled. The simulations are run with an initial time step of 1×10^{-6} for a total of 1.5 seconds and a coarsest grid with 17 nodes in both the x and y direction. Only PCGFR, PCGPR and Newtonian smoothers are considered as they demonstrated the highest performance in the two dimensional situation.

Time Taken (secs)			
Method	Case 1	Case 2	Case 3
PCGPR	127	101	145
PCGFR	127	108	149
Newt	121	103	134

TABLE D.3: Time taken to complete a full numerical simulation using a FMG and FAS method with time and mesh adaptivity for three-dimensional thin film flow over various topographies.

It is interesting to note that, although time and mesh adaptivity are enabled, the number of time iterations performed are the same for all methods; this is due to the same specified tolerance being used, showing that all methods achieve the tolerance level in very similar time frames, see Table D.3. Two-dimensional tests completed without time and mesh adaptation enabled have very similar running times whereas there are much larger disparities when considering three-dimensional film flow; this suggests that the two-dimensional problem is more suited to the conjugate gradient relaxation than the three-dimensional problem is. For example, for Case 3 with no adaptation, Newtonian relaxation takes 271 seconds, using PCGPR the solution

takes 279 seconds.

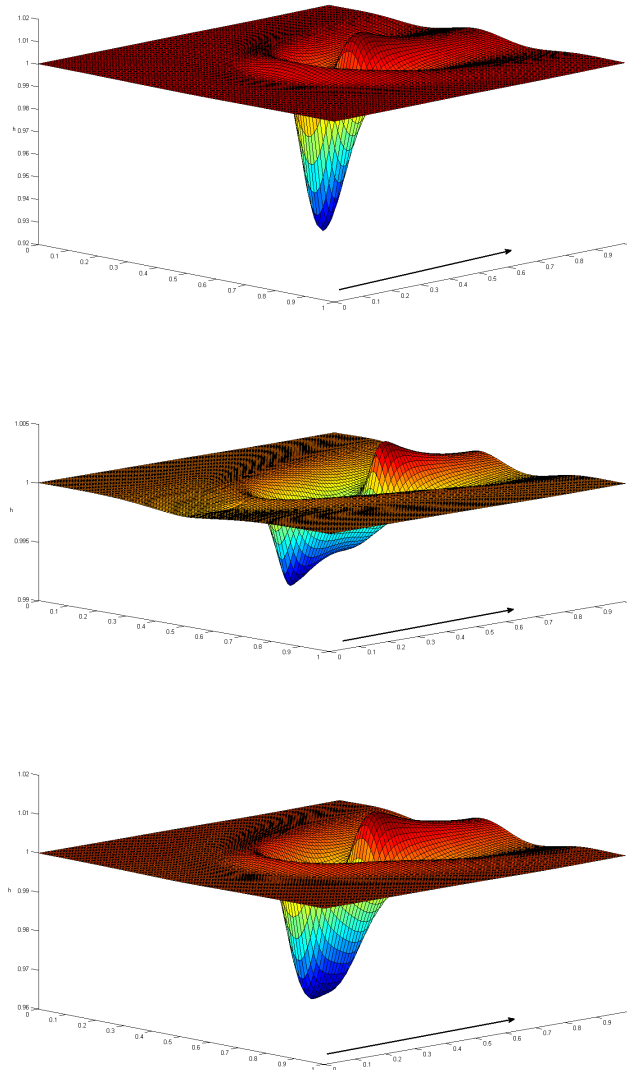


FIGURE D.9: Free-surface profile of flow over three different trenches: Case 1,2 and 3, which are ordered from top to bottom.

The three topographies used are specified as follows, in non-dimensional variables: Case 1 has $l_t = 0.1$, width $w_t = 0.1$ and $|s_0| = 0.1$. Case 2 has $l_t = 0.3$, width $w_t = 0.01$ and $|s_0| = 0.2$. Case 3 has $l_t = 0.2$, width $w_t = 0.1$ and $|s_0| = 0.05$. Each of the free-surface profiles formed at 1.5s are shown in Figure D.9.

Results reveal that, although the preconditioned conjugate gradient point smoother

is a comparatively efficient method, over large domains the Newtonian smoother is the most suitable and efficient iteration technique to employ as disparities in CPU time are magnified when using larger numbers of grid points and many time steps are being used. For this reason the Newtonian smoother is utilised in the multigrid algorithm described in Chapter 3 and was throughout the thesis in generating results based on solving the lubrication equations.

Bibliography

- AL-BAALI, M. AND FLETCHER, R. (1996) On the order of convergence of preconditioned nonlinear conjugate gradient methods. *SIAM J. Sci. Comput.* **17**(3), 658–665. 228, 229, 232
- ALEKSEENKO, S. V., NAKORYAKOV, V. E. AND POKUSAEV, B. G. (1994) Wave flow of liquid films 4
- AMESTOY, P. R., DUFF, I. S. AND L'EXCELLENT, J.-Y. (2000) Multifrontal parallel distributed symmetric and unsymmetric solvers. *Comp. Meth. Appl. Mech. Engrg.* **184**, 501–520. 163
- AMESTOY, P. R., DUFF, I. S., L'EXCELLENT, J.-Y. AND KOSTER, J. (2001) A fully asynchronous multifrontal solver using distributed dynamic scheduling. *SIAM J. Matr Anal. Appl.* **23**, 15–41. 163
- ARGYRIADI, K., VLACHOGIANNIS, M. AND BONTOZOGLOU, V. (2006) Experimental study of inclined film flow along periodic corrugations: The effect of wall steepness *Physics of Fluids* **18**(1), 012102. 20
- BALMFORTH, N. J. AND CRASTER, R. V. (2000) Dynamics of cooling domes of viscoplastic fluid. *Journal of Fluid Mechanics* **422**, 225–48. 3
- BAXTER, S. J., POWER, H., CLIFFE, K. A. AND HIBBERD, S. (2009) Three-dimensional thin film flow over and around an obstacle on an inclined plane. *Physics of Fluids* **21**. 16, 50
- BAXTER, S. J., POWER, H., CLIFFE, K. A. AND HIBBERD, S. (2010) Free surface stokes flows obstructed by multiple obstacles. *Internation Journal for Numerical Methods in Fluids* **62**(5), 530–564. 3, 16, 50
- BERTOZZI, A. L. AND BRENNER, M. P. (1997) Linear stability and transient growth in driven contact lines. *Physics of Fluids* **9**(3), 530–9. 8, 32, 39, 81, 137, 208
- BERTOZZI, A. L., MÜNCH, A., FANTON, X. AND CAZABAT, A. M. (1998) Contact line stability and "undercompressive shocks" in driven thin film flow. *Physical Review Letters* **81**(23), 5169. 32, 48

- BIELARZ, C. AND KALLIADASIS, S. (2003) Time-dependent free-surface thin film flows over topography. *Physics of Fluids* **15**(9). 40
- BLYTH, M. G. AND POZRIKIDIS, C. (2004) Effect of surfactant on the stability of film flow down an inclined plane *Journal of Fluid Mechanics* **521**, 241–250. 5
- BLYTH, M. G. AND POZRIKIDIS, C. (2006) Film flow down an inclined plane over a three-dimensional obstacle. *Physics of Fluids* **18**. 50
- BONN, D., EGGERS, J., INDEKEU, J., MEUNIER, J. AND ROLLEY, E. (2009) Wetting and spreading. *Reviews of Modern Physics* **81**(Article 739). 12
- BONTOZOGLOU, V. (2000) Laminar film flow along a periodic wall. *CMES - Comp. Model. Eng. Sci.* **1**(2), 133–142. 19
- BONTOZOGLOU, V. AND PAPAPOLYMEROU, G. (1997) Laminar film flow down a wavy incline *International Journal of Multiphase Flow* **23**(1), 69–79. 19
- BRANDT, ACHI AND LIVNE, OREN (1984) Multigrid techniques: 1984 guide with applications to fluid dynamics. 54
- BURELBACH, J. P., BANKOFF, S. G. AND DAVIS, S. H. (1988) Nonlinear stability of evaporating/condensing liquid films. *Journal of Fluid Mechanics Digital Archive* **195**(1), 463–494. 5
- BURELBACH, J. P., BANKOFF, S. G. AND DAVIS, S. H. (1990) Steady thermocapillary flows of thin liquid layers. ii. experiment *Physics of Fluids A: Fluid Dynamics* **2**(3), 322–333. 5
- BUTT, H-J., GRAF, K. AND KAPPL, M. (2013) Physics and chemistry of interfaces. pp. 118–119. 34
- CAIRNCROSS, RICHARD A., SCHUNK, P. RANDALL, BAER, THOMAS A., RAO, REKHA R. AND SACKINGER, PHILLIP A. (2000) A finite element method for free surface flows of incompressible fluids in three dimensions. part i. boundary fitted mesh motion. *International Journal for Numerical Methods in Fluids* **33**(3), 375–403. 62
- CASTREJON-PITA, J. R., BETTON, E. S., KUBIAK, K. J., WILSON, M. C. T. AND HUTCHINGS, I. M. (2011) The dynamics of the impact and coalescence of droplets on a solid surface *BiOMICROFLUIDICS* **5**(1), 014112. 3
- CAZABAT, A-M., HESLOT, F., TROIAN, S. M. AND CARLES, P. (1990) Fingering instability of thin spreading films driven by temperature gradients. *Nature* **346**. xv, xxiv, 2, 10, 14, 100, 101, 102, 107, 108, 109, 110, 121
- CHANG, H. (1994) Wave evolution on a falling film. *Annual Review of Fluid Mechanics* **26**(1), 103–136. 4

- CHARALAMBOUS, C. (1992) Conjugate gradient algorithm for efficient training of artificial neural networks. *Circuits, Devices and Systems, IEE Proceedings G* **139**(3). 226
- CHRISTODOULOU, K.N, KISTLER, S.F. AND SCHUNK, P. R. (1997) Advances in computational methods for free surface flows. pp. 297–366. 64
- CHUNG, T.J (2002) Computational fluid dynamics. 63, 70
- CHURAEV, N. V. AND DERJAGUIN, B. V. (1985) Inclusion of structural forces in the theory of stability of colloids and films. *Journal of Colloid and Interface Science* **103**(2), 542–553. 35, 36, 37
- CHURAEV, N. V. AND SOBOLEV, V. D. (1995) Prediction of contact angles on the basis of the frumkin-derjaguin approach. *Advances in Colloid and Interface Science* **61**(0), 1–16. 35, 36
- COWLING, N. P., GASKELL, P. H., LEE, Y. C. AND THOMPSON, H. M. (2011) Towards the efficient numerical solution of three-dimensional thin film flows on real surfaces: an evaluation of finite-difference-based schemes. *Proceedings of the Institution of Mechanical Engineers, Part C: Journal of Mechanical Engineering Science* . 32, 48, 212
- CRASTER, R. V. AND MATAR, O. K. (2006) On viscous beads flowing down a vertical fibre. *Journal of Fluid Mechanics* **553**, 85–105. 10, 124
- CRASTER, R. V. AND MATAR, O. K. (2009) Dynamics and stability of thin liquid films. *Reviews of Modern Physics* **81**. 2, 3, 207
- DAI, YU HONG AND YUAN, YA XIANG (2002) A note on the nonlinear conjugate gradient method. *J. Comp. Math.* **20**(6), 575–582. 226
- D’ALESSIO, S. J. D., PASCAL, J. P. AND JASMINE, H. A. (2009) Instability in gravity-driven flow over uneven surfaces. *Physics of Fluids* **21**(6), 062105–11. 5
- D’ALESSIO, S. J. D., PASCAL, J. P., JASMINE, H. A. AND OGDEN, K. A. (2010) Film flow over heated wavy inclined surfaces. *Journal of Fluid Mechanics* **FirstView**, 1–39. 5
- DAVIS, J. M. AND TROIAN, S. M. (2003) On a generalized approach to the linear stability of spatially nonuniform thin film flows. *Physics of Fluids* **15**(5), 1344–1347. 5, 8, 32, 41, 81, 207, 208
- DAVIS, S H (1987) Thermocapillary instabilities *Annual Review of Fluid Mechanics* **19**(1), 403–435. 5
- DE BRUYN, JOHN R. (1992) Growth of fingers at a driven three-phase contact line. *Physical Review A* **46**(8). 7

- DE GENNES, P. G. (1985) Wetting: statics and dynamics. *Reviews of Modern Physics* **57**(3), 827. 33, 34
- DE SANTOS, J. M., MELLI, T. R. AND SCRIVEN, L. E. (1991) Mechanics of gas-liquid flow in packed-bed contactors *Annual Review of Fluid Mechanics* **23**(1), 233–260. 3
- DECRÉ, M. M. J. AND BARET, J-C. (2003) Gravity-driven flows of viscous liquids over two-dimensional topographies. *Journal of Fluid Mechanics* **487**, 147–166. 16, 29, 47
- DERJAGUIN, B. V. (1940) Theory of capillary condensation and related capillary effects. calculation of spreading action of polymolecular liquid films. *Zh. Fiz. Khim.* **14** (2)(137). 35, 37
- DERJAGUIN, B. V. (1955) Definition of the concept of and magnitude of the disjoining pressure and its role in the statics and kinetics of thin layers of liquid. *Kolloidn. Zh.* **17**(191). 35
- DERJAGUIN, B. V., CHURAEV, N. V. AND MULLER, V. M. (1987) *Surface Forces*. Plenum Press. 13, 35
- DIEZ, J. A. AND KONDIC, L. (2001a) Contact line instabilities of thin liquid films. *Physical Review Letters* **86**(4). 32
- DIEZ, J. A. AND KONDIC, L. (2002) Computing three-dimensional thin film flows including contact lines. *Journal of Computational Physics* **183**(1), 274–306. 9, 32
- DIEZ, J. A., KONDIC, L. AND BERTOZZI, A. (2000) Global models for moving contact lines. *Physical Review E* **63**. 9
- DIEZ, J. A., KONDIC, L. AND BERTOZZI, A. (2001) Global models for moving contact lines. *Physical Review E (Statistical Physics, Plasmas, Fluids, and Related Interdisciplinary Topics)* **63**(1). 32
- DIEZ, JAVIER A. AND KONDIC, L. (2001b) Contact line instabilities of thin liquid films. *Physical Review Letters* **86**(4). 9, 102
- DORMAND, J.R. (1996) Numerical methods for differential equations: a computational approach. 54
- DUDDU, RAVINDRA, CHOPP, DAVID L. AND MORAN, BRIAN (2009) A two-dimensional continuum model of biofilm growth incorporating fluid flow and shear stress based detachment *Biotechnology and Bioengineering* **103**(1), 92–104. 3
- DUFFY, B. R. AND WILSON, S. K. (1999) Thin-film and curtain flows on the outside of a rotating horizontal cylinder. *Journal of Fluid Mechanics* **394**, 29–49. 10, 124

- EDMONSTONE, B. D., CRASTER, R. V. AND MATAR, O. K. (2006) Surfactant-induced fingering phenomena beyond the critical micelle concentration. *Journal of Fluid Mechanics* **564**, 105–38. 10
- EDMONSTONE, B. D., MATAR, O. K. AND CRASTER, R. V. (2005) Surfactant-induced fingering phenomena in thin film flow down an inclined plane. *Physica D: Nonlinear Phenomena* **209**(1-4), 62–79. 10
- ERES, M. H., SCHWARTZ, L. W. AND ROY, R. V. (2000) Fingering phenomena for driven coating films. *Physics of Fluids* **12**(6), 1278–1295. 9, 14
- EVANS, P. L., SCHWARTZ, L. W. AND ROY, R. V. (2004) Steady and unsteady solutions for coating flow on a rotating horizontal cylinder: Two-dimensional theoretical and numerical modeling. *Physics of Fluids* **16**(8), 2742–2756. 10, 124, 201
- FITT, A. D. AND POPE, M. P. (2001) De-icing by slot injection *Acta Mechanica* **147**(1-4), 73–86. 3
- FOCKE, W. W. AND KNIBBE, P. G. (1986) Flow visualization in parallel-plate ducts with corrugated walls *Journal of Fluid Mechanics* **165**, 73–77. 2
- FRANKEL, G. S. (1998) Pitting corrosion of metals: A review of the critical factors. *Journal of The Electrochemical Society* **145**(6), 2186–2198. 20
- FRAYSSE, N. AND HOMSY, G. M. (1994) An experimental study of rivulet instabilities in centrifugal spin coating of viscous newtonian and non-newtonian fluids. *Physics of Fluids* **6**(4), 1491–1504. 9
- FRUMKIN, A. N. (1938) On the phenomena of wetting and sticking of bubbles. *Zh. Fiz. Khim.* **12** (4)(337). 35
- GAO, L. M., MENG, Q. E., WANG, F. C., YANG, P. R. AND JIN, Z. M. (2007) Comparison of numerical methods for elastohydrodynamic lubrication analysis of metal-on-metal hip implants: Multi-grid verses newton-raphson *Proceedings of the Institution of Mechanical Engineers, Part J: Journal of Engineering Tribology* **221**(2), 133–140. 3
- GARRISON, BREVARD AND ROGERS, CHRIS (1994) An experimental study of enhanced fluid transfer mechanisms between a channel and a cavity. *Physics of Fluids* **6**(1), 421–423. 20
- GASKELL, P. H., JIMACK, P. K., KOH, Y. Y. AND THOMPSON, H. M. (2008) Development and application of a parallel multigrid solver for the simulation of spreading droplets. *International Journal for Numerical Methods in Fluids* **56**(8), 979–89. 48

- GASKELL, P. H., JIMACK, P. K., SELIER, M. AND THOMPSON, H. M. (2004) Efficient and accurate time adaptive multigrid simulations of droplet spreading. *International Journal for Numerical Methods in Fluids* **45**, 1161–1186. 13, 48, 49, 52, 53, 54, 201
- GASKELL, P. H., JIMACK, P. K., SELIER, M. AND THOMPSON, H. M. (2006) Flow of evaporating, gravity-driven thin liquid films over topography. *Physics of Fluids* **18**. 16, 49, 54
- GASKELL, P. H., JIMACK, P. K., SELIER, M., THOMPSON, H. M. AND WILSON, M. C. T. (2004) Gravity-driven flow of continuous thin liquid films on non-porous substrates with topography. *Journal of Fluid Mechanics* **509**, 253–280. x, 15, 16, 26, 40, 46, 47, 54, 136, 230
- GASKELL, P.H., LEE, Y.C. AND THOMPSON, H.M. (2010) Thin film flow over and around surface topography: a general solver for the long-wave approximation and related equations *Computer Modeling in Engineering and Sciences* **62**(1), 77–112. 16, 26, 57, 219, 224
- GLASS, C RICHARD, WALTERS, KEITH F A, GASKELL, P H, LEE, Y C, THOMPSON, H M, EMERSON, DAVID R AND GU, X-J (2009) Recent advances in computational fluid dynamics relevant to the modelling of pesticide flow on leaf surfaces. *Pest Management Science* **September**. 3
- GOMBA, J. M. (2012) Thin-film flows with moving contact lines: An approach to reducing computing time. *Physical Review E* **85**(5). 60
- GROSSMAN, CHRISTIAN, ROOS, HANS-GORG AND STYNES, MARTIN (2007) Numerical treatment of partial differential equations. 228
- GROTBERG, J B (1994) Pulmonary flow and transport phenomena. *Annual Review of Fluid Mechanics* **26**(1), 529–571. 3
- HAGER, W. W. AND ZHANG, HONGCHAO (2006) A survey of nonlinear conjugate gradient methods. *Pacific Journal of Optimisation* **2**(1). 228
- HEINING, C. AND AKSEL, N. (2009) Bottom reconstruction in thin-film flow over topography: Steady solution and linear stability. *Physics of Fluids* **21**(8). 50
- HEINING, C., BONTOZOGLOU, V., AKSEL, N. AND WIERSCHEM, A. (2009) Nonlinear resonance in viscous films on inclined wavy planes. *International Journal of Multiphase Flow* **35**(1), 78–90. 19, 20
- HEINING, C., POLLAK, T. AND AKSEL, N. (2012) Pattern formation and mixing in three-dimensional film flow *Physics of Fluids* **24**(4), 042102. 21, 50
- HOCKING, L. M. (1990) Spreading and instability of a viscous fluid sheet. *Journal of Fluid Mechanics* **211**, 373–392. 8

- HOLLAND, D., DUFFY, B. R. AND WILSON, S. K. (2001) Thermocapillary effects on a thin viscous rivulet draining steadily down a uniformly heated or cooled slowly varying substrate *Journal of Fluid Mechanics* **441**, 195–221. 10
- HOOD, P. AND TAYLOR, C. (1974) Navier-stokes equations using mixed interpolation. pp. 121–132. 64
- HORNER, M., METCALFE, G., WIGGINS, S. AND OTTINO, J. M. (2002) Transport enhancement mechanisms in open cavities. *Journal of Fluid Mechanics* **452**, 199–229. 20, 158, 161
- HORNER, MARC, MILLER, WILLIAM M., OTTINO, J. M. AND PAPOUTSAKIS, E. TERRY (1998) Transport in a grooved perfusion flat-bed bioreactor for cell therapy applications. *Biotechnology Progress* **14**(5), 689–698. 3, 20
- HOWES, TONY AND SHARDLOW, PAUL J. (1997) Simulation of mixing in unsteady flow through a periodically obstructed channel. *Chemical Engineering Science* **52**(7), 1215–1225. 20
- HUPPERT, H. E. (1982) Flow and instability of a viscous current down a slope. *Nature* **300**(5891), 427–9. ix, xiv, xvii, xix, 2, 6, 7, 8, 9, 72, 79, 91, 92, 93, 97, 134, 136, 146
- JAMEEL, AHMAD T. AND SHARMA, ASHUTOSH (1994) Morphological phase separation in thin liquid films: Ii. equilibrium contact angles of nanodrops coexisting with thin films. *Journal of Colloid and Interface Science* **164**(2), 416–427. 36
- JANA, S. C. AND OTTINO, J. M. (1992) Chaos-enhanced transport in cellular flows *Philosophical Transactions: Physical Sciences and Engineering*. **338**(1651), 519–532. 20
- JERRETT, J. M. AND BRUYN, J. R. DE (1992) Fingering instability of a gravitationally driven contact line. *Physics of Fluids A* **4**. 7, 9, 13, 83, 91
- JIMACK, P. K. AND WATHEN, A. J. (1991) Temporal derivatives in the finite element method on continuously deforming grids. *SIAM J. Num. Analysis* **28**, 990–1003. 64
- JOHNSON, M. F. G. (1997) Experimental study of a thin liquid film flowing down an inclined plane. *Northwestern University* . xii, xiii, 8, 32, 72, 73, 74, 75, 79, 85, 89, 91, 97
- JOHNSON, M. F. G., SCHLUTER, R. A., MIKSIS, M. J. AND BANKOFF, S. G. (1999) Experimental study of rivulet formation on an inclined plate by fluorescent imaging. *Journal of Fluid Mechanics* **394**, 339–354. xii, xiii, xiv, xxiv, 7, 9, 23, 72, 73, 74, 79, 80, 81, 83, 89, 91, 92, 93
- KALLIADASIS, S. (2000) Nonlinear instability of a contact line driven by gravity. *Journal of Fluid Mechanics* **413**, 355–78. 8

- KALLIADASIS, S., BIELARZ, C. AND HOMSY, G. M. (2000) Steady free-surface thin film flows over topography. *Physics of Fluids* **12**(8). 5, 40
- KALLIADASIS, S. AND HOMSY, G. M. (2001) Stability of free-surface thin-film flows over topography. *Journal of Fluid Mechanics* **448**, 387–410. 5, 47
- KALLIADASIS, SERAFIM AND CHANG, HSUEH-CHIA (1994) Drop formation during coating of vertical fibres. *Journal of Fluid Mechanics* **261**, 135–168. 124
- KATAOKA, D. E. AND TROIAN, S. M. (1997) A theoretical study of instabilities at the advancing front of thermally driven coating films . *Journal of Colloid and Interface Science* . 10, 14, 47, 100, 109, 110
- KATAOKA, D. E. AND TROIAN, S. M. (1999) Patterning liquid flow on the microscopic scale. *Nature* **402**(6763). 14, 100, 110
- KELLEY, C.T. (2003) Solving nonlinear equations with newton's method. 224, 225
- KISTLER, K. F. AND SCHWEIZER, P. M. (1997) Liquid film coating. 51, 62, 66
- KONDIC, L. (2003) Instabilities in gravity driven flow of thin fluid films. *SIAM Review* **45**(1), 95–115. 9, 81, 82, 207, 208
- KONDIC, L. AND DIEZ, J. (2001) Pattern formation in the flow of thin films down an incline: Constant flux configuration. *Physics of Fluids* **13**(11), 3168–3184. 9, 32, 39, 40, 47, 52, 76, 110, 154, 203
- KONDIC, L. AND DIEZ, J. (2002) Flow of thin films on patterned surfaces: Controlling the instability. *Physical Review E* **65**(4). 11, 110, 113
- KONDIC, L. AND DIEZ, J. A. (2005) On nontrivial traveling waves in thin film flows including contact lines. *Physica D: Nonlinear Phenomena* **209**(1-4), 135–144. 9, 74
- KONDIC, LOU AND DIEZ, JAVIER (2004) Instabilities in the flow of thin films on heterogeneous surfaces. *Physics of Fluids* **16**(9), 3341–3360. 9, 11, 14, 76
- LE GRAND-PITEIRA, NOLWENN, DAERR, ADRIAN AND LIMAT, LAURENT (2006) Meandering rivulets on a plane: A simple balance between inertia and capillarity. *Physical Review Letters* **96**(25), 254503. 191
- LEE, Y. C., THOMPSON, H. M. AND GASKELL, P. H. (2007) An efficient adaptive multigrid algorithm for predicting thin film flow on surfaces containing localised topographic features. *Computers and Fluids* **36**, 838–855. 16, 40, 47, 49, 51, 54, 56, 58, 204
- LEE, Y. C., THOMPSON, H. M. AND GASKELL, P. H. (2008) The efficient and accurate solution of continuous thin film flow over surface patterning and past occlusions. *International Journal for Numerical Methods in Fluids* **56**(8), 1375–81. 16, 40, 47

- LEE, Y. C., THOMPSON, H. M. AND GASKELL, P. H. (2009a) FilmPar: A parallel algorithm designed for the efficient and accurate computation of thin film flow on functional surfaces containing micro-structure *Computer Physics Communications* **180**(12), 2634–2649. 47, 48
- LEE, Y. C., THOMPSON, H. M. AND GASKELL, P. H. (2009b) Thin film flow over flexible membranes containing surface texturing: Bio-inspired solutions *Proceedings of the Institution of Mechanical Engineers, Part J: Journal of Engineering Tribology* **223**(3), 337–345. 49
- LESLIE, G. A., WILSON, S. K. AND DUFFY, B. R. (2011) Non-isothermal flow of a thin film of fluid with temperature-dependent viscosity on a stationary horizontal cylinder. *Physics of Fluids* **23**(6), 062101–14. 10, 124
- LI, YIBAO, LEE, HYUN GEUN, YOON, DAEKI, HWANG, WOONJAE, SHIN, SUYEON, HA, YOUNGSOO AND KIM, JUNSEOK (2011) Numerical studies of the fingering phenomena for the thin film equation. *International Journal for Numerical Methods in Fluids* **67**(11), 1358–1372. 59
- LIN, BINGCHENG (2011) *Microfluidics: technologies and applications*. 2
- LIN, T.-S., KONDIC, L. AND FILIPPOV, A. (2012) Thin films flowing down inverted substrates: Three-dimensional flow *Physics of Fluids* **24**(2), 022105. 10
- LIN, TE-SHENG AND KONDIC, LOU (2010) Thin films flowing down inverted substrates: Two dimensional flow *Physics of Fluids* **22**(5), 052105–10. 10
- LIU, JUN AND GOLLUB, J. P. (1993) Onset of spatially chaotic waves on flowing films *Physical Review Letters* **70**(15), 2289–2292. 4
- LIU, JUN AND GOLLUB, J. P. (1994) Solitary wave dynamics of film flows *Physics of Fluids* **6**(5), 1702–1712. 4
- LUO, H. AND POZRIKIDIS, C. (2007) Gravity-driven film flow down an inclined wall with three-dimensional corrugations. *Acta Mechanica* **188**(3), 209–225. 50
- MALAMATARIS, N. A. AND BONTOZOGLOU, V. (1999) Computer aided analysis of viscous film flow along an inclined wavy wall *Journal of Computational Physics* **154**(2), 372–392. 19
- MARSHALL, J. S. AND WANG, S. (2005) Contact-line fingering and rivulet formation in the presence of surface contamination. *Computers and Fluids* **34**(6), 664–683. 14, 84
- MATAR, O. K. AND TROIAN, S. M. (1999) The development of transient fingering patterns during the spreading of surfactant coated films. *Physics of Fluids* **11**(11), 3232–3246. 3, 10

- MAVROMOUSTAKI, A., MATAR, O. K. AND CRASTER, R. V. (2013a) Dynamics of a climbing surfactant-laden film i: Base-state flow. *Journal of Colloid and Interface Science* **371**(1), 107–120. 10
- MAVROMOUSTAKI, A., MATAR, O. K. AND CRASTER, R. V. (2013b) Dynamics of a climbing surfactant-laden film ii: Stability. *Journal of Colloid and Interface Science* **371**(1), 121–135. 10
- MAYO, LISA C., MCCUE, SCOTT W. AND MORONEY, TIMOTHY J. (2013) Gravity-driven fingering simulations for a thin liquid film flowing down the outside of a vertical cylinder. *Physical Review E* **87**(5), 053018. 10, 48, 124, 136, 137, 143, 146, 155
- MELO, F., JOANNY, J. F. AND FAUVE, S. (1989) Fingering instability of spinning drops. *Physical Review Letters* **63**(18), 1958–1961. 2, 9
- MENETRIER-DEREMBLE, LAURE AND TABELING, PATRICK (2006) Droplet breakup in microfluidic junctions of arbitrary angles *Physical Review E* **74**(3), 035303. 2
- MENG, Q E, LIU, F, FISHER, J AND JIN, Z M (2011) Transient elastohydrodynamic lubrication analysis of a novel metal-on-metal hip prosthesis with a non-spherical femoral bearing surface. *Proceedings of the Institution of Mechanical Engineers, Part H: Journal of Engineering in Medicine* **225**(1), 25–37. 3
- MITLIN, VLADIMIR S. (1995) Dewetting conditions for ionic liquid films: Novel features of the stability diagram. *Journal of Colloid and Interface Science* **170**(1), 65–70. 35
- MITLIN, VLADIMIR S. AND PETVIASHVILI, NIKOLAI V. (1994) Nonlinear dynamics of dewetting: kinetically stable structures. *Physics Letters A* **192**(5-6), 323–326. 36
- MOFFATT, H. K. (1964) Viscous and resistive eddies near a sharp corner *Journal of Fluid Mechanics* **18**(01), 1–18. 181
- MOYLE, D. T., CHEN, M. S. AND HOMSY, G. M. (1999) Nonlinear rivulet dynamics during unstable wetting flows. *International Journal of Multiphase Flow* **25**(6-7), 1243–1262. 9
- NONG, K. AND ANDERSON, D. (2010) Thin film evolution over a thin porous layer: Modeling a tear film on a contact lens *SIAM Journal on Applied Mathematics* **70**(7), 2771–2795. 3
- OGDEN, K. A., D’ALESSIO, S. J. D. AND PASCAL, J. P. (2011) Gravity-driven flow over heated, porous, wavy surfaces. *Physics of Fluids* **23**(12), 122102. 5
- ORON, A., DAVIS, S. H. AND BANKOFF, S. G. (1997) Long-scale evolution of thin liquid films. *Reviews of Modern Physics* **69**(3), 931–980. 4, 26, 29, 46, 195

- PETERS, K., WENGELER, L., SCHARFER, P. AND SCHABEL, W. (2013) Liquid film coating of small molecule oleds. *Journal of Coatings Technology and Research* **August**. 3
- POPESCU, M. N., OSHANIN, G., DIETRICH, S. AND CAZABAT, A.-M. (2012) Precursor films in wetting phenomena *Journal of Physics Condensed Matter* **24**(24). 32
- POZRIKIDIS, C. AND THORODDSEN, S. T. (1991) The deformation of a liquid film flowing down an inclined plane wall over a small particle arrested on the wall. *Physics of Fluids* **3**(11). 50
- PRESS, W.H., TEUKOLSKY, S.A., VETTERLING, W.T. AND FLANNER, B.P. (2002) Numerical recipes in c++ : the art of scientific computing. 224, 226, 227
- PYTLAK, R. AND TARNAWSKI, T. (2006) Preconditioned conjugate gradient algorithms for nonconvex problems. *Pacific Journal of Optimisation* **2**(1), 81–104. 228
- PYTLAK, R. (2009) Conjugate gradient algorithms in nonconvex optimization. **89**. 228
- RATHOD, H.T., NAGARAJA, K.V., VENKATESUDU, B. AND RAMESH, N.L. (2004) Gauss legendre quadrature over a triangle. *Journal of the Indian Institute of Science* **84**, 183–188. 70
- ROSEN, MILTON J. (2004) Wetting and its modification by surfactants. pp. 243–276. 33
- ROY, R. V., ROBERTS, A. J. AND SIMPSON, M. E. (2002) A lubrication model of coating flows over a curved substrate in space *Journal of Fluid Mechanics* **454**, 235–61. 124
- SCHMUKI, P. AND LASO, M. (1990) On the stability of rivulet flow. *Journal of Fluid Mechanics* **215**, 125–143. 8
- SCHOLLE, M. AND AKSEL, N. (2007) A general free surface rule for stokes flow of fluid films over obstacles. *Acta Mechanica* **191**, 155–159. 50
- SCHOLLE, M., HAAS, A., AKSEL, N., THOMPSON, H. M., HEWSON, R. W. AND GASKELL, P. H. (2009) The effect of locally induced flow structure on global heat transfer for plane laminar shear flow. *International Journal of Heat and Fluid Flow* **30**(2), 175–185. 18, 163
- SCHOLLE, M., HAAS, A., AKSEL, N., WILSON, M. C. T., THOMPSON, H. M. AND GASKELL, P. H. (2008) Competing geometric and inertial effects on local flow structure in thick gravity-driven fluid films. *Physics of Fluids* **20**. x, 18, 19, 50, 164, 165, 175, 178, 184

- SCHOLLE, M., HAAS, A., AKSEL, N., WILSON, M. C. T., THOMPSON, H. M. AND GASKELL, P. H. (2009) Eddy genesis and manipulation in plane laminar shear flow. *Physics of Fluids* **21**(7). 19
- SCHOLLE, M., RUND, A. AND AKSEL, N. (2006) Drag reduction and improvement of material transport in creeping films *Archive of Applied Mechanics* **75**(2), 93–112. 19, 21, 50, 165
- SCHOLLE, M., WIERSCHEM, A. AND AKSEL, N. (2004) Creeping films with vortices over strongly undulated bottoms. *Acta Mechanica* **168**(3-4), 167–93. 19, 50, 165
- SCHWARTZ, L. W. (1989) Viscous flows down an inclined plane: Instability and finger formation. *Physics of Fluids A: Fluid Dynamics* **1**(3), 443–445. 9, 48
- SCHWARTZ, L. W. (1998) Hysteretic effects in droplet motions on heterogeneous substrates: direct numerical simulation. *Langmuir* **14**(12), 3440–53. 13
- SCHWARTZ, L. W. AND ELEY, R. R. (1998) Simulation of droplet motion on low-energy and heterogeneous surfaces. *Journal of Colloid and Interface Science* **202**, 173–188. xi, 12, 32, 36, 37, 39, 48
- SCHWARTZ, L. W., ROY, R. V., ELEY, R. R. AND PRINCEN, H. M. (2004) Surfactant-driven motion and splitting of droplets on a substrate. *Journal of Engineering Mathematics* **50**, 157–175. 2
- SELLIER, M. (2003) The numerical solution of thin film flow over heterogeneous substrates. 28
- SELLIER, M. AND PANDA, S. (2009) Beating capillarity in thin film flows. *International Journal for Numerical Methods in Fluids* . 49
- SHKADOV, V. YA (1967) Wave flow regimes of a thin layer of viscous fluid subject to gravity. *Fluid Dynamics* **2**(1), 29–34. 17
- SILVI, N. AND DUSSAN, E. B. V. (1985) The rewetting of an inclined solid surface by a liquid. *Physics of Fluids* **28**. ix, 7, 9, 11, 13, 83, 84, 91, 138
- SMOLKA, LINDA B. AND SEGALL, MARC (2011) Fingering instability down the outside of a vertical cylinder. *Physics of Fluids* **23**(9), 092103. xvii, xviii, xix, 10, 124, 128, 134, 135, 138, 143, 146, 148, 154, 199
- SPAID, M. A. AND HOMSY, G. M. (1996) Stability of newtonian and viscoelastic dynamic contact lines. *Physics of Fluids* **8**, 460. 8, 32, 41, 81
- SPAID, M. A. AND HOMSY, G. M. (1997) Stability of viscoelastic dynamic contact lines: An experimental study. **9**. 8
- STILLWAGON, L. E. AND LARSON, R. G. (1988) Fundamentals of topographic substrate leveling. *Journal of Applied Physics* **63**(11), 5251–5258. 16, 31

- STILLWAGON, L. E. AND LARSON, R. G. (1990) Leveling of thin films over uneven substrates during spin coating. *Physics of Fluids A: Fluid Dynamics* **2**(11), 1937–1944. 16, 47
- STILLWAGON, L. E., LARSON, R. G. AND TAYLOR, G. N. (1987) Planarization of substrate topography by spin coating *Journal of The Electrochemical Society* **134**(8), 2030–2037. 16
- STONE, H. A., STROOCK, A. D. AND AJDARI, A. (2004) Engineering flows in small devices. **36**, 381–411. 3
- SZULCZEWSKA, B., ZBICINSKI, I. AND GRAK, A. (2003) Liquid flow on structured packing: Cfd simulation and experimental study. *Chemical Engineering & Technology* **26**(5), 580–584. 158
- TAKAGI, DAISUKE AND HUPPERT, HERBERT E. (2010) Flow and instability of thin films on a cylinder and sphere. *Journal of Fluid Mechanics* **647**(-1), 221–238. 10, 124
- TANEDA, S. (1979) Visualization of separating stokes flows *Journal of the Physical Society of Japan* **46**, 1935. 18
- TELETZKE, GARY F., DAVIS, H. TED AND SCRIVEN, L.E. (1987) How liquids spread on solids. *Chemical Engineering Communications* **55**(1), 41 – 82. 35, 36
- TIGHE, STEVEN AND MIDDLEMAN, STANLEY (1985) An experimental study of convection-aided removal of a contaminant from a cavity in a surface. *Chemical Engineering Communications* **33**(1-4), 149–157. 20
- TRIFONOV, YU (2007) Stability and nonlinear wavy regimes in downward film flows on a corrugated surface *Journal of Applied Mechanics and Technical Physics* **48**(1), 91–100. 5
- TROIAN, S. M., HERBOLZHEIMER, E., SAFRAN, S. A. AND JOANNY, J. F. (1989) Fingering instabilities of driven spreading films. *EPL (Europhysics Letters)* **10**(1), 25. xiv, 7, 8, 9, 41, 81, 92, 93, 110, 136, 137, 207, 208
- TROTTEBERG, U., OOSTERLEE, C.W. AND SCHULLER, A. (2001) Multigrid 49, 54, 56
- VEREMIEIEV, S. (2011) Gravity-driven continuous thin film flow over topography. 18, 46, 50, 62, 70
- VEREMIEIEV, S., THOMPSON, H. M., LEE, Y. C. AND GASKELL, P. H. (2010) Inertial thin film flow on planar surfaces featuring topography. *Computers and Fluids* **39**(3), 431–450. 17, 49, 191

- VEREMIEIEV, S., THOMPSON, H. M., SCHOLLE, M., LEE, Y. C. AND GASKELL, P. H. (2012) Electrified thin film flow at finite reynolds number on planar substrates featuring topography *International Journal of Multiphase Flow* **44**(0), 48–69. 17, 49
- VERETENNIKOV, I., INDEIKINA, A. AND CHANG, H. C. (1998) Front dynamics and fingering of a driven contact line. *Journal of Fluid Mechanics* **373**, 81–110. 7
- VLACHOGIANNIS, M. AND BONTOZOGLOU, V. (2002) Experiments on laminar film flow along a periodic wall. *Journal of Fluid Mechanics* **457**, 133–156. 5, 19
- WANG, C. Y. (1981) Liquid film flowing slowly down a wavy incline. *AIChE Journal* **27**(2), 207–212. 50
- WANG, C. Y. (2005) Low reynolds number film flow down a three-dimensional bumpy surface *Journal of Fluids Engineering* **127**(6), 1122–1127. 50
- WANG, M.C. AND CHOUD, F.C. (2001) Fingering instability and maximum radius at high rotational bond number *Journal of The Electrochemical Society* **148**(5), 283–290. 9
- WARNER, M. R. E., CRASTER, R. V. AND MATAR, O. K. (2004a) Fingering phenomena associated with insoluble surfactant spreading on thin liquid films. *Journal of Fluid Mechanics* **510**, 169–200. 10
- WARNER, M. R. E., CRASTER, R. V. AND MATAR, O. K. (2004b) Fingering phenomena created by a soluble surfactant deposition on a thin liquid film. *Physics of Fluids* **16**(8), 2933–2951. 10
- WEIDNER, DAVID E., SCHWARTZ, LEONARD W. AND ERES, MURAT H. (1997) Simulation of coating layer evolution and drop formation on horizontal cylinders. *Journal of Colloid and Interface Science* **187**(1), 243–258. 48
- WENGELER, L., SCHMITT, M., PETERS, K., SCHARFER, P. AND SCHABEL, W. (2013) Comparison of large scale coating techniques for organic and hybrid films in polymer based solar cells. *Chemical Engineering and Processing: Process Intensification* **68**, 38–44. 3
- WESSELING, P. (1992) An introduction to multigrid methods. *Chichester: Wiley* . 49, 54
- WIERSCHEM, A. AND AKSEL, N. (2003) Instability of a liquid film flowing down an inclined wavy plane. *Physica D: Nonlinear Phenomena* **186**(3-4), 221–237. x, 18, 19
- WIERSCHEM, A. AND AKSEL, N. (2004) Influence of inertia on eddies created in films creeping over strongly undulated substrates. *Physics of Fluids* **16**(12). xxi, 18, 19, 20, 158, 169, 173, 178

- WIERSCHEM, A., BONTOZOGLOU, V., HEINING, C., UECKER, H. AND AKSEL, N. (2008) Linear resonance in viscous films on inclined wavy planes *International Journal of Multiphase Flow* **34**(6), 580–589. 19
- WIERSCHEM, A., LEPSKI, C. AND AKSEL, N. (2005) Effect of long undulated bottoms on thin gravity-driven films. *Acta Mechanica* **179**(1), 41–66. 5
- WIERSCHEM, A., SCHOLLE, M. AND AKSEL, N. (2002) Comparison of different theoretical approaches to experiments on film flow down an inclined wavy channel *Experiments in Fluids* **33**, 429–442. 50
- WIERSCHEM, A., SCHOLLE, M. AND AKSEL, N. (2003) Vortices in film flow over strongly undulated bottom profiles at low reynolds numbers. *Physics of Fluids* **15**(2), 426–435. 19
- WILSON, MARK C. T., SUMMERS, J. L., KAPUR, N. AND GASKELL, P. H. (2006) Stirring and transport enhancement in a continuously modulated free-surface flow. *Journal of Fluid Mechanics* **565**(1), 319–351. x, 21, 50, 64, 65, 158
- WILSON, S. K. AND DUFFY, B. R. (1998) On the gravity-driven draining of a rivulet of viscous fluid down a slowly varying substrate with variation transverse to the direction of flow. *Physics of Fluids* **10**(1), 13–22. 47
- WILSON, S. K. AND DUFFY, B. R. (2005) When is it energetically favorable for a rivulet of perfectly wetting fluid to split? *Physics of Fluids* **17**, 078104. 47
- WILSON, S. K., DUFFY, B. R. AND ROSS, A. B. (2002) On the gravity-driven draining of a rivulet of a viscoplastic material down a slowly varying substrate. *Physics of Fluids* **14**(2), 555–571. 47
- WOODS, F.S. (1926) *Advanced calculus: A course arranged with special reference to the needs of students of applied mathematics.* pp. 141–144. 31
- XIAO, JUNFENG, STONE, HOWARD A. AND ATTINGER, DANIEL (2012) Source-like solution for radial imbibition into a homogeneous semi-infinite porous medium *Langmuir* **28**(9), 4208–4212. 3
- YE, YI AND CHANG, HSUEH-CHIA (1999) A spectral theory for fingering on a prewetted plane. *Physics of Fluids* **11**(9), 2494–2515. 8
- YIH, CHIA-SHUN (1963) Stability of liquid flow down an inclined plane. *Physics of Fluids* **6**(3), 321–334. 4
- YONG LIANG, ZHANG, MATAR, O. K. AND CRASTER, R. V. (2002) Surfactant spreading on a thin weakly viscoelastic film. *Journal of Non-Newtonian Fluid Mechanics* **105**(1), 53–78. 3

- ZHAO, L. AND CERRO, R. L. (1992) Experimental characterization of viscous film flows over complex surfaces *International Journal of Multiphase Flow* **18**(4), 495–516. 18
- ZHAO, Y. AND MARSHALL, J. S. (2006) Dynamics of driven liquid films on heterogeneous surfaces. *Journal of Fluid Mechanics* **559**, 355–378. ix, 12, 14, 74, 110, 111, 113